N° d'ordre: Année 1996

UNIVERSITE DES SCIENCES ET TECHNOLOGIES DE LILLE

LABORATOIRE DE MECANIQUE DE LILLE

EUDIL - Groupe Fiabilité des Structures

THESE DE DOCTORAT

(LABEL EUROPEEN)

Spécialité: Mécanique

Présentée par

Andreas GROSS-WEEGE

COMPORTEMENT ET ENDOMMAGEMENT DE COMPOSITES RENFORCES A MATRICE METALLIQUE- PREVISIONS NUMERIQUES A L'ECHELLE MICRO- ET MACROSCOPIQUE

DEFORMATION AND DAMAGE BEHAVIOUR OF PARTICLE REINFORCED METAL MATRIX COMPOSITES - NUMERICAL PREDICTIONS ON THE MICRO- AND MACROSCALE

Soutenue le devant le jury composé de:

Rapporteur:	**Mr D. BAPTISTE**	ENSAM, Paris
Rapporteur:	**Mr H. BERNS**	Lehrstuhl für Werkstofftechnik, Ruhr-Universität Bochum
Rapporteur:	**Mr H. J. BÖHM**	Institut für Leichtbau und Flugzeugbau, Technische Universität Wien
Directeur de thèse:	**Mr D. WEICHERT**	Institut für Allgemeine Mechanik, RWTH Aachen
Examinateur:	**Mr B. LANDJERIT**	Ecole Universitaire d'Ingénieurs de Lille

TABLE OF CONTENTS

	Page
ABSTRACT	-01-
RESUMÉ	-02-
GLOSSARY OF CONVENTIONS AND NOTATIONS	-03-
GENERAL INTRODUCTION	-06-
I. TWO PHASE MATERIALS-THEIR GEOMETRICAL AND MECHANICAL CHARACTERIZATION	**-I.1-**
I.1-Experimental investigations	**-I.2-**
I.1.1-Geometric characteristics	-I.2-
I.1.1.1-The components	-I.2-
I.1.1.2-The morphology	-I.3-
I.1.2-Deformation characteristics	-I.5-
I.1.3-Damage characteristics	-I.7-
I.2-Analytical approaches	**-I.10-**
I.2.1-Effective elastic properties	-I.10-
I.2.1.1-General consideration	-I.12-
I.2.1.2-The bounds of Voigt and Reuss	-I.12-
I.2.1.3-Eshelby's equivalent inclusion solution	-I.13-
I.2.1.4-Other bounds and estimates	-I.17-
I.2.1.5-Discussion and comparison of the different approaches	-I.19-
I.2.2-Analysis of irreversible processes	-I.21-
I.2.2.1-Elasto-plastic behaviour of the matrix	-I.21-
I.2.2.2-Damage behaviour of the reinforcements	-I.22-
I.3-Numerical investigations	**-I.23-**
I.3.1-The micromechanical model	-I.23-
I.3.1.1-Modelling the entire microstructure	-I.23-
I.3.1.2-Modelling a microscopic section ahead of a macroscopic crack	-I.26-
I.3.2-The material model	-I.26-
I.3.2.1-Deformation of the components and the composite	-I.26-
I.3.2.2-Damage of the components and the composite	-I.27-
I.3.3-Modelling strategies and results	-I.28-
I.3.3.1-Unit cell investigations	-I.28-
I.3.3.2-Crack tip modelling	-I.30-
II. THE MATERIAL AND EXPERIMENTAL FINDINGS	**-II.1-**
II.1-The composite under consideration	**-II.2-**
II.1.1-The elaboration process	-II.2-
II.1.2-The components	-II.4-
II.1.2.1-The metal matrix (MM)	-II.4-
II.1.2.2-The hard phases (HP) and the interface	-II.4-
II.1.3-The heat treatment	-II.4-
II.1.3.1-General remarks	-II.4-
II.1.3.2-The composite and the equivalent material of the metal matrix	-II.5-
II.2-Geometrical characterization	**-II.6-**

II.2.1-Morphology of the composite -II.6-
II.2.2-Geometry of the hard phases (HP) -II.7-
II.3-Mechanical characterization -II.8-
II.3.1-Deformation characteristics -II.8-
II.3.1.1-Tension test -II.8-
II.3.1.2-Compression test -II.9-
II.3.1.3-Elasto-plastic material parameters used for numerical computations -II.10-
II.3.2-Damage characteristics -II.10-
II.3.2.1-Damage behaviour on the surface (experimental observations) -II.10-
II.3.2.2-Crack path -II.15-

III. CONTINUUM MECHANICAL FRAMEWORK OF ELASTIC FINITE PLASTICITY -III.1-
III.1-Kinematics -III.2-
III.1.1-Deformation -III.2-
III.1.2-Strain measures -III.4-
III.1.3-Rate of deformation -III.5-
III.2-Stress measures -III.7-
III.3-Equilibrium and virtual work -III.8-
III.4-Constitutive model for elasto-plastic materials at finite strain -III.9-
III.4.1-Decomposition of the deformation -III.9-
III.4.2-Application to metal plasticity (Hypothesis of small elastic strains) -III.11-
III.4.3-Objectivity of the constitutive model -III.12-

IV. LOCAL APPROACH OF MICROSCALE DAMAGE - AND THE TRANSITION TO THE MACROSCALE -IV.1-
IV.1-The microscopic model - Damage characteristics of the components -IV.2-
IV.1.1-The hard phases (HP) and the interface -IV.2-
IV.1.1.1 Particle fracture -IV.2-
IV.1.1.2 Interfacial failure -IV.3-
IV.1.2-The metal matrix (MM) -IV.5-
IV.2-Transition between the microscopic and the macroscopic model -IV.9-
IV.3-The macroscopic model - *Effective* deformation and damage characteristics -IV.10-

V. THE FE-PROGRAM -V.1-
V.1-The FE-Discretization -V.2-
V.1.1-Virtual work principle -V.2-
V.1.2-Linearization of the virtual work principle -V.3-
V.1.3-Discretisation by interpolation functions -V.4-
V.1.4-Elements -V.5-
V.2-The resolution of the non-linear problem -V.6-
V.2.1-The Newton-Raphson scheme -V.6-
V.2.2-Test of convergence -V.6-
V.2.3-The numerical integration method -V.7-
V.2.4-The equation solver -V.8-
V.3-The constitutive model under consideration -V.8-
V.3.1-Linear elasticity for isotropic and orthotropic materials -V.8-
V.3.2-Rate-independent plasticity for isotropic and orthotropic materials -V.9-
V.3.3-Integration of the constitutive model at elastic-finite-plastic strains -V.12-
V.3.3.1-Kinematic approximations -V.14-
V.3.3.2-Local integration of elasto-plastic constitutive laws -V.14-

V.3.3.3-Evaluation of the elasto-plastic matrix C^{ep} -V.18-
V.4-Characterization of local failure **-V.19-**
V.4.1-Particle fracture -V.19-
V.4.2-Interfacial failure -V.19-
V.4.3-Ductile matrix damage -V.21-
V.5-Coupling between the micro- and the macroscale **-V.21-**
V.5.1-Transition from the macro- to the microscale - *Zooming technique* -V.22-
V.5.2-Transition from the micro- to the macroscale - *Averaging technique* -V.22-
V.6-Pre-and Postprocessing and interface programs **-V.24-**

VI. SEMI-ANALYTICAL AND NUMERICAL INVESTIGATIONS OF THE DEFORMATION AND DAMAGE BEHAVIOUR **-VI.1-**
VI.A-Semi-analytical approach - Homogeneous loading (uniform) **-VI.2-**
VI.A.1-Effective elastic properties -VI.2-
VI.A.2-Effective elastic-plastic properties -VI.4-
VI.B-FEM-Simulations - Homogeneous loading (uniform) **-VI.9-**
VI.B.1-Modelling of a single HP in an infinite matrix (Interaction between HP-MM) -VI.9-
VI.B.1.1-Stress concentrations in a rectangular HP -VI.9-
VI.B.1.2-Crack initiation at a spherical HP -VI.15-
VI.B.2-Modelling of different microscale arrangements (Interaction between HP-HP) -VI.25-
VI.B.2.1-Model description -VI.25-
VI.B.2.2-Microscopic response -VI.26-
VI.B.2.3-Macroscopic response -VI.35-
VI.C-FEM-Simulations - Inhomogeneous loading (non-uniform) **-VI.39-**
VI.C.1-Combined macro- microscopic simulation of a TPB-test -VI.39-

GENERAL CONCLUSION **-C1-**

REFERENCES **-R1-**

APPENDIX **-A1-**
Appendix A-Material parameters used in simulations **-A2-**
A.1-Elastic constants used in simulations for the composite and their components -A2-
A.2-Stress-strain curves used in simulations for the composite -A2-
A.3-Stress-strain curves used in simulations for the metal matrix (MM) -A3-
Appendix B-On the numerical implementation of the elasto-plastic constitutive model **-A4-**
B.1-Local integration algorithms -A4-
B.1.1-Explicit forward Euler integration algorithms -A4-
B.1.1.1-General matrix formulation -A4-
B.1.1.2-Classical forward Euler first order integration algorithm -A5-
B.1.1.3-Modified forward Euler second order integration algorithm -A6-
B1.2-Implicit backward Euler integration algorithm (radial return algorithm) -A8-
B.2-Evaluation of the elasto-plastic matrix (tangent operator) C^{ep} -A9-
B.2.1-Continuum tangent operator -A9-
B.2.2-Consistent tangent operator (consistent with radial return algorithm) -A9-
B.3-Polar decomposition scheme -A11-
Appendix C-The Mori-Tanaka approach **-A12-**
C.1-Elasticity (Formulation by Benveniste) -A12-
C.2-Extension to plasticity (Secant approach) -A13-

ABSTRACT

The rising industrial interest in advanced materials with better adapted properties to their specific function, intensified considerably the research effort on micromechanics in the past decade. The development of such materials demands an optimal design of the microstructure and requires a fundamental understanding of the role of the microstructure on the overall properties. The microstructural parameters controlling the macroscopic properties are on one hand the morphology of the microstructure and on the other hand the constitutive behaviour of each individual component (e.g. plastic deformation, damage).

Based on experimental findings on a two-phase tool steel, a numerical model is developed which aims to study the deformation and damage behaviour of general particle reinforced MMCs. Local damage criteria in conjunction with advanced simulation techniques are proposed to automatically simulate failure events at the hard phases (HP) like particle fracture and interfacial debonding, as well as to predict the onset of damage in the ductile metal matrix (MM). To deal with elevated plastic strains, the classical J_2-flow theory is extended to full large deformation analysis.

FE-simulations on the microscale exhibit the strong influence of geometrical aspects like amount, shape and spatial distribution of HP on the local stress and strain pattern. First occurrence of damage is found to be controlled by the HP-shape as well as by the spacing and orientation between neighbouring HP with regard to the principal load direction. The sudden loss of load carrying capacity by microcracking affects stress redistribution and promotes failure of neighbouring HP. When HP are not regularly distributed over the microstructure but concentrated within colonies, the degree of continuity of such colonies becomes an important parameter: The large "matrix net" within cluster arrangements is found to act as an obstacle for microcracks of neighbouring clusters to link together.

In addition, different transition schemes between the micro- and macroscale are developed. Homogenization methods are applied to predict the overall behaviour in terms of effective properties of the composite. A new approach to derive an effective damage parameter from automatic simulation of progressive microcracking is proposed. This scheme allows to effectively quantify the influence of microstructural parameters on the overall damage response.
Finally, a microscopic section ahead of a fatigue crack of a TPB-specimen under realistic boundary conditions is modelled, combining the macro- with the microscopic model. Progressive carbide fracture is monitored over the macroscopic load.

Keywords
two-phase materials, metal matrix composites, finite element method, homogenization, plasticity, damage, particle fracture, interfacial debonding, large deformation

RÉSUMÉ

Durant les dernières années, l'intérêt des industriels pour les matériaux avancés possédant des caractéristiques mieux adaptées à leur utilisation a intensifié considérablement la recherche en micromécanique. L'objectif est d'acquérir une meilleure compréhension de la liaison entre la microstructure et les caractéristiques mécaniques macroscopiques. Les paramètres d'influence de cette relation sont d'une part la topologie de la microstructure et d'autre part le comportement de chaque composant individuel (déformation plastique, endommagement, etc.).

Le développement d'un modèle numérique, basé sur les observations expérimentales d'un acier d'outil bi-phasique, a permis d'étudier le comportement et l'endommagement de composites renforcés à matrice métallique. Différents critères d'endommagement locaux combinés à des méthodes de simulations avancées ont été proposés. Ceci afin de simuler la défaillance locale des phases dures (HP) par fissuration ou décohésion et afin de prévoir l'initiation de l'endommagement ductile de la matrice métallique (MM). Pour une analyse précise du comportement de la matrice à hautes déformations plastiques, la théorie géométriquement linéaire élasto-plastique a été étendue aux grandes déformations.

Les simulations à l'échelle microscopique montrent une forte influence des paramètres géométriques tels que la quantité, la forme et la distribution des phases dures sur le champs local de contraintes et de déformations. L'apparition initiale d'endommagement est contrôlée par la forme, la distance et l'orientation des phases dures voisines par rapport à la direction principale de charge. La perte soudaine de capacité de charge par microfissuration affecte la redistribution des contraintes et favorise la défaillance des phases dures voisines. Dans le cas où celles-ci ne sont pas distribuées régulièrement sur la microstructure mais concentrées en dehors des colonies, le degré de la continuité de ces colonies devient un paramètre important. La largeur des "bandes de la matrice" dans le cas d'arrangements groupés ("clusters") agit comme un obstacle à l'unification des microfissures des"clusters" adjacents.

Par ailleurs, différentes méthodes de transition entre l'échelle micro et macroscopique ont été développées. Des méthodes d'homogénéisation sont appliquées afin de prévoir le comportement global a partir des propriétés équivalentes du composite. Une nouvelle approche est proposée qui consiste à dériver un paramètre d'endommagement équivalent par des simulations incrémentales de microfissuration progressive. Cette méthode permet de mettre en valeur l'influence des caractéristiques microstructurales sur la réponse globale d'endommagement. Finalement, une section microscopique à la pointe d'une fissure de fatigue d'une éprouvette sollicitée en flexion trois points est modélisée. Les conditions aux limites réelles sont reproduites en combinant le modèle macro et microscopique. La rupture progressive des phases dures est visualisée au fur et à mesure du chargement macroscopique.

Mots-clés
matériau bi-phasique, composite à matrice métallique, méthode des éléments finis, homogénéisation, plasticité, endommagement, rupture des particules, décohésion matrice/renfort, grandes déformations

GLOSSARY OF CONVENTIONS AND NOTATIONS

CONVENTIONS

Vectors are given in boldface
Tensors are given in boldface block letters
Einstein's summation convention is adopted throughout this thesis
Material quantities - upper case e.g. ε^e, ε^p, (elastic, plastic strains)
Spatial quantities - lower case e.g. ε_{xx}, ε_{yy}, (strain components)
Phase quantities - lower case e.g. $\mathbf{C}_0$, $\mathbf{C}_r$ (constitutive tensor of phase 0 (= matrix), of phase r)

NOTATIONS

ABBREVIATIONS

CDM	Continuum damage mechanics
HP	Hard phase
MM	Metal matrix
HHPc	Region with high HP content
LHPc	Region with low HP content
CMC	Ceramic matrix composites
MMC	Metal matrix composite
PMMC	Particle reinforced metal matrix composites
bcc	Body centered cubic
fcc	Face centered cubic
sc	Simple cubic
FPZ	Fracture process zone
RA	Retained austenite
RVE	Representative volume element
SEM	Scanning electron microscope
TPB	Three-Point-Bending

Analytical approaches

ESH	Eshelby's equivalent solution
SC	Self Consistent model
HSW-/+	Lower and upper bound by Hashin Shtrikman Walpole
MT	Mori Tanaka
TPM	Three Phase model (Generalized self consistent model)

TENSORS AND MATRICES

Latins

$\mathbf{A}$	Eulerian strain tensor (Almansi-Euler)
$\mathbf{A}_\alpha$	Strain localisation tensor of phase α
$\mathbf{B}$	Left Cauchy-Green tensor
$\mathbf{B}$	Strain-displacement matrix
$\mathbf{B}_\alpha$	Stress concentration tensor of phase α

C	Right Cauchy-Green tensor
$\mathbf{C}^e$	Elastic constitutive matrix
D	Rate-of-deformation
D	Tensor to transform stresses and strains from the physical into the effective space
E	Green-Lagrange strain tensor
F	Deformation gradient
G	Matrix of derivatives of the shape functions **N**
I	Unit tensor of second order
J	Unit tensor of fourth order
J	Jacobian matrix
$\mathbf{K}_T$	Tangent stiffness matrix
L	Velocity gradient
M	Compliance matrix
N	Interpolation function
Q	Orthogonal rotation tensor
R	Tensor of rigid body rotation
R	Residual forces
S	Second Piola-Kirchhoff stress tensor
$\mathbf{S}_\alpha$	Eshelby's tensor of phase α
U	Lagrangian right stretch tensor
V	Lagrangian left stretch tensor
W	Spin tensor

Greeks

E	Macroscopic strain tensor
ε	Linear strain tensor
ε*	Stress-free strain (or eigenstrain)
Ω	Spin tensor with respect to the orthogonal rotation tensor **Q**
Π	First piola-Kirchhoff stress tensor
Σ	Macroscopic stress tensor
σ	Cauchy stress tensor
τ	Kirchhoff stress tensor

VECTORS

b	Body force
f	Surface traction
n	Normal vector
u	Displacement
v	Velocity

SCALARS

Latins

A	Total strain at rupture
C_α	Contiguity parameter of phase α
E	Young's modulus
D	Damage parameter

D_α	Mean linear particle spacing of phase α
d_α	Diameter of phase α
F	Yield function
f	Porosity
G	Shear modulus
J_1, J_2, J_3	First, second and third invariants
K	Bulk modulus
L_α	Mean size of phase α
M_α	Matricity of phase α
n	Hardening exponent
Q	Plastic potential
R_{eH}, R_{eL}	Upper and lower yield limit, respectively
$R_{p0.01}$, $R_{p0.2}$	Yield limit (at 0,01 and 0,2 % plastic deformation, respectively)
R_m	Ultimate tensile stress
r_α	Fraction of cluster parameter of phase α
S	Surface
Sid_α	Interface density of phase α
V	Volume

Greeks

δ	Crack opening
ε_v^p	Equivalent plastic strain
κ	Hardening parameter
φ	Crack deflection
$d\lambda$ or $\dot{\lambda}$	Plastic multiplier
λ	Aspect ratio
ν	Poisson's ratio
ρ	Crack-path-width
σ^D	Deviatoric stress
σ_H	Hydrostatic stress
σ_v	Equivalent stress of v. Mises
σ_{Y0}	Initial yield stress
ξ	Volume fraction
Ω	Configuration of a structure
ζ	Stress triaxiality

General Introduction

Background and Objectives of this thesis

Metal-matrix composites (MMCs) are rather recent material developments. Research work on this class of materials has occured for thirty years, mainly pushed by the aerospace industry. The great potential of MMCs with regard to both performance / reliability and ductility makes them attractive in various branches of applications. Other materials can only meet either one of these requirements: Fiber reinforced plastics are not suitable for high temperature applications, ceramic-matrix composites (CMCs) suffer under low ductility.

The attractive compromise between performance and ductility is founded on the combination of the advantages of two different constituents inherent in the material. The potential of ductility is attributed to the matrix whereas the reinforcements contribute to a high hardness, wear resistance, stiffness and strength of the material.

Dependent on the structural applications, the reinforcements are long fibers, short fibers, whiskers or particulates. Fiber or whisker reinforced MMCs are mainly used when the primary aim is to enhance overall strength and stiffness. Among them, continuously reinforced MMCs promise the highest performance. However, this is coupled with elevated processing costs. A rather good compromise between high performance and production costs is provided by particle reinforced MMCs. In addition, hard particles contribute to increase overall wear resistance particularly when they are embedded in a hardened matrix. This makes this class of materials irreplaceable in structural applications under severe tribological conditions. The term "particle reinforced metal matrix composites" (PMMCs) as such allows to attribute additionally a wide class of tool steels to MMCs since they consist of ceramic particles (metallic carbides) embedded in a metal matrix (e.g. α mixed crystal or martensite).

The development of advanced materials with better adapted properties to their specific function demands an optimal design of the microstructure. This requires a fundamental understanding of the role of the microstructure (microscale) on the overall properties (macroscale). This relationship is in particular influenced by irreversible processes on the microscale like plastic deformation and damage of the individual phases.

To this end, the major objective is to reveal the influence of microstructural parameters on these processes. These parameters are of geometrical (amount, size, shape, and distribution of reinforcements) as well as of physical nature (mismatch of elasto-plastic and damage related properties).

The present work aims to get a deeper insight and comprehension on this subject. For this analysis the FE-method is used. The development of the proper FE-Code Crackan started ten years ago aiming to model the deformation and damage behaviour of PMMCs on the microscale. Following this strategy, the present work has complemented the former works completing gaps in some domains. This concerns in particular the constitutive relations chosen for the individual constituents on the microscale as well as suitable transition schemes from the microscopic to the macroscopic model. This was realized by specific extensions of the FE-Code Crackan and additionally by the numerical formulation of a semi-analytical mean field approach.

Both, the FE-Code Crackan and the semi-analytical model are applied to a specific material which is representative for the broad class of particle reinforced MMCs. Here the ledeburitic chromium steel SAE-D3 (X210Cr12) was addressed. The reason for this choice is twofold:

a) industrial motivation, since the material is used in various branches of applications,
b) practical motivation, since extensive experimental work has been performed in former investigations.

Outline and original contributions to this thesis

This study is presented within six chapters:

Chapter I aims to summarize main contributions to the geometrical and mechanical analysis of general two-phase materials. Special emphasis is placed on the description of the microstructure and on the analysis of deformation and damage characteristics of the individual constituents and of the composite. Basic methods and strategies as well as important findings from experimental, theoretical and numerical point of view are reviewed and discussed.

Chapter II addresses the considered material. Experimental findings of former works on this material are summarized. The outcome of these findings (geometrical and mechanical characterization) [BRO 94, LÜS 95] provides an important basis for the development of the numerical model and its calibration.

Chapter III is concerned with the continuum mechanical framework. Since the deformation of the ductile matrix during loading is accompanied by large plastic strains, the classical geometrically linear theory within the elastic-plastic constitutive relations is no longer adequate. Therefore a fully nonlinear elastic-plastic constitutive model allowing for large strains has been developed. Basics of this large strain theory are presented within this chapter.

Chapter IV describes the microscopic model chosen for the individual constituents including the consideration of local failure. A numerical homogenization scheme is presented to predict the overall properties which characterizes the mechanical behaviour of the composite. Special attention is here devoted to the prediction of an effective macroscopic damage parameter. This scheme allows to quantify damage in an effective manner. In addition, these parameters may be used as fitting material parameters for subsequent macroscopic simulations using continuum damage mechanics models (CDM). Finally an adequate CDM-model is presented to describe the effective deformation and damage characteristics of the composite.

Chapter V presents in detail the FE-program. It is explained how the above mentioned constitutive equations are implemented into the FE-Code Crackan. Attention has been attached to the integration of the non-linear set of equations satisfying locally the constitutive equations and the global (virtual work principle) equilibrium. Finally, the FE-based equations for the formulation of the microscopic model are presented as well as the coupling between the micro- and macroscopic model.

Chapter VI is devoted to the numerical and semi-analytical analysis in order to investigate the deformation and damage behaviour of the material. It is studied how specific microstructural parameters influence the local field quantities (microscopic response). Applying the homogenization scheme their influence on the overall field quantities (macroscopic response) is equally investigated. The results are discussed in detail.

The thesis ends with a general conclusion. An outlook of further possible developments is discussed.

CHAPTER I

TWO-PHASE MATERIALS-
THEIR GEOMETRICAL AND MECHANICAL CHARACTERIZATION

I.1-Experimental investigations
I.1.1-Geometric characteristics
I.1.1.1-The components
I.1.1.2-The morphology
I.1.2-Deformation characteristics
I.1.3-Damage characteristics

I.2-Analytical approaches
I.2.1-Effective elastic properties
I.2.1.1-General considerations
I.2.1.2-The bounds of Voigt and Reuss
I.2.1.3-Eshelby's equivalent inclusion solution
I.2.1.4-Other bounds and estimates
I.2.1.5-Discussion and comparison of the different approaches
I.2.2-Analysis of irreversible processes
I.2.2.1-Elasto-plastic behaviour of the matrix
I.2.2.2-Damage behaviour of the reinforcements

I.3-Numerical investigations
I.3.1-The micromechanical model
I.3.1.1-Modelling the entire microstructure
I.3.1.2-Modelling a microscopic section ahead of a macroscopic crack
I.3.2-The material model
I.3.2.1-Deformation of the components and the composite
I.3.2.2-Damage of the components and the composite
I.3.3-Modelling strategies and results
I.3.3.1-Unit cell investigations
I.3.3.2-Crack tip modelling

I.1-Experimental investigations

I.1.1-Geometric Characteristics

I.1.1.1-THE COMPONENTS

A microstructure is firstly characterized by the number of individual *components* (*phases* or *phase mixtures*). In general, a number of *microconstituents* is allocated to one *component* if they have same mechanical properties (e.g. own constitutive equations). It is the task of the quantitative metallography to provide adequate parameters when describing the geometry of each individual component as well as the morphology of the composite assembly (see e.g. [EXN 86]). The most important quantitative geometrical parameter is the volume fraction ξ to measure the amount of one component. For a material with n+1 phases the volume fraction is defined by

$$\xi_r = \frac{V_r}{V}; \qquad \text{with } \sum_{r=0}^{N} \xi_r = 1 \tag{I.1.1}$$

Within a metallographic polished section the area fraction is determined either from linear fraction (fraction of a straight line) or from point fraction (fraction of points of a point grid that fall on one component) [EXN 93]. For an isotropic material the volume fraction is identical with the area fraction, for an anisotropic one it is associated to the averaged value by three orthogonal polished sections.

The mean size L_r of one component r is measured by the arithmetic mean value of all chord lengths l (mean free path) formed by straight lines when intersecting adjacent components and is inversely proportional to the interface density Sid_r of that component

$$\overline{L}_r = \frac{4\xi_r}{Sid_r} \tag{I.1.2a}$$

with

$$Sid_r = \frac{S_r}{V} \tag{I.1.2b}$$

where S_r is the area of the interface between the phase r and its neighbouring phase (e.g. the matrix) and V is the considered volume (e.g. the total volume of the specimen).

Correspondingly, the mean linear particle spacing D_r may also be expressed in terms of either L_r or Sid_r

$$\overline{D}_r = \frac{4(1-\xi_r)}{Sid_r} = \frac{\overline{L}_r(1-\xi_r)}{\xi_r} \tag{I.1.3a}$$

Here it shall be noticed that for a discrete regular distribution of spherical particles α with diameter d_α in a continuous matrix, the mean particle spacing D_α is approximated in the plane by Ashby [ASH 64]

$$\overline{D}_\alpha = \frac{d_\alpha}{2}\sqrt{\frac{\pi}{\xi_\alpha}} \tag{I.1.3b}$$

and in the space by Hahn and Rosenfield [HAH 73]

$$\overline{D}_\alpha = d_\alpha \sqrt[3]{\frac{\pi}{6\xi_\alpha}} \qquad \text{(I.1.3c)}$$

The description of the shape of a component by only one parameter might be difficult due to its statistical distribution. A global quantitative parameter which describes the sphericity of a phase is proposed by Exner et al [EXN 93]. It compares the interface density of a phase with an hypothetical interface for spherical constituents of one phase with same size

$$\lambda_{rshape} = \frac{Sid_r(\text{spheres of identical size})}{Sid_r(\text{real microstructure})} \qquad \text{(I.1.4a)}$$

If the constituents of a phase are elongated in a preferred orientation their shape is effectively described by the aspect ratio; the fraction of highest h to lowest dimension b (Fig. I.1.1).

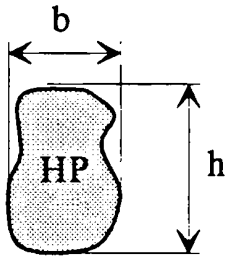

Fig.I.1.1. Geometrical illustration of the aspect ratio

$$\lambda_{rShape} = \frac{\overline{L}_{rh}}{\overline{L}_{rb}} = \frac{h}{b} \qquad \text{(I.1.4b)}$$

I.1.1.2-THE MORPHOLOGY

CONTINUITY

Besides amount, size and shape, the spatial arrangement of the individual components strongly influences the overall mechanical behaviour; hence its geometrical description is of prime interest. In this context, the degree of interconnectivity or the *continuity* are important qualities of the morphology of the microstructure. A first step to quantify these features was done by Gurland [GUR 58] who introduced the *contiguity* parameter to describe the spatial arrangement of grains; contiguity C_α is defined as the ratio of grain boundary area to the total interface area (grain and phase boundary area) belonging to that phase

$$C_\alpha = \frac{2S_{\alpha\alpha}}{2S_{\alpha\alpha} + S_{\alpha\beta}} \qquad \text{(I.1.4)}$$

S denotes the area per volume of the α/α- and β/β-grain boundaries and α/β-phase boundaries. A simple method of its measurement is reported by Exner et al [EXN 93]. The contiguity parameter is dependent on volume fraction (linearly) and grain size and due to the latter case, not adequate for the general use. In numerous multi-phase materials the spatial arrangement of a component is more significant with respect to overall macroscopic properties than the coherence within itself. Recently, Poech et al [POE 94] proposed a novel stereological parameter, measured by automatic image analysis, which is also applicable for phases without

grain boundaries. It evaluates the degree of connectivity of a microstructural component and hence provides information to what extent a matrix-inclusion topology or an interwoven network is present. By means of automatic image analysis, the topology of the structure (continuity and extent of branching) is reproduced by skeletonization of a binary image. The total length of the skeleton lines referred to one phase is a measure of its continuity. The parameter *matricity* of phase r is defined as the ratio of the total skeleton line length LSk_r of that phase to the overall line length (Fig. I.1.2a)

$$M_r = \frac{LSk_r}{\sum_{r=0}^{r=N} LSk_r}, \qquad \text{with } \sum_{r=0}^{r=N} M_r = 0 \tag{I.1.5}$$

For materials with intermediate volume fractions, the definition of an additional stereological parameter has been proven useful. For each phase the number of isolated grain clusters N_r is counted. The *fraction of cluster* parameter r_r is then defined as the ratio of N_r to the overall number of clusters [SIE 93] (Fig. I.1.2b)

$$r_r = \frac{N_r}{\sum_{r=0}^{r=N} N_r}, \qquad \text{with } \sum_{r=0}^{r=N} r_r = 0 \tag{I.1.6}$$

Siegmund et al. [SIE 93] have shown the relevance of this parameter in duplex-microstructures with respect to the prediction of the overall limit flow stress.

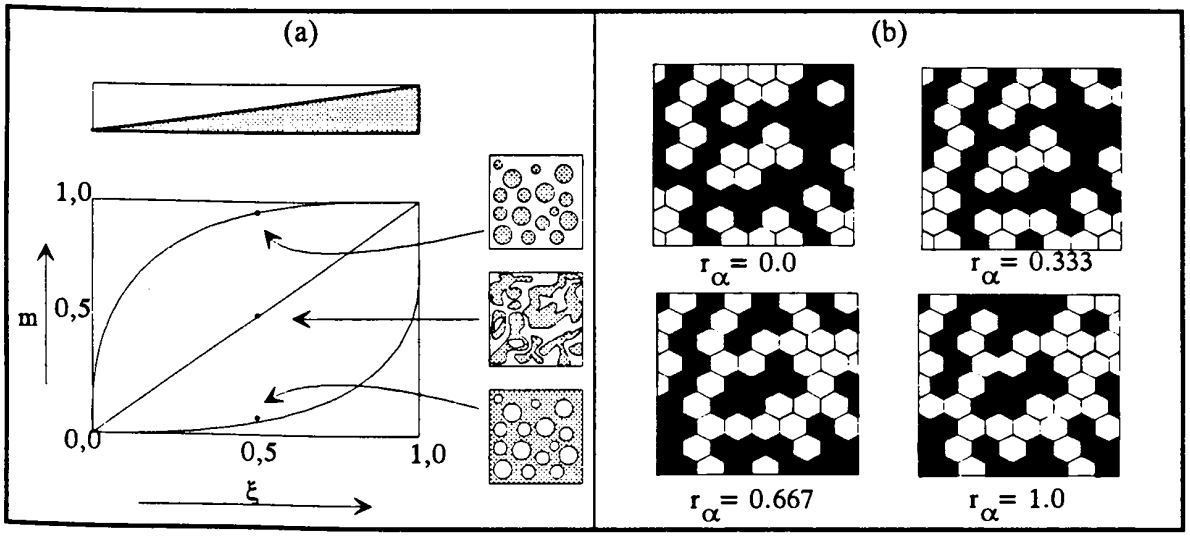

Fig. I.1.2. Schematical interpretations of geometrical quantities describing the degree of continuity: (a) matricity [POE 94] --(b) fraction-of cluster parameter [BÖH 94]

Remark

Matricity and fraction-of clusters parameter both aim to quantify the transition in topology from a matrix-inclusion arrangement (for m→ 0 or 1; r → 0 or 1) to an interwoven arrangement (for m→ 0,5; r→ 0,5) .

MICROSTRUCTURAL INHOMOGENEITY

The specific orientation of elongated components is an important geometrical feature since it may be the source of macroscopic anisotropic mechanical behaviour. Materials undergoing warm forging are one example of a microstructure with preferred orientation. In this case three axis are distinguished after norm ASTM E399-74 [AST 76]: the l-axis coincides with the axis of highest deformation, the s-axis with that of the highest forging load; and the t-axis perpendicular to both of them. The orientation of precracked specimen is specified by two letters, the former indicates the load direction and the latter the direction of crack propagation (Fig. I.1.3).

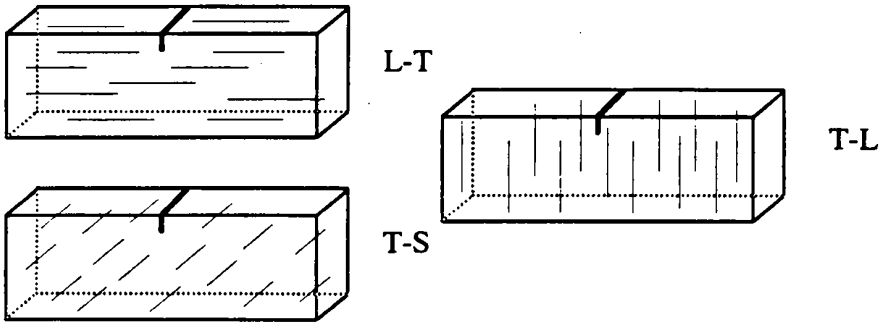

Fig. I.1.3. Specification of the orientation of precracked specimen

The interface density Sid or alternatively the mean size L may be used in order to quantify the orientation of microstructures. The degree of orientation is related to the ratio of the oriented boundary surface to the total boundary surface.

Alternatively the illustrative elongation parameter Λ_{elong} may be used, which is defined by the ratio of the mean linear chord length in the direction of the elongation L_l and perpendicular to it L_t [EXN 93]

$$\Lambda_{elong} = \frac{\overline{L}_l}{\overline{L}_t} \qquad (I.1.7)$$

I.1.2-Deformation Characteristics

With the addition of second-phase reinforcements to a monolithic matrix, one aims to combine favourable properties of the individual phases into one composite material. For example, the specific combination of hard and brittle with soft and ductile components promises an adapted compromise of overall stiffness and strength, with ductility and fracture toughness.

In general, the stiff and hard component carries the greater part of the load while the soft and ductile one undergoes the greater part of the strain. Plastic deformation in the material is initiated in the soft phase around the hard one. The overall stresses and strains can be obtained when the implicit stress and strain partitioning among the individual phases is known

$$\sigma_c = \xi_\alpha \sigma_\alpha + \xi_\beta \sigma_\beta \qquad (I.1.8a)$$

$$\varepsilon_c = \xi_\alpha \varepsilon_\alpha + \xi_\beta \varepsilon_\beta \qquad (I.1.8b)$$

σ and ε denote the stresses and strains in the composite (c) and in both components (α and β). The overall response is only uniquely determined by the above eqn. if σ_α, σ_β, ε_α, ε_β denote the *in-situ* stresses and strains. It is important to emphasise that the *in-situ* deformation

characteristics of the components within the composite strongly deviate from those in their respective *bulk* state. This is explained due to the following mechanisms

(i1)- enhanced density of geometrically necessary dislocations [FIS 73, ASH 70]
(i2)- strengthening due to back stresses [MOR 70]
(i3)- phase boundaries are stronger obstacles than grain boundaries with regard to slip transfer [WER 90]
(i4)- residual stresses emerging during cooling from either thermal contraction mismatch between the components or by phase transformations [FIS 92, PYZ 94]
(i5)- matrix and interfacial precipitation [CHR 88]
(i6)- mutual constraint of the deformation of adjacent components [CHR 89, DIE 93, SAU 93]

However, up to now the in-situ stress and strain partitioning in the sense of eqn (I.1.8) is not known and only approximated by experiments. For example strain measurements have been derived from microhardness indentations [FIS 77, OLA 93], from the distortion of a reference grid printed on a surface [ANK 82, ALL 94] or from X-ray measurements to determine average strains in hard phases, to mention only some techniques.

The prediction of the overall deformation characteristics in terms of the *bulk* properties of the components accounting implicitly for the for mentioned items is a complicated task.
A first model in this line was suggested by Tamura et al [TAM 73] termed as the *rules-of-mixture*. Derived from the linear bounds of Voigt and Reuss (see also I.2) it postulated that the stresses and strains are partitioned among the phases in proportion to their respective volume fraction (it is identical with eqn. (I.1.8) except that the stresses and strains of the components are taken in their respective bulk state). The partitioning is quantified by the parameter m (Fig. I.1.4. [SAU 93])

$$m = \frac{|\sigma_\alpha - \sigma_\beta|}{|\varepsilon_\alpha - \varepsilon_\beta|} = \frac{|\sigma_c - \sigma_\beta|}{|\varepsilon_c - \varepsilon_\beta|} = \frac{|\sigma_\alpha - \sigma_c|}{|\varepsilon_\alpha - \varepsilon_c|} \qquad \text{(I.1.9)}$$

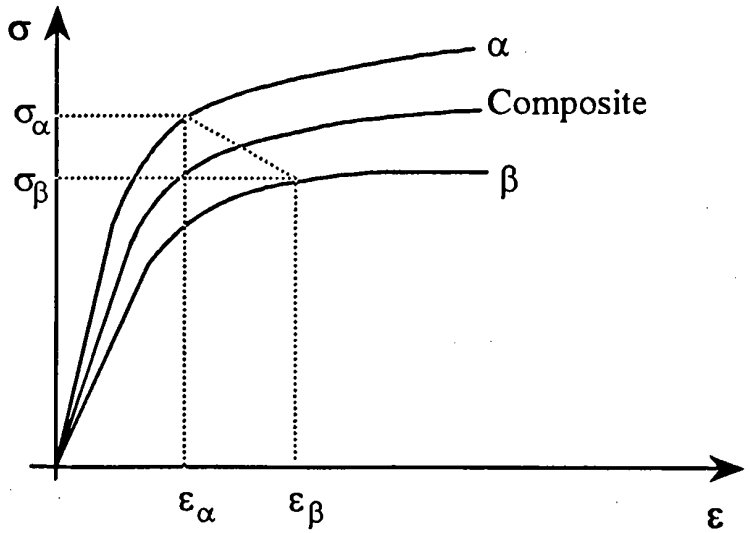

Fig. I.1.4. Schematic of the partitioning of equivalent stresses and strains among the phases

This empirical model addresses continuous fibre composites (parallel loading; eqn a) or sandwich composites (serial loading; eqn b) and has also been proven useful for the prediction

of the overall stress-strain behaviour of dual steels. However, it is not theoretically justified since it violates the condition of strain compatibility at the phase boundaries [item (i6)]:
The mutual constraint of deformation between adjacent phases for perfect interface bondings increases substantially the triaxial stress state and influences in particular the plastic straining of the matrix around hard particles. An important measure to describe the mutual constraint is the triaxiality defined as

$$\zeta = \frac{\sigma_H}{\sigma_v} \qquad (I.1.9)$$

where σ_H is the hydrostatic stress and σ_v the effective stress according to von Mises. A consequence of this mutual constraint is that the soft phase behaves harder and the hard phase softer than their respective bulk states [DIE 93].
Here it shall be mentioned that a modified rule-of-mixture based on the sandwich-model accounting for the condition of strain compatibility was proposed by Poech et al. [POE 92A,C]. The predicted overall stress-strain response was found to be in good agreement with experimental ones for WC-Co and martensitic-austenitic dual systems.

I.1.3-Damage Characteristics

Prior to the sudden rupture of structures, local failure events develop due to excessive loading (e.g. during material processing, thermal and/or mechanical loading). The damage behaviour of numerous composite systems has received much consideration by experimental investigations in the last three decades; among them two-phase steels (ferrite-cementite, high speed steels, tool steels), hard metals (e.g. WC-Co) and metal-matrix composites (Al-SiC_p being mostly studied). Due to the different amount of hard and soft components and the ductility of the soft components in those systems, different steps of damage have been reported. In Al-SiC_p systems for instance, progressive fracture of reinforcements was found to be the principal source of the composite failure [LLO 93, BOU 94]. Shape, size and orientation of the reinforcements are the relevant parameters in the early stage (large reinforcements elongated in load direction being privileged to fail); interaction between particles and microcracks in the later stage of damage.
Some authors have also detected particle/matrix debonding [e.g. MUM 93]. Microcracks developed by particle cracking were observed to be straight and to follow particular crystallographic planes and therefore assumed to be a result of exceeding the critical tensile stress [KAS 77]. Damage in Co-WC is initiated, as opposed to the Al-SiC system, in the softer phase. The small amount of the Co phase results in high plastic stretching of the ligaments in the binder phase and favours void nucleation at stacking fault intersections due to plastic accumulation [FIS 88, SIG 88].
Interface debonding plays a crucial role in the deterioration process of fiber and sandwich composites; in continuous reinforced fiber composites it triggers fiber pull-out under axial loading and delamination under transverse loading. Delamination by continuous interface debonding is also the principal failure mechanism in sandwich composites. In two-phase materials with discrete distribution of hard or soft particles two failure initiation mechanisms, interface decohesion and particle fracture are in competition. Sometimes one failure mechanism is dominant: Typically, softer and spherical particles are more prone to fail by decohesion (MnS in ductile steels, graphites in cast iron) and stiffer and harder particles by particle fracture (hard carbides in MM). In other materials both failure mechanisms coexist and the whole deterioration process is a result of their synergistic contribution.

Microvoids are nucleated by the previously described failure mechanisms and initiate crack growth in the matrix. The crack path follows the spread-out of the matrix plastification, while the growth-rate is strongly controlled by the triaxial stress state. The triaxial stress state quantified by the triaxiality (eqn. (I.1.9)) has often been emphasized in the literature as the driving force for crack growth [RIC 69, LEM 85A, KON 93]. It is also the major factor when predicting the brittle/ductile nature of crack propagation. Teirlinck et al. [TEI 88] distinguish between brittle fracture (inter- or transcrystalline), ductile (dimple) fracture and shear fracture. The transition between them is determined by the ratio of hydrostatic stresses to effective stresses (Fig. I.1.5).

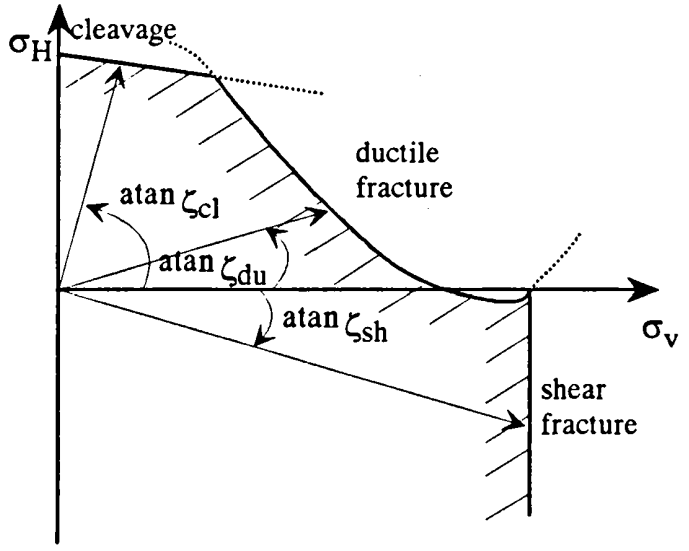

Fig. I.1.5. Interaction between competing fracture mechanisms and the influence of the triaxiality (for a 1045 spheroidized steel [see alsoTEI 88])

In all cases damage mechanisms are identified qualitatively by direct methods (optical micrographies, SEM/REM etc.). In addition, "real-time" fracture techniques such as *in situ* SEM observation of crack initiation and growth may be used to correlate microscopic damage evolution to macroscopic loading [e.g. BOU 94]. However, it describes only the damage processes on the free surface, the damage behaviour within the bulk might be different. Indirect methods such as acoustic emission, loading/unloading cycles to measure the loss of stiffness may be applied to quantify global damage in the bulk of the material [MUM 93, LLO 93]. A different crack propagation behaviour at the surface and in the bulk was discovered, when studying the fracture surface over the whole thickness. A more smooth fracture surface was observed at the surface [LÜS 95]. The smoothness of the fracture surface may also provide first information about the toughness of the material. In this context one important quantity is the crack-path-width ρ which is an indicator of the degree of crack deflection φ along the entire crack path (Fig. I.1.6).

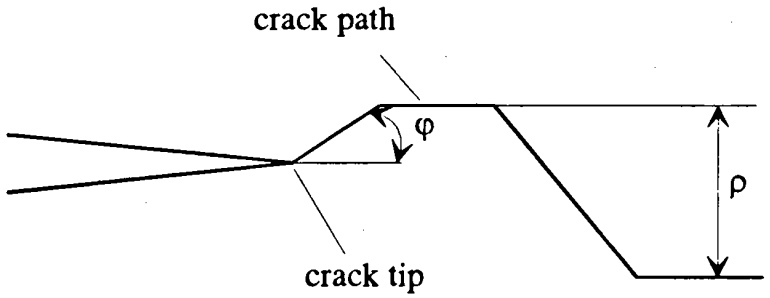

Fig. I.1.6. Definition of crack deflection φ and crack-path-width ρ

In all materials mentioned above these failure events decrease the overall ductility. In contrast microcracking in rocks, ceramics and their composites has been identified as an additional source of toughening [e.g. MEG 93, HUT 87, RÜH 87]. Whether the interaction of microcracks might have a shielding or an amplification character is strongly influenced by the location and orientation of microcracks in the fracture process zone (FPZ). The shielding effect by microcracking is explained by the reduction of the effective moduli and the strain arising from the release of residual stresses [HUT 87]. It has been suggested to relate toughening to the following quantities: microcrack density, microcrack length distribution, residual opening of microcracks.

A parallel is given to transformation toughening where the effective stresses at the macroscopic crack tip are reduced by the permanent dilatation [RÜH 87]. For instance stress induced martensitic transformation may occur in steels containing retainedaustenite ahead a macroscopic crack tip [BRO 94].

I.2-Analytical approaches

I.2.1-Effective elastic properties

I.2.1.1-GENERAL CONSIDERATIONS

In the past three decades considerable progress of analytical works in the field of micromechanics has been made. Its main objective, the correlation between the microstructure, its microconstituents and the macroscopic properties, is addressed by homogenization methods. To this end, the concept of a representative volume element (RVE) is introduced (e.g. [HIL 63]): A RVE for a material point of a continuum mass is a material volume which is statistically representative for the infinitesimal material neighbourhood of that material point [NEM 93]. Therefore it has to include the most dominant microscale features that have first-order influence on the overall properties of concern. The RVE may be viewed as a heterogeneous medium under prescribed boundary conditions which correspond to the uniform local continuum fields. The major scope then is to estimate the overall average properties of the RVE in order to describe the local properties of the continuum material element. More precisely, its task is to compute the overall (average) strain (strain increment, for an incremental formulation) as function of the corresponding prescribed (incremental) surface forces or, conversely, the average stress (stress increment) as function of the prescribed (incremental) surface displacements. Under the prescribed boundary conditions, the RVE must be in equilibrium and its overall deformation compatible. Considering uniform boundary conditions, the external surface of the RVE may be subjected to a displacement **u**

$$u_i = E_{ij}x_j \qquad x \in V \tag{I.2.1a}$$

which would provide an uniform strain **E**, if the material will be homogeneous. Conversely, a prescribed surface traction **f**, compatible with an uniform stress Σ is defined by

$$f_i = \sigma_{ij}n_j = \Sigma_{ij}n_j \qquad x \in V \tag{I.2.1b}$$

The general scheme of all micromechanical methods follows three main steps [BOU 94]:

1-Description of RVE

Respecting the above defined concept of RVE, all information concerning the geometrical and mechanical characterization of the microconstituents have to be covered. In general the mechanical behaviour of the "in-situ" constituents can not be determined experimentally; the micromechanical behaviour of the individual phase is assumed to be identical with the macroscopic behaviour of the respective bulk material. Considering elastic behaviour, the constitutive relation reads

$$\boldsymbol{\sigma}(\mathbf{x}_r) = \mathbf{C}_r\boldsymbol{\varepsilon}(\mathbf{x}_r) \quad \text{or} \tag{I.2.2a}$$

$$\boldsymbol{\varepsilon}(\mathbf{x}_r) = \mathbf{M}_r\boldsymbol{\sigma}(\mathbf{x}_r) \quad \text{with } \mathbf{C}_r = \mathbf{M}_r^{-1} \tag{I.2.2b}$$

Here, and in the following a composite is considered which consists of a matrix (subscript r=0) and N-reinforcing phases (subscript r=1, N). $\boldsymbol{\sigma}_r$ and $\boldsymbol{\varepsilon}_r$ represent the stresses and strains, respectively at point $\mathbf{x}_r$, belonging to phase r.

The phase which is distributed discretely, is geometrically quantified by the volume fraction, aspect ratio and its orientation to the load direction. In most of the methods the arrangement of

this phase is considered perfectly disordered; one exception within the concept of RVE is the assumption of a perfectly periodic microstructure.

2-Strain localisation or stress concentration

This section provides the link between the local stresses $\boldsymbol{\sigma}$ or strains $\boldsymbol{\varepsilon}$ and the macroscopic imposed stresses $\boldsymbol{\Sigma}$ or strains $\mathbf{E}$. The relations of strain localisation and stress concentration in the linear elastic setting read

$$\boldsymbol{\sigma}(\mathbf{x}_r) = \mathbf{B}(\mathbf{x}_r)\,\boldsymbol{\Sigma} \quad \text{and} \quad \boldsymbol{\varepsilon}(\mathbf{x}_r) = \mathbf{A}(\mathbf{x}_r)\mathbf{E} \tag{I.2.3}$$

The mean stress and mean strain within the phase r are given by

$$\boldsymbol{\sigma}_r = \langle \boldsymbol{\sigma}(\mathbf{x}_r) \rangle_r \quad \text{and} \quad \boldsymbol{\varepsilon}_r = \langle \boldsymbol{\varepsilon}(\mathbf{x}_r) \rangle_r \tag{I.2.4}$$

$\langle \mathbf{z} \rangle_r$ denoting the average of $\mathbf{z}$ over the volume V_r of phase r

$$\langle \mathbf{z} \rangle_r = \frac{1}{V_r} \int_{V_r} \mathbf{z}\, dV_r \tag{I.2.5}$$

In terms of their mean values, eqn. (I.2.3) becomes

$$\boldsymbol{\sigma}_r = \mathbf{B}_r\boldsymbol{\Sigma} \quad \text{and} \quad \boldsymbol{\varepsilon}_r = \mathbf{A}_r\mathbf{E} \tag{I.2.6}$$

$\mathbf{A}_r$ and $\mathbf{B}_r$ are called strain localisation and stress concentration tensor. They give information about how the external load is transmitted over the individual phases.

3-Homogenization scheme

Employing the virtual work principle, the relation between the overall average stress $\boldsymbol{\sigma}$ or strain $\boldsymbol{\varepsilon}$ and the macroscopic stress $\boldsymbol{\Sigma}$ or strain $\mathbf{E}$, respectively, may be derived by (Hill-Mandel relation)

$$\langle \boldsymbol{\sigma}\,\boldsymbol{\varepsilon} \rangle = \frac{1}{V} \int_V \boldsymbol{\sigma}\,\boldsymbol{\varepsilon}\, dV = \boldsymbol{\Sigma}\,\mathbf{E} = \frac{1}{V} \int_S \mathbf{f}^t \mathbf{u}\, dS \tag{I.2.7}$$

Satisfying the boundary conditions (I.2.1), it holds for the local stresses and strains

$$\langle \boldsymbol{\sigma} \rangle = \boldsymbol{\Sigma} \tag{I.2.8a}$$
$$\langle \boldsymbol{\varepsilon} \rangle = \mathbf{E} \tag{I.2.8b}$$

and by using (I.2.5), it follows

$$\boldsymbol{\Sigma} = \sum_{r=0}^{N} \xi_r \boldsymbol{\sigma}_r \tag{I.2.9a}$$
$$\mathbf{E} = \sum_{r=0}^{N} \xi_r \boldsymbol{\varepsilon}_r \tag{I.2.9b}$$

and gives finally the expression for the compliance and elastic tensor of the composite

$$\mathbf{M} = \sum_{r=0}^{N} \xi_r \mathbf{M}_r \mathbf{B}_r \tag{I.2.10a}$$

$$\mathbf{C} = \sum_{r=0}^{N} \xi_r \mathbf{C}_r \mathbf{A}_r \tag{I.2.10b}$$

It has to be noticed that the summation of $\mathbf{B}_r$ and $\mathbf{A}_r$ over all phases gives the identity matrix

$$\sum_{r=0}^{N} \xi_r \mathbf{B}_r = \mathbf{I} \quad \text{and} \quad \sum_{r=0}^{N} \xi_r \mathbf{A}_r = \mathbf{I} \tag{I.2.11}$$

Taking advantage of the above relation, eqn. (I.2.10) can be reformulated in order to specify the role of the matrix (phase 0) with respect to the other phases

$$\mathbf{M} = \mathbf{M}_0 + \sum_{r=1}^{N} \xi_r (\mathbf{M}_r - \mathbf{M}_0) \mathbf{B}_r \tag{I.2.12a}$$

$$\mathbf{C} = \mathbf{C}_0 + \sum_{r=1}^{N} \xi_r (\mathbf{C}_r - \mathbf{C}_0) \mathbf{A}_r \tag{I.2.12b}$$

Remark
All micromechanical models have these three steps in common. However, they propose different schemes in order to determine the matrices $\mathbf{A}_r$ and $\mathbf{B}_r$. These hypotheses concern in particular the geometrical description of the microstructure.

In the following, some estimates and bounds are reviewed.

I.2.1.2-THE BOUNDS OF VOIGT AND REUSS
First-order bounds are given by Voigt [VOI 10] and Reuss [REU 29] under the consideration that strains and stresses, respectively are uniform over all phases.
Accordingly, the strain localisation tensor $\mathbf{A}_r$ for the Voigt model and the stress concentration tensor $\mathbf{B}_r$ for the Reuss model become the identity matrix.

$$\mathbf{M}_{Reuss} = \sum_{r=0}^{N} \xi_r \mathbf{M}_r \tag{I.2.13a}$$

$$\mathbf{C}_{Voigt} = \sum_{r=0}^{N} \xi_r \mathbf{C}_r \tag{I.2.13b}$$

From a geometrical point of view they describe a specific morphology, where infinite aligned fibres are arranged parallel (Reuss) or perpendicular (Voigt) to the load direction. Their predicted elastic properties bound the true elastic properties in the material for an arbitrary microstructure. It holds [HIL 63]

$$\boldsymbol{\varepsilon}\, \mathbf{M}_{Reuss}^{-1}\, \boldsymbol{\varepsilon} \leq \boldsymbol{\varepsilon}\, \mathbf{M}^{-1}\, \boldsymbol{\varepsilon} = \boldsymbol{\varepsilon}\, \mathbf{C}\, \boldsymbol{\varepsilon} \leq \boldsymbol{\varepsilon}\, \mathbf{C}_{Voigt}\, \boldsymbol{\varepsilon} \qquad \forall\, \boldsymbol{\varepsilon} \tag{I.2.14}$$

For isotropic materials these bounds can be formulated in terms of bulk, shear or Young's modulus. A derivation for the Poisson's ratio is more complicated. For example for an isotropic two-phase material the Young's modulus is bounded by

$$E_{Reuss} \le E \le E_{Voigt} \tag{I.2.15a}$$

with

$$\frac{1}{E_{Reuss}} = \frac{\xi_0}{E_0} + \frac{\xi_1}{E_1} \quad \text{and} \quad E_{Voigt} \ge \xi_0 E_0 + \xi_1 E_1 \tag{I.2.15b}$$

The above given inequality is necessary for Poisson's ratio mismatch [HIL 63].

I.2.1.3-ESHELBY'S EQUIVALENT INCLUSION SOLUTION

Remark

In this context inclusion means a region with same elastic properties as the matrix containing *stress-free strains* (will be explained below) and should not be confused with second phase particles embedded in a matrix.

Many scientists were stimulated by the celebrated paper of Eshelby in 1957 [ESH 57] in order to work on the new domain of micromechanics. Since this work provides some fundamental results covered in many micromechanical models, its main ideas are reviewed in the following.

The transformation problem

A region (the 'inclusion') V_i which undergoes a spontaneous change of its geometrical form within an infinite homogeneous isotropic elastic medium V_m is considered .

The region, cut and removed from the matrix may be subjected to a free deformation (e.g. thermal dilatation) without any constraints. Therefore it holds for any point $\mathbf{x}$ of the volume V

$$\boldsymbol{\varepsilon}^*(x) = \boldsymbol{\varepsilon}^* \chi_{V_i}(x) \tag{I.2.16a}$$

with

$$\chi_{V_i}(x) = \begin{cases} 0 & \forall\, x \in V_m \\ 1 & \forall\, x \in V_i \end{cases} \tag{I.2.16b}$$

$\boldsymbol{\varepsilon}^*$ is named differently in the literature; *stress-free strain* [ESH 57], *polarization strain* [KRÖ 58], *eigenstrain* [MUR 87], [NEM 93].

Then, surface tractions are applied such that the region is restored to its original form. After putting it back in the hole of the matrix the surface tractions, becoming body forces now acting on the interface S between inclusion and matrix, are relaxed. The constraint of the surrounding matrix results in an elastic stress-strain field in both domains. Figure I.2.1 gives an illustration of the different imaginary operations.

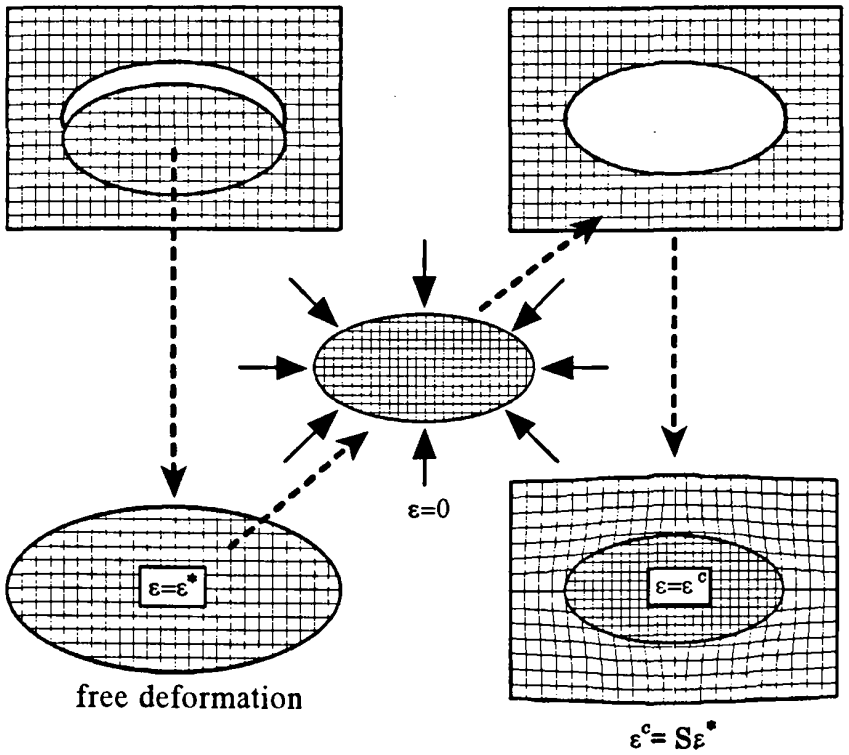

Fig. I.2.1. On the transformation problem [WIT 89]

The total strain in the inclusion is decomposed (in the range of infinitesimal deformations) into the stress-free strain ε^* and elastic strain ε^e.

$$\varepsilon_{ij} = \varepsilon^*_{ij} + \varepsilon^e_{ij} \tag{I.2.17}$$

The total strain must be compatible, thus

$$\varepsilon_{ij} = \frac{1}{2}(u_{i,j} + u_{j,i}) \tag{I.2.18}$$

The elastic stresses σ in $\mathbf{x}$ of the entire domain is given by Hooke's law

$$\sigma_{ij}(x) = C_{ijkl}(\varepsilon_{kl} - \varepsilon^*_{kl}\chi(x)) \tag{I.2.19}$$

Since the elastic tensor $\mathbf{C}$ is symmetric, the above equation becomes with eqn. (I.2.18)

$$\sigma_{ij}(x) = C_{ijkl}(u_{k,l} - \varepsilon^*_{kl}\chi(x)) \tag{I.2.20}$$

Formulating the equilibrium conditions it follows

$$C_{ijkl}u_{k,lj} + C_{ijkl}\varepsilon^*_{kl}n_j\delta(x) = 0 \tag{I.2.21a}$$

with

$$\delta(x) = \begin{cases} 1 & \forall\, x \in S; \begin{cases} S \text{ being the interface between } V_i \text{ and } V_m \\ n \text{ the outward normal to } S \end{cases} \\ 0 & \text{otherwise} \end{cases} \qquad \text{(I.2.21b)}$$

It can be seen that the contribution of the stress-free strain ε^* in eqn. (I.2.21a) is similar to that of a body force **b** for an equivalent homogeneous medium

$$b_i = C_{ijkl}\varepsilon^*_{kl}n_j \qquad \text{(I.2.22)}$$

The solution for eqn. (I.2.21) with given stress-free strain ε^* may be obtained applying methods of periodicity, Fourier series (integrals) or Green' s function [MUR 87]:

$$u_i = \int_S G_{ij}(x-x')C_{jklm}\varepsilon^*_{lm}n_k(x')dS' \qquad \text{(I.2.23)}$$

and with the help of Gauss theorem, finally

$$\varepsilon_{in} = \left\{-\frac{1}{2}C_{jklm}\left(\int_{V_i} G_{ij,kn}(x-x')dV' + \int_{V_i} G_{nj,ki}(x-x')dV'\right)\right\}\varepsilon^*_{lm} \qquad \text{(I.2.24)}$$

Green's function $G_{pk}(x\text{-}x')$ is the displacement component in the x_p-direction at point x when a unit body force in the x_k direction is applied at point x' in the infinitely extended material.

In general, it is not simple to calculate their derivations. However, if the inclusion is of ellipsoidal shape embedded in an isotropic medium, then the strain field within the inclusion is uniform and eqn. (I.2.24) becomes [ESH 57]

$$\varepsilon_{in} = S_{inlm}\varepsilon^*_{lm} \qquad \text{(I.2.25)}$$

with **S** being a 4th-rank tensor depending only on Poisson's ratio of the matrix and geometrical parameters of the inclusion. **S** is called Eshelby's tensor. Analytical expressions of **S** for some specific inclusion shapes can be found e.g. in [MUR 87].

The inhomogeneity problem

The inclusion problem of the last chapter where all elastic constants are the same is now extended to the inhomogeneous case: The ellipsoidal region V_i with elastic moduli $\mathbf{C}_i$ is embedded in an infinite elastic medium V_m with elastic tensor **C**. Here, we are interested in finding out how a uniform stress applied at large distances is disturbed by the inhomogeneity.
The local stress field in both domains due to an uniform stress $\boldsymbol{\Sigma}$ applied at large distances, which would cause a uniform strain **E** if the material will be homogeneous, is expressed by

$$\boldsymbol{\Sigma} + \boldsymbol{\sigma}^{pt} = \mathbf{C}_i(\mathbf{E} + \boldsymbol{\varepsilon}^{pt}), \qquad \text{in } V_i \qquad \text{(I.2.26a)}$$

$$\boldsymbol{\Sigma} + \boldsymbol{\sigma}^{pt} = \mathbf{C}(\mathbf{E} + \boldsymbol{\varepsilon}^{pt}), \qquad \text{in } V_m \qquad \text{(I.2.26b)}$$

where $\boldsymbol{\sigma}^{pt}$ and $\boldsymbol{\varepsilon}^{pt}$ denote the local perturbation stresses and strains, respectively.

The inhomogeneity of the inclusion is now replaced by the homogeneous inclusion with transformation strain $\boldsymbol{\varepsilon}^*$. We find

$$\boldsymbol{\Sigma} + \boldsymbol{\sigma}^{pt} = \mathbf{C}(\mathbf{E} + \boldsymbol{\varepsilon}^{pt} - \boldsymbol{\varepsilon}^*), \qquad \text{in } V_i \tag{I.2.27a}$$

$$\boldsymbol{\Sigma} + \boldsymbol{\sigma}^{pt} = \mathbf{C}(\mathbf{E} + \boldsymbol{\varepsilon}^{pt}), \qquad \text{in } V_m \tag{I.2.27b}$$

If both, the transformation and the inhomogeneity problem, are equivalent it must hold

$$\mathbf{C}_i(\mathbf{E} + \boldsymbol{\varepsilon}^{pt}) = \mathbf{C}(\mathbf{E} + \boldsymbol{\varepsilon}^{pt} - \boldsymbol{\varepsilon}^*) \qquad \text{in } V_i \tag{I.2.28}$$

The solution of the last chapter gives

$$\boldsymbol{\varepsilon}^{pt} = \mathbf{S}\boldsymbol{\varepsilon}^* \tag{I.2.29}$$

and therefore

$$\boldsymbol{\varepsilon}^* = \left[(\mathbf{C}_i - \mathbf{C})\mathbf{S} - \mathbf{C}\right]^{-1}(\mathbf{C}_i - \mathbf{C})\mathbf{E} \tag{I.2.30}$$

Finally, the elastic strain $\boldsymbol{\varepsilon}$ in the inhomogeneity V_i is related to the macroscopic strain $\mathbf{E}$ by [BOU 94]

$$\boldsymbol{\varepsilon} = \left[\mathbf{I} + \mathbf{S}\mathbf{C}^{-1}(\mathbf{C}_i - \mathbf{C})\right]^{-1}\mathbf{E} \qquad \text{in } V_i \tag{I.2.31}$$

or for the stresses explicitly

$$\boldsymbol{\sigma} = \mathbf{C}_i\left[\mathbf{I} + \mathbf{S}\mathbf{C}^{-1}(\mathbf{C}_i - \mathbf{C})\right]^{-1}\mathbf{C}^{-1}\boldsymbol{\Sigma} \qquad \text{in } V_i \tag{I.2.32}$$

The Dilute Solution-(ESH)

The assumption that the mean strain in all reinforcements is given by eqn (I.2.31) has led to the first homogenization method based on the theory of Eshelby. Each reinforcement is embedded in an infinite medium with elastic moduli $\mathbf{C}_0$ of the matrix. Interaction of elastic fields around neighbouring reinforcements is not accounted for by this model; hence it may only be applied to composites with low volume fractions of reinforcements.

The strain localisation tensor for this *dilute solution* becomes

$$\mathbf{A}_r^{Esh} = \left[\mathbf{I} + \mathbf{S}_r\mathbf{C}_0^{-1}(\mathbf{C}_r - \mathbf{C}_0)\right]^{-1} \tag{I.2.33}$$

and the elastic effective tensor is

$$\mathbf{C}^{Esh} = \mathbf{C}_0 + \sum_{r=1}^{N} \xi_r(\mathbf{C}_r - \mathbf{C}_0)\mathbf{A}_r^{Esh} \tag{I.2.34}$$

Quantities which are related to the specific phases are denoted by a subscript r. The phase r=0 is the matrix, all reinforcements are identified by r≠0. For convenience, a "phase", other than the matrix, is defined in this context as the collection of inhomogeneities whose shape (or aspect ratio), orientation and elastic moduli are identical.

I.2.1.4-OTHER BOUNDS AND ESTIMATES

Self-Consistent Scheme-(SCS)
The self-consistent scheme was originally developed by Hershey [HER 54] and Kröner [KRÖ 58] to estimate the elastic properties of polycrystals. These materials have no matrix instead they are aggregates of particles with different elastic properties and interaction among the different particles becomes more prominent in this case. To account for this effect, the main idea of the self-consistent scheme consists in placing successively all grains in a fictitious unbounded homogeneous medium with yet-unknown overall properties of the polycrystal. Later on Hill [HIL 65] and Budianski [BUD 65] extended this method to matrix composites.

The equivalent homogeneous medium is subjected at large distances to the macroscopic stress Σ or strain $\mathbf{E}$. The strain localisation tensor is similar to that defined by Eshelby (eqn. I.2.33) except that the homogeneous matrix is replaced by the homogeneous composite

$$\mathbf{A}_r^{SC} = \left[\mathbf{I} + \mathbf{S}_r\mathbf{C}^{-1}(\mathbf{C}_r - \mathbf{C})\right]^{-1} \tag{I.2.35}$$

Accordingly, Eshelby's tensor is calculated for a reinforcement embedded in an infinite matrix which has the properties of the equivalent composite. If the latter is not isotropic, the method involves more computational effort due to the complex mathematical expression of Eshelby's tensor. The elastic moduli are given by

$$\mathbf{C}^{SC} = \mathbf{C}_0 + \sum_{r=1}^{N} \xi_r(\mathbf{C}_r - \mathbf{C}_0)\mathbf{A}_r^{SC} \tag{I.2.36}$$

Since $\mathbf{A}_r$ depends on the effective elastic tensor $\mathbf{C}$, this scheme is implicit and therefore eqn. (I.2.36) has to be solved by iteration.

Remark
It should be noted that the self-consistent scheme yields a unique overall compliance (or elasticity) tensor whether the macrostress Σ or the macrostrain $\mathbf{E}$ is regarded prescribed. The term self-consistent is used in the literature to emphasize the existence of this inverse property.

Generalized Self-Consistent Scheme (Three-Phase Model)-(TPM)
In the self-consistent scheme the reinforcement is not in interaction with the matrix but with the equivalent composite; this leads to a "stiffer" estimation of the effective properties compared to the real composite material. To overcome this inconvenience, Christensen and Lo [CHR 79] have proposed to include three-phases into the model consisting of spherical reinforcements (phase 1 with radius a) surrounded by a "matrix-layer" (phase 0 with radius b) both embedded in an infinite equivalent homogeneous medium (EHM). The radius ratio a/b determines the volume fraction of the reinforcement and hence has to be respected.
The estimate for the bulk modulus K and shear modulus G is realized by two separate boundary value problems: hydrostatic pressure and simple shear. The effective bulk modulus e.g. is given by

$$K^{TPM} = K_0 + \frac{\xi_1(K_1 - K_0)}{1 + (1-\xi_1)\dfrac{(K_1 - K_0)}{\left(K_0 + \dfrac{4}{3}G_0\right)}} \tag{I.2.37}$$

The Bounds of Hashin-Shtrikman-Walpole-(HSW)

More rigorous bounds than those of the Voigt & Reuss type have been originally developed by Hashin & Shtrikman [HAS 63] restricted to isotropic materials using energy variational principles. They found that the strain and complementary strain energy functionals of the equivalent homogeneous medium, assuming the existence of *stress-free strains* (or *strain-free stresses*), are stationary for the exact *stress-free strains* (or *strain-free stresses*); These functionals give global maximum or minimum values for the actual total strain and complementary energy functionals. Schematically this model is close to the self-consistent scheme (SCS); however the surrounded matrix in the SCS is here replaced by a fictitious homogeneous medium. This medium has elastic properties and is either weaker $\mathbf{C}_{min}$ or stiffer $\mathbf{C}_{max}$ (in the sense of eqn. (I.2.35)) than all phases present in the composite. Accordingly, they provide lower and upper bounds for the overall elastic moduli of the composite. The imposed macroscopic strain $\mathbf{E}_0$ at infinity is that of the fictitious medium. For the lower bound the mean strains in the reinforcements are obtained by

$$\boldsymbol{\varepsilon}_r^{HSW^-} = \mathbf{T}_r^{HSW^-}\mathbf{E}_0 \tag{I.2.38a}$$

with

$$\mathbf{T}_r^{HSW^-} = \left[\mathbf{C}_r + \mathbf{C}_{min}(\mathbf{S}_r^{-1} - \mathbf{I})\right]^{-1}\mathbf{C}_{min}\mathbf{S}_r^{-1} \tag{I.2.38b}$$

and therefore the strain localisation tensor reads

$$\mathbf{A}_r^{HSW^-} = \mathbf{T}_r^{HSW^-}\left(\sum_{r=0}^{r=N}\xi_r\mathbf{T}_r^{HSW^-}\right)^{-1} \tag{I.2.39}$$

Finally the lower bound is expressed by

$$\mathbf{C}^{HSW^-} = \left(\sum_{r=0}^{N}\xi_r\mathbf{C}_r\mathbf{T}_r^{HSW^-}\right)\left(\sum_{r=0}^{N}\xi_r\mathbf{T}_r^{HSW^-}\right)^{-1} \tag{I.2.40}$$

and the upper bound by

$$\mathbf{C}^{HSW^+} = \left(\sum_{r=0}^{N}\xi_r\mathbf{C}_r\mathbf{T}_r^{HSW^+}\right)\left(\sum_{r=0}^{N}\xi_r\mathbf{T}_r^{HSW^+}\right)^{-1} \tag{I.2.41a}$$

with

$$\mathbf{T}_r^{HSW^+} = \left[\mathbf{C}_r + \mathbf{C}_{max}(\mathbf{S}_r^{-1} - \mathbf{I})\right]^{-1}\mathbf{C}_{max}\mathbf{S}_r^{-1} \tag{I.2.41b}$$

It should be noted that these bounds in their original formulation restricted to isotropic materials, have been extended to composites reinforced by long cylindrical same oriented fibers [WAL 69]. However, they are not applicable to short discontinuous reinforced composites.

The Mori-Tanaka Model-(MT)

For a long time the method originally proposed by Mori and Tanaka in 1973 [MOR 73] has suffered from the lack of a clear physical description. It addressed the problem of averaging stresses and elastic energy in the matrix (also called *mean-phase estimate* in the literature) including an inclusion (same properties) with a given *stress-free strain*. Lateron in 1987 Benveniste's [BEN 87] interpretation gave a physical sound explanation for this method and

provided as well the link to Eshelby's equivalent inclusion solution. All reinforcements are embedded in the matrix which is subjected at large distances to the mean strain experienced by itself

$$\boldsymbol{\varepsilon}_r^{MT} = \mathbf{T}_r^{MT}\boldsymbol{\varepsilon}_0 \tag{I.2.42a}$$

with

$$\mathbf{T}_r^{MT} = \left[\mathbf{C}_r + \mathbf{C}_0(\mathbf{S}_r^{-1} - \mathbf{I})\right]^{-1}\mathbf{C}_0\mathbf{S}_r^{-1} \tag{I.2.42b}$$

The strain localisation tensor reads

$$\mathbf{A}_r^{MT} = \mathbf{T}_r^{MT}\left(\sum_{r=0}^{N}\xi_r\mathbf{T}_r^{MT}\right)^{-1} \tag{I.2.43}$$

and the elastic effective tensor

$$\mathbf{C}^{MT} = \left(\sum_{r=0}^{N}\xi_r\mathbf{C}_r\mathbf{T}_r^{MT}\right)\left(\sum_{r=0}^{N}\xi_r\mathbf{T}_r^{MT}\right)^{-1} \tag{I.2.44}$$

These tensors are similar to those given by the Hashin-Sthrikman bounds (eqn. I.2.40, I.2.41a). In addition if the material consists of spherical reinforcements embedded randomly in a "weaker" matrix, than both methods give exactly the same results.

Remark

Like the self-consistent scheme, the predicted elastic tensor of the Mori-Tanaka scheme as well can be obtained indifferently by imposing either uniform macroscopic stress $\boldsymbol{\Sigma}$ or strain $\mathbf{E}$ which was proven by Weng [WEN 84].

I.2.5-DISCUSSION AND COMPARISON OF THE DIFFERENT APPROACHES

General considerations

Except the bounds of the Voigt and Reuss type and the generalized self-consistent scheme all micromechanical models adopted the equivalent inclusion model of Eshelby. The geometry of the reinforcement is taken analytically as spherical or ellipsoid. The latter characterized by their aspect ratio (l/d) (see I.1) is present in form of four different types: long fibers ($l/d=\infty$), short fibers ($10 \leq l/d \leq 50$), particles ($1 \leq l/d \leq 5$) and discs ($l/d \cong 0$).

The way how the different models account for the specific morphology of the material influences the accuracy of results. While the bounds of the Voigt and Reuss type consider infinite parallel aligned fibers, the others assume a perfect random discrete dispersion of reinforcements in the matrix and hence give a better estimation of the effective properties. However, some of them are not valid in the general case (TPM restricted to isotropic materials; HSW restricted to the shape of reinforcements (long fibers, spherical reinforcements, small discs), dilute solution of Eshelby restricted to a weak volume fraction of the reinforcements).

In general, the methods differ by the way how the surrounding equivalent medium is presented and how the boundary conditions are imposed at large distances (Fig. I.2.2).

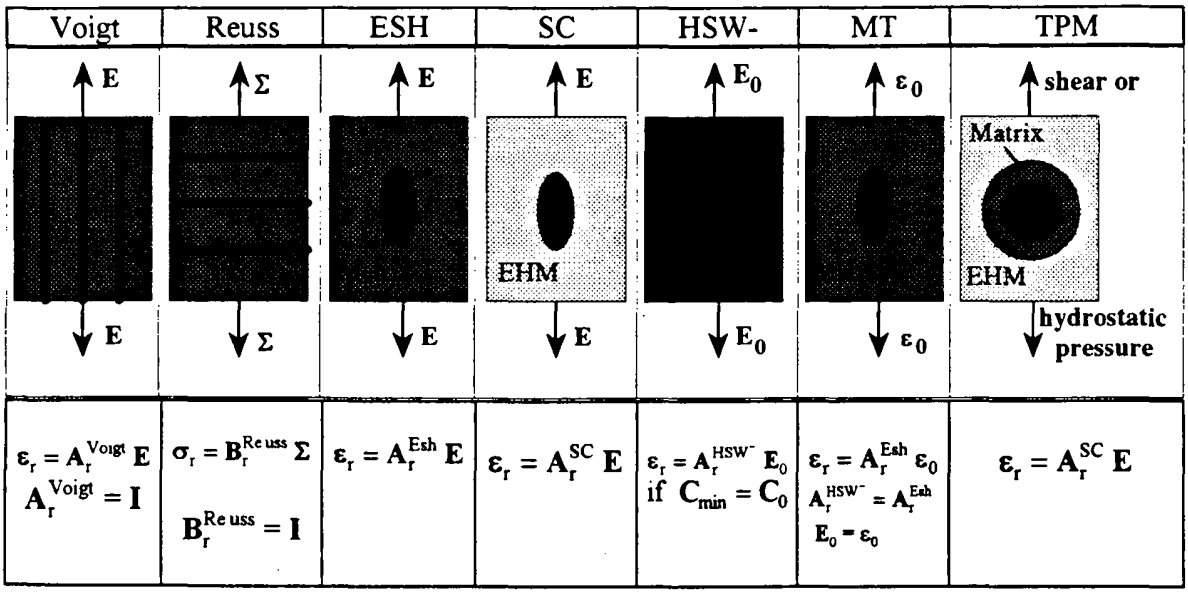

Fig. I.2.2. Comparison of the different approaches [BOU 94]

Isotropic two-phase material

As an example the different models are applied to an isotropic material with a matrix-inclusion topology where the reinforcements are of spherical shape and stiffer than the matrix. As an example the effective bulk modulus of an Al-SiC_p is computed as function of the reinforcement volume fraction.

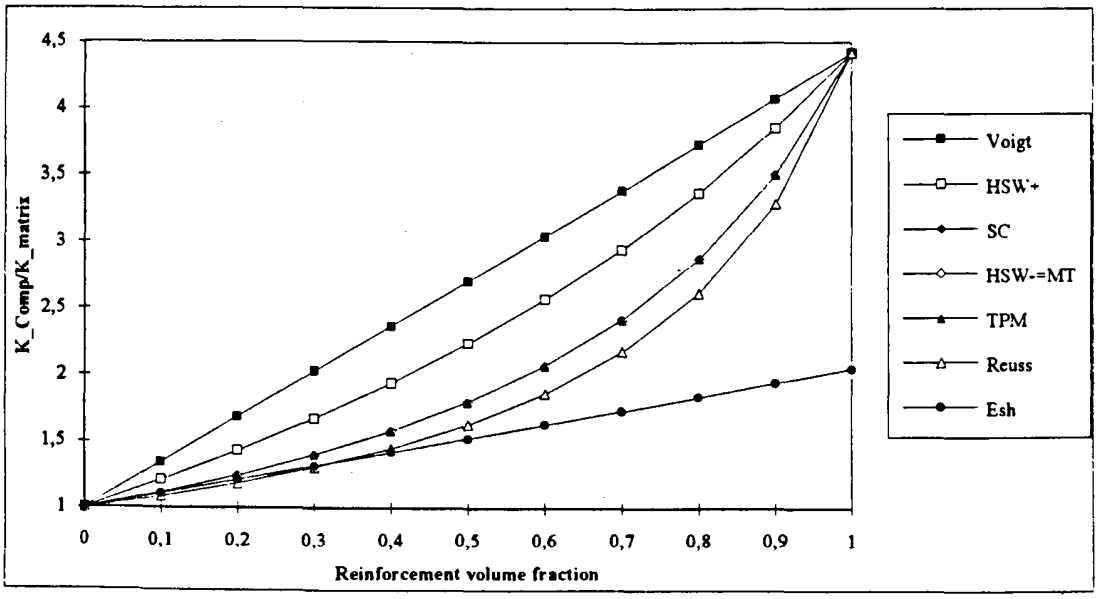

Fig. I.2.3. Normalized effective bulk modulus over the reinforcement volume fraction

As explained earlier, the bounds by Voigt and Reuss hold for any material. All other approaches must be bounded by these two curves. Accordingly, Eshelby's equivalent dilute solution can only be applied for low reinforcement volume content (ξ<0,2). For the chosen case (matrix weaker than the reinforcement (shape: spherical) the predictions by the Mori-Tanaka (MT) model and the lower bound of Hashin Shtrikman Walpole (HSW-) coincide, hence only one curve is found. The figure does not contain the results of the self-consistent model (SC), the corresponding curve will be found between the curves of HSW+ and TPM.

Other related models
Further analytical based approaches can be found in the literature. The review paper by Hashin [HAS 83], for instance, provides a comprehensive list of the literature. Among them one can cite the *differential scheme*, the bounds of the *composite spheres* (and *cylinders*) *assemblage* by Hashin, the *periodic solution* etc. Furthermore, recent extensions of the here presented models shall also be cited here: The concept of morphological motifs by [BOR 93] is a first approach to localise strain heterogeneities.

I.2.2-Analysis of irreversible processes

I.2.2.1-ELASTO-PLASTIC BEHAVIOUR OF THE MATRIX

Different schemes are proposed to include elasto-plastic behaviour into the model. Kröner [KRÖ 61] applied the concept of *stress-free strains* within the equivalent inclusion to elastoplasticity. Since the stress-free strains are added to the elastic strains this method is known in the literature as the *elastic accommodation of plastic deformation* (see e.g. [WIT 89]). If the matrix only possesses a plastic potential with plastic strains ε^p, then the stress-free strains ε^L within the reinforcements are assumed to be $\varepsilon^L=-\varepsilon^p$. The total macroscopic strains $\mathbf{E}$ are decomposed by

$$\mathbf{E} = \mathbf{E}^e + \mathbf{E}^L \tag{I.2.45a}$$

with

$$\mathbf{E}^e = \left\langle \mathbf{B}_r^T \boldsymbol{\varepsilon}_r^e \right\rangle = \left\langle \mathbf{M}_r \mathbf{B}_r \right\rangle \boldsymbol{\Sigma} \tag{I.2.45b}$$

$$\mathbf{E}^L = \left\langle \mathbf{B}_r^T \boldsymbol{\varepsilon}_r^L \right\rangle \tag{I.2.45c}$$

where the notation < > denotes the volumetric mean.
Hill [HIL 65] firstly suggested the use of the *tangent moduli* $\mathbf{C}^{tg}$ to describe the softening effect due to the plastification of the matrix. Accordingly, the tangent Young's modulus decreases with increasing matrix plasticity. The constitutive equations are therefore formulated in rate form

$$\dot{\boldsymbol{\sigma}}_r - \dot{\boldsymbol{\Sigma}} = -\mathbf{C}^{tg}(\dot{\boldsymbol{\varepsilon}}_r - \dot{\mathbf{E}}) \tag{I.2.46}$$

The decrease of the Young's modulus in terms of the total values leads to the use of *secant moduli* C^{sec} (see e.g. [TAN 88]). It is a simple extension from elastic to plastic behaviour; in all equations the elastic moduli are replaced by their secant moduli.
The plastic behaviour of the matrix may be expressed by the model of Ludwik

$$\sigma_v = \sigma_{Y0} + h_0 \left(\varepsilon_v^p\right)^n \tag{I.2.47}$$

where σ_v and ε_v^p are the equivalent stress (von Mises) and strain, respectively. σ_{Y0}, h_0 and n denote the initial yield stress, plastic resistance coefficient and hardening exponent, respectively. Assuming that the total strains are the sum of the elastic ε_v^e and plastic ε_v^p (equivalent) strains allows to define the secant modulus E_0^{sec} by (equivalence of uniaxial and triaxial stress state)

$$E_0^{sec} = \frac{\sigma_v}{\varepsilon_v^e + \varepsilon_v^p} = \frac{1}{\frac{1}{E_0} + \frac{\varepsilon_v^p}{\sigma_{Y0} + h_0\left(\varepsilon_v^p\right)^n}} \qquad (I.2.48)$$

The advantage of the easy implementation is compromised by its restriction to monotone loading.

I.2.2.2-DAMAGE BEHAVIOUR OF THE REINFORCEMENTS

The problem to analyse analytically local failure in composites is much more complicated than the prediction of elasto-plastic properties. The evaluation of failure criteria might be difficult since their determination in terms of critical stresses and strains strongly depends on the local morphology of the microstructure. In addition, the analysis of interacting microcracks is limited and therefore the evolution of progressive damage is found to be difficult to predict. In spite of these difficulties, much valuable work has been done in this line, however the results have to be interpreted necessarily in a qualitative rather than in a deterministic manner. Often, damage at the reinforcements is introduced into micromechanical methods by specifying the geometry and the elastic properties of the damaged phase. Simple physical models for different damage mechanisms at reinforcements have for example been suggested by Mochida et al. [MOC 91]: Cavities in the matrix are replaced by spherical phases, cracked particles by penny-shape ellipsoids; both "phases" with zero stiffness. In contrast to the static analysis of damage (assuming an initial state of damage being constant during loading), the study of damage evolution demands for an adequate failure criterion. Since stresses and strains, which provide in general the basis for local failure criteria, are equal for same phases, Bourgeois [BOU 94] introduced a statistical criterion based on the Weibull law. If the failure criterion is satisfied the particle has to be replaced. The simultaneous change of geometry and stiffness by replacing e.g. an ellipsoid by a penny-shape ellipsoid with zero stiffness gives rise to an unsymmetric elastic tensor. One alternative consists in preserving the particle geometry and to modify the elastic moduli such that the stress in the load direction is no longer transmitted by the particle (Introduction of an equivalent anisotropic undamaged inhomogeneity EAUI [FIT 95]).

I.3-Numerical investigations

I.3.1-The micromechanical model

Beside the fields of structure-, fluid mechanics and heat transfer, micromechanics is rather a new branch for the application of the FEM. Mostly based on a continuum mechanics formulation, the micromechanical FE-model may be applied to a large class of materials with coarse microstructure (see chapter I.2). Plastic behaviour of the ductile matrix may only be described by continuum plasticity when the reinforcement size/spacing is large as compared to the characteristic dislocation structural scale (such as slip distance). FE-studies on a smaller scale use atomistic models in order to study dislocation movements and separation of atoms via a potential theory.

I.3.1.1-MODELLING THE ENTIRE MICROSTRUCTURE

Continuum Micromechanics aims to reveal the influence of microstructural characteristics on the local (microscale) and global (overall) response of the material. Microstructural characteristics are of geometrical nature (e.g. amount, size, shape and distribution of reinforcements) or of physical nature (e.g. mismatch of mechanical properties like stiffness etc.). These characteristics are the controlling mechanisms of the interaction behaviour between matrix-inclusion and inclusion-inclusion. The latter may be effectively studied by imposing symmetric boundary conditions where interaction between reinforcements, besides in the inner of the model, is also established over the boundaries. These conditions are satisfied when the edges of the model are kept straight and parallel during loading.
In the most simple form a model consists of a single matrix-inclusion system. The interior of the model (the unit cell) is thereby considered to repeat periodically over the whole microstructure; the approach being consequently termed *unit-cell technique* or *periodic microfield approach*. Hence, geometrically it describes hence a perfect regular distribution of reinforcements. The unit cell chosen should be representative for the whole microstructure.
Mostly three different approaches have been practiced varying in their degree of complexity and randomness:
1-perfect periodic arrangement of the reinforcements [e.g. BÖH 93A,B, COR 95, MCH 94]
2-random distribution of reinforcements [e.g. BRO 91, CHR 89]
3-random cut-out from the microstructure seen on a plane section through the material [e.g. SAU 93, DIE 93, POE 93]

The question, how far the reality is covered by these cell calculations is strongly influenced by the precision of the chosen geometrical model. Seldom 3D-cells have been modelled up to now, due to the lower computational effort the third dimension has been involved by axisymmetric or plane stress / (generalized) plane strain cells. Materials which show an invariance in one direction are therefore suitable to be modelled two-dimensionally. Unidirectional continuously or non-staggered reinforced MMCs are modelled for instance by imposing symmetry conditions on all boundaries of the unit cell [e.g. BÖH 93B]; on the other hand staggered reinforced MMCs [TVE 90B, SÖR 94] by prescribing point symmetry (Fig. I.3.1-I.3.2).

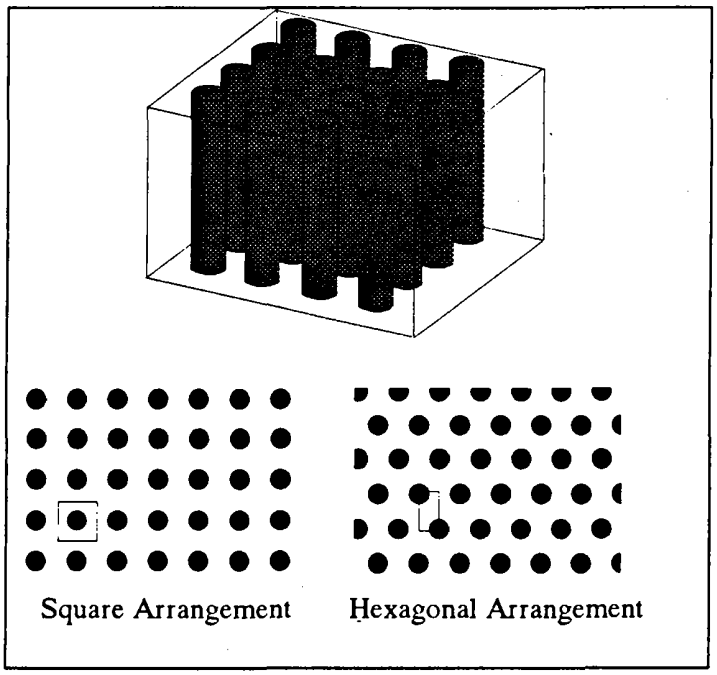

Fig. I.3.1. Unidirectional continuously reinforced MMCs and selected periodic reinforcement arrangements ((generalized) plane strain model)

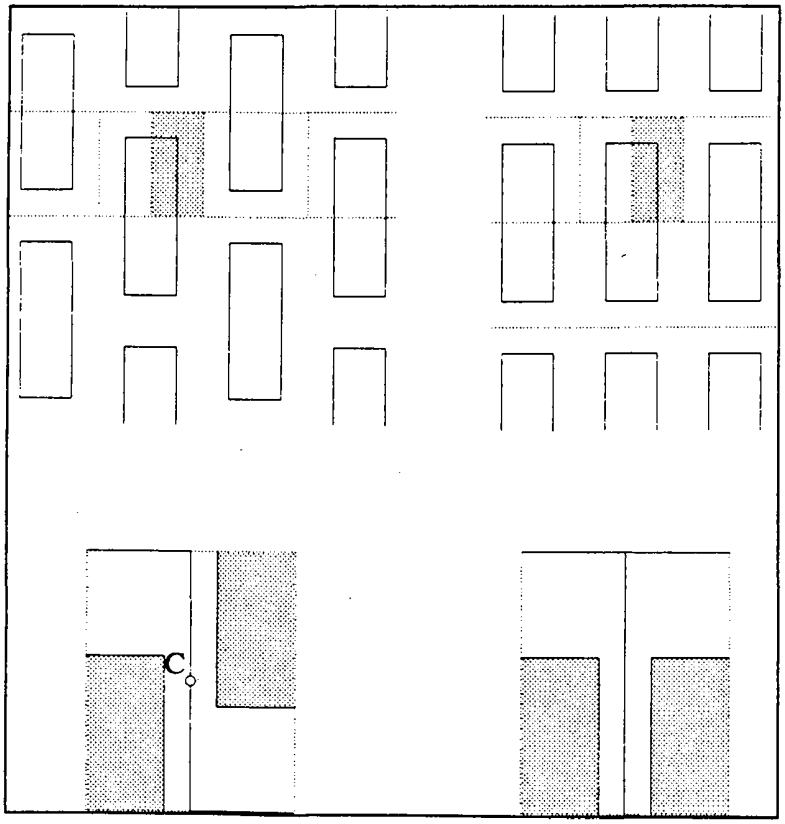

Fig. I.3.2. Aligned staggered and non-staggered short fibers and the respective unit cell (point-symmetry with respect to the midpoint C, and axis-symmetry)

Particle (with spherical, or cylindrical shape) reinforced MMCs may be modelled by an axisymmetric cell model. Bao and co-workers [BAO 91] have shown that the 2D-axisymmetric cell is a good approximation to the 3D-hexagonal cell (Fig. I.3.3).

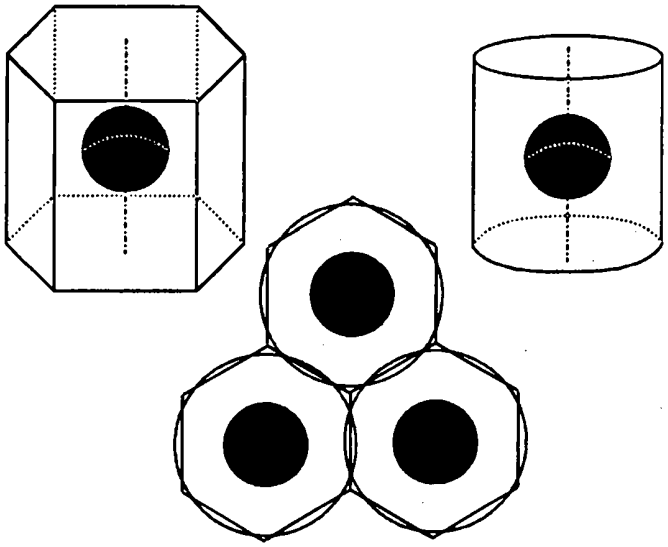

Fig. I.3.3. 3D-hexagonal cell and the approximation by a 2D-axisymmetric cell

When the number of reinforcements inherent in the cell is increasing up to some dozens of reinforcements, an additional problem might arise at the edges of the cells: The periodic extensions of the cell may produce "ghost" reflections of reinforcements intersected by the cell edges which result in artificial shapes of the reinforcements [SAU 93 Fig. I.3.4].

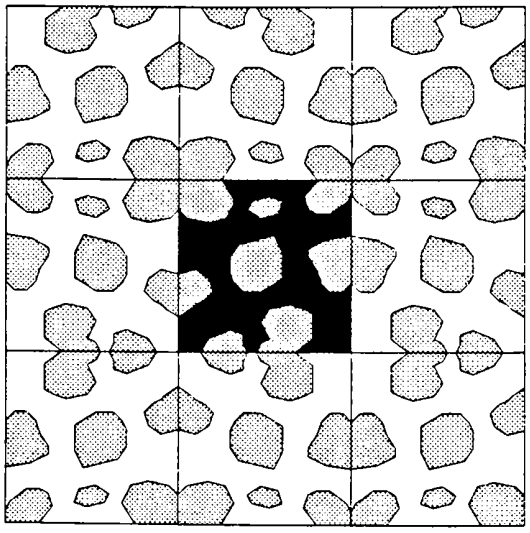

Fig. I.3.4. Multi-inclusion unit cell with symmetry boundary conditions-
artificial inclusion shapes at cell edges

To overcome this drawback, some authors [e.g. DIE 93] have proposed to embed the matrix-inclusion system in a surroundings with the average properties of the composite in the sense similar to the three-phase model presented in the previous chapter.
The overall response is predicted as the homogenized response of the unit cell; the overall stress-strain relationship is obtained from the reaction forces and the prescribed displacements

of the cell edges. Therefore elasto-plastic properties of the composite may be predicted by the unit cell-technique.

I.3.1.2-MODELLING A MICROSCOPIC SECTION AHEAD OF A MACROSCOPIC CRACK

Another important topic in the field of micromechanical modelling was to explore the influence of microstructural parameters on the deformation and damage behaviour ahead of a crack tip. This analysis mostly aims to predict the (fracture) toughness of the material. Only in few examples a fully 3D numerical analysis was carried out [e.g. NAR 92, MEE 90, HAD 95], mostly the problem was simplified by a two-dimensional analysis; a plane strain or/and a plane stress model to describe the mechanical behaviour in the bulk or/and at the surface, respectively. The different situation becomes visible when studying the plastic zone in front of the crack tip (Fig. I.3.5).

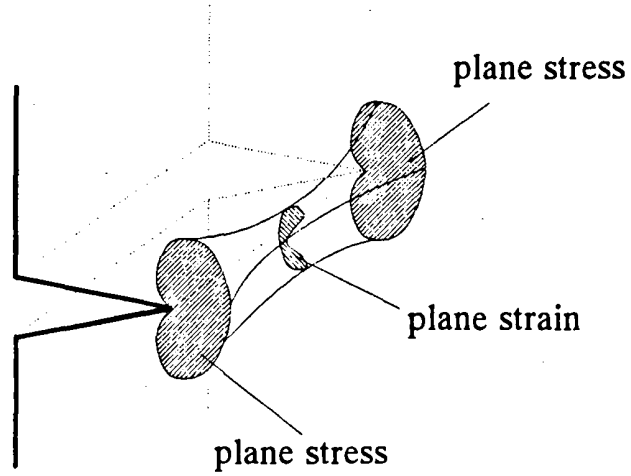

Fig. I.3.5. Size and extent of the plastic zone in front of the crack tip

In many cases, the stress and strain field in front of the crack tip was described by fracture mechanics based parameters. In the linear setting or within small-scale yielding the concept of stress intensity factors (SIFs) associated to different failure modes or that of the energy release rate was applied. If the plastic zone in front of the crack tip reaches a non-neglectable size they are no longer justified and the J-integral concept has to be used [e.g. ROS 82]. The influence of the heterogeneous nature of the material on these parameters has been investigated by some authors [e.g. BRO 94, WEI 93A]. Recently, a fully 3D-formulation of the J-integral concept for heterogeneous materials was proposed [HAD 95].

I.3.2-The Material Model

I.3.2.1-DEFORMATION OF THE COMPONENTS AND THE COMPOSITE

(An-)isotropy

In general the components are assumed to be isotropic. The composite is considered either as an isotropic or orthotropic continuum depending on the microstructure. Orthotropy was involved in the material model in the case of an anisotropic distribution or/and orientation of the components (Fig. I.3.6)

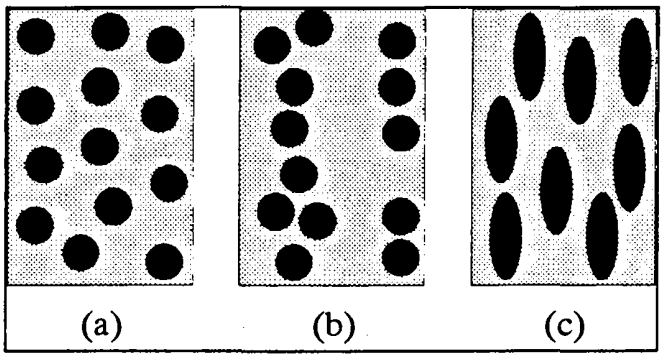

Fig. I.3.6. Schematic of isotropy (a) and anisotropy (b-c) due to a (b) non-homogeneous distribution (c) elongation along preferred orientation of the components

Plasticity

The elasto-plastic behaviour of the matrix is mostly described by the J_2-flow theory of v. Mises that of the orthotropic composite by the flow theory of Hill. Grain size and arrangements are seldom taken into account. The former is commonly considered by the Hall-Petch relation, the latter by a crystal plasticity theory. McHugh et al. [McH 93] use such a crystal plasticity theory in order to account for the orientation of slip systems between the individual grains in an Al-SiC system. The resulting microscale pattern of stresses and strains is qualitatively similar to that obtained with the v. Mises theory but strain localization and stress concentrations are found to be more pronounced. Mostly the analysis has been restricted to the small deformation theory which is not justified in some cases. Such examples are the analysis of ductile damage processes like void formation, growth and coalescence and the blunting effect at the crack tip. In theses cases moderate or even large plastic strains occur, and the use of a geometrical linear theory would give false results.

I.3.2.2-Damage of the components and the composite

Damage is generally modelled by either continuum damage mechanics (CDM) concepts or by a local approach to damage.

1-Continuum damage mechanics

The former one is a phenomenological description, hence uses internal (damage) variables and smears different damage mechanisms. Since the pioneer work of Kachanov on creep damage in 1958 [Kac 58], the CDM-concepts have been spread out fastly and proven successful in many applications (creep-, ductile plastic-, brittle- and fatigue damage (LCF, HCF) [e.g. Lem 85a, Cha 88]). In general, the damage variable is related to the reduction of the load-carrying surface due to microdefects like voids and cracks. The evolution laws for the internal variables are derived from thermodynamical principles and calibrated by damage material parameters. The damage variable enters then the constitutive equations in the following two possible ways (see also chapter IV.3):

(i)-Formulation in the strain-space: The formulation in the strain space is founded on the principle of strain equivalence: Damage of the material is taken into account by transforming the stress tensor $\boldsymbol{\sigma}$ with the help of the transformation tensor $\mathbf{D}$ into the effective stress tensor $\tilde{\boldsymbol{\sigma}}$. The undamaged material is loaded by the effective stresses. It is assumed that the resulting strains correspond to the real strains

$$\tilde{\boldsymbol{\sigma}} = \mathbf{D}^{-1}\,\boldsymbol{\sigma} \qquad \text{(I.3.1)}$$

(ii)-Formulation in the stress space: An analogous formulation is to replace the strains ε by the effective strains $\tilde{\varepsilon}$ while the stresses are remaining according to the principle of stress equivalence.

$$\tilde{\varepsilon} = \mathbf{D}\,\varepsilon \qquad \text{(I.3.2)}$$

The internal variable may be a scalar, if only isotropic damage is considered, or a tensor to account for anisotropic damage. In the latter case, more adjustable parameters are involved and the resolution of the unknown set of equations becomes more difficult.
The internal variables may be interpreted physically, however, often they do not reflect a direct microstructural parameter. The Gurson Model is one of few CDM-concepts which correlate the damage variable to a specific microstructural parameter (the porosity f). This model is mostly adopted and essentially applied to damage evolution in a ductile porous matrix by void formation, growth and coalescence [GUR 77, NEE 84] (see also chapter IV.1). In all CDM-Concepts the stress, deformation and damage analysis is coupled.

2-Local damage approach
In contrast, the local damage approach distinguishes different damage mechanisms by evaluating individual local damage criteria. The damage criterion may operate as a *damage indicator* or as a *failure criterion*.
The damage indicator localizes the susceptibility of the material to the onset of damage. Its evaluation has no consequences on neither the geometry, the material properties nor the stress-strain analysis; hence it is used in an uncoupled manner and may therefore be evaluated in a quasi-postprocessing procedure. The use of that concept is no longer meaningful, if one concentrates on the effects of damage on the subsequent material behaviour. In this case the damage indicator has to be extended to a failure criterion.
The failure criterion determines the local critical condition of the occurrence of a microdefect (cracks, voids). The microdefect (microcracks,-voids) is then introduced either geometrically (modification of the geometry) or physically (modification of the mechanical properties of the components). When the load is applied in a quasi-static manner, the coupling between damage and deformation is covered indirectly by the subsequent load step.
Both, damage indicators and failure criteria, are typically based on stress- or/and strain components. Mostly they are defined in a deterministic manner, statistical failure criteria are employed as fracture criteria for brittle components, often in a Weibull formulation [e.g. BOU 94, LLO 95] For a recent review of different damage indicators the reader is referred to [ZHU 92].

I.3.3-Modelling strategies and results

Almost all investigations fall into one of the following topics:
1-Unit cell investigations studying local effects and predicting the overall tensile behaviour of the composite.
2-FE-simulations analysing the mechanical behaviour ahead of a crack tip.

I.3.3.1-UNIT CELL INVESTIGATIONS

Deformation analysis
Systematic cell computations have investigated the favourable role of the reinforcements on the overall stiffness and strength when compared to those of the respective monolithic alloy. The results generally agree that the development of significant triaxial stresses within the composite matrix, due to the constraint imposed by the reinforcements on the adjoining matrix, is one important contribution to strengthening. Several microstructural parameters have been found

to have a marked influence on this constraint-effect and therefore on the overall deformation characteristics:

(i)-Reinforcement shape: Different reinforcement geometries (spheres and cylinders with different aspect ratio (see chapter I.1)) have been analyzed. High hydrostatic stresses are found in the matrix close to the interface; a consequence of the mutual constraint of the deformation. Sharp corners and high aspect ratio promote the development of hydrostatic stresses. This local effect implies that the macroscopic stiffness, flow strength and strain hardening are elevated for this reinforcement geometry [LLO 91A, CHR 89, BAO 91].

(ii)-Reinforcement content: With increasing volume fraction, the ratio spacing between inclusions to inclusion-size decreases, and interaction between inclusions becomes more important. The above described constraint effect is amplified by the increasing interaction of reinforcements. As a result overall stiffness, flow strength and strain hardening are considerably elevated regardless of the shape of the reinforcement [BAO 91, LLO 91A].

(iii)-Reinforcement morphology: The significant influence of the morphology of the microstructure on the global mechanical behaviour begins to receive serious attention. Two different topologies were addressed: the *interwoven arrangement* and the *matrix-inclusion topology* (see also chapter I.1):

Interwoven arrangement: The pronounced influence of morphological characteristics like the contiguity, and the fraction-of-cluster parameter (see chapter I.1) for instance on the overall behaviour was investigated in [SIE 93, UGG 82]. Modified rules-of-mixture accounting for these parameters were verified by FE-predictions. The relationship between the plastic flow properties of the composite and the morphological continuity of the different ductile phases was quantified: Increasing the continuity of the weaker phase causes the overall flow strength to decrease steadily [BÖH 94].

Matrix-inclusion topology: FE-investigations on microscale arrangement effects of metal matrix composites (MMCs) started only six years ago and are still subject of current research analysis. Continuously- [BÖH 93B, BÖH 94, BRO 91] as well as discontinuously reinforced MMCs (reinforcements being whiskers, short fibers or particulates) [BAO 91, LLO 91A, CHR 89, BÖH 93A] have been investigated under axial and transverse mechanical loading as well as under thermomechanical loading.
For the former class of materials, perfectly symmetric arrangements like the square and hexagonal arrangement and clustered arrangements have been considered [BÖH 93B, BÖH 94]. The results displayed a strong influence of the arrangement on the microscale field quantities. In addition the overall (macroscopic) response to transverse mechanical loading was found to be dependent on the microscale topology [BÖH 93B]. Brockenbrough and co-workers [BRO 91] used a multi-fiber unit cell (30 fibers in a pseudo-random arrangement) in order to visualize the effect of local clustering of the fibers on the microscale stress and strain fields. Under axial loading no marked influence was found. The fibers carried the load almost fully and the ultimate failure is reached prior to plastic deformation of the matrix. Consequently, the overall properties are insensitive to the way how the fibers are distributed in the matrix. In contrast, under transverse tension or shear, the load is transmitted across the fibers via the ductile matrix and gives rise to a highly inhomogeneous matrix strain field. The constrained flow of the matrix affects the evolution of hydrostatic stresses which, in turn influence the overall flow properties of the composite.
The influence of the arrangement of aligned fibers in discontinuously reinforced MMCs in an uniform remote array on the overall response has been studied via plane strain and

axisymmetric models. In general the plastic flow response seems to be markedly affected while the overall elastic response seems to be insensitive to the reinforcement distribution. Overlapping fibers were found to decrease the flow strength when compared to that of non-staggered fibers [see Fig. I.3.2, BAO 91, TVE 90B].
Christman et al. [CHR 89] and Llorca et al. [LLO 91A] both investigated clustering effects by shifting the whiskers from the perfect uniform distribution in the axial (vertical) or radial (horizontal) directions. For both types of clustering, the flow strength and strain hardening were significantly reduced as compared to those for the perfectly uniform distribution. This reduction was more dramatic for axial clustering. These effects were equally attributed to the way how plastic strains and particularly hydrostatic stresses evolved in the matrix.

Damage analysis
At present, first attempts are made to extend the above discussed analysis to account for the effects of local damage events and evolution on overall strength and ductility.
The use of damage indicators like the triaxiality or parameters based on it [e.g. FIS 96, BÖH 94] was suggested for the damage analysis of continuously reinforced MMCs.

In discontinuously reinforced MMCs the effects of particle cracking and interfacial failure has been studied [MIC 93, BAO 92, MCH 94]. To the knowledge of the author damage was always simulated in a static manner: a progressive damage behaviour was not modelled. This might have been for two reasons:
Mostly a single matrix-reinforcement unit cell is used. For this reason local failure at reinforcements is assumed to occur simultaneously in all reinforcements inherent in the material. Another reason might be that most scientists use commercial FE-codes; the incorporation of failure criteria might be a complicated task. Therefore it is assumed that particles are already initially broken or debonded. The important effect of stress distribution in the structure due to the damage events could hence not be accounted for. Nevertheless, even with these severe hypothesis one was able to give qualtitative tendencies for the prediction of the overall ductility [e.g. MIC 93].
Ductile damage processes in the matrix like initiation, growth and coalescence of voids at smaller-scale particles were most often studied by the CDM-model of Gurson within the framework of large deformation analysis [e.g. MIC 93, LLO 91A].

I.3.3.2-CRACK TIP MODELLING

First attempts to include the heterogeneous nature of the material into the deformation analysis of the near crack tip zone have been made by Aravas, McMeeking and Hom [ARA 85, MEE 90]. In these works the near crack tip growth of spherical and cylindrical voids (parallel to the crack front) ahead of a blunting crack were examined. These voids were assumed to be nucleated at large (elongated) particles. The presence of smaller-scale cavities in the ligaments between the holes and the blunting crack was accounted for by the CDM-model of Gurson. The numerical computations were based on finite strain theory.
Aravas and Mc Meeking [ARA 85] found that the interaction between the void and the blunting crack strongly influences the stress and strain field in the ligament as well as the growth rate. The latter one was found to depend additionally on the void shape: cylindrical voids grow approximately five times the rate of initially spherical voids, the principal direction being towards the crack tip. The bearing effect of *void-crack interaction* was evidenced by comparing the growth rate (in terms of the rate of the void radius $\dot{R}$) with that predicted by previous models on *isolated* cylindrical and spherical voids [CLI 68, RIC 69 see also chapter IV.1.2] :

spherical voids	*cylindrical voids*
$\frac{\dot{R}_{FEM}}{\dot{R}_{[Ric\ 69]}} \approx 2$	$\frac{\dot{R}_{FEM}}{\dot{R}_{[Cli\ 68]}} \approx 6$

where $\dot{R}$ is the rate of the void radius R.

Lateron Mc Meeking and Hom [MEE 90] carried out full three-dimensional computations. Initially, spherical voids were placed periodically along a line directly ahead of and parallel to the crack front. The growth rate of the holes was evaluated for three orthogonal directions: (I) towards the crack tip, (II) towards each other and (III) in the tensile direction (mode I plane strain crack tip). It was found $\dot{R}_I > \dot{R}_{II} > \dot{R}_{III}$ indicating that the interaction between void and crack is dominant.
Lipetzki et al. [LIP 93] investigated the influence of a soft, ductile inclusion in the near crack tip on fracture mechanics based parameters. The interaction between inclusion and crack under pure mode I was studied by an elastic, plane strain model. The influence of the inclusion on the crack decreases with increasing crack-inclusion distance. A definition for the size of the zone where the crack-inclusion-interaction is still apparent was suggested as function of the crack length and inclusion size.
Similar studies in this line but extended to the 3D-case were performed by Haddi and Weichert [HAD 95]. In the same paper, a new analytical expression of the J-integral for inhomogeneous materials was presented.

Only few attempts have been made to investigate occurrence and evolution of damage within the individual phases inherent in the material [BRO 94, GRO 95, LÜS 95, WUL 93, SCH 96]. In all of these works a section of a real microstructure ahead of a fatigue crack in TPB-specimen was modelled.
Broeckmann [BRO 94] and Lüsebrink [LÜS 95] simulated automatically progressive carbide cracking ahead of the crack tip of the SAE-D3 steel after warm forging and in the as-cast condition, respectively. The simulations were conducted under realistic loading conditions to correlate them with experimental findings. In addition, the influence of the development of the fracture process zone (FPZ) on the (brittle) crack propagation behaviour could be quantified.

The ductile growth of the main crack in the matrix was simulated by Schmauder, Wulf and co-workers [WUL 93, SCH 96]. The propagation of the crack was simulated using a local failure criterion in conjunction with the element-removal-technique. Several local failure criteria have been investigated which were based on stress triaxiality, plastic strains or a combination of them. Using a damage failure criterion based on the model of Rice and Tracey [RIC 69, see also chapter IV.2] the crack path experimentally observed in an Al/SiC(20%) MMC could be simulated with high accuracy.

CHAPTER II

THE MATERIAL AND EXPERIMENTAL FINDINGS

II.1-The composite under consideration
II.1.1-The elaboration process
II.1.2-The components
II.1.2.1-The metal matrix (MM)
II.1.2.2-The hard phases (HP) and the interface
II.1.3-The heat treatment
II.1.3.1-General remarks
II.1.3.2-The composite and the equivalent material of the metal matrix

II.2-Geometrical characterization
II.2.1-Morphology of the composite
II.2.2-Geometry of the hard phases (HP)

II.3-Mechanical characterization
II.3.1-Deformation characteristics
II.3.2-Damage characteristics

II.1-The composite under consideration

The considered material is the ledeburitic chromium steel SAE-D3 (German norm: X210Cr12). It consists of ceramic hard phases (HP) discontinuously embedded in a hardeningable metal matrix (MM). The basic element in the matrix is ferrum with body centred cubic structure (bcc). In the annealed state the MM consists mainly of a α-mixed crystal, in the hardened state of martensite and retainedaustenite. The ceramic hard phases reinforce the composite and enhance considerably wear resistance and macroscopic hardness. The high volume fraction of ξ_{HP}=0.17 motivates the use of this material in structural applications under severe tribological conditions. High volume content of chromium and carbon favours the formation of these hard particles in form of Fe-Cr-carbides. The high volume content of carbon serves additionally for a high hardness in the martensite. The chemical composition of steel SAE-D3 is given below [HAE 90].

Material	C in %	Cr in %	Si in %	Mn in %	Fe in %
SAE-D3	2,10	12,00	0,3	0,3	~85

Tab. II.1.1. Chemical composition of the composite under consideration

II.1.1-The elaboration process

After slow cooling, steel SAE-D3 consists of a α-mixed crystal and of hard carbides of type M_7C_3 [BUN 58]. The latter are present as large eutectic carbides crystallizing between 1200°C and 1180°C or as secondary carbides forming by further cooling. Both types were identified by Zum Gahr [ZUM 80] as $(Cr_4Fe_3)C_3$-carbides with hardness between 1100 and 1550 HV 0,05 [BER 93]. Almost the whole chromium goes in reaction to form carbides; only 1,1% remains in the matrix and contributes to its solid solution hardening [BER 76]. After casting the HP exist in a netlike structure. A hot forging process with a degree of deformation $\lambda \geq 10$ destroys this arrangement and gives rise to a banded structure where carbides are aligned in rolling direction and concentrated in these bands. A high degree of forging leads to a dispersion of aligned carbides. Fig. II.1.1 shows the different arrangements.

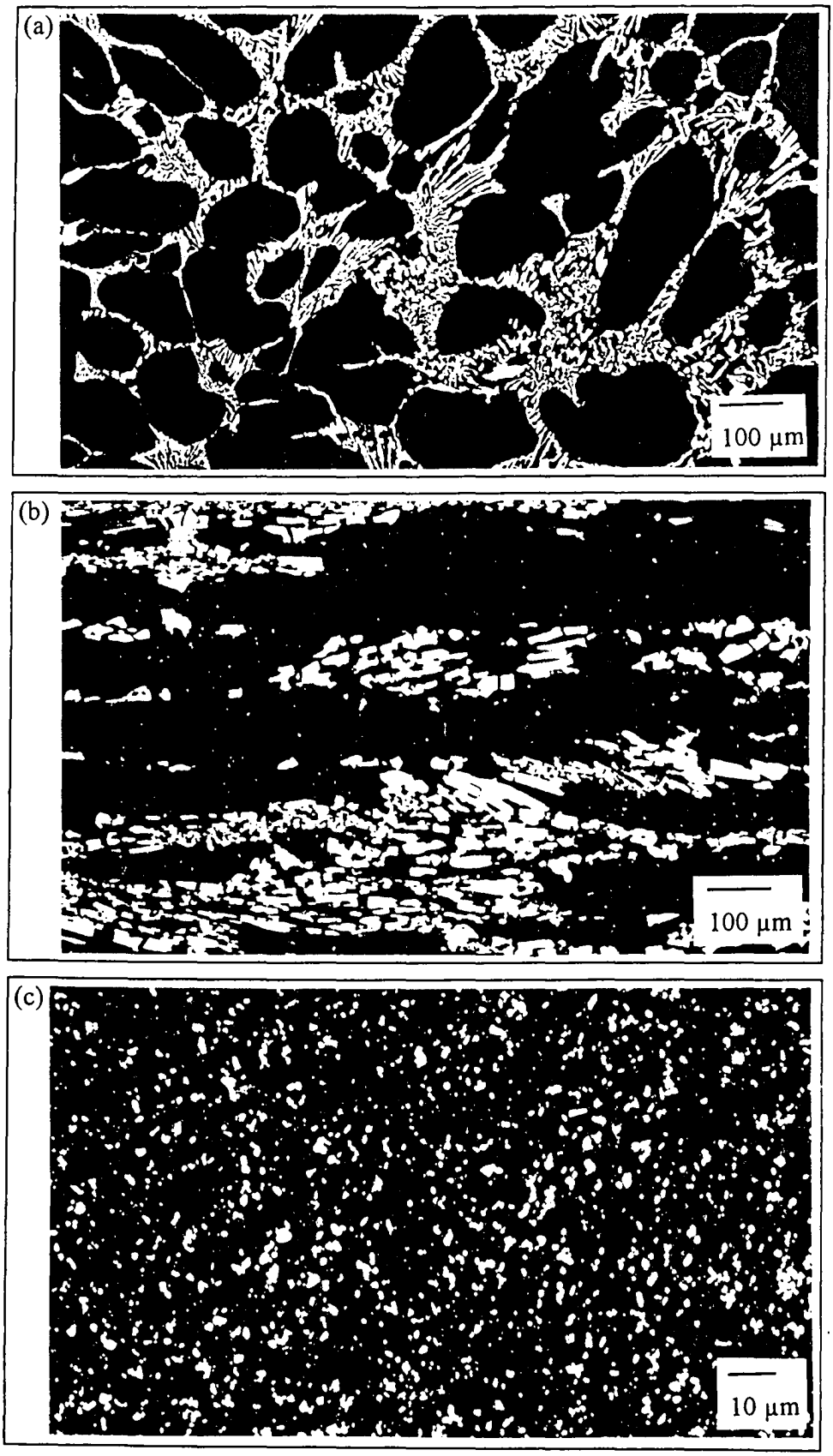

Fig. II.1.1. Microstructure of SAE-D3 [BER 93]
(a) netlike structure (b) banded structure (c) Dispersion

II.1.2-The components

II.1.2.1-THE METAL MATRIX (MM)

Since the mechanical characterization of the metal matrix on the microscale is rather complicated, an equivalent material has to be chosen representing the microstructural characteristics of the matrix. In the annealed state the matrix is defined as a conglomerate of iron mixed crystals and secondary carbides, whereas in the hardened and tempered state it consists of martensite and retainedaustenite. Differences in their mechanical behaviour demand for a different criterion in order to select the model matrix:
annealed state: coincidence of the whole chemical composition
hardened state: coincidence of the carbon content, because it is the driving force (energy) for martensitic transformation.

With the chemical composition of the MM in the composite estimated by Broeckmann [BRO 94] (Tab.II.1.2), the following materials are proposed to describe the mechanical behaviour of the MM:
annealed state: X 100 CrMoV 5 1 (German norm)
hardened state: 90 MnCrV 8 (German norm)

Material	C in %	Cr in %	Mo in %	Mn in %	V in %
MM*	0,95	6,45	-	-	-
X 100 CrMoV 5 1	1,00	5,30	1,10	-	0,20
90 MnCrV 8	0,90	0,40	-	2,00	0,10

Tab. II.1.2. Chemical composition of the materials used as model for the MM of SAE-D3
* estimated chemical composition of the MM in the composite after [BRO 94]

II.1.2.2-THE HARD PHASES (HP) AND THE INTERFACE

Hard phases are classified with respect to their type of bonding (covalent, ionic or metallic bonding) which strongly affects their properties. The strength of metallic bonding in M_7C_3 is higher than in the metal matrix and results in high hardness but also in brittle behaviour even at room temperature. Hard phases possess lower dislocation density. In general, high shear stresses are necessary to initiate crystal slip so that in most cases cleavage occurs prior to slip. Due to the metallic bonding of both, MM and HP, the interface between them is likely to be coherent or semicoherent which provides good strength properties. However, excessive stress concentrations at the interface due to enhanced dislocation density by progressive plastic deformation might initiate debonding between HP and MM.

II.1.3-The heat treatment

II.1.3.1-GENERAL REMARKS

The steel SAE-D3 is investigated in different states of heat treatment: annealed as well as hardened and tempered at different temperatures.
Annealing:
The extraction of interstitial elements from the matrix during annealing above $A_{c_{1f}}$ by forming carbides gives rise to a drop of the mixed crystal hardness of the matrix. The spherical shape of the secondary carbides favours crystal slip and drops the macroscopic hardness. In the annealed state nearly the whole carbon is found in the carbides.
Hardening:

Heating in the austenite state affects the solution of the secondary carbides, while the eutectic carbides remain. The sudden drop of temperature in oil (quenching) triggers martensitic transformation. Since martensitic finishing temperature M_f is under room temperature, retainedaustenite remains in the microstructure. The austenising temperature influences M_f and therefore also the content of retainedaustenite (between 20 and 90 %) [BER 74].
Tempering:
Retainedaustenite can be eliminated by deep cooling or tempering. The latter serves furthermore for lower hardness and higher ductility of the material. For low steel alloys different chemical processes can be attributed to different tempered states [HAE 90]:

Step 1 (T<100°C):	Diffusion of carbon into the vacancy (sinks) of the martensite
Step 2 (100°C<T<250°C):	Diffusion of carbon and formation of Fe_2C
Step 3 (350°C<T<600°C):	Transformation of retainedaustenite into bainite
Step 4 (T>600°C):	Transformation of Fe_2C into Fe_3C (cementite)

II.1.3.2-THE COMPOSITE AND THE EQUIVALENT MATERIAL OF THE *METAL MATRIX*
The steel SAE-D3 is investigated at three different states of heat treatment, characterized by the following indices:
"Ann": annealed state (800°C<T<820°C)
"380": hardened (950°C, oil) and tempered (380°C) state
"600": hardened (950°C, oil) and tempered (600°C) state

The matrix in the annealed state is replaced by the material X 100 CrMoV 5 1, and in the hardened and tempered state by the material 90 MnCrV 8. The influence of the heat treatment on hardness and content of retainedaustenite is illustrated in Table II.1.3.

Material	state of heat treatment	hardness [HV30]	ξ_{RA} [%]
SAE-D3	*"Ann"*	250	-
SAE-D3	*"600"*	460	0,0
SAE-D3	*"380"*	648	6,2
X 100 CrMoV 5 1	*"Ann"*	217	-
90 MnCrV 8	*"600"*	396	0,0
90 MnCrV 8	*"380"*	543	6,0

Tab. II.1.3. Hardness and retainedaustenite of all materials under consideration for different states of heat treatment [BRO 94]

II.2-Geometrical Characterization

II.2.1-Morphology of the composite

The steel was already characterized in II.1 as a composite material containing two main phases, where one phase (HP) is distributed discretely in a continuous second phase (MM). Its morphology is identified as a coarse microstructure after Fischmeister [FIS 73], since both phase sizes are in the range between 1 and 100 µm. It was already emphasized that the carbides are generally non-homogeneously distributed over the whole microstructure. In the as-cast condition they are mainly distributed in a net, after hot forging mainly along bands. Only for higher degrees of forging, is a nearly homogeneous distribution (dispersion) of hard phases over the whole microstructure obtained. Schematics of the different microscale morphologies are given below

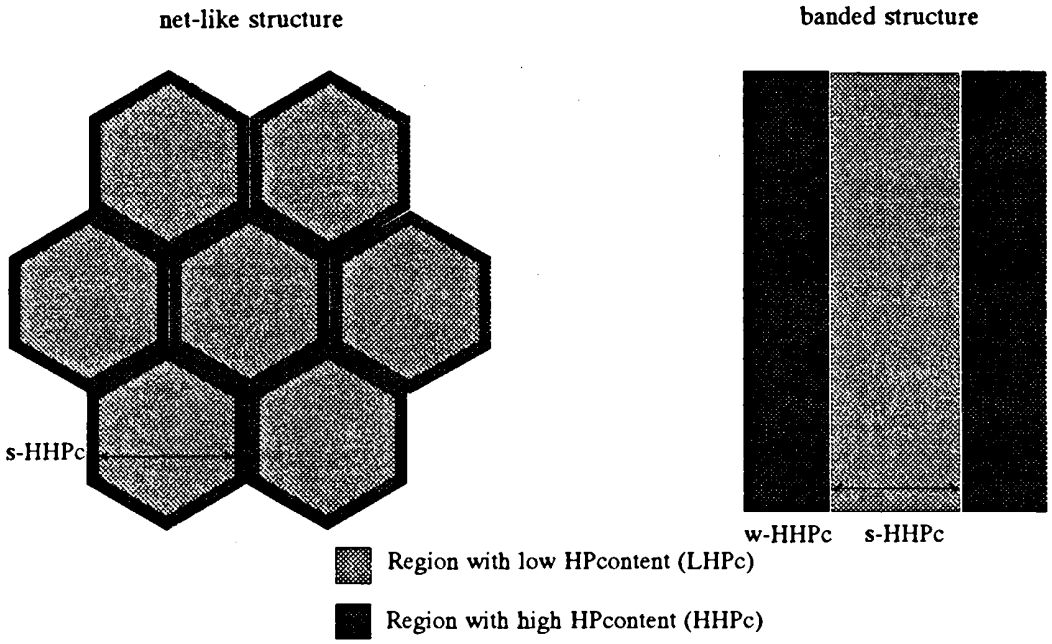

Fig. II.2.1. Schematics of the microstructure in SAE-D3 in the as-cast condition (a) and after hot forging (b)

The geometrical parameters introduced in these schematics have been quantified by optical micrographies

banded	structure	netlike structure
w-HHPc in µm	s-HHPc in µm	s-HHPc in µm
44,73 ± 14,27	60,21 ± 15,69	270

Tab. II.2.1. Width (w-HHPc) and spacing (s-HPPc) of regions with high HP content (HHPc) after hot forging [BRO 94] and in the as-cast condition [LÜS 95]

II.2.2-Geometry of the hard phases (HP)

It has been seen in the previous chapter that the amount of hard phases quantified by the volume fraction is not homogeneous over the whole microstructure but seems to be constant in specific regions (inner and outer of the bands, eutecticum of the net-like structure). Therefore the volume fraction has been determined individually for these regions.

Banded structure

The macroscopic anisotropic behaviour of the material after hot forging is mainly related to the non-uniform distribution of the eutectic carbides and to their aligned orientation. This necessitates a quantification under each orthogonal cut. The relative values are listed in table II.2.2, together with the mean free path L_{HP}, the mean aspect ratio h/b and the mean particle spacing D_{HP} (see also figure).

	longitudinal cut			transversal cut	Volume
	carbide band (HHPc)	region between carbide band (LHPc)	total		
ξ_{HP} [%]	20,15	14,00	17,00	15,00	16,00
L_{HP} [µm]	-	-	5,95	4,26	5,11
h/b	-	-	1,427	0,926	-
D_{HP} [µm]	11,75	14,09	12,79	9,75*	7,59**

Tab. II.2.2. Geometrical characteristics of the hard phases within SAE-D3 in the annealed state [BRO 94] after hot forging
* after eqn. (I.1.3b); **after eqn. (I.1.3c)

Netlike structure

Image analysis of the microstructure under three orthogonal cuts turned out no noticeable anisotropy. The following geometrical characteristics were found [LÜS 95]

	eutectic net	total
ξ_{HP} [%]	42	16
h_{HPmax} [µm]	130	130
h/b_{HPmax}	10	10

Tab. II.2.3. Geometrical characteristics of the hard phases within SAE-D3 in the as-cast condition [LÜS 95]

II.3-Mechanical characterization

In the forgoing chapter, the morphology was described by appropriate geometrical characteristics. These characteristics may be of relevance for any kind of modelisation that means they are absolutely independent of the chosen constitutive model. However, the use of a certain constitutive model demands to identify specific material parameters. The table below shows how microcomponents may be attributed to a certain constitutive model which has to be fitted by specific material characteristics.

possible constitutive models for the components	elastic	elastic-plastic	elastic-brittle	elastic-plastic with damage
material parameters	E, ν	E, ν, σ_{Y0}, n	E, ν, σ_{Ic}	E, ν, σ_{Y0}, n, D

Tab. II.3.1. Different constitutive models for the individual components and their fitting with material parameters

The determination of some of these parameters is described in the following. The experimental investigations are only done on hot forged specimens.

II.3.1-Deformation characteristics

Micro residual stresses have emerged from cooling and heat treatment of the material due to thermal coefficient mismatch and phase transformation, and cause an initial anisotropy in the material. The mechanical behaviour under tensile and compressive conditions might not be the same. The determination of the elasto-plastic properties is therefore not unique and can not be ascertained with only one test.

II.3.1.1-TENSION TEST

Specimens have been cut out from the material with their length side along both axis, the L and T axis to account for the anisotropy. The geometry of the specimen is given in [BRO 94]. The smoothness of the surface has been improved by a polishing treatment in order to reduce its influence on the experimental results particularly in the hardened state. Deformation was measured by strain gauges. The results are given in Tab. II.3.2. The yield limit is determined at 0,01 % plastic deformation ($R_{p0,01}$) and at 0,2 % plastic deformation ($R_{p0,2}$). For a large yield limit area these values are replaced by the upper yield limit R_{eH} and the lower yield limit R_{eL}. A denotes the total strain at rupture, R_m the fracture strength and n is a hardening exponent.

Material	heat treatment	orientation	$R_{p0.01}$ [MPa]	$R_{p0,2}$ [MPa]	R_m [MPa]	A [%]
SAE-D3	"Ann"	L	311	403	710	9,17
		T	343	347	651	3,09
	"600"	L	1073	1316	1484	1,04
		T	1071	-	1252	0,12
	"380"	L	980	1429	1734	0,46
		T	1079	-	1253	0,05
X 100 CrMoV 5 1	"Ann"	L	481*	427*	726	23,87
		T	465*	429*	742	21,03
90 MnCrV 8	"600"	L	1006	1195	1420	6,35
		T	1042	1162	1343	2,28
	"380"	L	1465	-	1671	0,18
		T	1126	-	1164	0,01

Tab. II.3.2. Results of the tension test [BRO 94]
* $R_{p0,01}$ and $R_{p0,2}$ are replaced by R_{eH} and R_{eL} (due to a large yield limit area)

II.3.1.2-COMPRESSION TEST

The results of the tension tests are showing that several specimen are fractured before 0,2% plastic deformation. Locally however, plastic deformation greater than this value may be achieved. A relationship between stresses and strains beyond this value is required. For this reason compression tests are performed, since under compressive conditions the material behaves more ductile. For more details on the conditions of the conducted experiments we refer to [BRO 94]. The following results were obtained

Material	heat treatment	orientation	$R_{p0,01}$ [MPa]	$R_{p0.2}$ [MPa]	n* [ ]	E [MPa]
SAE-D3	"Ann"	L	381	400	0,243	223230
		T	259	395	0,207	207534
	"600"	L	953	1303	0,268	226909
		T	1071	1378	0,339	204796
	"380"	L	1448	1991	0,450	220338
		T	1438	2096	0,483	220085
X 100 CrMoV 5 1	"Ann"	L	436	456	0,200	216459
		T	430	438		218491
90 MnCrV 8	"600"	L	597	1475	0,382	206349
		T	798	1151		209887
	"380"	L	894	1783	0,448	220689
		T	1510	1827		218368

Tab. II.3.3. Results of the compression test [BRO 94]
* n is the hardening exponent of the relation $\sigma_Y = \sigma_{Y0}(\varepsilon / \varepsilon_{Y0})^n$

II.3.1.3- ELASTO-PLASTIC MATERIAL PARAMETERS USED FOR NUMERICAL COMPUTATIONS

In the beginning, the relationship between the constitutive model and fitting material data was emphasized. If an isotropic hardening model is chosen, differences in the flow behaviour under tension or compression are neglected, hence a unique hardening curve has to be found. Since our numerical model assumes isotropic hardening, the results of the tension and pressure tests are combined. It seems likely that the Young's modulus is not affected by the heat treatment. Their deviations in table II.3.3 seems to be of statistical nature. The arithmetic mean is taken as general value. The resulting values are in accordance with those found in former works [HAE 90] (see Appendix A.1) which were used for computations. The elasto-plastic parameters have been determined in the following way:

Up to the ultimate tensile strength of the composite, the stress-strain curve obtained by the tension test is also used for simulations. For larger plastic deformation the hardening curve obtained from the compression test is used. Finally the stress-strain curve is extrapolated to strains up to 10%. The overall stress-strain curves are plotted in the Appendix (Appendix A.2).

II.3.2-Damage characteristics

II.3.2.1-DAMAGE BEHAVIOUR ON THE SURFACE (EXPERIMENTAL OBSERVATIONS)

The damage behaviour of steel SAE-D3 has mainly been investigated on precracked specimen under inhomogeneous loading. The advantage of precracked specimen over e.g. tensile specimen is that damage events are clearly localized in front of the crack tip and that propagation of the main crack can be followed during loading. The damage behaviour of the surface was mostly studied by three-point bending tests (TPB) in both interrupted and continuous manner. In the interrupted way the specimen is loaded stepwise where after each step the specimen is withdrawn from the loading device and investigated under the SEM to characterize the new damage zone. In the continuous way, (in-situ tests) the specimen is directly mounted into the chamber of the SEM. By this method it is possible to measure the reaction force as function of the displacement and simultaneously to follow the evolution of damage ahead of the main crack during loading. The geometry of the TPB-specimen used for both, interrupted and in-situ tests is given below

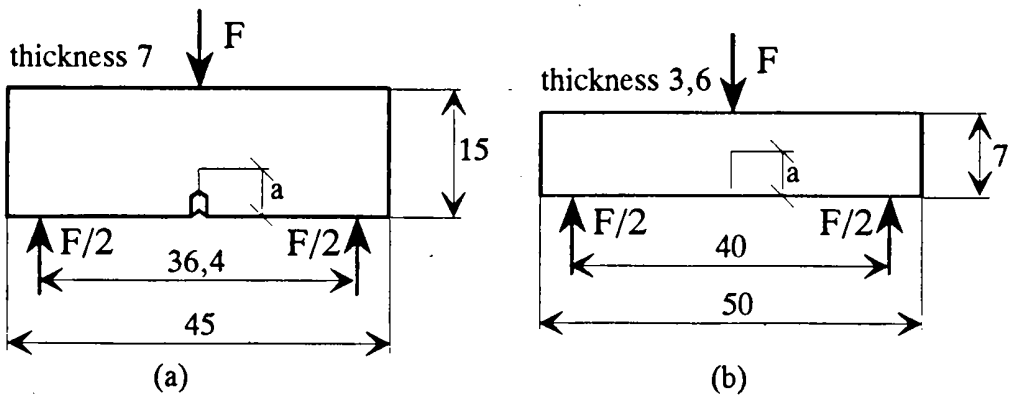

Fig. II.3.1. Geometry of the TPB-specimen used for (a) interrupted and (b) continuous tests (in-situ)

Specimen in the orientation T-S and after heat treatment "Ann", "600" and "380" were investigated. The resulting force-displacement curves are given below

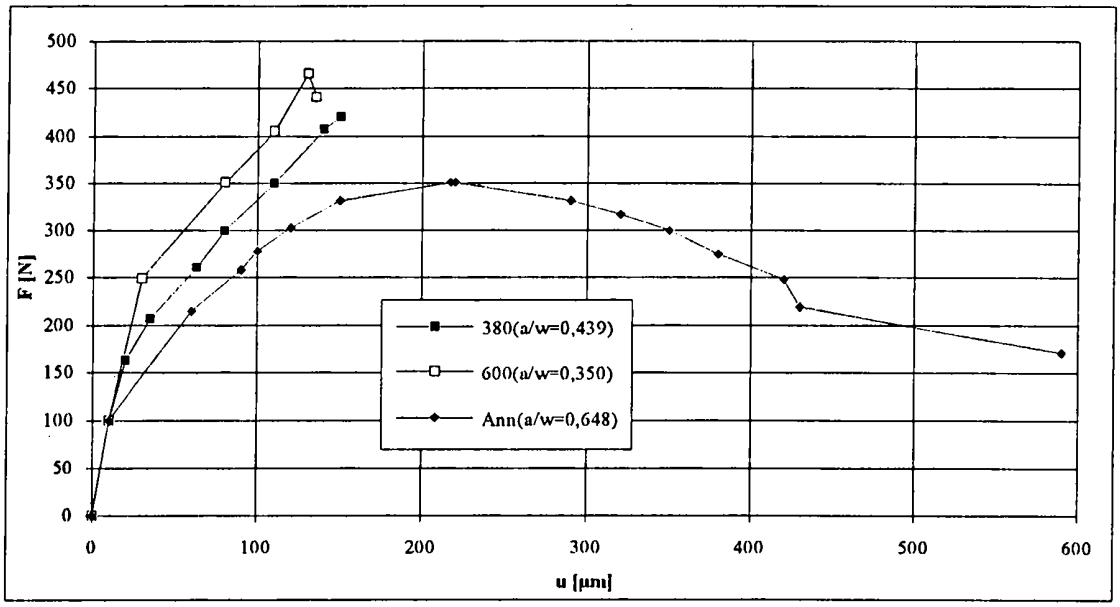

Fig. II.3.2. Force-displacement curves of TPB-in-situ tests [BRO 94]

A-Crack initiation stage

The most frequent damage mechanism was identified as cleavage of eutectic M_7C_3-carbides. It was observed that larger carbides were more prone to fail. Often these big carbides with aspect ratio of h/b~1 were fractured simultaneously along different crystallographic planes. Generally microcracks developed perpendicular to the principal normal stress-direction. When carbides were aligned in this direction, they were often fractured at their mid-length. Only few small, spherical eutectic carbides were found to be debonded from the matrix. However, all secondary carbides which have been attributed to the matrix were found to have failed by decohesion. Both damage mechanisms are illustrated below

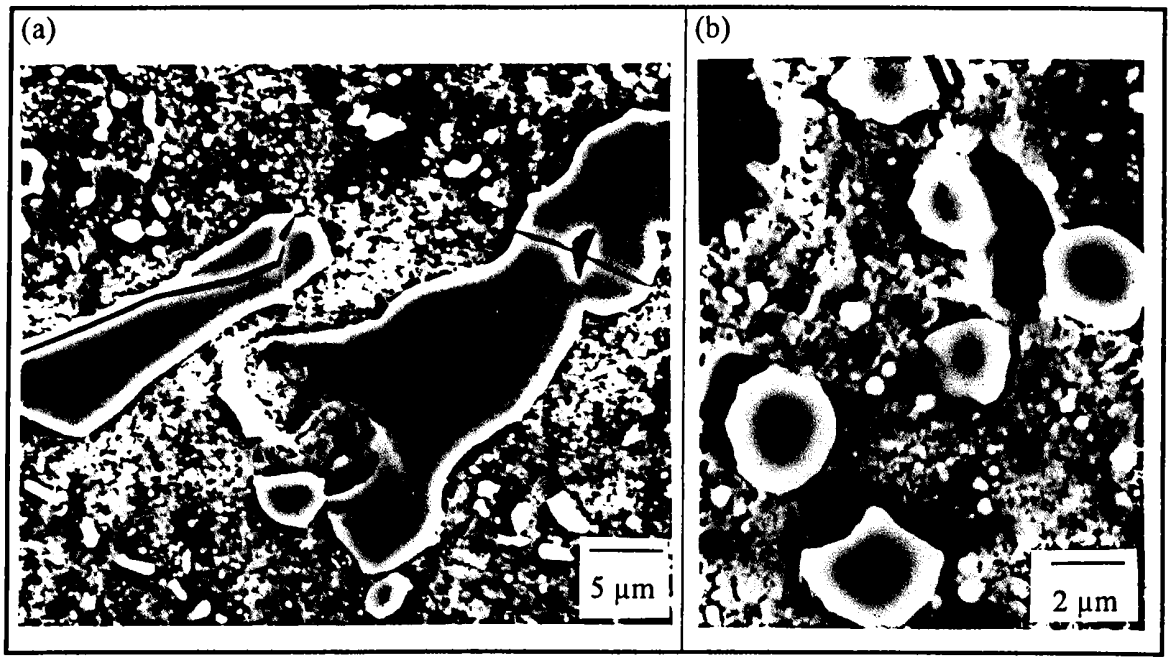

Fig. II.3.3. Damage mechanisms in steel SAE-D3 ("600") [BRO 94]
(a) particle cracking; (b) interfacial failure

Often it was also observed that a microcrack developed by particle cleavage initiates interfacial failure. The figure below shows where after carbide cleavage, the microcrack was propagating into the matrix and on the other side along the interface.

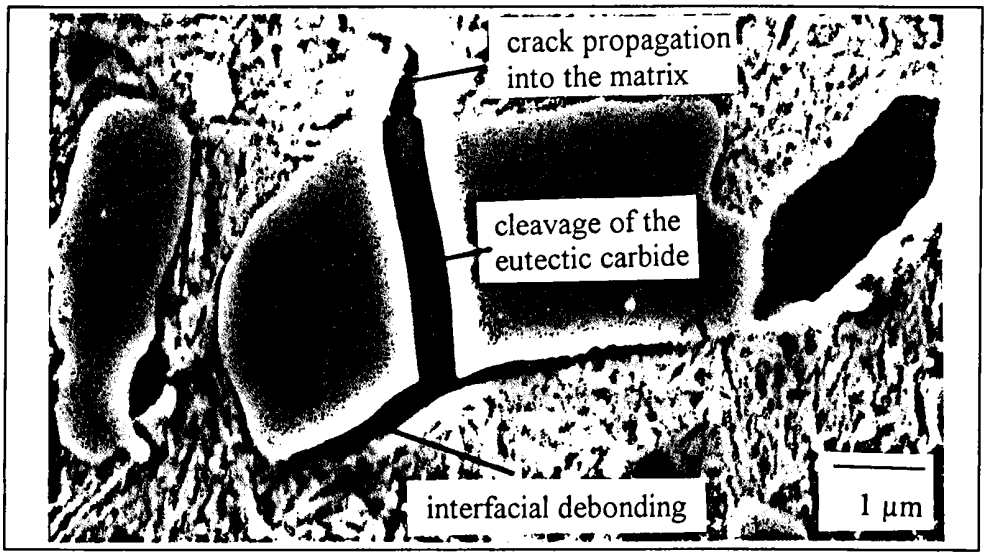

Fig. II.3.4. Microcrack propagation after carbide cleavage [BRO 94]

B-Crack propagation stage

Stable damage growth can be characterized by three stages which go hand in hand. In the first stage the main crack will open and high plastic strains are accumulated in front of the crack tip. This intense plastification is known as crack tip blunting. Depending on the ductility of the matrix the plastic zone will spread out over a limit zone. The opening of the main crack leads to high stress concentrations at HP ahead of the crack tip. The exceedence of local stresses at HP ahead of the crack tip causes microcracking due to HP-cleavage or particle-matrix-debonding. The figure below shows where a coarse carbide just in front of the fatigue crack of a TPB specimen (interrupted test, S-T orientation, in the annealed state) was fractured after a single monotonic loading (F=3590 N). A noticeable crack tip opening (δ= 5,88 µm) was measured.

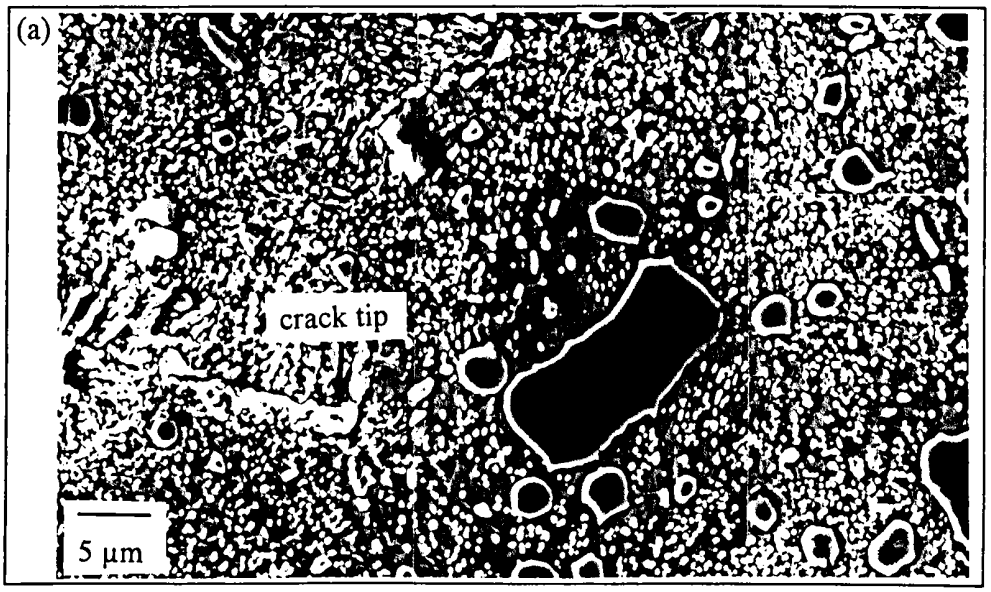

Fig. II.3.5. Crack tip of a TPB-specimen (interrupted test) of steel SAE-D3 [BRO 94] (S-T orientation, "Ann") (a) before and (b) after monotonic loading with F=3590 N

Once one HP has failed the sudden release of energy causes stress concentrations in front of the microcrack. With increasing hardness of the matrix, the ability to absorb the released energy by plastification decreases and hence neighbouring particles fail instantaneously. In these states initial damage ahead of the crack tip might trigger immediately instable crack propagation. In the more ductile state the orientation of microcracks within the damaged zone to each other and to the main crack controls the failure mode of the matrix ligaments. In his doctoral thesis Broeckmann [BRO 94] quantified the size of the plastic zone and of the fracture process zone for all possible orientations and states of heat treatment. He also estimated the crack tip opening displacement and the strains just in front of the crack tip. Since these quantities were not correlated with predictions by numerical simulations the tables are not given here. The reader is referred to [BRO 94].
The following figures are micrographies of the TPB-in-situ tests. They illustrate the evolution of microscale damage in front of the crack tip at selected load steps.

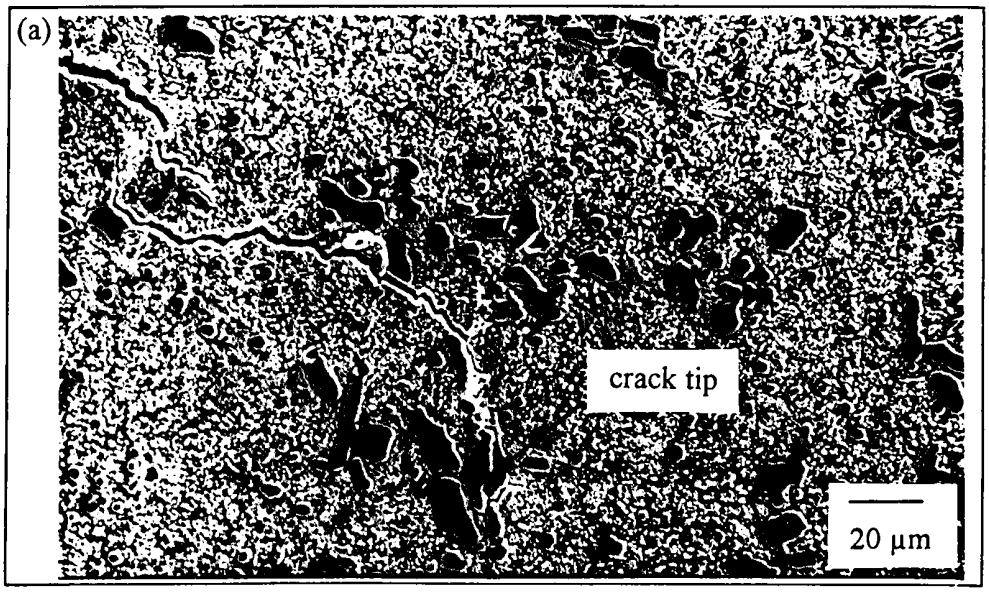

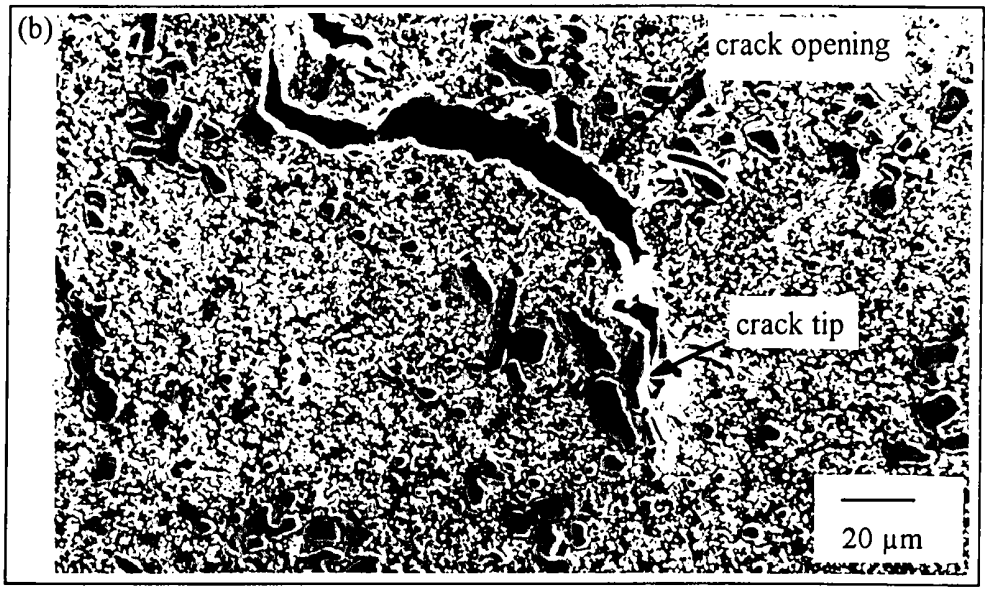
(b)
crack opening
crack tip
20 µm

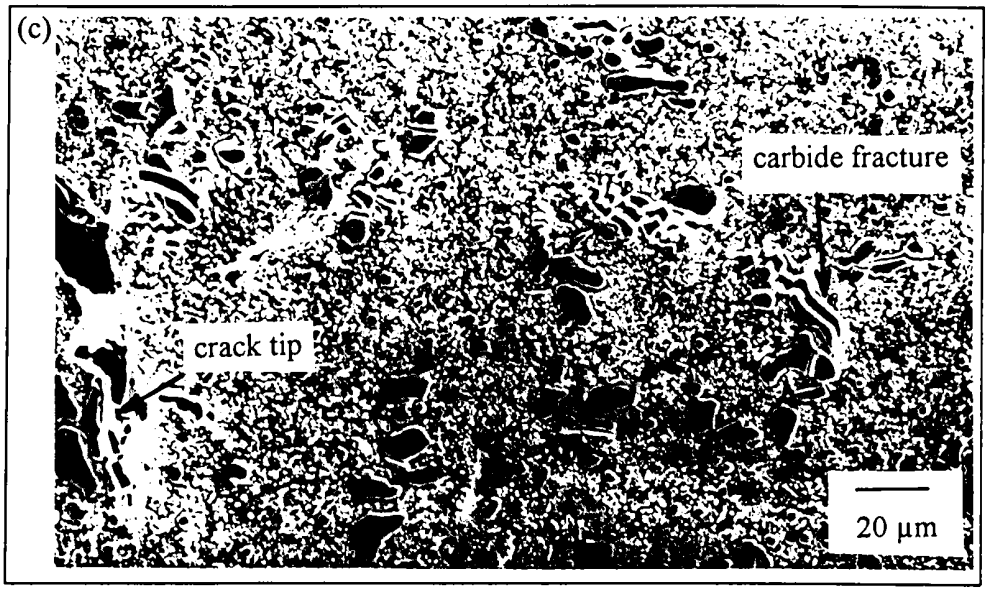
(c)
carbide fracture
crack tip
20 µm


(d)
crack tip
microcrack growth
20 µm

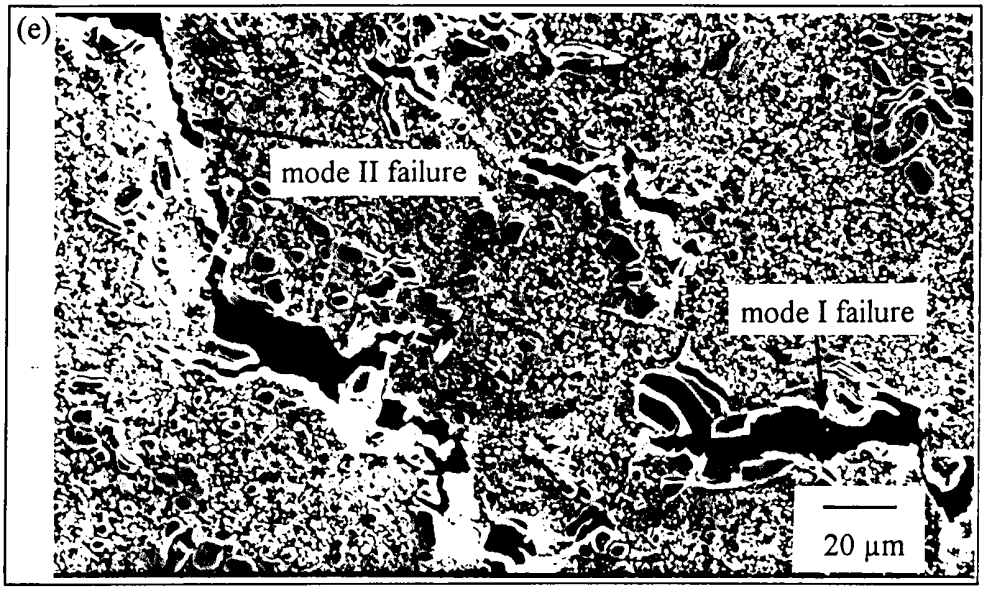

Fig. II.3.6. Crack propagation in the in-situ TPB specimen ("Ann", T-S orient.) in three stages
(a,b) Crack tip opening-Blunting F=217 N→F=350 N
(c,d) Microcracking in the regime of the main crack F=332 N(=F_{max})→F=245 N
(e) Failure of the ligaments F=219 N [BRO 94]

II.3.2.2-CRACK PATH

Beside the ductility of the matrix (different states of heat treatment), the arrangement of the microstructure (dispersion, netlike structure, banded structure) strongly influences crack propagation. This is particularly controlled by the distance and orientation of non-homogeneous inclusion colonies to the main crack.

Netlike microstructure

Lüsebrink [LÜS 95] investigated the fracture behaviour of SAE-D3 in the as-cast condition. TPB-specimen have been studied in different states of heat treatment. It was observed that the crack path follows the eutectic net. This implies that the crack could not always propagate straightforward because of the hexagonal geometrical form of the eutectic net (Fig. II.2.1). The crack was deflected since carbides were fractured within the eutectic net ahead of the crack tip. Progressive failure of neighbouring carbides leads to crossing of microplastic zones and to ductile failure of the remaining matrix ligaments.

However, in the annealed state the crack tends to propagate straightforward even when it had to propagate into the more ductile matrix. In this case brittle failure of the matrix cell was found. This was assumed to be a result of the big plastic zone approximately twice of the netsize. Plasticity amplifies the deformation constraint of the MM, leads to higher stress concentrations within the carbide and causes particle cracking over the whole eutectic net. Carbide cracking on the opposite side give rise to increasing stress levels in the matrix and favours brittle failure under mode I. An enlarged plastic- and fracture process zone was experimentally observed [LÜS 95].

The crack path along the eutectic carbides in the hardened state is shown in Fig. II.3.7a, that through the matrix by brittle failure in the annealed state is given in Fig. II.3.7b.

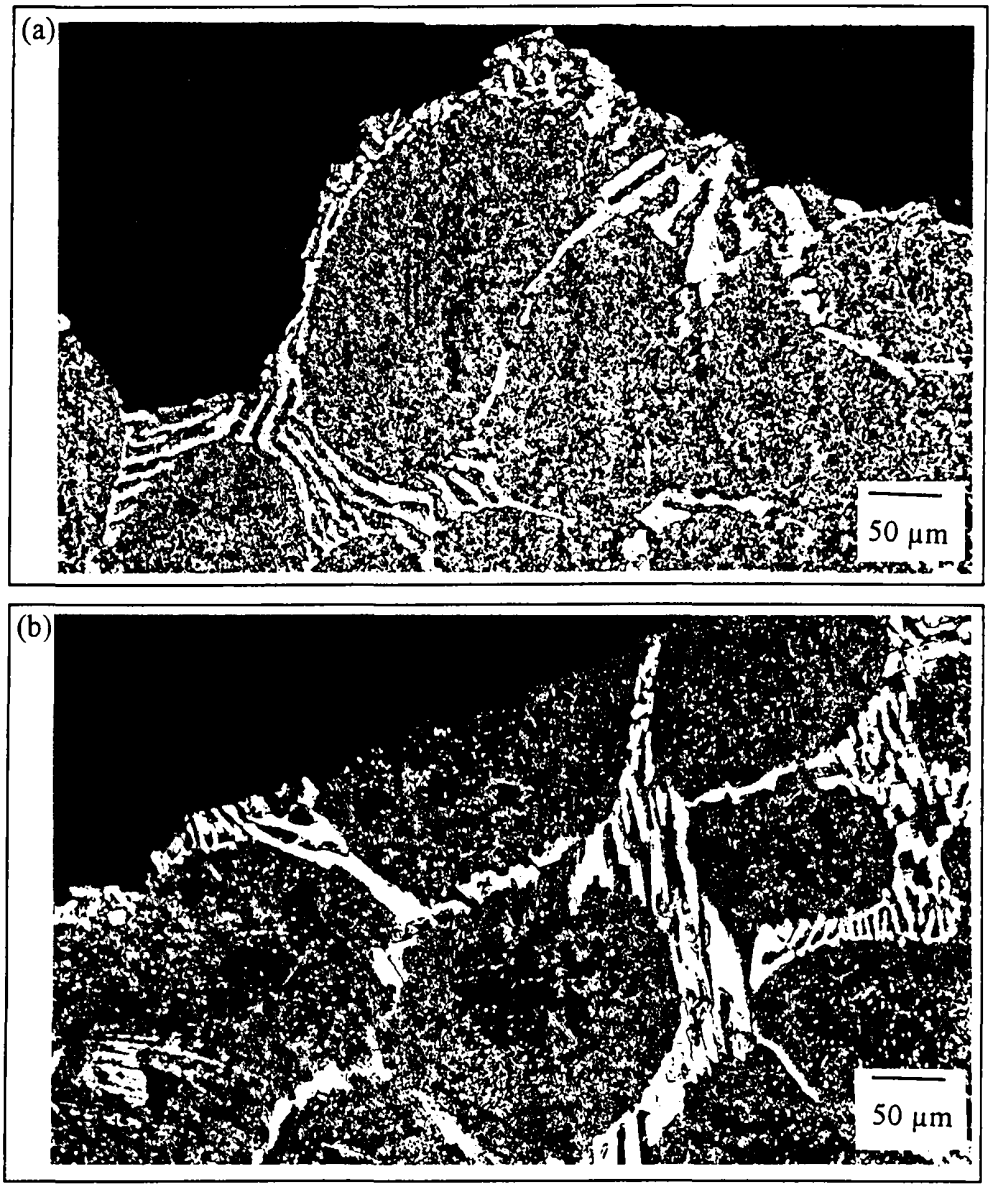

Fig. II.3.7 Crack pathes in SAE-D3 in the as-cast condition [LÜS 95]:
(a) through the eutectic net ("380") (b) through the matrix ("Ann")

Banded microstructure

After hot forging the fracture behaviour is mainly controlled by the orientation of the carbide bands to the crack tip. The fatigue crack in specimens in the T-L orientation was deflected to enter into the carbide bands. Then it followed straightforward the energetic favourable way of the carbide bands (Fig. II.3.8)

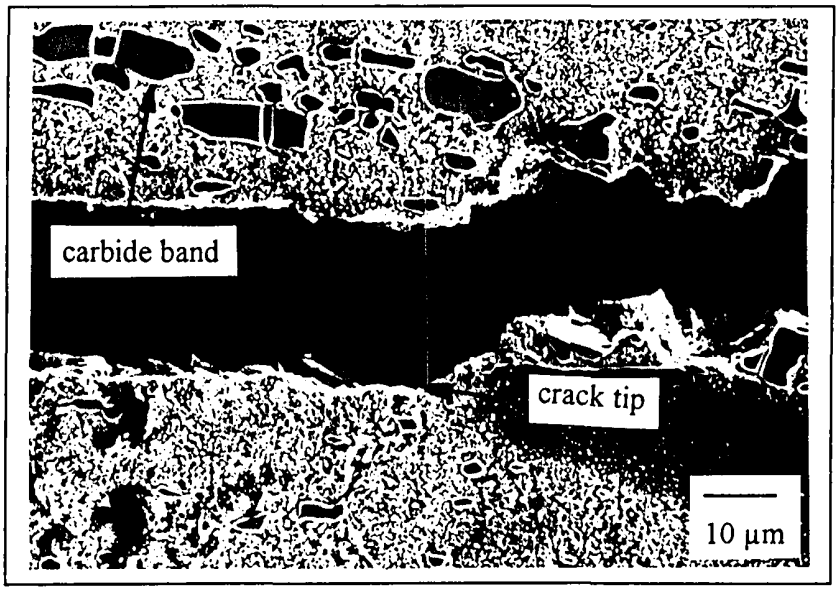

Fig. II.3.8. Crack path in SAE-D3 after hot forging (T-L specimen) [BRO 94]

In addition, with increasing ductility (increasing tempering temperature) the role of the plastic- and the fracture process zone for the behaviour of the propagating crack becomes more dominant. This becomes visible when studying the fracture surface throughout the specimen thickness. At the surface (state of plane stress) the plastic zone is spread out straightforward whereas in the bulk (state of plane strain) it is under 70 degree. Therefore the effects of crack deflection becomes more pronounced in the inner of the specimen. This was confirmed by the smooth and crumbled fracture surface at the surface and in the bulk, respectively.

CHAPTER III

CONTINUUM MECHANICAL FRAMEWORK OF ELASTIC FINITE PLASTICITY

III.1-Kinematics
III.1.1-Deformation
III.1.2-Strain measures
III.1.3-Rate of deformation

III.2-Stress measures

III.3-Equilibrium and virtual work

III.4-Constitutive model for elasto-plastic materials at finite strain
III.4.1-Decomposition of the deformation
III.4.2-Application to metal plasticity (Hypothesis of small elastic strains)
III.4.3-Objectivity of the constitutive model

III.1-Kinematics

III.1.1-Deformation

In structural problems one generally considers an initial configuration Ω_0 of the structure at time t_0 and is interested in its deformation throughout the history of loading. The material particle P, described in the initial configuration by its coordinates **X** will move to a new position **x** due to the deformation of the structure (Fig. III.1.1).

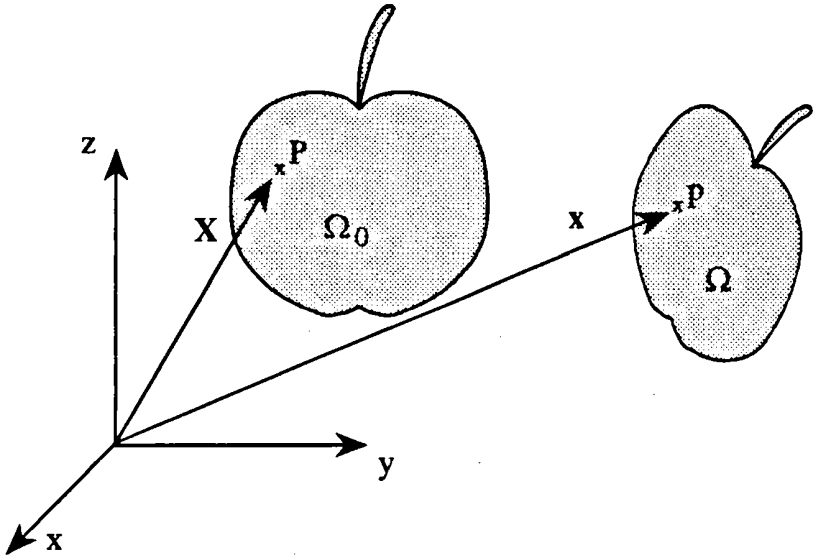

Fig. III.1.1. Initial and deformed configuration

Following the axiom of continuity, adjacent particles are always found at adjacent points and a one-to one correspondence between **x** and **X** is given. The location of a particle is described at any time t by

$$\mathbf{x} = \mathbf{x}(\mathbf{X}, t) \tag{III.1.1a}$$

or by its inversion

$$\mathbf{X} = \mathbf{X}(\mathbf{x}, t) \tag{III.1.1b}$$

Introducing the deformation gradient tensor **F**

$$\mathbf{F} = \frac{\partial \mathbf{x}}{\partial \mathbf{X}} \tag{III.1.2a}$$

the mapping between the initial and current configuration is given by

$$d\mathbf{x} = \mathbf{F} \cdot d\mathbf{X} \tag{III.1.2b}$$

Kinematic and static measures defined in the initial configuration are called Lagrangian, those defined in the current configuration Eulerian. The deformation gradient is used to transform any tensor from one configuration into the other. It contains both parts of the motion: straining and rigid body rotation. In order to distinguish them, we consider an infinitesimal line segment $d\mathbf{X}$ emanating from the particle initially at **X** . Its initial and current lengths are

$$dL^2 = d\mathbf{X}^T \cdot d\mathbf{X}, \qquad dl^2 = d\mathbf{x}^T \cdot d\mathbf{x} \tag{III.1.3}$$

A "stretch ratio" of this segment length is defined by

$$\lambda = \frac{dl}{dL} = \sqrt{\frac{d\mathbf{x}^T \cdot d\mathbf{x}}{d\mathbf{X}^T \cdot d\mathbf{X}}} \tag{III.1.4}$$

Now, using eqn. (III.1.2b), leads to

$$d\mathbf{x}^T \cdot d\mathbf{x} = d\mathbf{X}^T \cdot \mathbf{F}^T \cdot \mathbf{F} \cdot d\mathbf{X} \tag{III.1.5}$$

so that, from eqn. (III.1.4)

$$\begin{aligned} \lambda^2 &= \frac{d\mathbf{X}^T}{\sqrt{d\mathbf{X}^T \cdot d\mathbf{X}}} \cdot \mathbf{F}^T \cdot \mathbf{F} \cdot d\mathbf{X} \cdot \frac{d\mathbf{X}}{\sqrt{d\mathbf{X}^T \cdot d\mathbf{X}}} \\ &= \mathbf{N}^T \cdot \mathbf{F}^T \cdot \mathbf{F} \cdot \mathbf{N} \end{aligned} \tag{III.1.6}$$

where $\mathbf{N}$ is the unit vector in the direction of the segment length $d\mathbf{X}$ [HIB 90]. If one finds the "principal stretches" λ_I, λ_{II}, λ_{III} and their corresponding directions $\mathbf{N}_I$, $\mathbf{N}_{II}$, $\mathbf{N}_{III}$ and $\mathbf{n}_I$, $\mathbf{n}_{II}$, $\mathbf{n}_{III}$ in the reference and current configuration, respectively, it is possible to isolate the rigid body rotation tensor $\mathbf{R}$ and the pure stretch. This is an eigenvalue problem and $\mathbf{R}$ is obtained from [HIB 90]

$$\begin{aligned} \mathbf{n}_I &= \mathbf{R} \cdot \mathbf{N}_I \\ \mathbf{n}_{II} &= \mathbf{R} \cdot \mathbf{N}_{II} \\ \mathbf{n}_{III} &= \mathbf{R} \cdot \mathbf{N}_{III} \end{aligned} \tag{III.1.7}$$

Consequently, the deformation gradient $\mathbf{F}$ may be decomposed by

$$\mathbf{F} = \mathbf{V} \cdot \mathbf{R} \tag{III.1.8}$$

with

$$\mathbf{V} = (\lambda_I \mathbf{n}_I \cdot \mathbf{n}_I^T + \lambda_{II} \mathbf{n}_{II} \cdot \mathbf{n}_{II}^T + \lambda_{III} \mathbf{n}_{III} \cdot \mathbf{n}_{III}^T) \tag{III.1.9}$$

$\mathbf{V}$ is a symmetrical, positive-definite Eulerian objective left stretch tensor. Analogously the Lagrangian objective right stretch tensor $\mathbf{U}$, also symmetric and positive-definite, is defined by the relation

$$\mathbf{F} = \mathbf{R} \cdot \mathbf{U} \tag{III.1.10}$$

$\mathbf{R}$ is an orthogonal non-objective tensor representing the rigid body rotation with reference to the principal axes of $\mathbf{U}$ or $\mathbf{V}$. The identities (III.1.8) and (III.1.10) represent the *polar decompo-sition theorem*: Any motion can be considered as a pure rigid body rotation of the principal axes of stretch, $\mathbf{R}$, followed by a stretch along those axes, $\mathbf{V}$, or, alternatively, a stretch along the principal axes, $\mathbf{U}$, followed by a rigid body rotation of those axes, $\mathbf{R}$ (Fig. III.1.2).

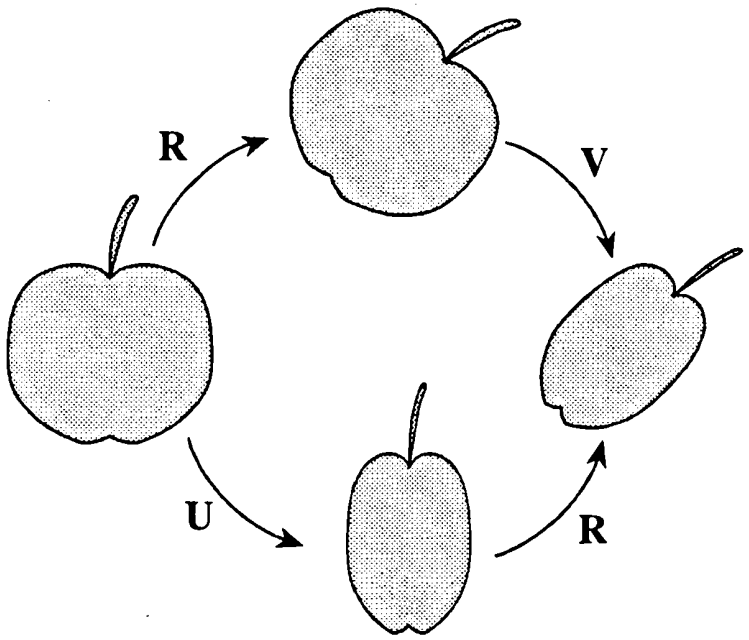

Fig. III.1.2. Illustration of the polar decomposition theorem

Remark
The motion of one body might be described by the subsequent mapping of configurations. The respective decomposition of the deformation can be derived by applying the chain rule. For example if the motion passes subsequently the time steps t_0, t_1 and t_2, the total deformation gradient can be decomposed by

$$\mathbf{F} = \frac{\partial \mathbf{x}_2}{\partial \mathbf{x}_0} = \frac{\partial \mathbf{x}_2}{\partial \mathbf{x}_1}\frac{\partial \mathbf{x}_1}{\partial \mathbf{x}_0} = \mathbf{F}_2\,\mathbf{F}_1 \tag{III.3.11}$$

This illustrates the order within the formulation of tensor decomposition.

III.1.2-Strain measures

In a simple way, a first strain measure can directly be defined by the change of the infinitesimal segment length $d\mathbf{X}$

$$\begin{aligned} dl^2 - dL^2 &= d\mathbf{x}^T \cdot d\mathbf{x} - d\mathbf{X}^T \cdot d\mathbf{X} \\ &= \left(\frac{d\mathbf{x}^T \cdot d\mathbf{x}}{d\mathbf{X}^T \cdot d\mathbf{X}} - \mathbf{I} \right) d\mathbf{X}^T \cdot d\mathbf{X} \\ &= (\mathbf{C} - \mathbf{I}) d\mathbf{X}^T \cdot d\mathbf{X} \end{aligned} \tag{III.1.12}$$

where $\mathbf{C}$, called right Cauchy-Green Tensor, is defined by (compare with eqn. (III.1.2b))

$$\mathbf{C} = \mathbf{F}^T\mathbf{F} \tag{III.1.13}$$

Introducing $\mathbf{E}$ by

$$\mathbf{E} = \frac{1}{2}(\mathbf{C} - \mathbf{I}) \tag{III.1.14}$$

relation (III.1.12) becomes

$$dl^2 - dL^2 = 2d\mathbf{X}^T\,\mathbf{E}\,d\mathbf{X} \tag{III.1.15}$$

E is called Green-Lagrange strain tensor. The components of **C** and **E** are referred to the initial configuration, so that both are tensors of Lagrange-type. Analogously, we derive the Eulerian tensor from

$$\begin{aligned} dl^2 - dL^2 &= \left(\mathbf{I} - \frac{d\mathbf{X}^T d\mathbf{X}}{d\mathbf{x}^T d\mathbf{x}}\right) d\mathbf{x}^T d\mathbf{x} \\ &= \left(\mathbf{I} - \mathbf{B}^{-1}\right) d\mathbf{X}^T d\mathbf{X} \end{aligned} \tag{III.1.16}$$

where **B** is called left Cauchy-Green tensor given by

$$\mathbf{B} = \mathbf{F}\mathbf{F}^T \tag{III.1.17}$$

The Eulerian tensor corresponding to **E**, is obtained by

$$\mathbf{A} = \frac{1}{2}\left(\mathbf{I} - \mathbf{B}^{-1}\right) \tag{III.1.18}$$

and confirms

$$dl^2 - dL^2 = 2d\mathbf{X}^T\,\mathbf{A}\,d\mathbf{X} \tag{III.1.19}$$

It should be noticed that **E** can also be written in terms of the displacement gradients

$$\mathbf{E} = \frac{1}{2}\left(\frac{\partial \mathbf{u}}{\partial \mathbf{X}} + \left[\frac{\partial \mathbf{u}}{\partial \mathbf{X}}\right]^T + \left[\frac{\partial \mathbf{u}}{\partial \mathbf{X}}\right]^T \left[\frac{\partial \mathbf{u}}{\partial \mathbf{X}}\right]\right) \tag{III.1.20}$$

Neglecting the non-linear terms, **E** is identical to the familiar "small strain" measure $\boldsymbol{\varepsilon}$

$$\boldsymbol{\varepsilon} = \frac{1}{2}\left(\frac{\partial \mathbf{u}}{\partial \mathbf{X}} + \left[\frac{\partial \mathbf{u}}{\partial \mathbf{X}}\right]^T\right) \tag{III.1.21}$$

which is only useful for small displacement gradients, that is, both the strains and the rotations must be small for this strain measure to be appropriate.

III.1.3-Rate of deformation

A definition of the strainrate is required since the used elasto-plastic material model is path-dependent and therefore defined in rate form. The velocity of a material particle is

$$\mathbf{v}(\mathbf{x},t) = \frac{\partial \mathbf{x}}{\partial t} \tag{III.1.22}$$

Here, the Lagrangian viewpoint is adopted: We follow the motion of the material particle, rather than looking at a fixed point in space and watching the material flowing through this point. The velocity difference between two adjacent particles in the current configuration is

$$d\mathbf{v} = \frac{\partial \mathbf{v}}{\partial \mathbf{x}} d\mathbf{x} = \mathbf{L} d\mathbf{x} \tag{III.1.23a}$$

where

$$\mathbf{L} = \frac{\partial \mathbf{v}}{\partial \mathbf{x}} \tag{III.1.23b}$$

is the velocity gradient in the current configuration. With the definition of the deformation gradient, **F**, we obtain

$$d\mathbf{v} = \mathbf{L}\, d\mathbf{x} = \mathbf{L}\,\mathbf{F}\, d\mathbf{X} \tag{III.1.24}$$

We could also derive the velocity difference directly by

$$d\mathbf{v} = \frac{\partial}{\partial \mathbf{x}}(\mathbf{F}\, d\mathbf{X}) = \dot{\mathbf{F}}\, d\mathbf{X} \tag{III.1.25}$$

Comparing the two identities for dv we notice that

$$\mathbf{L}\,\mathbf{F} = \dot{\mathbf{F}} \tag{III.1.26a}$$

or

$$\mathbf{L} = \dot{\mathbf{F}}\,\mathbf{F}^{-1} \tag{III.1.26b}$$

We want to isolate, in a similar way to the polar decomposition theorem, the rate-of-deformation from the rate-of-rotation. The conventional Euler-Cauchy-Stokes decomposition (see e.g. [TRU 77]) defines the symmetric part of **L** as the rate-of-deformation, whereas the antisymmetric part is called spin tensor. Therefore it is

$$\mathbf{L} = \mathbf{D} + \mathbf{W} \tag{III.1.27a}$$

and

$$\mathbf{D} = \frac{1}{2}(\mathbf{L} + \mathbf{L}^T), \qquad \mathbf{W} = \frac{1}{2}(\mathbf{L} - \mathbf{L}^T) \tag{III.1.27b}$$

In order to check the uniqueness of this decomposition, we apply the polar decomposition theorem on eqn. (III.1.26b)

$$\begin{aligned} \mathbf{L} = \dot{\mathbf{F}}\,\mathbf{F}^{-1} &= \dot{\mathbf{R}}\mathbf{U}\mathbf{U}^{-1}\mathbf{R}^{-1} + \mathbf{R}\dot{\mathbf{U}}\mathbf{U}^{-1}\mathbf{R}^{-1} \\ &= \dot{\mathbf{R}}\mathbf{R}^T + \mathbf{R}\dot{\mathbf{U}}\mathbf{U}^{-1}\mathbf{R}^T \end{aligned} \tag{III.1.28}$$

and using eqn. (III.1.27b)

$$\mathbf{D} = \frac{1}{2}\mathbf{R}\left(\dot{\mathbf{U}}\mathbf{U}^{-1} + \mathbf{U}^{-1}\dot{\mathbf{U}}\right)\mathbf{R}^T \tag{III.1.29a}$$

$$\mathbf{W} = \dot{\mathbf{R}}\mathbf{R}^T + \frac{1}{2}\mathbf{R}\left(\dot{\mathbf{U}}\mathbf{U}^{-1} - \mathbf{U}^{-1}\dot{\mathbf{U}}\right)\mathbf{R}^T \qquad \text{(III.1.29b)}$$

From Eqn. (III.1.29b), we see that the spin tensor does not only depend on the Lagrangian material rotation rate $\dot{\mathbf{R}}\mathbf{R}^T$, but has also a contribution from the straining by **U**.
Since **W** is not totally isolated from **U**, the spin tensor is not a proper tensor in describing the rotation of the deformation process. So, the spin tensor can not be used without care in the general large rotation problem. However, it can be shown that the Euler-Cauchy-Stokes decomposition is correct in an infinitesimal sense, if the external load is applied in small steps and if the reference configuration will be updated at each load step [CHE 92].

III.2-Stress measures

Let V denote a volume occupied by a part of the body in the current configuration, and let S be the surface bounding this volume. Let the surface traction at any point on S be the force **f** per unit of current area and **n** the unit outward normal to S at a point of S (Fig. III.2.1).

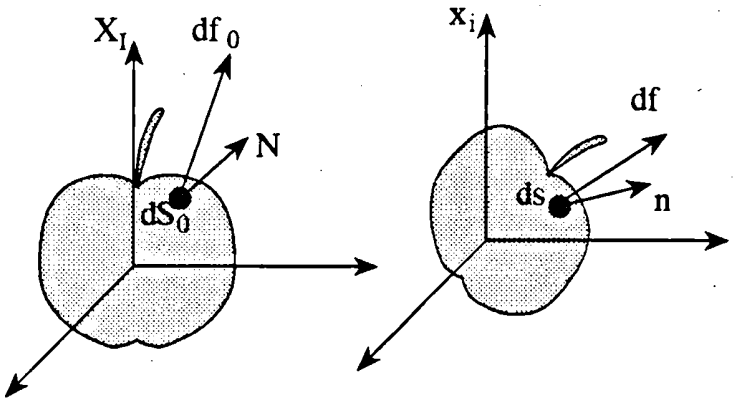

Fig. III.2.1. To the definition of stress measures

The "true" or Cauchy stress tensor $\boldsymbol{\sigma}$ at this point is then defined by

$$\mathbf{df} = \boldsymbol{\sigma}\mathbf{n}\, ds \qquad \text{(III.2.1)}$$

$\boldsymbol{\sigma}$ is a symmetric and Eulerian tensor. If we relate the load state to the initial configuration Ω_0, we obtain

$$\mathbf{df} = \boldsymbol{\Pi}\, \mathbf{N} dS_0 \qquad \text{(III.2.2)}$$

$\boldsymbol{\Pi}$ is the first Piola-Kirchhoff stress tensor, which is neither Lagrangian nor Eulerian nor symmetric. To overcome this inconvenience we also transform the element load **df** by

$$\mathbf{df} = \mathbf{F}^{-1}\mathbf{df}_0 \qquad \text{(III.2.3)}$$

so that

$$\mathbf{dF}_0 = \mathbf{S}\, \mathbf{N} dS_0 \qquad \text{(III.2.4)}$$

S is the second Piola-Kirchhoff stress tensor, symmetric and totally Lagrange. The three stress tensors are related by the relation

$$\det \mathbf{F}\,\boldsymbol{\sigma} = \boldsymbol{\tau} = \boldsymbol{\Pi}\,\mathbf{F}^T = \mathbf{F}\,\mathbf{S}\,\mathbf{F}^T \tag{III.2.5}$$

where $\boldsymbol{\tau}$ is the well known Kirchhoff stress tensor. In general, any stress measure can be used to formulate the equilibrium conditions. If the virtual work principle is employed however, a proper coupling between stresses and conjugate strain measures is necessary to respect the concept of work conjugacy. According to Hill's definition [HIL 68], the work rate per unit volume in the elastic reference state must be constant for any arbitrary stress and strain measures

$$dW^\circ = \boldsymbol{\tau}^\circ\, d\boldsymbol{\varepsilon}^\circ = \text{konst.} \tag{III.2.6}$$

where $\boldsymbol{\varepsilon}^\circ$ represents a certain strain measure and $\boldsymbol{\tau}^\circ$ the stress measure work conjugate to $d\boldsymbol{\varepsilon}^\circ$. Work conjugate couple of stresses and strain rates are given by

$$dW^\circ = \frac{1}{\rho_0}\boldsymbol{\Pi}\,\dot{\mathbf{F}} = \frac{1}{\rho_0}\mathbf{S}\,\dot{\mathbf{E}} = \frac{1}{\rho_0}\boldsymbol{\tau}\,\mathbf{D} = \frac{1}{\rho}\boldsymbol{\sigma}\,\mathbf{D} \tag{III.2.7}$$

III.3-Equilibrium and virtual work

Let the body force at any point within the volume of material under consideration be **b** per unit of current volume and **f**, S and V those quantities introduced in III.2. Force equilibrium holds, if

$$\int_S \mathbf{f}\,dS + \int_V \mathbf{b}\,dV = 0 \tag{III.3.1}$$

Using the definition of the Cauchy stress tensor (III.2.1), eqn. (III.3.1) becomes

$$\int_S \mathbf{n}\cdot\boldsymbol{\sigma}\,dS + \int_V \mathbf{b}\,dV = 0 \tag{III.3.2}$$

Applying the Gauss theorem to the surface integral in the equilibrium equation gives

$$\int_S \mathbf{n}\cdot\boldsymbol{\sigma}\,dS = \int_V \left(\frac{\partial}{\partial \mathbf{x}}\right)\cdot\boldsymbol{\sigma}\,dV \tag{III.3.3}$$

Since this equation must be valid for any arbitrary volume, it must apply pointwise in the body, thus providing the differential equation of translational equilibrium

$$\left(\frac{\partial}{\partial \mathbf{x}}\right)\cdot\boldsymbol{\sigma} + \mathbf{b} = \mathbf{0} \tag{III.3.4}$$

Momentum equilibrium is automatically satisfied due to the symmetrical property of the Cauchy stress tensor. For the development of a displacement-interpolation finite element model the three equilibrium eqns. (III.3.4) are replaced by an equivalent "weak form" by a single scalar equation over the entire body; in the case of equilibrium with a general stress tensor; this equivalent "weak form" is the virtual work principle

$$\int_V \left[\left(\frac{\partial}{\partial \mathbf{x}} \right) \cdot \boldsymbol{\sigma} + \mathbf{b} \right] \delta \mathbf{v} \, dV = 0 \tag{III.3.5}$$

$\delta \mathbf{v}$ is a "virtual" velocity field, which is completely arbitrary except that it must satisfy the kinematic constraints and must have sufficient continuity. Using the chain rule and Gauss theorem, the following relation is valid

$$\int_V \left[\left(\frac{\partial}{\partial \mathbf{x}} \right) \cdot \boldsymbol{\sigma} \right] \cdot \delta \mathbf{v} \, dV = \int_S \mathbf{n} \cdot \boldsymbol{\sigma} \cdot \delta \mathbf{v} \cdot dS - \int_V \boldsymbol{\sigma} \cdot \left(\frac{\partial \delta \mathbf{v}}{\partial \mathbf{x}} \right) \cdot dV \tag{III.3.6}$$

and with the definition of Cauchy stress (III.2.1), the virtual work principle can be rewritten as

$$\int_V \boldsymbol{\sigma} \left(\frac{\partial \delta \mathbf{v}}{\partial \mathbf{x}} \right) dV = \int_S \mathbf{f} \, \delta \mathbf{v} \, dS + \int_V \mathbf{b} \, \delta \mathbf{v} \, dV \tag{III.3.7}$$

The virtual velocity gradient in the current configuration is given by

$$\delta \mathbf{L} = \frac{\partial \delta \mathbf{v}}{\partial \mathbf{x}} \tag{III.3.8}$$

which can be decomposed in familiar manner

$$\delta \mathbf{L} = \delta \mathbf{D} + \delta \mathbf{W} \tag{III.3.9}$$

This allows to write

$$\boldsymbol{\sigma} \delta \mathbf{L} = \boldsymbol{\sigma} \delta \mathbf{D} + \boldsymbol{\sigma} \delta \mathbf{W} \tag{III.3.10}$$

and since $\boldsymbol{\sigma}$ is symmetric it follows

$$\boldsymbol{\sigma} \left(\frac{\partial \delta \mathbf{v}}{\partial \mathbf{x}} \right) = \boldsymbol{\sigma} \delta \mathbf{L} = \boldsymbol{\sigma} \delta \mathbf{D} \tag{III.3.11}$$

Finally, we obtain the equation of the virtual work principle in its classical form

$$\int_V \boldsymbol{\sigma} \delta \mathbf{D} \, dV = \int_S \mathbf{f} \, \delta \mathbf{v} \, dS + \int_V \mathbf{b} \, \delta \mathbf{v} \, dV \tag{III.3.12}$$

III.4-Constitutive model for elasto-plastic materials at finite strain

III.4.1-Decomposition of the deformation

Over the last two decades one can follow much controversial discussions about the mathematical representation of the physical entities involved in finite elastoplasticity. In particular the question, how to decouple elastic and plastic deformations was a crucial one. In small strain theory, the additive split of the total strain rate in their elastic and plastic parts is generally accepted

$$\dot{\boldsymbol{\varepsilon}} = \dot{\boldsymbol{\varepsilon}}^e + \dot{\boldsymbol{\varepsilon}}^p \tag{III.4.1}$$

However, great difficulties arise in finding an equivalent formulation to (III.4.1) in finite elastoplasticity. First, Green and Naghdi [GRE 65] proposed such a decomposition for the Green-Lagrange strain tensor

$$\mathbf{E} = \mathbf{E}^{e'} + \mathbf{E}^p \tag{III.4.2}$$

but it suffered from the lack of physical significance ($\mathbf{E}^{e'}$ not being purely elastic). A few years later the idea of a local, current, relaxed, intermediate configuration was introduced:
A body undergoing nonhomogeneous plastic flow is considered to be cut into infinitesimal elements, so that due to relaxation, locally a stress free state exists. The body is in an elastic regime in view of that mobile configuration and in a pure plastic state in view of the reference configuration [FOX 68, MAN 72, LEE 67, LEE 69] (Fig. III.4.1).

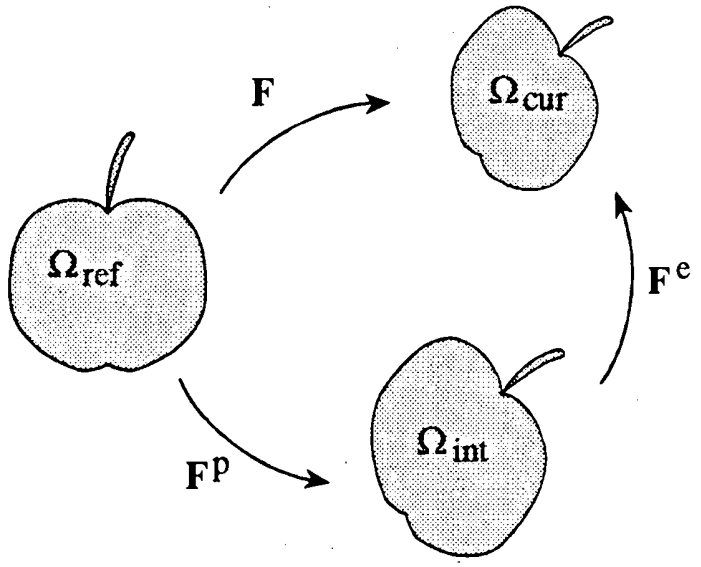

Fig. III.4.1. Schematic sketch of reference Ω_{ref}, intermediate Ω_{int} and current Ω_{cur} configurations and the associated multiplicative decomposition of the deformation gradient

This leads to the multiplicative decomposition of the deformation gradient into elastic and plastic constituents:

$$\mathbf{F} = \mathbf{F}^e \mathbf{F}^p \tag{III.4.3}$$

The concept of the relaxed intermediate configuration and the associated multiplicative decomposition of the deformation gradient had been the basic departure point for the theory of finite elastoplasticity in the past and had been successfully applied by many authors. However, this decomposition can only be viewed as a kinematic concept and one must derive from this decomposition suitable physical measures to formulate elastic and plastic constitutive equations.
It was shown by Stumpf [STU 93] that an additive decomposition into purely elastic and purely plastic parts referred to all three configurations is in the general case not possible. Up to now the analysts do not agree about a constitutive model without loss of generality in finite

elastoplasticity. Most often the derivation of a model from (III.4.3) is achieved by restrictions which are reasonable in particular cases.

In the following kinematic and constitutive relations will be restricted to the assumption that the elastic strains are small which generally holds for elasto-plastic behaviour of metals.

III.4.2-Application to metal plasticity (Hypothesis of small elastic strains)

The definition of the velocity gradient by eqn. (III.1.26b) becomes with (III.4.3)

$$\mathbf{L} = \dot{\mathbf{F}}^e \mathbf{F}^{e-1} + \mathbf{F}^e \dot{\mathbf{F}}^p \mathbf{F}^{p-1} \mathbf{F}^{e-1} \tag{III.4.4}$$

We define the elastic and plastic constituents by

$$\mathbf{L}^e = \dot{\mathbf{F}}^e \mathbf{F}^{e-1} \quad \text{and} \quad \mathbf{L}^p = \dot{\mathbf{F}}^p \mathbf{F}^{p-1} \tag{III.4.5}$$

In the case of small elastic deformation, the intermediate configuration coincides with the current configuration and we postulate therefore

$$\mathbf{F}^e \approx \mathbf{I} \tag{III.4.6}$$

Relation (III.4.4) of $\mathbf{L}$ is then approximated by

$$\mathbf{L} = \mathbf{L}^e + \mathbf{L}^p \tag{III.4.7}$$

and the rate of deformation, symmetric part of $\mathbf{L}$, can be additively decomposed into an elastic and a plastic part

$$\mathbf{D} = \mathbf{D}^e + \mathbf{D}^p \tag{III.4.8}$$

The elastic rate of deformation is related to an objective stress rate by Hooke's law:

$$\dot{\sigma}^{obj} = \mathbf{C}^e : (\mathbf{D} - \mathbf{D}^p) \tag{III.4.9}$$

where σ is the Cauchy stress tensor and $\mathbf{C}^e$ the constitutive matrix. In the isotropic case we have

$$\mathbf{C}^e = 2G\mathbf{J} + (K - \frac{2}{3}G)\mathbf{I}:\mathbf{I} \tag{III.4.10}$$

where G and K are the shear and bulk modulus and $\mathbf{J}$ and $\mathbf{I}$ the unit tensors of fourth and second order, respectively.

During plastic flow the yield condition is fulfilled by

$$\begin{aligned} F(\sigma,\kappa) &= 0 \\ \dot{F}(\sigma,\kappa) &= 0 \end{aligned} \tag{III.4.11}$$

where F is the yield criterion and κ the hardening parameter depending on the history of plastic deformation. For metal plasticity the associated normality rule gives the direction of plastic flow

$$\mathbf{D}^p = \dot{\lambda}\frac{\partial F}{\partial \sigma}, \quad -\dot{\varepsilon}_v^p = \dot{\lambda}\frac{\partial F}{\partial \kappa} \tag{III.4.12}$$

where $\dot{\varepsilon}_v^p$ is the equivalent plastic strain. $\dot{\lambda}$ is the plastic multiplier

$$\begin{cases} \dot{\lambda} = 0 & \text{if} \quad F < 0 \quad \text{or if} \quad F = 0 \text{ and } \dot{F} < 0 \\ \dot{\lambda} \geq 0 & \text{if} \quad F = \dot{F} = 0 \end{cases}$$

which can be determined using the precedent relations

$$\dot{\lambda} = \frac{\frac{\partial F}{\partial \sigma}\mathbf{C}^e\,\mathbf{D}}{\frac{\partial F}{\partial \sigma}\mathbf{C}^e\frac{\partial F}{\partial \sigma} + \frac{\partial F}{\partial \kappa}\frac{\partial \kappa}{\partial \varepsilon_v^p}\frac{\partial F}{\partial \kappa}} \tag{III.4.13}$$

Using eqns. (III.4.9, III.4.11 and III.4.12), we construct the stress-strain relation in elasto-plasticity

$$\dot{\sigma}^{obj} = \mathbf{C}^{ep}(\sigma, \varepsilon_v^p)\mathbf{D}\,, \quad \dot{\varepsilon}_v^p = \mathbf{P}(\sigma, \varepsilon_v^p)\mathbf{D} \tag{III.4.14}$$

with

$$\mathbf{C}^{ep} = \mathbf{C}^e - \mathbf{C}^p \tag{III.4.14a}$$

$$\mathbf{C}^p = \frac{\mathbf{C}^e\frac{\partial F}{\partial \sigma}\frac{\partial F}{\partial \sigma}\mathbf{C}^e}{\frac{\partial F}{\partial \sigma}\mathbf{C}^e\frac{\partial F}{\partial \sigma} + \frac{\partial F}{\partial \kappa}\frac{\partial \kappa}{\partial \varepsilon_v^p}\frac{\partial F}{\partial \kappa}} \tag{III.4.14b}$$

$$\mathbf{P} = -\frac{\frac{\partial F}{\partial \kappa}\frac{\partial F}{\partial \sigma}\mathbf{C}^e}{\frac{\partial F}{\partial \sigma}\mathbf{C}^e\frac{\partial F}{\partial \sigma} + \frac{\partial F}{\partial \kappa}\frac{\partial \kappa}{\partial \varepsilon_v^p}\frac{\partial F}{\partial \kappa}} \tag{III.4.14c}$$

III.4.3-Objectivity of the constitutive model

A crucial step in the formulation of the constitutive equation consists in respecting the principle of material frame indifference: It postulates that the stress state must not change under rigid body rotation in order to reasonably describe the material response. Tensors obeying this principle are called objective. While Eulerian rate tensors are non-objective, all Lagrangian rate tensors are objective by definition. Since the virtual work principle will be expressed in terms of the Eulerian Cauchy stresses, a proper material derivative for this tensor has to be chosen.

Objective derivatives

In general, two different types of objective derivatives are distinguished: the *convective derivatives* and the *rotational derivatives* [BAG 93].

1-Convective derivative

The convective transport of the stress tensor in the reference configuration leads to this class of derivatives. These derivatives consist of a pull-back of the Cauchy stress tensor to the reference configuration (second Piola-Kirchhoff) followed by a material time derivative of the ensuring material tensor and then a push forward of this result to the current configuration. Among others the following derivatives are mostly used:

a) The convective contravariant (Lie-) derivative:

$$\dot{\boldsymbol{\sigma}}^{c} = \frac{d}{dt}\left({}^{c}\boldsymbol{\sigma}\right) = \mathbf{F}\left\{\frac{d}{dt}\left(\mathbf{F}^{-1}\boldsymbol{\sigma}\mathbf{F}^{-T}\right)\right\}\mathbf{F}^{T} \tag{III.4.15a}$$

$$\dot{\boldsymbol{\sigma}}^{c} = \dot{\boldsymbol{\sigma}} - \mathbf{L}\boldsymbol{\sigma} - \boldsymbol{\sigma}\mathbf{L}^{T} \tag{III.4.15b}$$

b) The convective covariant derivative:

$${}^{c}\dot{\boldsymbol{\sigma}} = \frac{d}{dt}\left({}_{c}\boldsymbol{\sigma}\right) = \mathbf{F}^{-T}\left\{\frac{d}{dt}\left(\mathbf{F}^{T}\boldsymbol{\sigma}\mathbf{F}\right)\right\}\mathbf{F}^{-1} \tag{III.4.16a}$$

$${}^{c}\dot{\boldsymbol{\sigma}} = \dot{\boldsymbol{\sigma}} + \mathbf{L}^{T}\boldsymbol{\sigma} + \boldsymbol{\sigma}\mathbf{L} \tag{III.4.16b}$$

c) The derivative of Truesdell:

$$\dot{\boldsymbol{\sigma}}^{Tr} = \frac{d}{dt}\left({}^{Tr}\boldsymbol{\sigma}\right) = J^{-1}\mathbf{F}\left\{\frac{d}{dt}\left(J\mathbf{F}^{-1}\boldsymbol{\sigma}\mathbf{F}^{-T}\right)\right\}\mathbf{F}^{T} \tag{III.4.17a}$$

$$\dot{\boldsymbol{\sigma}}^{Tr} = \dot{\boldsymbol{\sigma}} - \mathbf{L}\boldsymbol{\sigma} - \boldsymbol{\sigma}\mathbf{L}^{T} + \boldsymbol{\sigma}\left(\mathrm{tr}\mathbf{D}\right) \tag{III.4.17b}$$

2-Rotational derivative

They are relative to an orthogonal coordinate system rotating with respect to the coordinate system of the observator with the spin $\boldsymbol{\Omega}_{Q}$. The objective derivative can effectively evaluated by a simple transformation of any tensor $\mathbf{Z}$ with the help of the orthogonal rotation tensor $\mathbf{Q}$:

$$\frac{d_{Q}}{dt}\mathbf{Z} = \mathbf{Q}\left\{\frac{d}{dt}\left[\mathbf{Q}^{T}\mathbf{Z}\,\mathbf{Q}\right]\right\}\mathbf{Q}^{T} = \dot{\mathbf{Z}} - \mathbf{Z}\boldsymbol{\Omega}_{Q} + \boldsymbol{\Omega}_{Q}\mathbf{Z} \tag{III.4.18a}$$

with

$$\boldsymbol{\Omega}_{Q} = \mathbf{Q}\,\dot{\mathbf{Q}}^{T} \tag{III.4.18b}$$

In the context of this work the concept of the local rotational system is adopted due to its simple formulation. Equivalent to relation (III.4.18), we define any objective stress rate by

$$\dot{\boldsymbol{\sigma}}^{obj} = \boldsymbol{\sigma} = (\dot{}) - \boldsymbol{\Omega}(\,) + (\,)\boldsymbol{\Omega} \tag{III.4.19a}$$

or alternatively by the rotation tensor $\mathbf{Q}$ so that

$$\dot{\overline{\boldsymbol{\sigma}}} = \mathbf{Q}^{T}\dot{\boldsymbol{\sigma}}^{obj}\mathbf{Q} = \mathbf{C}^{e}:\left(\overline{\mathbf{D}} - \overline{\mathbf{D}}^{p}\right) \tag{III.4.19b}$$

and

$$\begin{aligned}\overline{\boldsymbol{\sigma}} &= \mathbf{Q}^{T}\boldsymbol{\sigma}\mathbf{Q}\\ \overline{\mathbf{D}} &= \mathbf{Q}^{T}\mathbf{D}\mathbf{Q}\\ \overline{\mathbf{D}}^{p} &= \mathbf{Q}^{T}\mathbf{D}^{p}\mathbf{Q}\end{aligned} \tag{III.4.19c}$$

Also, the constitutive model is formulated in the corotational coordinate system by

$$\begin{aligned} \overset{\circ}{\overline{\sigma}} &= \mathbf{C}^{ep}(\overline{\sigma}, \varepsilon_v^p)\overline{\mathbf{D}} \\ \dot{\varepsilon}_v^p &= \mathbf{P}(\overline{\sigma}, \varepsilon_v^p)\overline{\mathbf{D}} \end{aligned} \tag{III.4.20}$$

Choice of the local rotational system

The point, which rotational rate is suitable for the formulation of elasto-plastic constitutive equations in rate form, has largely been discussed in the literature during the past decade. The spin tensor **W** introduced in chapter III.1.3 has been used for a long time by many authors (e.g. [KEY 82, HIB 90]) to define the co-rotational coordinate system, which corresponds to the Zaremba-Jaumann co-rotational rate. In this case the general entities $\mathbf{\Omega}_Q$ and **Q** introduced in eqn. (III.4.19) become

$$\begin{aligned} \mathbf{\Omega} &= \mathbf{W} \\ \dot{\mathbf{Q}}(t)\,\mathbf{Q}(t)^T &= \mathbf{W}(t) \qquad \mathbf{Q}(0) = \mathbf{I} \end{aligned} \tag{III.4.21}$$

The low computational effort to calculate **W** from the Cauchy-Stokes decomposition might already explain that the Zaremba-Jaumann stress rate is implemented into most of the commercial FE-codes. However, the theoretical background is questionable; relation (III.1.33) exhibits the dependence of **U** on **W** which might not be reasonable. As a further negative outcome, Lee [LEE 69, 83] and Dafalias [DAF 83] have shown that this objective rate leads to inadmissible oscillations in the simple shear problem. Other insufficient outcome of this objective stress rate has been studied by Molenkamp [MOL 86].

By use of the Lagrangian rate of rotation instead of **W**, which corresponds to the Green-Naghdi stress rate, Dienes [DIE 79] realized to eliminate the stress oscillations in the simple shear problem. In that case $\mathbf{\Omega}$ and **Q** become

$$\begin{aligned} \mathbf{\Omega} &= \dot{\mathbf{R}}\mathbf{R}^T \\ \mathbf{Q} &= \mathbf{R} \end{aligned} \tag{III.4.22}$$

Nevertheless, the Zaremba-Jaumann stress rate is applicable for a large number of problems. Cheng [CHE 92] showed that under an updated-Lagrangian formulation with small successive load steps, its application is justified and correct.

Recently, Stumpf [STU 94] proposed without loss of generality and restrictions a formulation for the substructure spin $\mathbf{\Omega}$

$$\begin{aligned} &\mathbf{\Omega} = \dot{\mathbf{Q}}\,\mathbf{Q}^{-1}\,, \quad \mathbf{\Omega} = \mathbf{w} - \mathbf{w}^e - \mathbf{w}^p \\ &\mathbf{Q} = \mathbf{R}^e\,\mathbf{R}^p \end{aligned} \tag{III.4.23}$$

where $\mathbf{w}$, $\mathbf{w}_e$, $\mathbf{w}_p$ denote the actual, elastic and plastic spin, which are functions of the elastic and plastic stretch rate. In the special case of small elastic-finite plastic deformations, which is our main assumption, the proposed objective stress rate coincides with that proposed by Green-Naghdi.

CHAPTER IV

LOCAL APPROACH OF MICROSCALE DAMAGE - AND THE TRANSITION TO THE MACROSCALE

IV.1-The microscopic model - Damage characteristics of the components
IV.1.1-The hard phases (HP) and the interface
IV.1.1.1 Particle fracture
IV.1.1.2 Interfacial failure
IV.1.2-The metal matrix (MM)

IV.2-Transition between the microscopic and the macroscopic model

IV.3-The macroscopic model - *Effective* deformation and damage characteristics

IV.1-The microscopic model - Damage characteristics of the components

IV.1.1-The hard phases (HP) and the interface

IV.1.1.1 PARTICLE FRACTURE

Metallurgical observations have yielded the following main issues:

i1) Fracture surfaces of broken carbides are plane and smooth.

i2) Microcracks have often been found perpendicular to the principal load direction.

i3) Fracture takes place preferred at larger particles

i4) Elongated particles oriented in the principal load direction are more prone to fracture, mostly they crack at their mid-length.

It can be concluded from i1) that the particles are fractured by cleavage along preferred crystallographic orientations and this may imply that fracture will occur prior to plastic deformation. A local failure criterion is necessary to describe their brittle behaviour. A normal stress criterion might be useful since it has found wide acceptance on the macroscopic scale if the fracture surface is characterized by features i1) and i2). In addition, it can be shown that normal stresses increase on one hand with increasing aspect ratio and on the other hand from the edge to the centre of the particle [GRO 95]. This is in accordance with the experimental observation of i4). While the particle size does not directly influence the normal stress distribution within the particle (since it is not a relative quantity), the ratio of particle size to spacing does. However, this effect might not be pronounced enough to explain i3). In general, it is explained that larger particles contain more microdefects which act as local stress concentrators and may lead to premature loss of atomic bonds. Due to their brittle nature (low K_{Ic}) immediate fracture of the whole carbide takes place. The scattering of brittle fracture over the particle size has motivated some authors to apply a statistical model mostly formulated by the Weibull approach. A probability for fracture (P) may be calculated as function of volume (V) and stress level (σ):

$$P(V) = 1 - \exp\left[-\frac{V}{V_0}\left(\frac{\sigma}{\sigma_0}\right)^m\right] \qquad \text{(IV.1.1)}$$

where V_0, σ_0 and m are empirical constants, m being known as the "Weibull modulus" for the material. For equal fracture probability the fracture strength (σ) of the particle varies with its size. For a spherical particle it holds

$$r^3\sigma^m = \text{constant} \qquad \text{(IV.1.2a)}$$

and therefore for the fracture strength σ_{Ic} :

$$\sigma_{Ic} = \alpha \cdot r^{3/m} \qquad \text{(IV.1.2b)}$$

where α and m are adjustable parameters. Values of m for ceramics are found to vary between 5 and 20 [KNO 90].

In this work the following model is suggested.

i1) Prior to cleavage, the behaviour of hard phases is isotropic, elastic and described by Hooke's law.

i2) Cleavage occurs, if the normal stress within the HP reaches a critical value (fracture strength).

IV.1.1.2 INTERFACIAL FAILURE

The bonding between HP and MM and the respective load transfer in the virgin state might depend on whether the interface is coherent, semi-coherent or incoherent. In addition, the interface possesses a high potential of energy, e.g. it might act as paths for rapid diffusion, vacancy sinks, sites for inhomogeneous precipitate formation and for segregation of embrittling impurity elements such as hydrogen etc. [KNO 90]. All these issues might influence the onset of interfacial debonding. Early works on interfacial decohesion models considered energy balance conditions [GUR 63, TAN 70, GOO 79]. They proposed that debonding will be initiated when the local elastic strain energy becomes comparable to the energy needed to create the free surface. However, it was pointed out [see e.g. BRO 71] that this is only a necessary but not a sufficient condition for inclusion-matrix separation. In [TAN 70] it was shown that the energy criterion is satisfied almost immediately upon yielding for particles greater than about 250 Å. As a result, stress based failure criteria seem to be more appropriate.

Different failure modes are possible [e.g. WEI 93B, also Fig. IV.1.1.]:

Mode I (tensile failure) - A discontinuity of the interface surface is initiated perpendicular to the principal load direction due to exceedence of the interfacial fracture strength. For cyclic loading the crack may close and friction conditions within the interface become important: While the transmission of the load in the normal direction remains (as if no crack was present), that in the tangential direction is influenced by the local friction conditions.

Mode II (shear failure) - The exceedence of a critical shear stress initiates sliding. With increasing slip the crack surface becomes smooth and friction may be described by the model of Mohr-Coulomb.

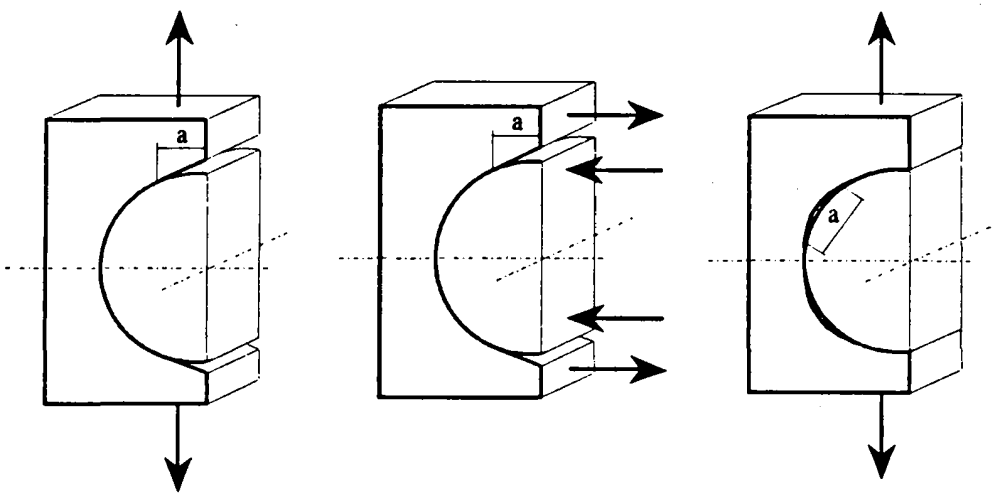

Fig. IV.1.1. Schematic of the principal failure modes

A multiaxial stress state favours failure under mixed mode which may be considered as a combination of the two first mentioned failure modes.

Microcracks developed at the interface by initial debonding may grow along the interface causing complete separation and subsequent void growth or propagate into the matrix. An attractive model for the former case has been developed by Needleman [NEE 87]. His "cohesive zone type interface model" implies own constitutive relations for the interface. Unlike the stress-strain relation for the individual phases, the interface relation is described by a traction-displacement response. As the interface separates, the magnitude of the tractions increases, achieves a maximum and ultimately falls to zero when complete separation occurs [NEE 91]. Assuming elastic behaviour of the interface (interfacial tractions may be derived from a potential), the interface response being dissipative, he constructed a polynomial potential that describes this behaviour (Fig. IV.1.2.)

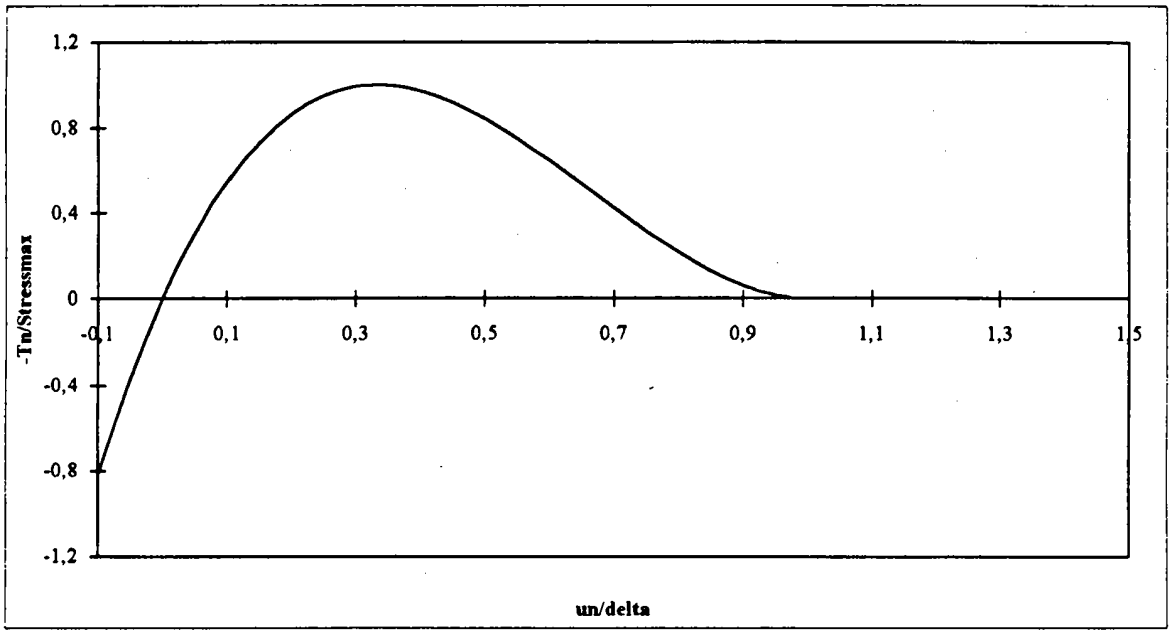

Fig. IV.1.2. Needleman's cohesive model

In the case of total separation, the normal interfacial opening displacement u_n becomes δ, called characteristic length. σ_{max} is the maximum traction carried by the interface undergoing a purely normal separation (u_t=0). Modelling of decohesion with imperfect interfaces (containing microdefects with length a) have brought about the important issue [NEE 90] that a transition in decohesion mode occurs from more or less uniform separation to crack-like propagation in the range $10^2 < a/\delta \leq 10^3$. The application of fracture mechanics based concepts for the propagation of the interface crack, may therefore only be suitable for $a/\delta > 10^3$.
Broeckmann [BRO 94] and McHugh et al. [MCH 94] have used a particle/matrix interface layer with own elastic(-plastic) properties. This model has been motivated by experimental observations that a thin reaction zone exists differing structurally (due to diffusion), and presumably mechanically, from the phases on either side. Since the interface layer represents a transition zone, the elastic-(plastic) properties have been averaged from those of particle and matrix.
In this work the following model is suggested.

i1) The interface is modelled as one phase with own properties. In the undamaged state isotropic, elastic-plastic behaviour is assumed.

i2) Sudden interfacial failure under mode I may occur, if the stress normal to the interface reaches a critical value (interfacial fracture strength). The local failure process is modelled assuming orthotropic behaviour: The normal elastic modulus and the shear modulus are reduced to a value close to zero.

i3) Interfacial failure under mode II may occur, if the interfacial shear stress reaches a critical value (interfacial shear strength). The local failure process is modelled assuming orthotropic behaviour: While the elastic modulus is retained (for a compressive stress state), the shear modulus is reduced to a value close to zero.

For both models fracture mechanics concepts are not used to model interface crack propagation.

Concluding Remarks
In general, both failure mechanisms are in competition and it depends on the respective local stress state at the HP, if local failure takes first place within the HP or at the interface. Typically, cleavage is more likely for particles with a Young's modulus greater than that of the matrix ($E_{HP}>E_{MM}$ e.g. carbides, oxides), interfacial failure will be promoted for $E_{HP}<E_{MM}$ (e.g. sulphides). It seems desirable to construct failure mechanism maps in the stress space in order to find transition zones between the two competing mechanisms as in the concept of fracture mechanism maps originally developed by Ashby [see e.g. TEI 88].

IV.1.2-The metal matrix

Ductile damage in the matrix is characterized by the subsequent processes of void formation, growth and coalescence. Void formation occurs privileged at secondary phases due to interfacial debonding. These secondary annealed carbides have been attributed to the "matrix" since application of an own continuum mechanics description might be questionable due to the small scale. Larger eutectic carbides are more prone to fail by cleavage, whereas all secondary annealed carbides tend to decohese. Void formation at the secondary carbides does not occur arbitrarily, but is often localized along small bands of plastic stretching. These bands emerge from crossing of neighbouring local plastic zones around the microcrack tip of failed particles.
The processes of void formation could be identified by in-situ tests but are also evidenced by the dimple structure on fracture surfaces. In addition, the small bands of high plastic stretching could be found.
Whereas the formation of voids is promoted by a plastic deformation field, their growth is controlled by the local deformation constraint. One important indicator for this deformation constraint is the triaxiality (eqn. I.1.9). A low local triaxiality implies preferred directions of stretching and void growth. In contrast, a high local triaxiality favours a spherical void growth. Experimental studies have clearly demonstrated that void growth rates increase substantially for increasing stress triaxiality. For example, the central portion of the typical cup-cone fracture which occurs at the neck of a tensile specimen is produced by the coalescence of internal voids which grow by plastic deformation under the influence of the prevailing triaxial stress system. The tunnelling effect in a three-point bending specimen is an additional prove for the effect of triaxiality on void growth: The crack grows faster in the centre of the plate, due to the higher stress triaxiality leading ultimately to the formation of a tunnelled region. The tunnelled region adjoining the centre-plane progressively spreads forward and also sideways with increasing load. The load is then carried by the side ligaments. The excessive softening of the material in the tunnelling zone, together with the triaxial stress state along the crack front triggers the shear failure of the remaining ligaments adjacent to the free surface through the formation of shear-lips [NAR 92]. These shear lips (compare cup-cone fracture) are small bands with intense strain localization under 45° to the free surface (Fig. IV.1.3).
Systematic experimental studies of the influence of triaxiality on ductile failure have been performed at tensile specimen with different notches at the centre producing local differences in triaxiality [KON 93].

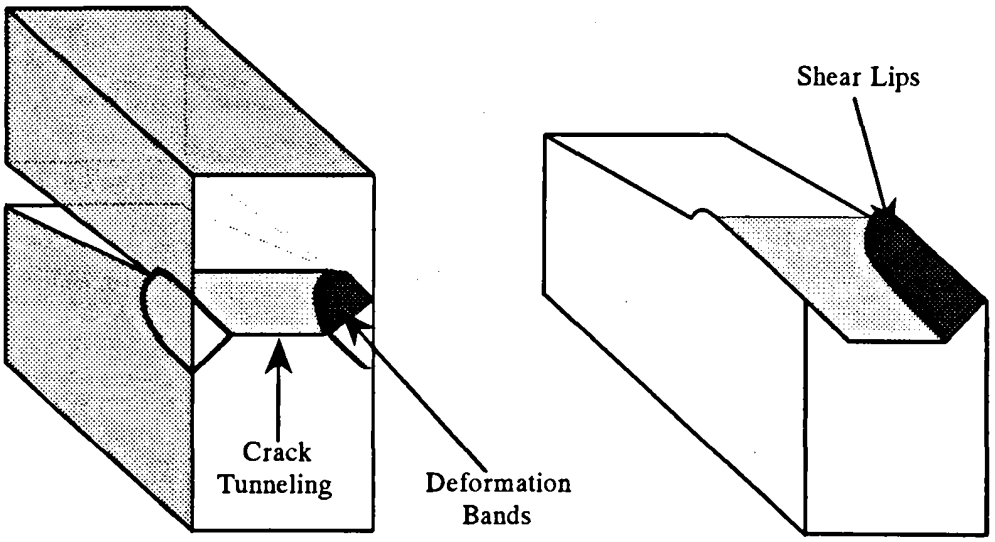

Fig. IV.1.3. Crack tunnelling and shear lips as a result of variation of triaxiality through specimen thickness

Ultimate failure emerges from void coalescence either due to necking of ligaments connecting large voids or due to a void-sheet formation. The latter one is a result of an intense deformation band which begins to concentrate along the ligaments connecting neighbouring voids after they have grown to a critical size in relation to their spacing. Mostly void sheet formation occurs in the steel X210Cr12 under mode I or mixed mode (Fig. IV.1.4).

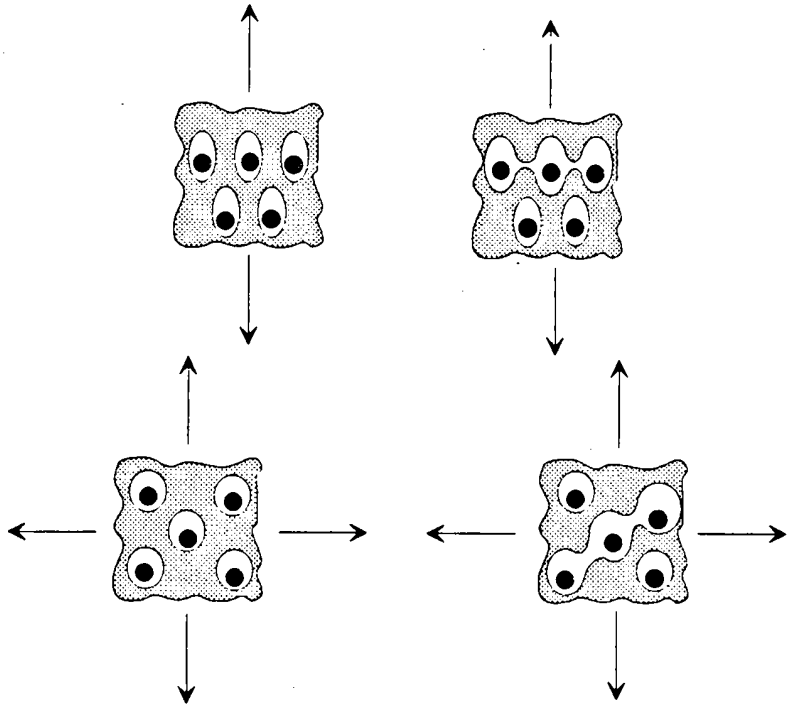

Fig. IV.1.4. Void coalescence by necking or by void sheet formation

Considerable theoretical work has been done on the mechanisms of ductile failure. The two most widely applied models for void growth and coalescence based on the works of Rice&Tracey [RIC 69] and Gurson [GUR 77] are presented more in detail below.

Rice&Tracey Model

This model considers a single void in an infinite rigid plastic (non-hardening) matrix subjected to remote normal strain rates ε_i and remote normal stresses σ_i. During deformation the initially spherical void becomes ellipsoidal. The rate of change of radius along the principal directions has been found by the following semi-empirical relationship

$$\frac{dR}{R} = 0.283\, d\varepsilon^p \exp\left(\frac{3\sigma_H}{2\sigma_{Y_0}}\right) \tag{IV.1.3}$$

Integrating the above equation and assuming that it holds even for a strain hardening matrix when the initial yield strength is replaced by the effective stress, gives

$$\ln\left(\frac{\overline{R}}{R_0}\right) = 0.283 \int_0^{\varepsilon_v^p} \exp\left(\frac{3\sigma_H}{2\sigma_v}\right) d\varepsilon_v^p \tag{IV.1.4}$$

with $\overline{R} = (R_1+R_2+R_3)/3$ and the initial hole radius R_0.

Since the Rice and Tracey model is based on a single void, it does not account for void interaction, nor is it able to predict ultimate failure. If it is assumed that the failure strain is inversely proportional to the hole growth-rate, then the failure strain can be expressed as

$$\varepsilon_{vcri}^p = \alpha \exp\left(-\frac{3\sigma_H}{2\sigma_v}\right) \tag{IV.1.5a}$$

where α is a material constant. If the failure strain is compared with that of the uniaxial case ε_0 (ζ=1/3) then it holds

$$\varepsilon_{vcri}^p = 1.65 \cdot \varepsilon_0 \exp\left(-\frac{3\sigma_H}{2\sigma_v}\right) \tag{IV.1.5b}$$

From this relation, the increment of a damage indicator dD_i may be suggested by [GUN 91]

$$dD_i = \frac{d\varepsilon_v^p}{\varepsilon_{v_{cri}}^p} \tag{IV.1.5c}$$

and by integrating

$$D_i = \int_0^{\varepsilon_v^p} \frac{\exp(1.5 \cdot \zeta)}{1.65 \cdot \varepsilon_0} d\varepsilon_v^p \tag{IV.1.5d}$$

The critical value of D_i for uniaxial loading is unity, since $D_i = \varepsilon_v^p / \varepsilon_0$. The damage indicator depends in addition to ε_0 on the triaxiality ζ. The significance of the triaxiality on ductile failure has also been found by other authors [e.g. CLI 68, FIS 89, ZHA 89]. Some of them however exclude a coupling of triaxiality to plastic strain, which seems questionable since they exhibit a singularity for a perfect hydrostatic stress state. For example Fischmeister et al. [FIS 89] have proposed the following criterion

$$D_i = \frac{\sigma_H^2}{\sigma_v} \qquad \text{(IV.1.6)}$$

In the case of a perfect hydrostatic stress state ($\sigma_{xx}=\sigma_{yy}=\sigma_{zz}$) D_i becomes infinity even for small stress magnitudes when failure is not likely to occur. A multiplicative coupling with the plastic strain overcomes this singularity problem. For this reason the damage indicator based on Rice &Tracey's void growth model is believed to be more appropriate. Recently Fischer et al. [FIS 96] presented an experimental procedure in order to determine ε_0. It is proposed that the first appearance of a microcrack in the necking area (sharp change in the slope of the stress vs. strain curve) should be used to find the relevant failure parameter.

Gurson-Model

The first macroscopic approach to account for void nucleation and growth within a continuum mechanics formulation has been given by Gurson [GUR 77]. This model uses a yield condition of the form

$$\Phi(\sigma,\sigma_Y,f) = 0 \qquad \text{(IV.1.7)}$$

with the additional parameter f: the current void volume fraction. σ_Y is the equivalent flow stress of the matrix material. Since the model does not predict ductile failure due to the coalescence of voids, Tvergaard and Needleman [NEE 84] proposed to limit its application to a void volume fraction below a critical value f_c. The following modification to Gurson's plastic potential has been suggested

$$\Phi = \frac{\sigma_v^2}{\sigma_Y^2} + 2f^* q_1 \cosh\left(\frac{3q_2\sigma_H}{2\sigma_Y}\right) - \left[1+\left(q_1 f^*\right)^2\right] = 0 \qquad \text{(IV.1.8)}$$

q_1 and q_2 are fitting parameters describing the interaction between voids. Setting q_1=1.25 and q_2=1 gives good agreement between predictions of the model and the results of a numerical study of void coalescence in isotropically hardening materials [LLO 91].
f^* is defined in [NEE 84] as

$$f^* = \begin{cases} f, & \text{for } f \le f_c \\ f_c + \dfrac{f_u^* - f_c}{f_f - f_c}(f - f_c), & \text{for } f > f_c \end{cases} \qquad \text{(IV.1.9)}$$

The gradient of the function for $f>f_c$ has been derived by the requirement $f^*(f_f)=f^*_u$, which implies that the void volume fraction at final failure ($f=f^*_u$) is f_f.
Unlike classical plasticity (e.g. v. Mises plasticity), the modified Gurson model exhibits a weak hydrostatic stress dependence on the plastic flow. For a material with no voids (f=0), its yield surface (eqn. IV.1.8) reduces to that of von Mises.
The evolution law for the void volume fraction distinguishes the growth of existing voids and nucleation of new voids

$$\dot{f} = \dot{f}_{growth} + \dot{f}_{nucleation} \qquad \text{(IV.1.10)}$$

The plastic incompressibility condition is assumed to hold for the matrix but not for the composite due to the existence of voids. Accordingly, the rate of void volume fraction due to growth is related to the time derivative of the total volume as

$$\dot{f}_{growth} = (1-f)\,\mathrm{tr}\,\mathbf{D}^p \qquad \text{(IV.1.11)}$$

As already mentioned, nucleation of new voids mainly occurs by cleavage or interfacial failure of second phase particles. Several macroscopic nucleation models have been reported in the literature. They are assumed to be controlled by either stress [e.g. Roy 81] or strain or strain-energy criteria [e.g. Goo 79].

Although the Gurson-model seems to appear most useful, a main difficulty arises in the fitting of material parameters by experiments. In addition some non-trivial modifications in programming are required by a FE-code implementation and has for these reasons not been considered in this work.

In this work the following model is suggested for ductile matrix damage.

i1) Undamaged plastic deformation is modelled with large deformation analysis within the J_2-flow theory.

i2) Void initiation at second phase particles (annealed carbides) and its growth is averaged throughout the matrix. The model of Rice and Tracey has been adopted to formulate a failure criterion by eqn. (IV.1.5b) for ductile damage in the matrix.

IV.2-Transition between the microscopic- and the macroscopic model

The prediction of elasto-plastic effective properties for the composite has already been briefly summarized in Chapter I.2. They have been found to be governed by the constitutive behaviour of each individual component and the (geometrical) interaction in the composite assembly. In a similar way a FE-based method (see next Chapter) may be used in order to predict the overall behaviour. In this method the defined representative volume element (R.V.E., Chapt. I.2) is assumed to be distributed periodically over the whole microstructure. This specific type of RVE is called *unit cell*, the respective FE-based method *periodic microfield approach* or simply *unit-cell technique*. In the simplest case it contains one matrix-inclusion system where the interaction between inclusions is established by the symmetry of the boundary conditions. Increasing their degree of randomness, unit cells describe more realistic microstructures but do cost more computational effort. Attention has to be devoted to the appropriate choice of symmetric boundary conditions. These conditions are not correctly chosen for instance if the edges are not remaining straight and parallel (as in the initial configuration) during deformation. The macroscopic values for stresses and strains are derived from displacement and force values at the boundaries. In the inner of the unit cell, the non-uniform field of strains and stresses characterizes the local deformation behaviour on the microscale.

A link between non-uniform local strain fields $\boldsymbol{\varepsilon}$ and overall strains $\mathbf{E}$ has to be established. Employing the virtual work principle, such a relation can be derived by (Hill-Mandel relation [HIL 65, MAN 72])

$$\langle \boldsymbol{\sigma}\,\boldsymbol{\varepsilon} \rangle = \frac{1}{V}\int_V \boldsymbol{\sigma}\,\boldsymbol{\varepsilon}\,dV = \boldsymbol{\Sigma}\,\mathbf{E} = \frac{1}{V}\int_S \mathbf{f}^t\mathbf{u}\,dS \qquad \text{(IV.2.1)}$$

σ is the local stress field satisfying mechanical equilibrium with the surface traction **f**, ε is the local strain field deduced from the displacement field **u** respecting the boundary conditions, $\langle \mathbf{x} \rangle$ is the volume average of **x**. The equality of macroscopic and averaged measures for strains or stresses in the elasto-plastic regime motivates the introduction of an effective damage tensor by (e.g. for component y)

$$D_y = 1 - \frac{\langle \varepsilon_y \rangle}{E_y} \tag{IV.2.2}$$

By this definition damage is effectively quantified on the macroscale in consideration of the microscale strain heterogeneity. In addition by applying subsequently small load increments, the evolution of macroscopic damage may be estimated. By this definition of D

$$D_y = 1 - \frac{\langle \varepsilon_y \rangle}{E_y} \Rightarrow \langle \varepsilon_y \rangle = E_y (1 - D_y) \tag{IV.2.3}$$

one notes that the strain tensor is transformed by the damage tensor into the effective strain tensor in addition to the application of the principle of stress equivalence [LEM 85A]. In the following it will be shown how this damage parameter can be implemented into a continuum damage mechanics model (CDM) useful for computations on the macroscale.

IV.3-The macroscopic model-*Effective* deformation and damage characteristics

In Continuum damage mechanics models (CDM), damage processes like initiation and growth of microcracks and -voids are reflected by internal variables. The ideology is the same as in classical plasticity, where internal variables are introduced to describe the processes of dislocation movements on the microscale. As opposed to plasticity (ε^P, κ), the internal variables describing damage can not be measured directly but require indirect experimental methods. The most employed approach to quantify damage is by analysing microdefects on the microstructure. Kachanov [KAC 86] firstly defined a damage parameter considering an equivalent surface density of microcracks or intersection of microcavities in any plane (Fig. IV.3.1)

$$D_n = \frac{S_D}{S} = \frac{S - \tilde{S}}{S} \tag{IV.3.1}$$

S is the overall section area of the damaged element defined by its normal **n**. The total area of intersections of microcracks and cavities is denoted by S_D and the effective resisting area taking into account this area S_D is denoted by $\tilde{S}$ [LEM 85A](Fig. IV.3.1).

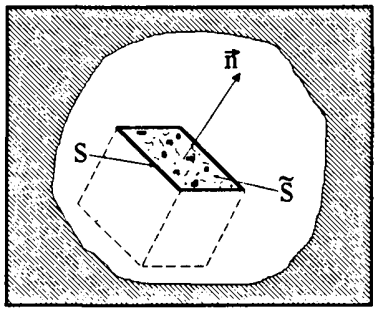

Fig. IV.3.1. Damaged Microelement

The state of damage is framed by the following two bounds: the non-damaged state for $D_n=0$, and the state of rupture for $D_n=D_c$ with $D_c \in [0,1]$. In the following only isotropic damage is considered which implies that D is a scalar.
In the damaged microelement, stresses are only transmitted by the effective resisting area $\tilde{S}$; they are termed effective stresses $\tilde{\sigma}$. The macroscopic equivalent model containing no defects (total area S) is supposed to give the same material response

$$\tilde{\sigma}\tilde{S} = \sigma S \qquad \text{(IV.3.2)}$$

or

$$\tilde{\sigma} = \frac{\sigma}{1-D} \qquad \text{(IV.3.3)}$$

in addition to the application of the principle of strain equivalence stating that any strain constitutive equation for a damaged material is derived in the same way as for the virgin material except that the stress is replaced by the effective stress [LEM 85B]. Analogously, damage may also be introduced in the stress-space (principle of stress equivalence), where the stresses are remaining and the strains are replaced by the effective strains $\tilde{\varepsilon}$

$$\tilde{\varepsilon} = (1-D)\varepsilon \qquad \text{(IV.3.4)}$$

We see that the definition of the damage parameter in the last chapter is consistent with that described above. Both transformations are illustrated below

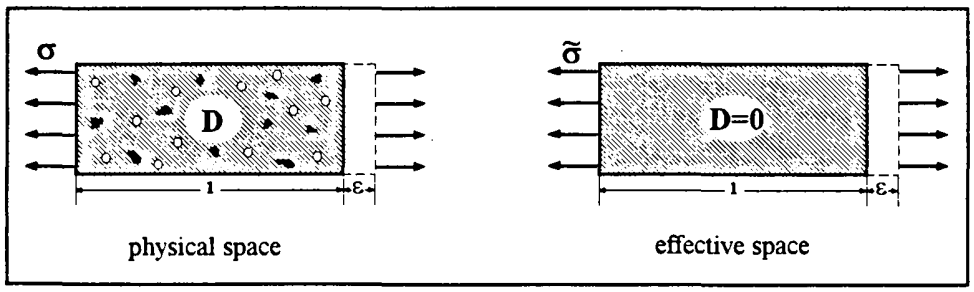

(a)

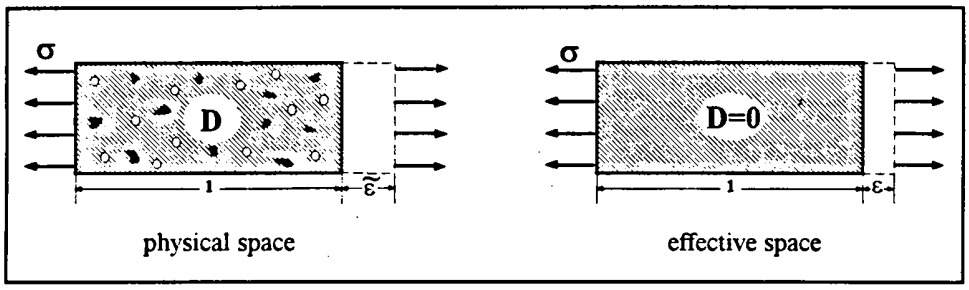

(b)

Fig. IV.3.2. Principle of strain (a) and stress (b) equivalence

CDM Model of Lemaitre

An attractive CDM model for ductile damage has been developed within a general thermodynamic framework by Lemaitre [LEM 85A]. In the following the main steps shall be briefly summarized:

The model uses the concept of effective stresses for isotropic damage. The evolution law for the damage parameter D is expressed as function of its associated variable, the rate of plastic strain. The free energy is splitted into an elastic-damage and a plastic part assuming isothermal processes, linear elasticity and isotropic damage:

$$\Psi = \frac{1}{2\rho}\mathbf{C}^e\boldsymbol{\varepsilon}^e\boldsymbol{\varepsilon}^e(1-D)+\Psi^p(\kappa) \tag{IV.3.5}$$

The elastic law is obtained by derivation of Ψ with respect to the elastic strains

$$\boldsymbol{\sigma} = \rho\frac{\partial\Psi}{\partial\boldsymbol{\varepsilon}^e} = \mathbf{C}^e\boldsymbol{\varepsilon}^e(1-D) \tag{IV.3.6}$$

The thermodynamic force (Y) conjugate to the damage parameter is derived from

$$\overline{Y} = -Y = -\rho\frac{\partial\Psi}{\partial D} = \frac{1}{2}\mathbf{C}^e\boldsymbol{\varepsilon}^e\boldsymbol{\varepsilon}^e \tag{IV.3.7}$$

which is identical to the specific elastic non-damaged strain energy W^e: $Y=W^e/(1-D)$. When splitting the energy into one part due to distortion and one due to volumetric deformation, one obtains

$$W^e = \frac{1}{2}\left[\frac{(1+\nu)}{E}\frac{\boldsymbol{\sigma}^D\boldsymbol{\sigma}^D}{(1-D)}+3\frac{(1-2\nu)}{E}\frac{\sigma_H^2}{(1-D)}\right] \tag{IV.3.8}$$

and with the equivalent stress of von Mises, $\sigma_v = \sqrt{\frac{3}{2}\boldsymbol{\sigma}^D\boldsymbol{\sigma}^D}$ one obtains

$$\overline{Y} = \frac{W^e}{(1-D)} = \frac{\sigma_v^2}{2E(1-D)^2}\left[\frac{2}{3}(1+\nu)+3(1-2\nu)\left(\frac{\sigma_H}{\sigma_v}\right)^2\right] \tag{IV.3.9}$$

This quantity can be computed for an "equivalent" one-dimensional case defined by its stress σ^*, giving the same value of Y. With $\sigma_v=\sigma^*$ and $\sigma_H=1/3\ \sigma^*$ and Y(*1-Dim.*)=Y(*3-Dim.*) follows

$$\sigma^* = \sigma_v \left[\frac{2}{3}(1+\nu) + 3(1-2\nu)\left(\frac{\sigma_H}{\sigma_v}\right)^2 \right]^{\frac{1}{2}} \qquad \text{(IV.3.9)}$$

Since the evolution of D is controlled by values of Y (Y being conjugate to D), σ^* is called damage equivalent stress, in analogy to the v. Mises equivalent stress for plasticity, and may be used as a criterion for damage [LEM 85A].
The evolution law for D is derived from the second principle of thermodynamics. In order to describe the dissipative processes due to plastic deformation and damage and to determine the evolution of the internal variables, a convex potential over all conjugate variables is assumed satisfying the Clausius-Duhem inequality:

$$\Phi = \Phi\left(\dot{\varepsilon}^p, \dot{\kappa}, \dot{D}\right) \geq 0 \qquad \text{(IV.3.10)}$$

With the potential chosen to be

$$\Phi = \frac{S_0}{2}\left(\frac{\overline{Y}}{S_0}\right)^2 \dot{\varepsilon}_v^p \qquad \text{(IV.3.11)}$$

with S_0 being a material parameter, the evolution law for D is derived from

$$\dot{D} = \frac{\partial \Phi}{\partial \overline{Y}}\left(\dot{\varepsilon}_v^p, \overline{Y}\right) = \left(\frac{\overline{Y}}{S_0}\right)\dot{\varepsilon}_v^p \qquad \text{(IV.3.12)}$$

The equivalent stress in eqn (IV.3.9) is coupled with the equivalent plastic strain through the hardening law, e.g. in the form proposed by Ramberg-Osgood accounting additionally for damage:

$$\varepsilon_v^p = \left[\frac{\sigma_v}{(1-D)K}\right]^M \quad \Rightarrow \quad \frac{\sigma_v}{(1-D)} = K\left(\varepsilon_v^p\right)^{\frac{1}{M}} \qquad \text{(IV.3.13)}$$

where K and M are material characteristics. The general evolution law is obtained with eqn (IV.3.13) and (IV.3.9)

$$\dot{D} = \left(\frac{K^2}{2ES_0}\left[\frac{2}{3}(1+\nu) + 3(1-2\nu)\left(\frac{\sigma_H}{\sigma_v}\right)^2 \right] \varepsilon_v^{p\,2/M} \right) \dot{\varepsilon}_v^p \qquad \text{(IV.3.14)}$$

depending on the elastic-plastic properties E, ν, K and M and on S_0. Special attention is devoted to proportional loading with constant triaxiality parameter. Eqn (IV.3.14) is integrated over the interval $0<D<D_C$ and $\varepsilon_D<\varepsilon<\varepsilon_R$, with ε_D being the damage threshold and ε_R the strain at rupture corresponding to the intrinsic value of damage at failure D_C. Furthermore it is assumed that damage is initiated ($\varepsilon=\varepsilon_D$) when no more macroscopic hardening is present ($M \to \infty$). Under these assumptions the evolution law for the damage parameter D becomes

$$\dot{D} = \frac{D_c}{\varepsilon_R - \varepsilon_D}\left[\frac{2}{3}(1+\nu)+3(1-2\nu)\left(\frac{\sigma_H}{\sigma_v}\right)^2\right]\dot{\varepsilon}_v^p \qquad \text{(IV.3.15)}$$

and in the integrated form

$$D \equiv \frac{D_c}{\varepsilon_R - \varepsilon_D}\left\langle \varepsilon_v^p\left[\frac{2}{3}(1+\nu)+3(1-2\nu)\left(\frac{\sigma_H}{\sigma_v}\right)^2\right]-\varepsilon_D\right\rangle \qquad \text{(IV.3.16)}$$

Concluding Remarks

In accordance with the microscopic models for void growth [e.g. CLI 68, RIC 69], the CDM-model of Lemaitre also exhibits the strong influence of the triaxiality parameter on damage evolution. Its range of validity for eqn (IV.3.16) is limited to isotropic plasticity and isotropic damage and to a constant triaxiality ratio during deformation. The three coefficients ε_D, ε_R and D_C are identified by uniaxial loading-unloading cycles through the loss of stiffness during deformation (Fig. IV.3.3):

$$D = 1 - \frac{\tilde{E}}{E} \qquad \text{(IV.3.17)}$$

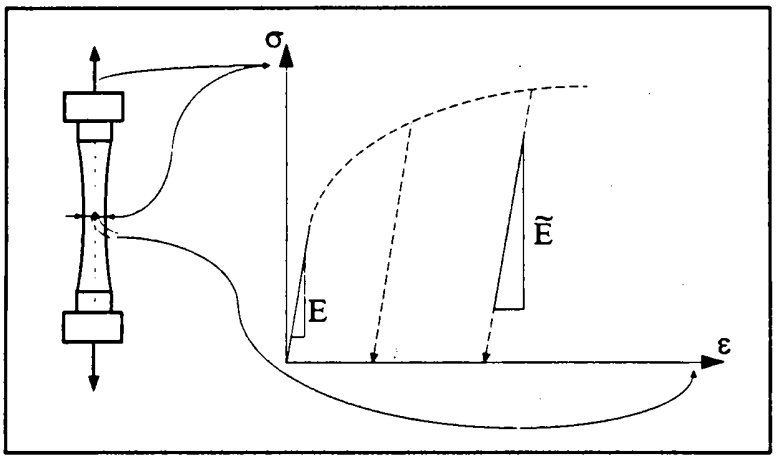

Fig. IV.3.3. Measure of loss of stiffness

These uniaxial tension tests provide a linear relationship between the strains and D which is in accordance with the predictions of the model (eqn.IV.3.16 for ζ=1/3) (Fig. IV.3.4).

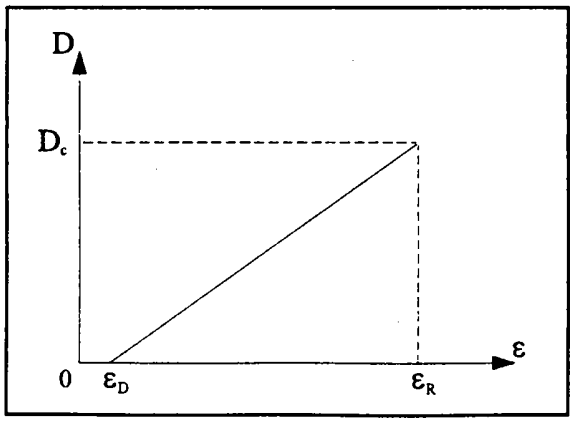

Fig. IV.3.4. Evolution of the damage parameter for the uniaxial case

CHAPTER V

THE FE-PROGRAM

V.1-The FE-Discretization
V.1.1-Virtual work principle
V.1.2-Linearization of the virtual work principle
V.1.3-Discretisation by interpolation functions
V.1.4-Elements

V.2-The resolution of the non-linear problem
V.2.1-The Newton-Raphson scheme
V.2.2-Test of convergence
V.2.3-The numerical integration method
V.2.4-The equation solver

V.3-The constitutive model under consideration
V.3.1-Linear elasticity for isotropic and orthotropic materials
V.3.2-Rate-independent plasticity for isotropic and orthotropic materials
V.3.3-Integration of the constitutive model at elastic-finite-plastic strains
V.3.3.1-Kinematic approximations
V.3.3.2-Local integration of elasto-plastic constitutive laws
V.3.3.3-Evaluation of the elasto-plastic matrix $\mathbf{C}^{ep}$

V.4-Characterization of local failure
V.4.1-Particle fracture
V.4.2-Interfacial failure
V.4.3-Ductile matrix damage

V.5-Coupling between the micro- and the macroscale
V.5.1-Transition from the macro- to the microscale - *Zooming technique*
V.5.2-Transition from the micro- to the macroscale - *Averaging technique*

V.6-Pre-and Postprocessing and interface programs

V.1-The FE-Discretization

The FE-Code CRACKAN is an extension of the Program by Owen, Hinton and Fawkes [OWE 77 80 83]. It is based on the displacement formulation and is at present restricted to 2D-problems assuming conditions of plane strain or plane stress. The conditions of force and momentum equilibrium are expressed in this method in the weak form. Under the assumption of small displacement theory, shape and volume change of the body is neglected in the equilibrium equations. As explained earlier, this is not justified in some cases (e.g. the analysis of ductile damage processes or blunting effects at the crack tip). Consequently, the integration of the equilibrium conditions is performed in the current configuration.

V.1.1-Virtual work principle

The virtual work principle has been derived in chapter III

$$\int_V \sigma \delta \mathbf{D} dV = \int_S \mathbf{f} \delta \mathbf{v} dS + \int_V \mathbf{b} \delta \mathbf{v} dV \qquad \text{(V.1.1a)}$$

It has been formulated in the current configuration; the stress and strain measures are Eulerian quantities. The concept of work conjugacy allows to transform this term into the initial configuration.

$$\int_{V_0} \tau \delta \mathbf{D} dV_0 = \int_{S_0} \mathbf{f}_0 \delta \mathbf{v} dS_0 + \int_{V_0} \mathbf{b}_0 \delta \mathbf{v} dV_0 \qquad \text{(V.1.1b)}$$

or

$$\int_{V_0} \mathbf{S} \delta \dot{\mathbf{E}} dV_0 = \int_{S_0} \mathbf{f}_0 \delta \mathbf{v} dS_0 + \int_{V_0} \mathbf{b}_0 \delta \mathbf{v} dV_0 \qquad \text{(V.1.1c)}$$

The linearization of the virtual work principle is generally possible for each formulation. It is also the point at which reference configuration will be considered. A first concise finite element formulation has been given by Hibbit et al. [HIB 70] using a total Lagrangian description. The reference configuration has been chosen as the initial configuration using only Lagrangian quantities. However, due to the fact that plasticity problems are formulated in rate-equations, an updated Lagrange analysis procedure is preferred, because at each instant the reference state is updated to coincide with the current state. This formulation has been pioneered by Mc Meeking and Rice [MEE 75] based on Hill's rate equation of virtual work [HIL 59]. Today most numerical implementations adopt the updated Lagrangian formulation [see e.g. BAT 75, HIB 90, BRA 86].
In our work we use the first expression of the virtual work principle (V.1.1a). The internal (left side) and external virtual work (right side) must be equilibrated.

$$P(t,\delta v) = P_{int}(t,\delta v) - P_{ext}(t,\delta v) = 0 \qquad \text{(V.1.2a)}$$

with

$$P_{int}(t,\delta v) = \int_V \sigma \delta \mathbf{D} dV \qquad \text{(V.1.2b)}$$

$$P_{ext}(t,\delta v) = \int_S \mathbf{f} \delta \mathbf{v} dS + \int_V \mathbf{b} \delta \mathbf{v} dV \qquad \text{(V.1.2c)}$$

V.1.2-Linearization of the virtual work principle

In order to solve the nonlinear set of equations generated from eqn V.1.2 by the finite element discretization, iterative techniques must be used (e.g. Newton's method, Newton-Raphson). These methods require the linearization of V.1.2

$$dP(t,\delta v) = dP_{int}(t,\delta v) - dP_{ext}(t,\delta v) = 0 \qquad (V.1.3)$$

In many structural analyses it can be considered that external forces are assumed to be independent of the displacements of the body on which they act ("dead loads"). Buckling of thin bodies under external pressure is one example where this assumption is inadequate [see HIB 79]. These cases are excluded in this work. Consequently, the gradient of the external work rate becomes zero unlike to the internal work rate. The variation of the internal virtual work yields

$$dP_{int}(t,\delta v) = \int_V d\sigma \delta \mathbf{D} dV + \int_V \sigma d(\delta \mathbf{D} dV) \qquad (V.1.4a)$$

and

$$dP_{int}(t,\delta v) = \int_V d\sigma \delta \mathbf{D} dV + \int_{V_0} \sigma d(\delta \mathbf{D} \det \mathbf{F}) dV_0 \qquad (V.1.4b)$$

$d\sigma$ and σ are evaluated at the end of the increment. The current stresses expressed in the co-rotational coordinate system are transformed into the global coordinate system by (see eqn. III.4.24)

$$\sigma = \mathbf{Q}\,\bar{\sigma}\,\mathbf{Q}^T \qquad (V.1.5)$$

The differentiation yields

$$d\sigma = d\mathbf{Q}\,\bar{\sigma}\,\mathbf{Q}^T + \mathbf{Q}\,\bar{\sigma}\,d\mathbf{Q}^T + \mathbf{Q}\,d\bar{\sigma}\,\mathbf{Q}^T \qquad (V.1.6a)$$

with

$$d\bar{\sigma} = \bar{\mathbf{C}}^{ep}\,d\bar{\mathbf{D}} \qquad (V.1.6b)$$

where $\bar{\mathbf{C}}^{ep}$ is the elastic-plastic tangent modulus (see V.3.3). $\mathbf{Q}$, $d\mathbf{D}$ and $\bar{\mathbf{C}}^{ep}$ depend on the kinematic approximations (see V.2.3.1). The computation of the tangent matrix for the Newton method on this basis leads to a more general and precise formulation. Consequently, the rate of convergence may be efficiently improved. However, the price to pay for this approach is an elevated computational effort, in particular due to the treatment of a non-symmetric stiffness matrix [DAB 94, WEB 90].
Experience with practical cases suggests that the tangent stiffness given by the following approximations

$$dP_{int}(t,\delta v) = \int_V \left(\delta \mathbf{D}\,\mathbf{C}^{ep} d\mathbf{D} - \frac{1}{2}\sigma\,\delta\left(2\mathbf{D}\,\mathbf{D} - \frac{\partial \mathbf{v}^T}{\partial \mathbf{x}}\frac{\partial \mathbf{v}}{\partial \mathbf{x}}\right)\right) dV \qquad (V.1.7)$$

provides an acceptable rate of convergence in most applications with real materials [HIB 90] and shall be used in our work since the symmetric properties of the stiffness matrix are retained. Indeed, it is the tangent stiffness which has been obtained by McMeeking and Rice's [MEE 75] formulation based on Hill's rate equation of virtual work [HIL 59] by using the co-

rotational rate of Kirchhoff instead of Cauchy ($\tau^{obj} = \sigma^{obj} + \sigma \operatorname{tr} \mathbf{D}$). Under the assumption of small elastic strains and incompressibility of plastic deformation this difference however will be barely detectable in computations.

V.1.3-Discretisation by interpolation functions

In the displacement based FE-method, the kinematic field quantities are expressed by a linear combination of interpolation functions N_i dependent on the element type and the nodal degrees of freedom, i.e.

$$\mathbf{u} = \mathbf{N}_N \hat{\mathbf{u}}^N \tag{V.1.8}$$

where $\hat{\mathbf{u}}^N$ are nodal variables. The summation convention is adopted for the upper case subscripts and superscripts which indicate nodal variables.
The virtual field, $\delta\mathbf{v}$, must be compatible with all kinematic constraints. Introducing the above interpolation constrains the displacement having a certain spatial variation, so that $\delta\mathbf{v}$ must also have the same spatial form:

$$\delta\mathbf{v} = \mathbf{N}_N \delta\hat{\mathbf{v}}^N \tag{V.1.9}$$

Finally $\delta\mathbf{D}$ is the virtual rate-of-deformation associated linearly with $\delta\mathbf{v}$. Hence, the interpolation assumption gives

$$\delta\mathbf{D} = \mathbf{B}_N \delta\hat{\mathbf{v}}^N \tag{V.1.10}$$

The matrices **N** and **B** are related by

$$B_{ij} = \frac{1}{2} N_{i,j} + \frac{1}{2} N_{j,i} \tag{V.1.11}$$

This discretization procedure by interpolation functions allows the virtual work [see also e.g. ZIE 79, BAT 86] to be written

$$P(t, \delta\mathbf{v}) = \delta\mathbf{v}^T \left(\int_V \mathbf{B}^T \boldsymbol{\sigma} dV - \int_S \mathbf{N}^T \mathbf{f} dS - \int_V \mathbf{N}^T \mathbf{b} dV \right) \tag{V.1.12}$$

For the Newton-Raphson algorithm, the Jacobian of this equation is needed: The variation of the virtual internal work under the assumption of (V.1.9) yields

$$dP_{int}(t, \delta\mathbf{v}) = \delta\mathbf{v}^T \left(\int_V \mathbf{B}^T \mathbf{C}^{ep} \mathbf{B} \, dV + \int_V \left(\mathbf{G}^T \boldsymbol{\sigma} \mathbf{G} - 2\mathbf{B}^T \boldsymbol{\sigma} \mathbf{B} \right) dV \right) \mathbf{du} \tag{V.1.13}$$

where **G** is the matrix of derivatives of the shape functions **N**.
The terms within the bracket form the stiffness matrix, where the first term is the conventional *small strain stiffness matrix*, except that, since the strains will always be nonlinear in displacement, the **B** matrix in this term will be a function of displacements. The second term is called the *initial stress matrix.*

The residual forces which have to be minimized during iterations are defined by

$$\mathbf{R}(\mathbf{u}) = \mathbf{F}_{ext} - \mathbf{F}_{int}(\mathbf{u}) \tag{V.1.14a}$$

with

$$\mathbf{F}_{int} = \int_V \mathbf{B}^T \sigma dV \quad \text{and} \quad \mathbf{F}_{ext} = \int_S \mathbf{N}^T \mathbf{f} dS + \int_V \mathbf{N}^T \mathbf{b} dV \tag{V.1.14b}$$

Therefore it holds

$$P(t,\delta v) = -\delta \mathbf{v}^T \mathbf{R}(\mathbf{u}) \quad \text{and} \quad dP(t,\delta v) = -\delta \mathbf{v}^T d\mathbf{R}(\mathbf{u}) \tag{V.1.15}$$

V.1.4-Elements

The specification of the interpolation function depends on the chosen element type. Today a large variety of elements is available. In this work only isoparametric quadratic quadrilateral elements have been used. The isoparametric family is a group of elements in which the interpolation functions are used to define the fields of initial coordinates as well as of displacements.

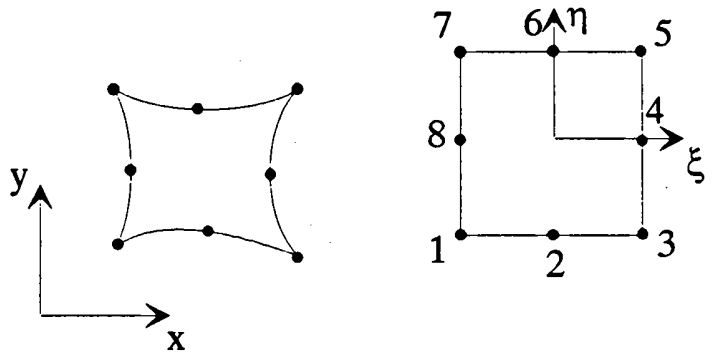

Fig. V.1.1. Isoparametric eight-node quadratic quadrilateral element in the global coordinate system (x,y) and in the local coordinate system (ξ,η).

The displacements are exactly represented in the nodes and approximated by a quadratic function between them. The interpolation function in terms of the local coordinates ξ and η is formulated by

$$N_i^e = \frac{1}{4}(1+\xi\xi_i)(1+\eta\eta_i)(\xi\xi_i + \eta\eta_i - 1) \qquad i = 1,3,5,7 \tag{V.1.19a}$$

$$N_i^e = \frac{\xi_i^2}{2}(1+\xi\xi_i)(1-\eta^2) + \frac{\eta_i^2}{2}(1+\eta\eta_i)(1-\xi^2) \qquad i = 2,4,6,8 \tag{V.1.19b}$$

V.2-The resolution of the non-linear problem

V.2.1-The Newton-Raphson scheme

The equation of global equilibrium is given in the classical form by

$$\mathbf{R}(\mathbf{u}(t)) = \mathbf{F}_{ext}(t) - \mathbf{F}_{int}(\mathbf{u}(t)) = 0 \tag{V.2.1}$$

In the elasto-plastic setting this equation is strongly nonlinear particularly for large deformation analysis. In this case a time discretization which implies that the external load is applied in increments is necessary to obtain the solution. For each load step eqn. (V.2.1) must be solved. The solution of the nonlinear set of equations requires iterative methods. In this context the Newton-Raphson method has been proved to be stable and efficient. Starting from the known and balanced configuration at time t_n, iterative solutions are obtained which converge to the exact solution at time $t_{n+1}=t_n+h_n$. The linear equation is derived from Taylor expansion series of order one:

$$\mathbf{R}\left(\mathbf{u}_{n+1}^{(i+1)}\right) \cong \mathbf{R}\left(\mathbf{u}_{n+1}^{(i)} + \delta\mathbf{u}_{n+1}^{(i)}\right) \cong \mathbf{R}\left(\mathbf{u}_{n+1}^{(i)}\right) + \left.\frac{\partial \mathbf{R}(\mathbf{u})}{\partial \mathbf{u}}\right|_{\mathbf{u}=\mathbf{u}_{n+1}^{(i)}} \delta\mathbf{u}_{n+1}^{(i)} \tag{V.2.2}$$

The total set of equations of the iterative scheme becomes

$$\mathbf{K}_T\left(\mathbf{u}_{n+1}^{(i)}\right)\delta\mathbf{u}_{n+1}^{(i)} = \mathbf{R}\left(\mathbf{u}_{n+1}^{(i)}\right) \tag{V.2.3}$$

and

$$\Delta\mathbf{u}_{n+1}^{(i+1)} = \Delta\mathbf{u}_{n+1}^{(i)} + \delta\mathbf{u}_{n+1}^{(i)} \tag{V.2.4a}$$

$$\mathbf{u}_{n+1}^{(i+1)} = \mathbf{u}_{n+1}^{(i)} + \Delta\mathbf{u}_{n+1}^{(i)} \tag{V.2.4b}$$

where $\Delta\mathbf{u}_{n+1}^{(0)} = \mathbf{0}$ and $\mathbf{u}_{n+1}^{(0)} = \mathbf{u}_n$ and the tangent stiffness matrix is given by

$$\mathbf{K}_T\left(\mathbf{u}_{n+1}^{(i)}\right) = -\left.\frac{\partial \mathbf{R}(\mathbf{u})}{\partial \mathbf{u}}\right|_{\mathbf{u}=\mathbf{u}_{n+1}^{(i)}} \tag{V.2.5}$$

It can be seen now using eqns. (V.1.13), (V.1.15) and (V.2.3) that this matrix is identical to

$$\mathbf{K}_T\left(\mathbf{u}_{n+1}^{(i)}\right) = \int_{V_{n+1}^{(i)}} \mathbf{B}^T \mathbf{C}_c^{ep} \mathbf{B}\, dV + \int_{V_{n+1}^{(i)}} \left(\mathbf{G}^T\boldsymbol{\sigma}\,\mathbf{G} - 2\mathbf{B}^T\boldsymbol{\sigma}\,\mathbf{B}\right) dV \tag{V.2.6}$$

V.2.2-Test of convergence

The convergence of the nonlinear iteration process is assumed to be satisfied if the relative norm of the residual forces becomes less than a specified tolerance value:

$$\left(\frac{\sum_{k=1}^{NTDF} \left(R_k\left(u_{n+1}^{(i+1)}\right)\right)^2}{\sum_{k=1}^{NTDF} \left(F_{ext,k}\right)^2} \right)^{\frac{1}{2}} \leq \text{Toler} \qquad \text{(V.2.7)}$$

where NTDF is the total number of degrees of freedom. In practice a sufficient tolerance for the residual forces based convergence is Toler=0.01.

V.2.3-The Numerical integration method

The exact determination of the consistent load vector and the tangent stiffness matrix by analytical integration may not be generally possible, hence numerical methods are adopted. Typically the Gauss-Legendre quadrature is employed for its high accuracy, which approximates the integrals by a linear combination of integrands within the integration points. The integration is performed in the natural coordinate system. The Jacobian matrix **J** of the transformation from the global coordinate system into the natural one for the considered element is given by

$$\mathbf{J}^{(e)} = \begin{bmatrix} \frac{\partial x}{\partial \xi} & \frac{\partial y}{\partial \xi} \\ \frac{\partial x}{\partial \eta} & \frac{\partial y}{\partial \eta} \end{bmatrix} = \begin{bmatrix} \sum_{i=1}^{NNE} \frac{\partial N_i^{(e)}}{\partial \xi} x_i^{(e)} & \sum_{i=1}^{NNE} \frac{\partial N_i^{(e)}}{\partial \xi} y_i^{(e)} \\ \sum_{i=1}^{NNE} \frac{\partial N_i^{(e)}}{\partial \eta} x_i^{(e)} & \sum_{i=1}^{NNE} \frac{\partial N_i^{(e)}}{\partial \eta} y_i^{(e)} \end{bmatrix} \qquad \text{(V.2.8a)}$$

and

$$\det \mathbf{J} = \frac{\partial x}{\partial \xi}\frac{\partial y}{\partial \eta} - \frac{\partial x}{\partial \eta}\frac{\partial y}{\partial \xi} \qquad \text{(V.2.8b)}$$

The stiffness matrix has been found as (see V.2.6)

$$\mathbf{K}_T\left(\mathbf{u}_{n+1}^{(i)}\right) = \int_{V_{n+1}^{(i)}} \left(\mathbf{T}_1 + \mathbf{T}_2\right) dV \qquad \text{(V.2.9a)}$$

with

$$\mathbf{T}_1 = \mathbf{B}^T \mathbf{C}^{ep} \mathbf{B} \quad \text{and} \quad \mathbf{T}_2 = \left(\mathbf{G}^T \boldsymbol{\sigma}\, \mathbf{G} - 2\mathbf{B}^T \boldsymbol{\sigma}\, \mathbf{B}\right) \qquad \text{(V.2.9b)}$$

It can now be written in terms of the natural coordinates. Considering only one element, the element stiffness matrix becomes

$$\mathbf{K}^e{}_T = \int_{-1}^{+1}\int_{-1}^{+1} \left(\mathbf{T}^e{}_1 + \mathbf{T}^e{}_2\right) t^e \det \mathbf{J}^e \, d\xi d\eta \qquad \text{(V.2.10)}$$

where t^e is the thickness of the element. The numerical integration by the Gaussian quadrature for the considered quadrilateral element with NGPxNGP sampling points leads to

$$\mathbf{K}^e{}_T = \sum_{p=1}^{NGP}\sum_{q=1}^{NGP} \left(\mathbf{T}^e{}_1 + \mathbf{T}^e{}_2\right)\Big|_{\bar{\xi}_p, \bar{\eta}_p} t^e \det \mathbf{J}^e \, W_p W_q \qquad \text{(V.2.11)}$$

where W_p and W_q are weighting factors and $\bar{\xi}_p, \bar{\eta}_p$ the local coordinates of the sampling points. The consistent load vector will be evaluated in the same way.

Remark
It should be noted that an n-point rule integrates any polynomial of degree x^{2n-1} or less, exactly [OWE 77]. Accordingly, in view of the chosen element full integration is achieved by a (3x3)-Gauss rule [BAT 86]. However, experience has shown that in certain cases reduced integration (2x2-Gauss rule) has to be preferred: For example at elevated plastic deformations, the results by full integration exhibit an excessively stiff behaviour (*locking effect*) [see e.g. NAG 81].

V.2.4-The equation solver

The set of equations in (V.2.3) is solved using the frontal technique [OWE 77]. It belongs to the class of direct methods. The frontal method can be considered as a particular technique for first assembling finite element stiffness and nodal forces into a global stiffness matrix and load vector and then solving for the unknown displacements by means of a Gaussian elimination and back-substitution process [OWE 77]. In particular this method offers two main advantages:
(i) The size of the array for the global stiffness has been minimised since assembling and equation elimination are simultaneously performed.
(ii) Nodal numbering is irrelevant, instead the ordering of elements is important.
However, since the values are continuously stored and read from disc files, the effective CPU-time increases. The implementation of an alternative solver which aims to minimise CPU-time is in preparation [BRA 94]. This solver is based on the conjugate gradient method with preconditioning. The latter aims to minimise the space for the storage of the global stiffness matrix stocking only the non-zero values within the bandwidth.

V.3-The constitutive model under consideration

V.3.1-Linear Elasticity for isotropic and orthotropic materials

In linear elasticity the stresses and strains are related through the compliance matrix by

$$\boldsymbol{\varepsilon} = \mathbf{M}\,\boldsymbol{\sigma} \tag{V.3.1a}$$

or inversely through the constitutive matrix by

$$\boldsymbol{\sigma} = \mathbf{C}^e\,\boldsymbol{\varepsilon} \tag{V.3.1b}$$

with $\mathbf{M}^{-1}=\mathbf{C}^e$ and where $\boldsymbol{\varepsilon}$ and $\boldsymbol{\sigma}$ are given in vector form for plane states of stresses resp. strains by

$$\boldsymbol{\sigma} = (\sigma_{11}, \sigma_{22}, \sigma_{12})^T \quad \text{or} \quad \boldsymbol{\varepsilon} = (\varepsilon_{11}, \varepsilon_{22}, 2\varepsilon_{12})^T \tag{V.3.1c}$$

where the indices 1 and 2 are associated to the principal axis of orthotropy. The identification of principal directions is necessary when the material exhibits different mechanical properties under orthogonal directions (orthotropic behaviour). The orthotropy may be initially present in

the material due to the anisotropic microstructure (banded structure caused by the rolling process) or may be induced by anisotropic irreversible processes during deformation (under low triaxiality values by plastic deformation or damage).
The compliance matrix **M** is given for plane stress by

$$\mathbf{M} = \begin{pmatrix} \frac{1}{E_1} & -\frac{\nu_{12}}{E_1} & 0 \\ -\frac{\nu_{12}}{E_1} & \frac{1}{E_2} & 0 \\ 0 & 0 & \frac{1}{G_{12}} \end{pmatrix} \qquad \text{(V.3.2a)}$$

and for plane strains

$$\mathbf{M} = \begin{pmatrix} \frac{1-(\nu_{13}^2 E_3)/E_1}{E_1} & -\frac{\nu_{12}+(\nu_{13}\nu_{23}E_3)/E_2}{E_1} & 0 \\ -\frac{\nu_{12}+(\nu_{13}\nu_{23}E_3)/E_2}{E_1} & \frac{1-(\nu_{23}^2 E_3)/E_2}{E_2} & 0 \\ 0 & 0 & \frac{1}{G_{12}} \end{pmatrix} \qquad \text{(V.3.2b)}$$

The global coordinate system (x,y,z) may not be identical with the principal axis of orthotropy (1,2,3); hence a transformation of the compliance matrix is necessary. For this purpose the transformation matrix **T** is used

$$\mathbf{T} = \begin{pmatrix} \cos\beta & \sin\beta \\ -\sin\beta & \cos\beta \end{pmatrix} \qquad \text{(V.3.3)}$$

where β denotes the angle between the global coordinate-system and the principal axis of orthotropy [SCH 91].

Calibration of orthotropic elasticity
For orthotropic behaviour the following material parameters have to be known:
E_1, E_2, E_3, ν_{12}, ν_{13}, ν_{23} and G_{12}.

V.3.2-Rate-independent plasticity for isotropic and orthotropic materials

The main ingredients of the theory of plasticity have already been described in chapter III.4. Here, emphasis is rather placed on its numerical implementation. In particular an adequate elastic-plastic model has to meet three requirements:
(a) an explicit stress-strain relation before the onset of plastic deformation (see previous chapter)
(b) a yield criterion which allows for the separation of elastic from plastic deformation
(c) a flow rule which describes the evolution of the plastic strains

Initial Yielding - The Yield criterion

The yield function has been defined in (III.4.11) as

$$F(\sigma,k) = f(\sigma) - k(\kappa) \tag{V.3.4}$$

It mainly depends on the stress state σ and the material parameter k which in turn is a function of the hardening parameter κ. For F<0 elastic behaviour is assumed, for F=0 plastic behaviour, F>0 is physically not allowed.

Isotropic behaviour:

Due to physical reasons any yield criterion must be independent of the orientation of the coordinate system and therefore it is a function of the three invariants only

$$J_1 = \sigma_{ii} \tag{V.3.5a}$$

$$J_2 = \frac{1}{2}\sigma_{ij}\sigma_{ij} \tag{V.3.5b}$$

$$J_3 = \frac{1}{3}\sigma_{ij}\sigma_{jk}\sigma_{ki} \tag{V.3.5c}$$

In addition experiments have yielded that plastic deformation of a continuum is largely independent of the hydrostatic stress state. Consequently the yield criterion may only be of the form

$$f(\sigma) = f\left(J_2^D, J_3^D\right) \tag{V.3.6}$$

where J_2^D and J_3^D are the second and third invariants of the deviatoric stresses. Today the mostly adopted yield criterion to describe isotropic metal plasticity is that of v. Mises also known as J_2 flow theory: It postulates that yielding occurs when the (recoverable) elastic energy of distortion (J_2^D) reaches a critical value:

$$F(\sigma,k) = \sigma_v - \sqrt{3}k = \sqrt{3J_2^D} - \sqrt{3}k = 0 \tag{V.3.7}$$

where σ_v is termed the effective or equivalent stress.

Orthotropic behaviour:

Hill has extended the yield criterion of v. Mises to orthotropic materials. He introduced additional factors which differently weight the plastic deformation under orthogonal directions. The yield criterion becomes

$$\begin{aligned} 2f(\sigma_{ij}) &= F\cdot(\sigma_{22}-\sigma_{33})^2 + G\cdot(\sigma_{33}-\sigma_{11})^2 + H\cdot(\sigma_{11}-\sigma_{22})^2 \\ &+2L\cdot\sigma_{23}^2 + 2M\cdot\sigma_{31}^2 + 2N\cdot\sigma_{12}^2 = 1 \end{aligned} \tag{V.3.8a}$$

and

$$F(\sigma,\kappa) = f(\sigma,\kappa) - \frac{1}{2} = 0 \tag{V.3.8b}$$

The coefficients F, G, H, L, M and N are dependent of the uniaxial yield stresses under orthogonal directions (σ_{y1}, σ_{y2}, σ_{y3}) and of the shear yield stresses (τ_{y12}, τ_{y23}, τ_{y31}).

$$2F = \frac{1}{\sigma_{y_2}^2} + \frac{1}{\sigma_{y_3}^2} - \frac{1}{\sigma_{y_1}^2} \qquad 2L = \frac{1}{\tau_{y_{23}}^2}$$
$$2G = \frac{1}{\sigma_{y_3}^2} + \frac{1}{\sigma_{y_1}^2} - \frac{1}{\sigma_{y_2}^2} \qquad 2M = \frac{1}{\tau_{y_{31}}^2} \qquad \text{(V.3.8c)}$$
$$2H = \frac{1}{\sigma_{y_1}^2} + \frac{1}{\sigma_{y_2}^2} - \frac{1}{\sigma_{y_3}^2} \qquad 2N = \frac{1}{\tau_{y_{12}}^2}$$

Both yield criteria are illustrated in the stress space below

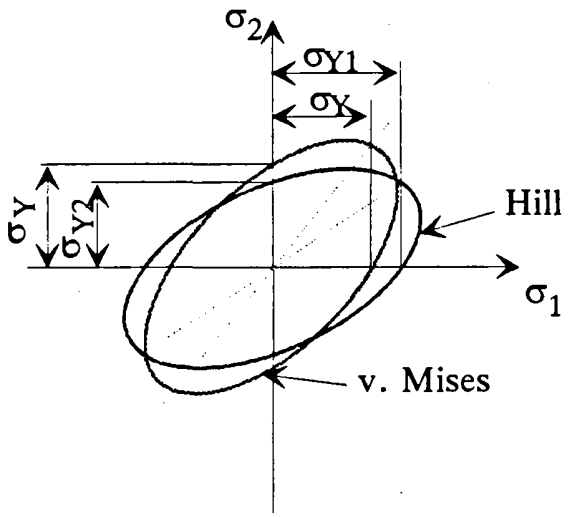

Fig V.3.1. Flow curves in the σ_1-σ_2-plane

If the coefficients are chosen to be L=M=N=3F=3G=3H the yield criterion reduces to that of v. Mises for isotropic material behaviour.

Post Yielding - The normality rule and isotropic hardening

The hardening function characterizes the evolution of the yield surface. In the context of this work only isotropic hardening is considered. This restriction is justified since numerical simulations are only performed under monothonic loading. To describe the progressive development of the yield surface, the yield stress is associated to the plastic deformation by means of the hardening parameter κ which in turn is related to the effective or equivalent plastic strain:

$$\dot{\kappa} = \dot{\varepsilon}_v^p = \sqrt{\frac{2}{3}\dot{\varepsilon}_{ij}^p \dot{\varepsilon}_{ij}^p} \qquad \text{(V.3.9)}$$

The plastic strain increments are assumed to be proportional to the stress gradient of a quantity called the plastic potential Q, so that

$$\dot{\varepsilon}_{ij}^p = \dot{\lambda}\frac{\partial Q}{\partial \sigma_{ij}} \qquad \text{(V.3.10)}$$

$\dot{\lambda}$ is termed the plastic multiplier and is obtained with the aid of the loading-unloading criterion. This can be expressed in Kuhn-Tucker form as

$$F(\sigma,\kappa) \le 0 \qquad \text{(V.3.11a)}$$

$$\dot{\lambda} \ge 0 \qquad \text{(V.3.11b)}$$

$$F\dot{\lambda} = 0 \qquad \text{(V.3.11c)}$$

Along any process of loading, conditions (V.3.11) must hold simultaneously. During plastic flow e.g. it holds $\dot{\lambda}>0$ which, in view of (V.3.11c) enforces fulfillment of the yield criterion F=0. From this latter constraint, along a process of plastic loading the so-called plastic consistency condition is obtained

$$\dot{F} = \frac{\partial F}{\partial \sigma}\dot{\sigma} + \frac{\partial F}{\partial \kappa}\dot{\kappa} = 0 \qquad \text{(V.3.12)}$$

Eqn. (V.3.10) is termed the flow rule since it governs the plastic flow for yielding. In the context of this work an associated flow rule is considered which assumes that the plastic potential is equal to the yield function F. The associated flow rule is generally accepted to hold for metal plasticity. Therefore (V.3.10) becomes

$$\dot{\varepsilon}^p_{ij} = \dot{\lambda}\frac{\partial F}{\partial \sigma_{ij}} \qquad \text{(V.3.13)}$$

and is termed the normality condition. The normality condition holds for both, isotropic and ortho-tropic behaviour. For the latter one it follows

$$\begin{aligned}
\dot{\varepsilon}^p_{11} &= \dot{\lambda}\left[H(\sigma_{11}-\sigma_{22}) + G(\sigma_{11}-\sigma_{33})\right] & \dot{\varepsilon}^p_{23} &= \dot{\lambda}\, L\, \sigma_{23} \\
\dot{\varepsilon}^p_{22} &= \dot{\lambda}\left[F(\sigma_{22}-\sigma_{33}) + H(\sigma_{22}-\sigma_{11})\right] & \dot{\varepsilon}^p_{31} &= \dot{\lambda}\, M\, \sigma_{31} \\
\dot{\varepsilon}^p_{33} &= \dot{\lambda}\left[G(\sigma_{33}-\sigma_{11}) + F(\sigma_{33}-\sigma_{22})\right] & \dot{\varepsilon}^p_{12} &= \dot{\lambda}\, N\, \sigma_{12}
\end{aligned} \qquad \text{(V.3.14)}$$

Calibration of orthotropic plasticity

For plane problems initial yielding has to be identified by the initial yield stress σ_{Y0} for isotropic material and by the initial values F_0, G_0, H_0, N_0 as well as the uniaxial stress-strain curve of the first principal axis of orthotropy. Isotropic hardening is characterized by either linear hardening (plastic tangent modulus has to be entered) or by piece-wise linear hardening (discrete stress-strain couples have to be entered) [SCH 91].

V.3.3-Integration of the constitutive model at elastic-finite-plastic strains

V.3.3.1-KINEMATIC APPROXIMATIONS

The deformation path during the resolution of the set of unknown equations within one time step is not a priori known, only the displacements at the beginning and the end of the time step are known. The derivation of kinematic measures (e.g. for **F** or **L**) from the displacements requires therefore kinematic approximations. The choice of these approximations is not arbitrary, they are constrained by the principle of frame invariance. Here three numerical

algorithm schemes are presented using either the material time differentiation of Zaremba-Jaumann or of Green-Naghdi [DAB 94].

1st kinematical Approximations (KA1)
The first kinematical concept has been inspired by Hughes and Winget [HUG 80] using the Jaumann derivative. It is assumed that the deformation gradient remains linear within the time step, the rate-of deformation and the spin being constant and calculated at the mid-time interval. The following steps have to be performed:
1. calculate the deformation gradient at the middle and at the end of the time step

$$\mathbf{F}_{n+1} = \frac{\partial \mathbf{x}_{n+1}}{\partial \mathbf{X}}, \quad \mathbf{F}_{n+\frac{1}{2}} = \frac{1}{2}(\mathbf{F}_{n+1} + \mathbf{F}_n) = \frac{\partial(\frac{1}{2}(\mathbf{x}_{n+1} + \mathbf{x}_n))}{\partial \mathbf{X}} \tag{V.3.15}$$

2. estimate the velocity gradient $\mathbf{L}$ by

$$\mathbf{L} = \frac{1}{\Delta t}\Delta \mathbf{F}\mathbf{F}^{-1}_{n+\frac{1}{2}} \tag{V.3.16a}$$

where

$$\Delta \mathbf{F} = (\mathbf{F}_{n+1} - \mathbf{F}_n) = \frac{\partial(\mathbf{x}_{n+1} - \mathbf{x}_n)}{\partial \mathbf{X}} \tag{V.3.16b}$$

3. estimate the rate of deformation and rotation by the Cauchy-Stokes decomposition

$$\begin{aligned} \mathbf{D} &= \frac{1}{2}(\mathbf{L} + \mathbf{L}^T) \\ \mathbf{W} &= \frac{1}{2}(\mathbf{L} - \mathbf{L}^T) \end{aligned} \tag{V.3.17}$$

4. calculate the rotation of the local coordinate system $\mathbf{Q}_{n+1}$ by use of the approximation proposed by Hughes and Winget [HUG 80]

$$\mathbf{Q}_{n+1} = (\mathbf{I} - \frac{1}{2}\mathbf{W})^{-1}(\mathbf{I} + \frac{1}{2}\mathbf{W})\mathbf{Q}_n \tag{V.3.18}$$

5. transform the stresses and the deformation rates in the local coordinate system

$$\begin{aligned} \overline{\boldsymbol{\sigma}}_n &= \mathbf{Q}_n{}^T \boldsymbol{\sigma}_n \mathbf{Q}_n \\ \overline{\mathbf{D}} &= \mathbf{Q}_{n+1}{}^T \mathbf{D} \mathbf{Q}_{n+1} \end{aligned} \tag{V.3.19}$$

2nd kinematical Approximations (KA2)
By use of the Green-Naghdi stress rate the only modification in the above presented scheme is found due to the new definition of the co-rotational coordinate system. Here we use the rotation $\mathbf{R}$ obtained by the polar decomposition theorem of $\mathbf{F}$ [see Appendix B.3]

$$\mathbf{F}_{n+\frac{1}{2}} = \mathbf{R}_{n+\frac{1}{2}}\mathbf{U}_{n+\frac{1}{2}}, \quad \mathbf{F}_{n+1} = \mathbf{R}_{n+1}\mathbf{U}_{n+1} \tag{V.3.20}$$

3rd kinematical Approximations (KA3)
Several authors [e.g. BRA 86] have assumed the rate-of-deformation being constant within one time step. This approximation supposes that the right pure stretch tensor **U** calculated at the mid-time step relative to the balanced configuration remains his principal axis. The following steps have to be performed [WEB 90]:
1. calculate the relative deformation gradient

$$ {}^{n}\mathbf{F}_{n+1} = \mathbf{F}_{n+1}\mathbf{F}_{n}^{-1} = \frac{\partial \mathbf{x}_{n+1}}{\partial \mathbf{x}_{n}} \tag{V.3.21} $$

2. perform the polar decomposition [see Appendix B.3]

$$ {}^{n}\mathbf{F}_{n+1} = {}^{n}\mathbf{R}_{n+1}\,{}^{n}\mathbf{U}_{n+1} \tag{V.3.22} $$

3. estimate the rate of deformation

$$ \overline{\mathbf{D}} = \frac{2}{\Delta t}\left({}^{n}\mathbf{U}_{n+1} - \mathbf{I}\right)\left({}^{n}\mathbf{U}_{n+1} + \mathbf{I}\right)^{-1} \tag{V.3.23} $$

Consistency, stability and objectivity conditions for the presented algorithms were proved by Dabounou [DAB 94].

V.3.3.2-LOCAL INTEGRATION OF ELASTO-PLASTIC CONSTITUTIVE LAWS
Unlike elasticity, rate-independent plasticity is characterized by the rate form of constitutive equations. This is realized as discussed earlier by an incremental procedure. Accordingly, numerical integration of the rate constitutive equations over a discrete sequence of time steps has to be performed. The problem to be addressed is therefore to determine $\boldsymbol{\varepsilon}_{n+1}$, $\boldsymbol{\varepsilon}^{p}_{n+1}$, $\boldsymbol{\sigma}_{n+1}$ and κ_{n+1} of the unknown configuration V_{n+1} by updating the known state variables $\boldsymbol{\varepsilon}_{n}$, $\boldsymbol{\varepsilon}^{p}_{n}$, $\boldsymbol{\sigma}_{n}$ and κ_{n} associated with the balanced configuration V_{n}. In this process the displacements **u** defining the geometric update $V_n \rightarrow V_{n+1}$ are known (see V.2). The computation of the total strain increments from the displacement increments have been discussed in the last chapter. It remains to update the stresses and the internal variables by integration along the deformation path in an iterative manner. This integration can only be exact in the case of perfect plasticity. When the material exhibits strain hardening, different integration algorithms may be used. Most of them are based on an *operator splitting (elastic-plastic) methodology*, where the integration is performed in two steps: an *elastic predictor* and a subsequent *plastic corrector* step. This procedure may become more clear considering the so-called *generalized trapezoidal* integration algorithm introduced by Ortiz and Popov [ORT 85]. It is formulated as (for simplicity the integration of internal variables has not been included)

$$ \boldsymbol{\sigma}_{n+1} = \mathbf{C}^{e}\left(\boldsymbol{\varepsilon}_{n+1} - \boldsymbol{\varepsilon}^{p}_{n+1}\right) \tag{V.3.24a} $$

$$ \boldsymbol{\varepsilon}^{p}_{n+1} = \boldsymbol{\varepsilon}^{p}_{n} + \dot{\lambda}\left[(1-\alpha)\frac{\partial f}{\partial \boldsymbol{\sigma}}\Big|_{t_n} + \alpha\frac{\partial f}{\partial \boldsymbol{\sigma}}\Big|_{t_{n+1}}\right] \tag{V.3.24b} $$

$$ F_{n+1} = 0 \tag{V.3.24c} $$

where α is an adjustable parameter ranging from 0 to 1. The algorithm becomes implicit for $\alpha > 0$ and provides unconditionally stability for $\alpha \geq 0.5$. A revealing geometric interpretation of the algorithm can be given by rewriting it as [ORT 85]

$$\sigma_{n+1} = \sigma_{n+1}^{trial} - \dot{\lambda}\, C^e \left[(1-\alpha) \frac{\partial f}{\partial \sigma}\Big|_{t_n} + \alpha \frac{\partial f}{\partial \sigma}\Big|_{t_{n+1}} \right] \qquad \text{(V.3.25a)}$$

$$F_{n+1} = 0 \qquad \text{(V.3.25b)}$$

with

$$\sigma_{n+1}^{trial} = \sigma_n + C^e(\varepsilon_{n+1} - \varepsilon_n) \qquad \text{(V.3.25c)}$$

being the elastically updated *stress predictor* termed as *trial stress*. A graphical illustration of this algorithm is given in Fig. V.3.2

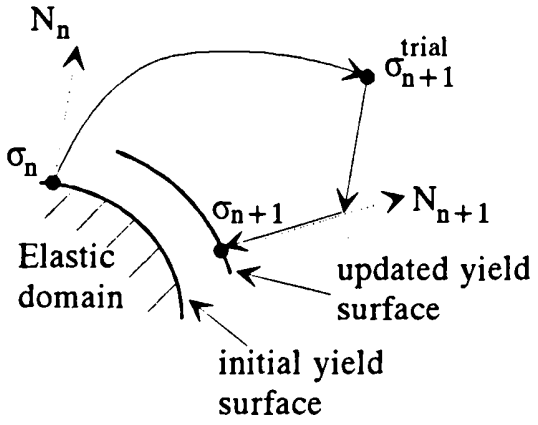

Fig. V.3.2. Geometric interpretation of the generalized trapezoidal rule [ORT 85]

It can be seen from this figure that the stress update is performed in two steps (operator split). In the first step (*elastic predictor*) a trial stress state is calculated by integration of the elastic stress-strain relations. The elastic predictor is then subsequently mapped onto a suitably updated yield surface, thus restoring plastic consistency (*plastic corrector*). The reprojection step itself is performed in two substeps (for $0<\alpha<1$): First, the stresses are reduced along the initial plastic flow direction $\frac{\partial f}{\partial \sigma}\Big|_{t_n}$. The stresses so obtained are then projected along the final plastic flow direction $\frac{\partial f}{\partial \sigma}\Big|_{t_{n+1}}$ [ORT 85].

This algorithm provides a general framework for the integration algorithms implemented in FE-Codes. Indeed, the three most employed algorithms may be viewed to some extent as particular cases of the generalized trapezoidal algorithm. They are known as:

1- tangent stiffness-radial corrector [e.g. OWE 80] (explicit forward Euler scheme for $\alpha=0$)
2- mean normal or secant stiffness [RIC 73] (for v. Mises associated perfect plasticity identical with generalized trapezoidal algorithm for $\alpha=0.5$)
3- elastic predictor-return mapping (plastic corrector) [e.g. SIM 85, SIM 86] (implicit backward Euler scheme for $\alpha=1$)

1-Tangent stiffness-radial corrector
The tangent stiffness method has been used in most FE-Codes for a long time. In its original form it describes an Euler one-step-forward scheme. This method is explicit and to this conditionally stable. Its stability limit for a strain increment has been proved by Nagtegaal and de Jong [NAG 81] and is equal to twice the elastic strain up to yield. Even within this stability limit, the time step strongly influences the accuracy of the stress update. To overcome this inconvenience, the time step is subdivided into a certain number of subincrements. Integration is then performed within each subincrement (multistepping). The number of the subincrements are determined in an empirical manner and each substep is assumed to be of the same size. In general the updated stresses at the end of the time step do not satisfy the yield criterion. Therefore they are corrected through a scaling factor in order to be reprojected onto the yield surface. In the case of transition from elastic to plastic behaviour within one strain increment, it is necessary to determine firstly the portion of the purely elastic stress increment that lies on the initial yield surface. To this a factor R is determined empirically defining the full elastic region. This method is implemented in the FE-Code originally developed by Owen and Hinton [OWE 80] (see Appendix B.1).
Summing up this algorithm suffers from the following drawbacks:
a) It is conditionally stable
b) The determination of the portion of the purely elastic stress increment is done in an empirical manner as well as for the number of subincrements
c) Stress correction is needed to reduce the stresses to the yield surface

Sloan [SLO 87] modifies the first order Euler scheme to become a second order one. With this it is possible to control the error in the integration process by selecting the size of each substep automatically as the integration proceeds over each time interval. In addition this algorithm does not require any form of stress correction. Since it is believed that this algorithm improves accuracy and stability of the integration process, it has been additionally implemented into the FE-Code "CRACKAN" (see Appendix B.1).

2-Mean normal or secant stiffness:
In this method originally proposed by Rice and Tracey [RIC 73] the flow rule is chosen such that the yield criterion is satisfied exactly at the end of the increment. It belongs to the class of implicit algorithms and to this it is unconditionally stable. However, this does not hold in the case of plane stress [NAG 81] and is for this reason not further investigated.

3-Elastic predictor-return mapping:
The concept of return mapping dates back to the early work of Wilkins [WIL 64] for v. Mises ideal plasticity. It has been extended later on for hardening materials by Krieg and Key [KRI 76]. For associated, linear hardening v. Mises plasticity this algorithm is known as *radial return algorithm*. Unlike the first two algorithms, the determination of the "fully elastic term" is not required, instead this is performed automatically at the end of the plastic corrector step. The implicit integration in the plastic corrector phase is a trivial task in the case of perfect plasticity, but demands for an iterative solution traditionally of Newton-Raphson type for hardening materials. The general 3D-radial return algorithm is trivially adapted to a plane strain formulation but this is in contrast with the plane stress situation where the plane stress condition forces a non-trivial constraint on the return algorithm [SIM 86]. This algorithm is known to be effective and robust. In particular for large strain increments it gives the most accurate results compared with other algorithms. In addition since a consistent analytical expression for the elasto-plastic matrix has been developed (see next chapter), this algorithm is very efficient and has been for this reason additionally incorporated into the FE-Code "CRACKAN" (see Appendix B.1).

A flowchart for the overall general update procedure as present now in "Crackan" is listed below:

(i) Geometric update:

$$\mathbf{D}_{n+1} = \mathbf{D}_{n+1}(\mathbf{D}_n, \mathbf{u}_{n+1})$$

The exact calculation depends of the chosen kinematic approximation (see previous chapter)

(ii) Transformation of the stresses and strain rates into the corotational coordinate system ↓

$$\bar{\boldsymbol{\sigma}}_n = \mathbf{Q}_n{}^T \boldsymbol{\sigma}_n \mathbf{Q}_n$$
$$\bar{\mathbf{D}} = \mathbf{Q}_{n+1}{}^T \mathbf{D} \mathbf{Q}_{n+1}$$

(iii) Elastic predictor: ↓

Calculation of the trial stress by
$$\bar{\boldsymbol{\sigma}}_{n+1}^{trial} = \bar{\boldsymbol{\sigma}}_n + \mathbf{C}^e \bar{\mathbf{D}}_{n+1}$$

(iv) Check for yielding: ↓

$$F(\bar{\boldsymbol{\sigma}}_{n+1}^{trial}, \kappa_n) \le 0 \ ?$$

↓ Yes

$\bar{\boldsymbol{\sigma}}_{n+1} = \bar{\boldsymbol{\sigma}}_{n+1}^{trial}$, $\boldsymbol{\varepsilon}_{n+1}^p = \boldsymbol{\varepsilon}_n^p$, $\kappa_{n+1} = \kappa_n$
goto (vii)

No ↓

goto (v)

(v) Plastic correctors (see Appendix B.1): ↓

	(v.a)	backward Euler scheme (Radial return, for isotropic v. Mises plasticity) + calculation of the consistent tangent operator
or	(v.b)	forward Euler scheme
or	(v.c)	modified forward Euler scheme

(vi) Plastic update : ↓

$$\bar{\boldsymbol{\sigma}}_n \to \bar{\boldsymbol{\sigma}}_{n+1}, \quad \boldsymbol{\varepsilon}_n^p \to \boldsymbol{\varepsilon}_{n+1}^p, \quad \kappa_n \to \kappa_{n+1}$$

(vii) Retransformation of the stresses into the global coordinate system: ↓

$$\boldsymbol{\sigma}_{n+1} = \mathbf{Q}_{n+1} \bar{\boldsymbol{\sigma}}_{n+1} \mathbf{Q}_{n+1}{}^T$$

Remark on point (i) and (iii) of the flow chart
Traditionally, the total stress increment over the load increment is computed by summing up the increment stresses over each iteration. Since the intermediate configurations within the iterations (except the last one) are not balanced and therefore the stress increments neither, this algorithm leads to a very *path-dependent* solution. In this case $\mathbf{D}_{n+1}$ is obtained from $\delta\mathbf{u}$ (see V.2.1).
In a more precise manner $\mathbf{D}_{n+1}$ is obtained from the total displacement increment $\Delta\mathbf{u}$. Then the stresses are updated from the balanced configuration of the last iteration step of the previous increment. However, this might lead to convergence problems for large load steps as might occur after discrete damage events.
The choice for either one solution scheme should therefore depend on the considered problem.

V.3.3.3-EVALUATION OF THE ELASTO-PLASTIC MATRIX $\mathbf{C}^{EP}$

The elasto-plastic matrix is introduced by

$$\dot{\sigma} = \mathbf{C}^{ep}\,\mathbf{D} \qquad \text{(V.3.26)}$$

The elasto-plastic matrix gives a main contribution to the first part of the global stiffness matrix (see V.1). Hence, a correct evaluation of the elasto-plastic matrix is essential for the convergence rate and stability. The most applied approaches to evaluate the elasto-plastic matrix $\mathbf{C}^{ep}$ [ZHU 92] fall into the following three groups:

1-*Continuum tangent operator*. This approach has been applied for a long time and still exists in many FE-Codes [see e.g. OWE 80]. The elasto-plastic matrix $\mathbf{C}^{ep}$ is here obtained from the *continuum* rate constitutive model by enforcement of the consistency condition (dF=0) (see Annex B.2). The use of the continuum tangent operator leads to only a linear asymptotic rate of convergence for the global iteration [NAG 82, SIM 85]. In addition for certain constitutive models other than plasticity (e.g. viscoplasticity) a plastic consistency condition does not exist and therefore neither a continuum tangent.

2-*Consistent tangent operator*. This approach was firstly introduced within the context of the FE-method by Simo and Taylor [SIM 85] for rate-independent elastoplasticity. In their paper they demonstrated that *consistency* between the tangent operator and the used integration algorithm plays a crucial role in preserving the quadratic rate of asymptotic convergence of iterative solution schemes based upon Newton's method. However, obviously the construction of this tangent operator depends on the specific integration algorithm. A closed form for certain algorithms, among them sub-incremental techniques may be difficult to establish. The tangent operator consistent with the radial return algorithm has been implemented into the FE-Code CRACKAN (see Annex B.2).

3-*Numerical perturbation technique*. This method consists in applying a small perturbation on each component of $\mathbf{D}$ and to calculate the respective stresses by the chosen integration scheme. This allows to construct $\mathbf{C}^{ep}$ column by column [ZHU 92]. The advantage of this approach is its generality. A main drawback is however, the elevated computational cost and has for this reason not been considered here.

V.4-Characterization of local failure

V.4.1-Particle fracture

The theoretical model for particle fracture has already been presented in chapter IV. Here attention is given to the numerical implementation. Particle fracture is explained to occur if the normal stress in the HP reaches the critical value. Keeping the complexity of programming reasonable, possible crack paths within the HP are predefined, therefore the HP are subdivided into subgroups. Each subgroup consists of two halves containing several elements. The line separating the two halves characterizes the possible crack path. The local failure criterion is evaluated for each subgroup by calculating a weighted total value (Fig.V.4.1). The normal direction is derived from the coordinates of the edge nodes of the subgroup. The stress tensor is transformed into this direction using the transformation matrix introduced in eqn. (V.3.3).

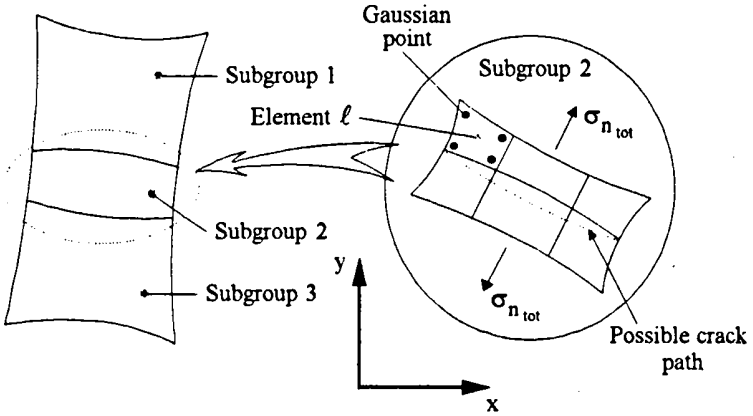

Fig. V.4.1. Schematic of particle cracking

If the criterion is satisfied by

$$\sigma_{n_{tot}} = \frac{W_{lm} \cdot \sigma_{lm}}{\sum_{l}\sum_{m} W_{lm}} \geq \sigma_c \qquad (V.4.1)$$

where W_{lm} are weight functions, additional nodes are introduced to automatically simulate microcracking [GRO 92]. In order to better account for stress distribution effects the next load increment is applied with $\Delta F=0$.

V.4.2-Interfacial failure

Interfacial failure may be simulated for pure mode I and mode II (see chapter IV). The interface is taken as an orthotropic layer. Initially the interface possesses the isotropic elastic-plastic characteristics of the matrix. Interfacial failure is modelled by replacing the elastic-plastic properties within this layer by an anisotropic equivalent layer with modified properties such that the conditions on the created free (or sliding surfaces) surfaces are satisfied.
The evaluation of the fracture criteria under mode I and mode II requires a transformation of the stress components in normal or tangential direction of the interface layer. This is realized with the help of the transformation matrix **T** (see V.3.2). The angle beta in this matrix is determined by the edge node coordinates of the interface element. In order to reduce the

complexity of programming, it is assumed that the side length parallel to the interface is greater than that perpendicular to it (Fig. V.4.2).

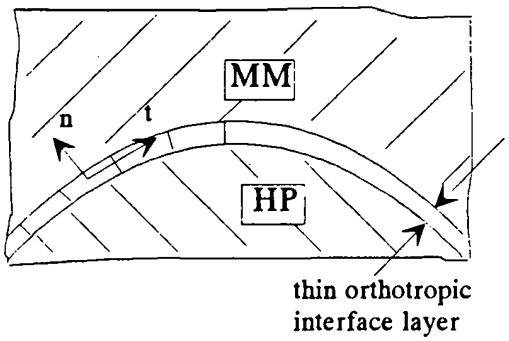

V.4.2. Schematic of the interface layer

Interfacial failure under mode I is assumed to occur if

$$\sigma_{nn} \geq \sigma_{I_c} \tag{V.4.2a}$$

and under mode II if

$$\sigma_{nt} \geq \sigma_{II_c} \tag{V.4.2b}$$

The global elastic and the global compliance matrix is in general a function of the orthotropic elastic moduli expressed in the principal axis of orthotropy and of the transformation angle β between the global coordinate system and the principal axis of orthotropy:

$$\mathbf{C}^e_{glo} = f\left(\mathbf{C}^e_{loc}(E_1, E_2, E_3, \nu_{12}, \nu_{23}, \nu_{31}, G_{12}), T(\beta)\right) \tag{V.4.3}$$

The modification of these moduli depends of the failure mode:

1- Mode I (tensile) failure is simulated setting the Young's modulus perpendicular to the interface and the shear modulus equal to zero: $E_1=G_{12}=0$.
2- Mode II (shear) failure is simulated by setting: $E_1=G_{12}=0$ *under tensile conditions* and $G_{12}=0$ *under conditions of pressure* where friction effects are neglected.
In addition the angle beta (giving the orientation of the interface contour with respect to the global coordinate system) has to be specified for each interface element, which has been failed.

However, from numerical point of view these conditions are not sufficient. The only change of the elastic moduli does not provoke iterations within the next load increment. Hence a stress distribution does not take place. Several approaches for the reduction of stresses and elastic moduli have been tried. It has been observed that only if one reduces first the respective stress components (σ_{nn} equivalent to E_1, and σ_{nt} equivalent to G_{12}) and subsequently the elastic moduli, stress distribution does take place in a reasonable manner. To improve the convergence stability of this algorithm four subsequent load free increments are applied. In the first one the respective stress components are reduced by factor 0.5. In the second they are set to zero, in the third the respective elastic moduli are reduced by the factor 0.5 and in the last step they are reduced to quasi-zero.

V.4.3-Ductile matrix damage

The local processes of void initiation, growth and coalescence at secondary (annealed) carbides is averaged within the metal matrix. It is assumed that these processes lead locally (that means within one element) to material failure. The chosen fracture criterion is derived from the local damage model of Rice and Tracey (see Chapter IV). If

$$D_i = \int_0^{\varepsilon_v^p} \frac{\exp(1.5\cdot\zeta)}{1.65\cdot\varepsilon_0} d\varepsilon_v^p \geq D_c \qquad (V.4.4)$$

then it is assumed that this element will fail. The element stresses and stiffness are successively reduced to zero in the way described in the previous chapter. However, here isotropic damage is considered. Hence, the $\mathbf{C}^e$ matrix becomes a zero matrix and does therefore not contribute to the element stiffness matrix. For this reason this method is also termed *element elimination* or (*removal*) *technique*. Special attention is given to the case where nodes belong to only removed elements. In this case the global stiffness matrix possesses on the line corresponding to the respective global degree of freedom only zero values and hence the (equation) system becomes singular. Therefore in the last (fourth) subsequent load increment, the diagonal element of the global stiffness matrix is set to one and the respective element of the global load vector is set to zero. Obviously, the computed displacement increment is zero.

Remark
The element elimination technique has been successfully applied by several authors. Tvergaard [TVE 82] reported on the good agreement of these results with those obtained by the Gurson Model. Wulf et al. [WUL 94] used the method to simulate experimental force vs. displacement curves in TPB-tests.
An important requirement for its successful application is a fine discretization of the mesh and the load increments.

V.5-Coupling between the micro- and the macroscale

The coupling between the micro-and the macroscale is of great importance to correlate experimental with numerical results. In this context two approaches may be possible:

1-One concentrates on one microregion of a sample used in experiments and observes directly the microscale damage behaviour of this section during loading (e.g. by in-situ tests). The same section is then reproduced in the numerical model. To get realistic boundary conditions the full sample is first simulated on a macroscopic level. Then the computed displacement data within the considered section are taken as input data for a subsequent microscopic analysis (see V.5.1).

2-One concentrates on the macroscopic behaviour of samples (e.g. tensile test). The microstructure of the corresponding material is experimentally investigated with care. From these experimental findings a microstructure is then recovered by so-called unit cells. These unit cells are able to reproduce the important effect of interaction between HP by imposing symmetry conditions along the boundaries of the model. By volumetric averaging of the discrete stress and strain values one can predict the effective elastic-plastic properties of the composite (see V.5.2).

V.5.1-Transition from the macro- to the microscale - *Zooming technique*

As described above the former approach implies a transition from a macroscopic model to a microscopic model. This transition is realized in an uncoupled manner within two steps:

1-From results of the macroscopic (*homogeneous*) model only the initial coordinates and displacement data of the considered section are taken and stored in a file. Calculations are performed with the macroscopic properties of the composite.

2- A microscopic model (*inhomogeneous*) is generated within the considered section. The obtained displacement data are interpolated to fit in the microscopic model. These interpolated displacement data become the kinematic boundary conditions of the microscopic model. By choice, a linear or quadratic interpolation may be used. The interpolation program is realized with the help of the Fortran Program Zoom.

The transition from the macroscale to the microscale is illustrated by the figure below.

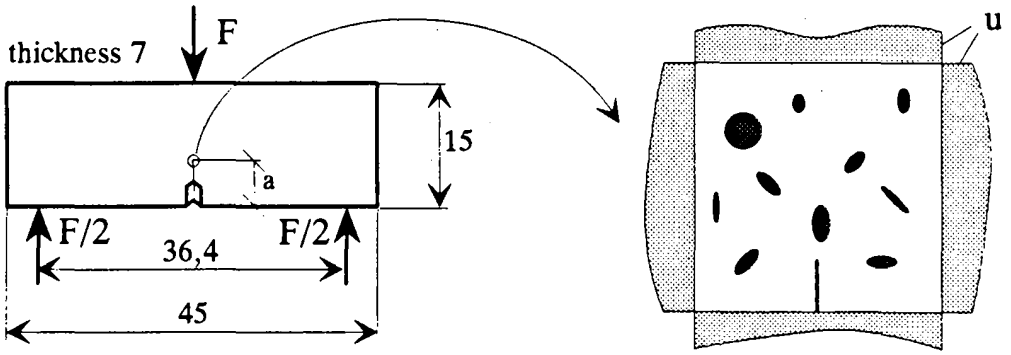

Fig. V.5.1. The transition from the macroscopic to the microscopic model

V.5.2-Transition from the micro- to the macroscale - *Averaging technique*

The second approach implies the transition from the microscale to the macroscale. Here a microscopic model is employed using the unit-cell technique. This technique might be viewed as an approximate method to cover whole microstructures within a more or less idealized manner. Under homogeneous loading the results become strongly non-homogeneous due to the presence of multiphases with different properties. The macroscopic response may be predicted by homogenization technique. The macroscopic overall stresses and strains are obtained by numerical integration (see V.2.3).

$$\langle \sigma \rangle = \frac{1}{V} \sum_{ielem=1}^{nelem} \left(\sum_{p=1}^{NGP} \sum_{q=1}^{NGP} \sigma(\xi,\eta)\Big|_{\bar{\xi}_p,\bar{\eta}_p} t^e \det \mathbf{J}^e \, W_p W_q \right) \tag{V.5.1a}$$

$$\langle \varepsilon \rangle = \frac{1}{V} \sum_{ielem=1}^{nelem} \left(\sum_{p=1}^{NGP} \sum_{q=1}^{NGP} \varepsilon(\xi,\eta)\Big|_{\bar{\xi}_p,\bar{\eta}_p} t^e \det \mathbf{J}^e \, W_p W_q \right) \tag{V.5.1b}$$

$$\langle \varepsilon^p \rangle = \frac{1}{V} \sum_{ielem=1}^{nelem} \left(\sum_{p=1}^{NGP} \sum_{q=1}^{NGP} \varepsilon^p(\xi,\eta)\Big|_{\bar{\xi}_p,\bar{\eta}_p} t^e \det \mathbf{J}^e \, W_p W_q \right) \tag{V.5.1c}$$

where nelem denotes the total number of elements. All other quantities are dependent on the above computed values and are derived by the relations found in chapter V.3. Also the mean stresses and the mean strains within the individual phases are calculated in the same manner except that summation is only carried out over elements belonging to the same material phase. In the special case of uniaxial tension, these relations provide the prediction of macroscopic effective properties like E_c, ν_c, σ_{Y0} etc.. They may also be derived from the imposed macroscopic boundary conditions. In the case of prescribed stresses Σ, only the displacement values u on the boundary have to be determined in order to obtain the macroscopic strain E by

$$E = \frac{u}{l} \tag{V.5.2a}$$

where l is the length of the model. In the case where displacements u are prescribed, the macroscopic strains are immediately given by eqn (V.5.2a) and only the forces f on the boundary have to be found in order to obtain the macroscopic stress Σ by

$$\Sigma = \frac{f}{b \cdot t} \tag{V.5.2a}$$

where b and t are the width and thickness of the model, respectively. In the elastic-plastic setting the macroscopic measures derived from the boundary conditions coincide with the averaged values obtained by numerical integration. When damage occurs, however, they deviate. This motivates to define a damage measure D by (see Chapter IV)

$$D = 1 - \frac{E}{\langle \varepsilon \rangle} \tag{V.5.3}$$

The prediction of effective properties by a suitable transition scheme from the microscale to the macroscale is illustrated below

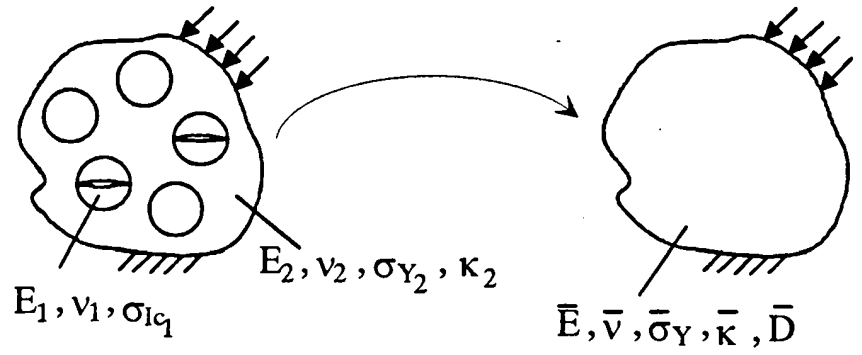

Fig. V.5.2. Prediction of effective properties describing the composite behaviour

A special developed postprocessing program evaluates all quantities of interest after each increment. In addition, the computation of the damage parameter D (eqn. V.5.3) after each load step is effective in order to quantify damage evolution in the structure.

V.6-Pre-and Postprocessing and interface programs

The transfer of data starting from the initial mesh to the output of results are illustrated in Fig. V.6.1.

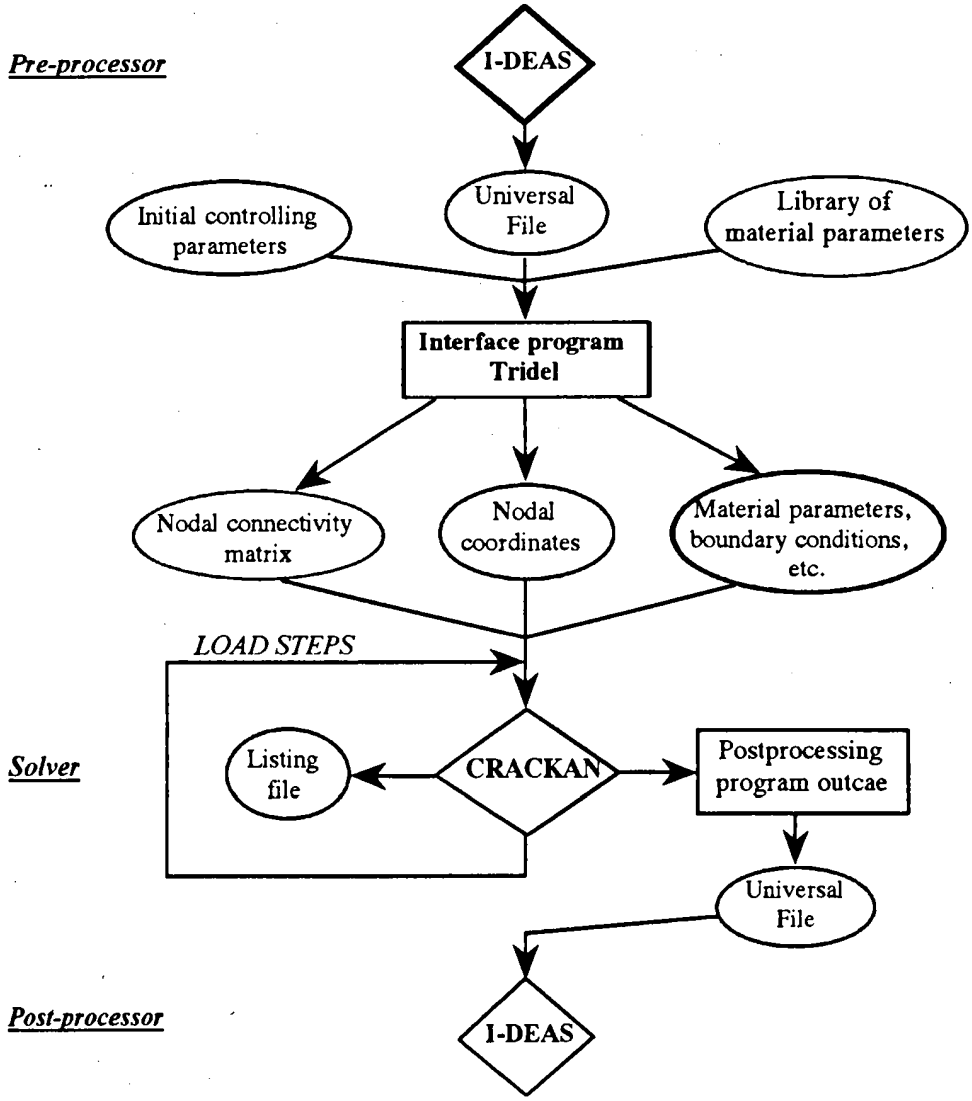

Fig. V.6.1. Transfer of data during processing

The FEM-Code I-DEAS [CAE 90] is used as Pre- and Postprocessing. As Preprocessor I-DEAS generates all data concerning the geometry, topology and boundary conditions and stores them in a so-called universal file. This file is then automatically transformed with help of the interface Fortran program Tridel [GIN 94] into a required format of the FE-Code Crackan. The results of Crackan themselves may be stored by choice in a listing file, or/and an universal file which is necessary to use I-DEAS also as Postprocessor. These files are created either after each load increment or only after the last one. The former is preferred if one aims to illustrate graphically the evolution of irreversible processes (plastic deformation, damage).
The universal file contains the geometrical and topological data as well as output data like stresses, plastic strains and other output data (e.g. triaxiality). The storage of the geometrical and topological data for each increment is necessary since they will change in the case of damage occurrence. The output data (stresses, strains etc.) have to be given in the nodal points. Since these entities are only evaluated within the Gaussian points, a bilinear extrapolation scheme has been applied [HIN 74].

CHAPTER VI

SEMI-ANALYTICAL AND NUMERICAL INVESTIGATIONS OF THE DEFORMATION AND DAMAGE BEHAVIOUR

VI.A-Semi-analytical approach - Homogeneous loading (uniform)
VI.A.1-Effective elastic properties
VI.A.2-Effective elastic-plastic properties

VI.B-FEM-Simulations - Homogeneous loading (uniform)
VI.B.1-Modelling of a single HP in an infinite matrix (Interaction between HP-MM)
VI.B.1.1-Stress concentrations in a rectangular HP
VI.B.1.2-Crack initiation at a spherical HP with a strong or weak interface
VI.B.2-Modelling of different microscale arrangements (Interaction between HP-HP)
VI.B.2.1-Model description
VI.B.2.2-Microscopic response
VI.B.2.3-Macroscopic response

VI.C-FEM-Simulations - Inhomogeneous loading (non-uniform)
VI.C.1-Combined macro- microscopic simulation of a TPB-test

VI-SEMI-ANALYTICAL AND NUMERICAL INVESTIGATIONS OF THE DEFORMATION AND DAMAGE BEHAVIOUR

This chapter is subdivided into three parts aiming to address different topics.

In Part A semi-analytical 3D-models have been employed to predict the effective elastic-plastic properties of the composite from the specific information on the microstructure.

Part B is mainly concerned with studies of the deformation and damage behaviour on the microscale under homogeneous loading. Single HP-MM systems as well as different classes of microstructures have been studied in order to reveal HP-MM-, HP-HP interaction effects as well as the influence of the morphology on the deformation and damage behaviour. For the latter one unit cell techniques have been employed. By imposing symmetry conditions they serve on one hand to cover complete microstructures and on the other hand by numerical averaging to predict the macroscopic response (Transition from micro- to macroscale).

Part C aims to simulate samples used in three-point bending tests. Special emphasis is placed on those sections which are highly loaded. The way is inverse to that one of the previous chapter. First a macroscopic analysis of the sample used in the experiment is performed. The output is used for a second microscopic analysis at the considered section (Transition from macro- to microscale).

VI.A- Semi-analytical approach - Homogenous loading (uniform)

The Mori-Tanaka model [see MOR 73, BEN 87] has been implemented into the Fortran programme "Tractan" [PLA 95] with the primary aim to predict effective properties of the composite. This model belongs to the semi-analytical approaches based on Eshelby's equivalent solution method which have already been described in chapter I. The model as implemented in "Tractan" is restricted to some hypothesis concerning geometrical features of the microstructure (see also Chapter I.2). These are
H1: Only a perfect disordered microstructure is considered
H2: Only a perfect matrix-inclusion topology is considered
H3: Particle shape is a (a) sphere or a (b) cylinder or an (c) ellipsoid
H4: No damage is considered

VI.A.1-Effective elastic properties

In most cases the microcomponents may be manufactured in their respective bulk state, so that their elastic properties may be determined by experiments. However, this is in general not possible for metallic hard-phases as present in the here investigated material. Consequently, they have to be estimated from the elastic properties of the matrix and the composite. The procedure following here is to vary the elastic modulus of the HP in an iterative manner until the computed effective Young's modulus fits the experimental data. The following microstructural characteristics for MM and HP are taken in the calculations:

	ξ	Shape	E_l [GPa]	E_q [GPa]	ν_l [-]	ν_q [-]
HP	0.16	ellipsoid h/b=1.43			0.3	0.3
MM	0.84		210	210	0.3	0.3
Comp.			220	215	0.3	0.3

Tab. VI.A.1.1. Microstructural characteristics in SAE-D3

With the above used characteristics the effective Young's modulus of the composite in longitudinal (Ecl) and transverse (Ecq) was predicted. The respective values are plotted in the figure below as function of the Young's modulus of the HP.

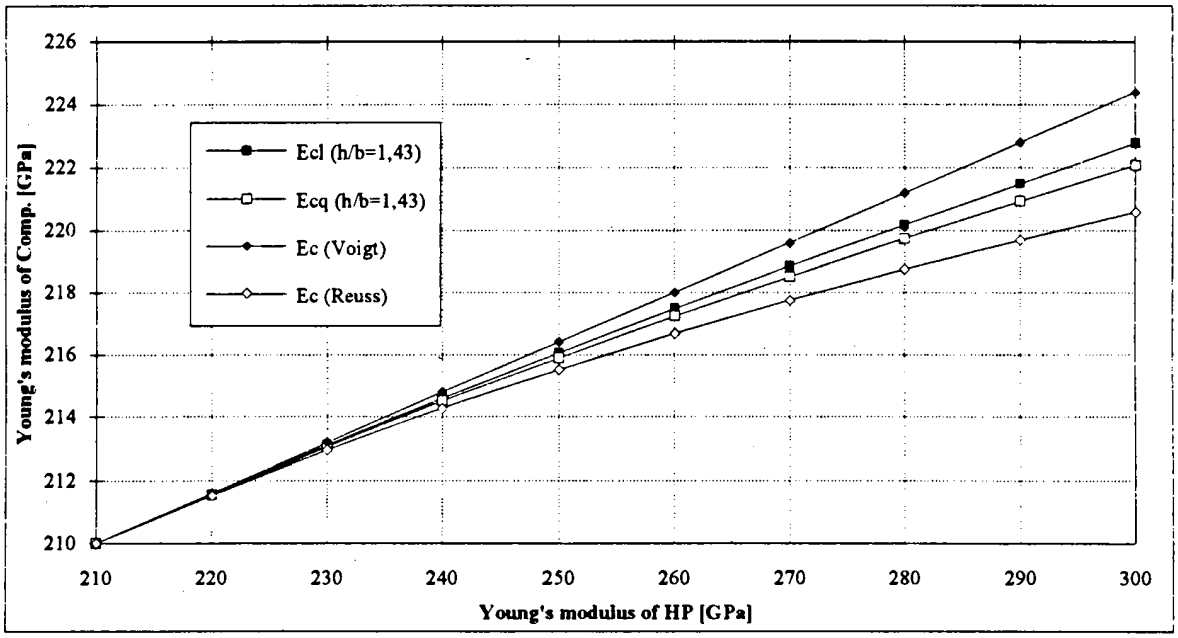

Fig. VI.A.1.1. Predicted Young's modulus of SAE-D3 as function of that of the HP

It can be seen from this figure that the Mori-Tanaka model does not exhibit considerably the elastic anisotropy present in the microstructure. For a given aspect ratio of 1.43, the Young's modulus in longitudinal and transverse direction does not vary much. The general bounds of Voigt and Reuss show that only with increasing stiffness mismatch between MM and HP the elastic anisotropy becomes more important. With a Young's modulus of 280 GPa of the HP the predicted value of the longitudinal component of the composite coincides with that obtained by experiments (E_{cl}=220GPa, see Appendix A1). However, the transverse value is slightly overestimated compared with experimental results (E_{cq}=215GPa, see Appendix A1).
For all subsequent computations the value of 280 GPa is taken. This value was also found in previous studies using combined experimental and numerical methods [BRO 94].

When the Young's modulus of both, MM and HP is known, then the overall stiffness is mainly influenced by the volume fraction and the aspect ratio of the particle. This dependence is quantified in the figure below. The upper bound of Voigt assumes a linear relationship between volume fraction and effective Young's modulus (eqn. I.2.15b), the gradient of the function remaining hence constant. In all other approaches the gradient is lower than this constant for $\xi_{HP}<0,5$ and higher for $\xi_{HP}>0,5$. The slight variation between the upper and lower bound

shows that particle shape does not affect much the overall stiffness. Recall that the Voigt and Reuss models describe geometrically infinite aligned particles (see fig. I.2.2) parallel and perpendicular to the load direction.
Particle shape becomes most important for intermediate volume fraction (ξ_{HP}=0,5).

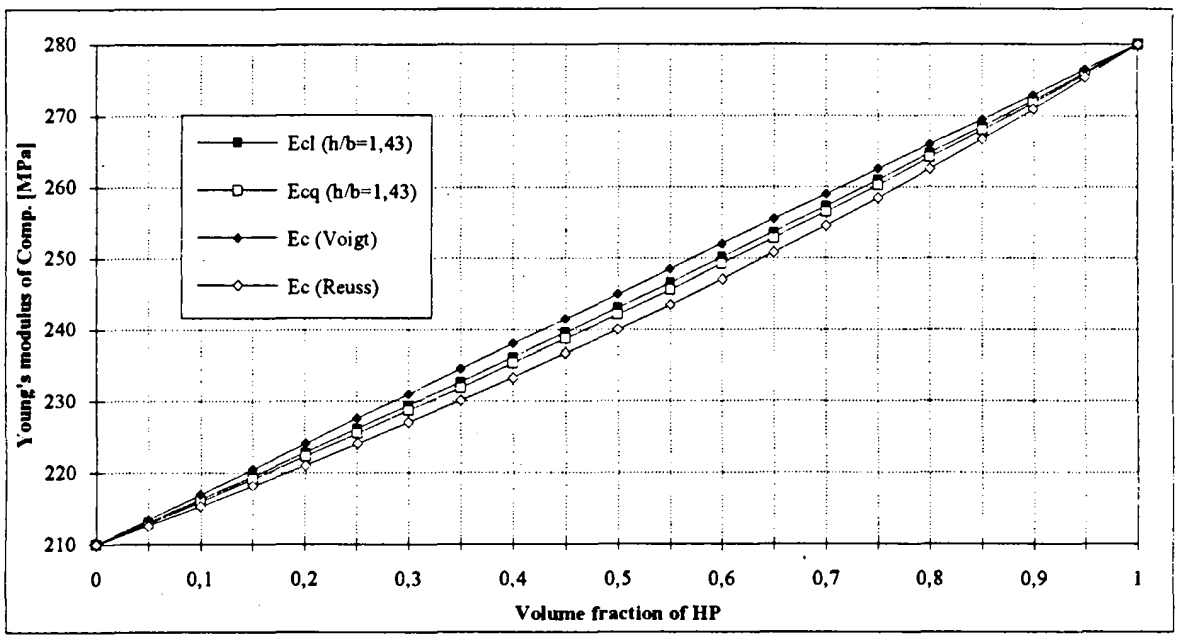

Fig. VI.A.1.2. Predicted Young's modulus of SAE-D3 as function of the HP-content

VI.A.2 Effective elastic-plastic properties

Plasticity was implemented into "Tractan" using the secant approach (chap. I.2.2, also Appendix C.2). The hardening behaviour of the matrix is assumed to obey the following relationship proposed by Ludwig (eqn. I.2.47).

$$\sigma_v = \sigma_{Y_0} + h_0\left(\varepsilon_v^p\right)^n \quad . \qquad \text{(VI.A.2.1)}$$

The hardening curve of the matrix was determined combining experimental and numerical methods in a former work [BRO 94]. The adjustable parameters h_0 and n within the model of Ludwik have to be adapted to these curves. Figure VI.A.2.1 lists together both results for all states of heat treatment, the hardening curve obtained in the former work and described by a piece-wise hardening curve (indicated in the fig. by the extension Exp), and that obtained by the model of Ludwik (indicated by the extension Mod). By choice of the following parameters a good agreement is achieved (Fig. VI.A.2.1):

state of heat treatment	σ_{Y0} [MPa]	h_0 [MPa]	n [-]
Ann	310	2000	0,6
600	900	2250	0,4
380	1550	2500	0,4

Tab. VI.A.2.1. Calibration of the model of Ludwik for the matrix material

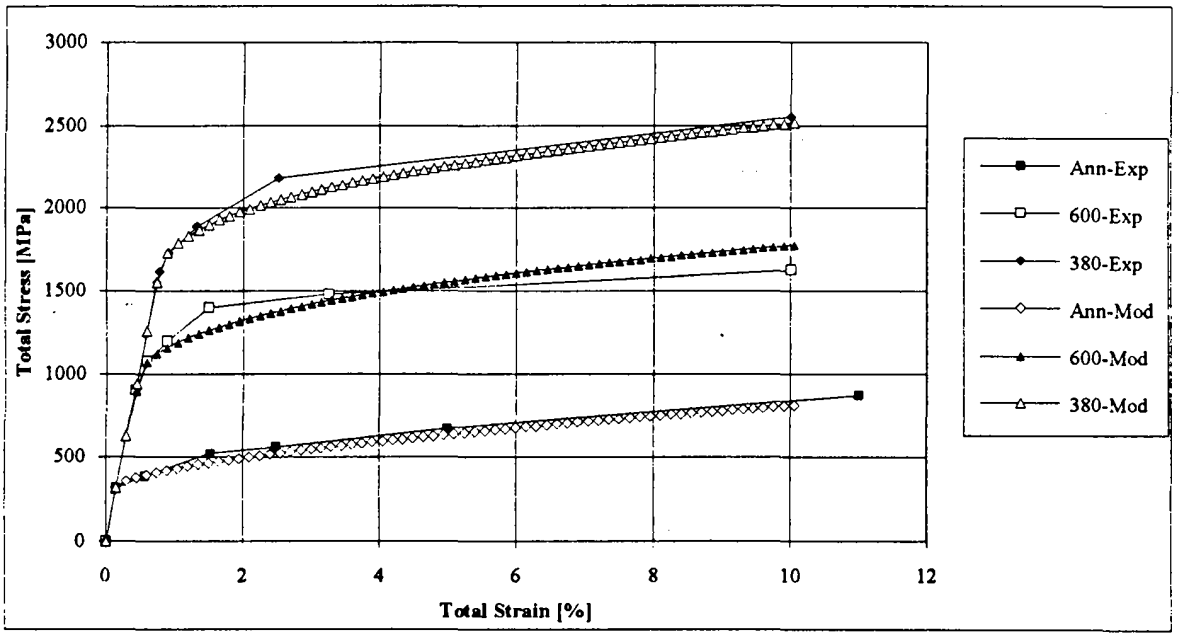

Fig. VI.A.2.1. Stress-Strain curves of the matrix predicted by the model of Ludwik

With the model of Ludwik the effective stress-strain curves of the composite have been simulated. Exemplarly the results are plotted for the longitudinal direction (Comp(l)) in the figures VI.A.2.2a-c and listed together with the experimental results (Exp(l)). For all states of heat treatment rather good agreement between the model predictions and the experimental results has been achieved, the predicted response of Mori-Tanaka is only slightly stiffer compared to the experimental results.

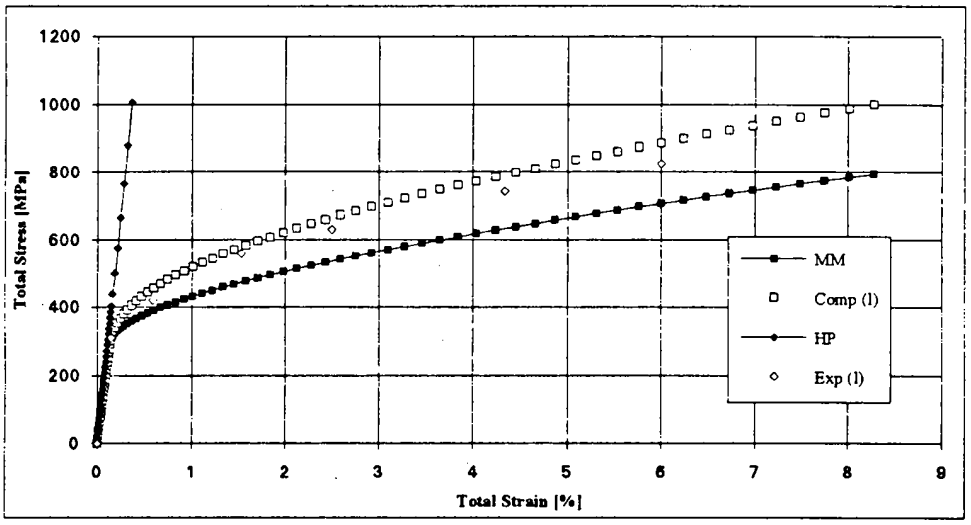

(a)

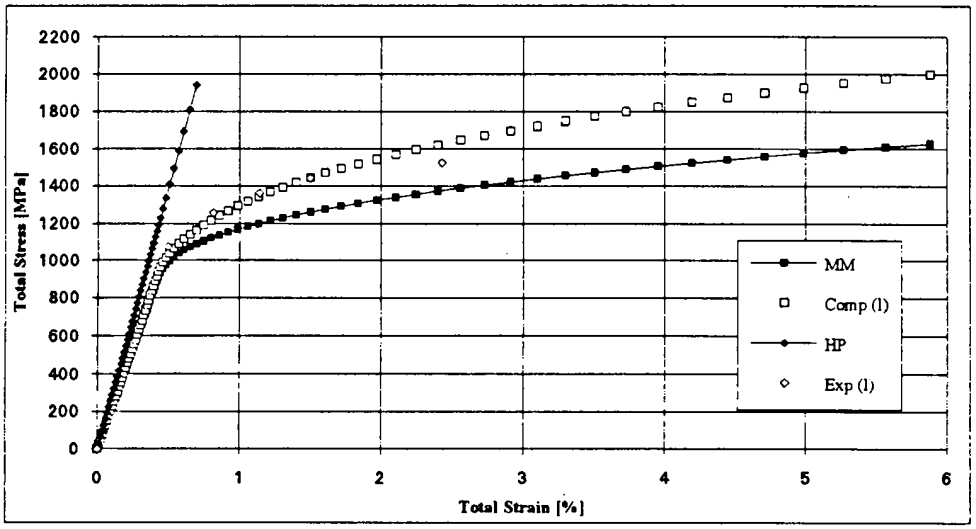

(b)

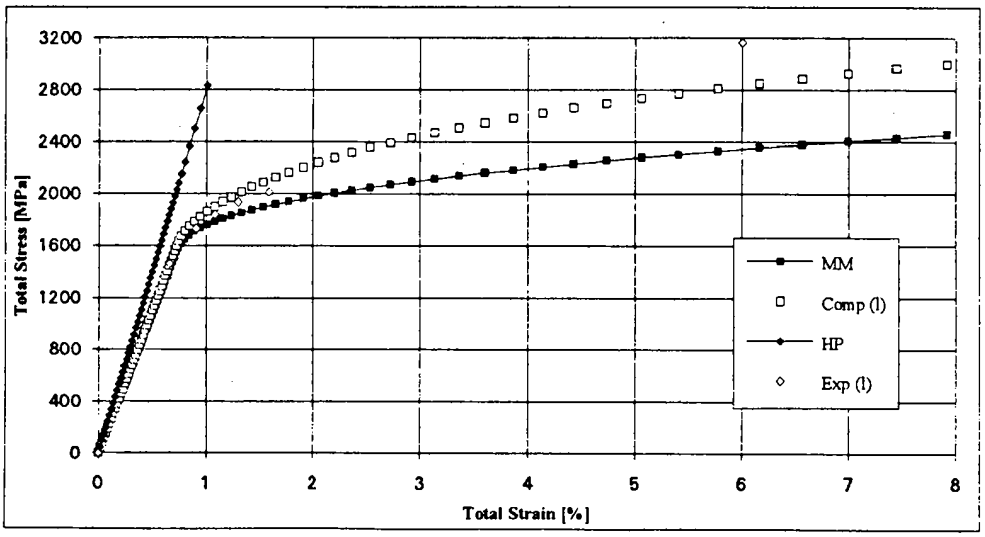

(c)

Fig. VI.A.2.2. Effective stress-strain curves predicted by MT (a) *Ann* (b) *600* (c) *380*

Finally, the favorable role of the HP on the strengthening of the composite has been investigated for the tempering states "Ann" and "380". The effective yield stress (the respective stress value corresponding to $0{,}00\% < \varepsilon_{pl} < 0{,}01\%$) in longitudinal and transverse direction has been evaluated as function of the HP-volume content. The HP are assumed to be aligned in longitudinal direction with aspect ratio of 1,43 according to the metallographical findings and of 1000 in order to bound these functions. The figures below exhibit the dependence of the effective yield stress of both, HP content and HP-shape. The effective yield stress has been normalized by the yield stress of the MM.

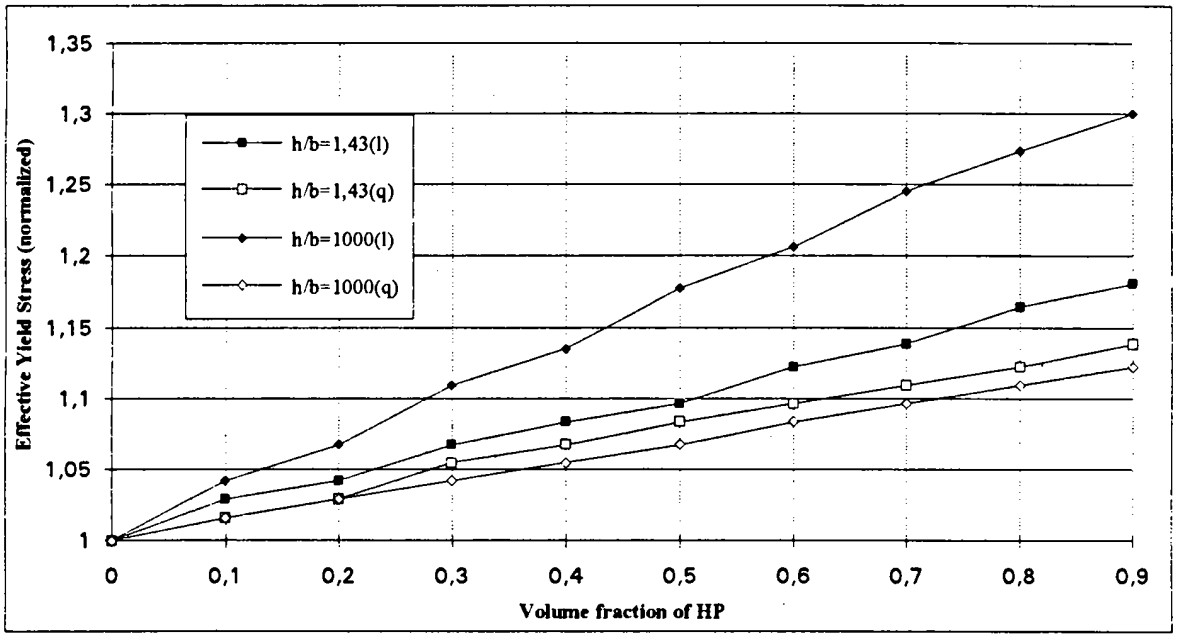

(a)

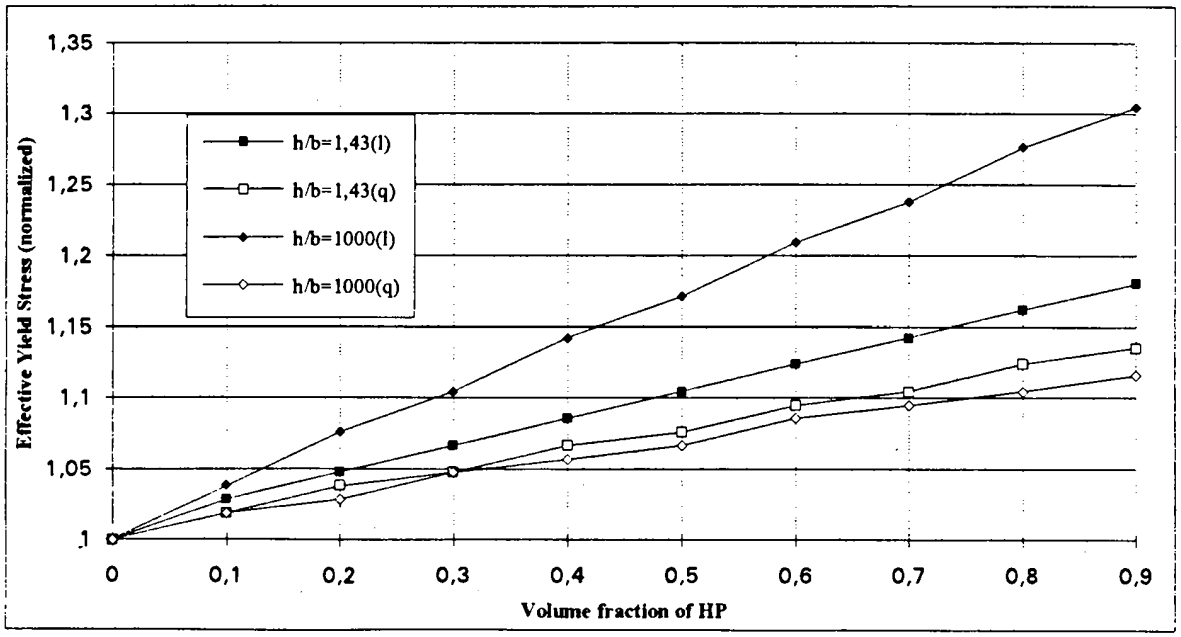

(b)

Fig. VI.A.2.3. Effective yield stress predicted by MT for different tempering states
(a) "Ann" (b) "380"

The figures reveal that the effective yield stress increases linear with the HP content. The slope of this function is strongly influenced by the particle shape. The change of this slope is stronger for aspect ratios of h/b>1 and declines for values tending to zero. For example one may consider two materials, an isotropic one with an aspect ratio of unity and an anisotropic one with an aspect ratio different from unity. Compared with the isotropic material, the effective yield stress of the anisotropic material in longitudinal direction is obviously higher and in transverse direction obviously lower. However, this increase in longitudinal direction is much more pronounced than the respective decrease in transverse direction.

It could also be concluded from these figures that differences of the hardening behaviour of the matrix does not affect initial plastification. This view is supported by the fact that both figures are even quantitatively identical despite of the difference in the hardening curve (h_0 and n are different in the tempering states "Ann" and "380", see Tab. VI.A.2.1)

VI.B- FEM-Simulations - Homogeneous loading (uniform)

VI.B.1-Modelling of a single HP in infinite matrix-(Interaction between HP-MM)

VI.B.1.1-STRESS CONCENTRATIONS IN A RECTANGULAR HP

Parameter studies on single HP structures have been carried out to investigate particle shape effects on the stress concentrations in the HP, which is in view of the chosen failure criteria an indicator for the occurrence of these phenomena. Fig. VI.B.1.1a illustrates the FE-model. Three different configurations are considered; in all of them, the structure is subjected to uniaxial tension in y-direction. In example C, the structure contains in the centre a single rectangular HP, with side-lengths b and h. In examples A and B the HP applies to a stripe in x- and y-direction, respectively. These two examples are chosen to get bounds for the solution (see Voigt and Reuss bounds in chapter I.1). For both, the stress distribution is constant over the single phases and in example A the stresses are even homogeneous over the whole structure. In contrast, the stress distribution in example C is highly inhomogeneous and no simple relation between the applied load and the stresses can be found:

Ex. A: $$\sigma_{HP} = \sigma_{MM} = \sigma^{\circ} \quad \Rightarrow \quad \varepsilon_{HP} = \varepsilon_{MM} \frac{E_{HP}}{E_{MM}} \qquad \text{(VI.B.1.1a)}$$

Ex. B: $$\varepsilon_{HP} = \varepsilon_{MM} \quad \Rightarrow \quad \sigma_{HP} = \sigma_{MM} \frac{E_{HP}}{E_{MM}} \qquad \text{(VI.B.1.1b)}$$

Ex. C: $$\varepsilon_{HP} \neq \varepsilon_{MM} \neq \text{const.} \qquad \sigma_{HP} \neq \sigma_{MM} \neq \text{const.} \qquad \text{(VI.B.1.1c)}$$

The particle shape is changed in terms of the aspect ratio h/b varying from h/b=0.5 to 5.0. A high aspect ratio applies to an elongated HP oriented in tensile direction. A plane strain, plane stress model and an axisymmetric model are employed as representatives for a 2- and a 3D model, respectively. Elastic material behaviour is assumed. The Young's modulus of the metal matrix was changed to 200 GPa so that the ratio of Young's moduli between HP and MM takes the value 1.4. To illustrate the results, a local normalized coordinate y_n along the side of the HP in y-direction is introduced ranging from 0.0 to 1.0. y_n=0.0 is the edge and y_n=1.0 the centre of the HP (Fig. VI.B.1.1b).

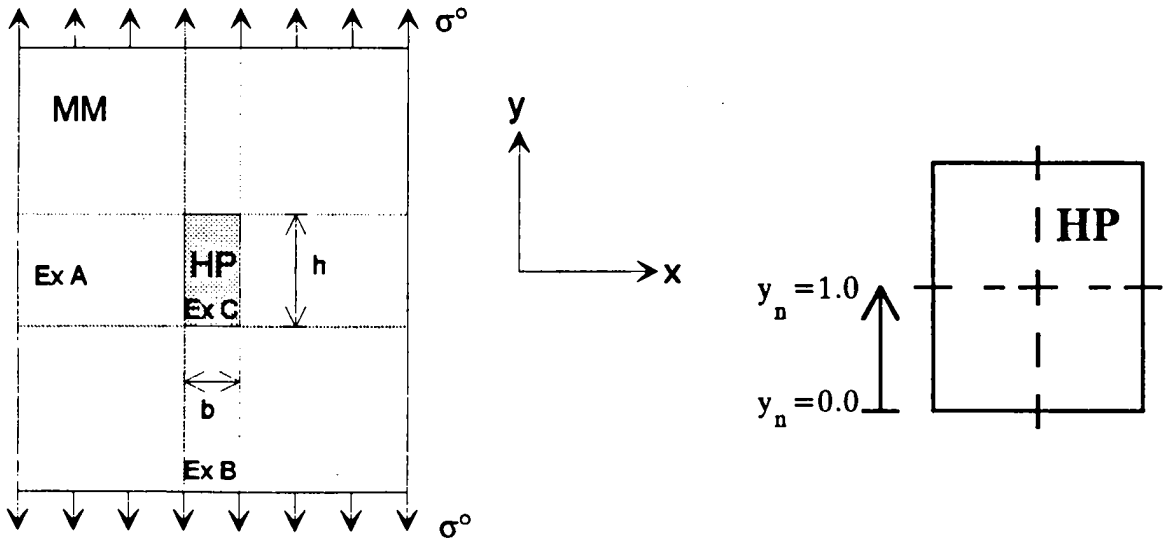

Fig. VI.B.1.1. Schematic of FE-model and HP geometry (a) and local normalized coordinate y_n (b)

The results are shown in Fig. VI.B.1.2 under the assumption of a state of plane strain (a) and axisymmetry (b). Relative values for the stress concentration in the HP are given on the vertical axis and geometrical data in terms of the local normalized coordinate on the horizontal axis. The curves are bounded by the results of example A and example B. Recall that in example A the stresses are homogeneous over the whole structure and so the stress concentration is equal to 0; in example B the stress concentration in the HP is equal to the ratio of the elastic moduli. Both curves exhibit the same main features:

(i) normal stresses increase with an increasing ratio of h/b.
(ii) they also increase with y_n beginning at the edge and reaching their maximum in the centre of the HP.

In connection with the use of the normal stress criterion for cleavage in HP, the results coincide with experimental observations (see chapter IV.1):

(i) slim HP oriented in load direction crack sooner than others
(ii) slim HP do not break randomly along their length; instead, fracturing is more likely in the vicinity of the centre of the HP.

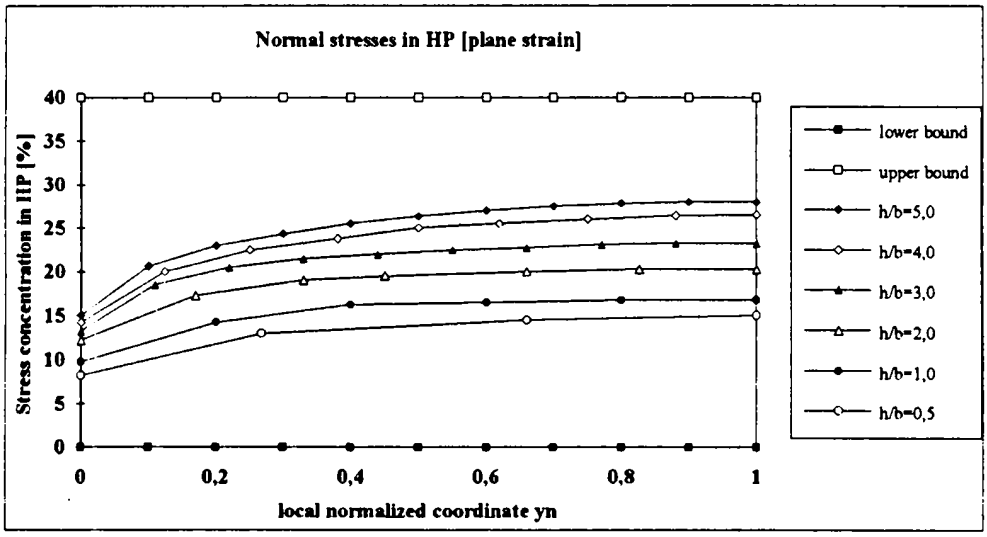

(a)

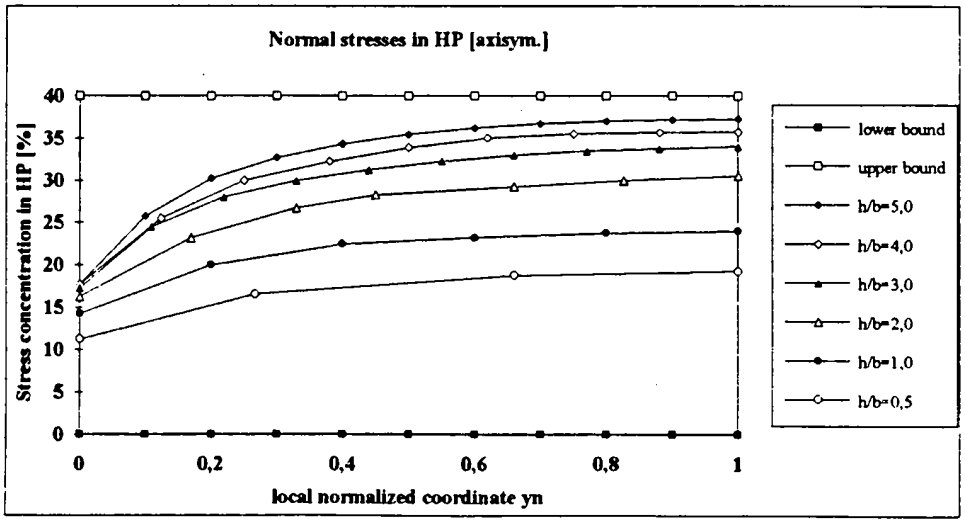

(b)

Fig. VI.B.1.2. Stress concentration as function of particle shape,
a) plane strain model b) axisymmetric model

The results of the different cases are compared in Fig. VI.B.1.3 for the aspect ratio of h/b=5.0. The assumption of plane stress and plane strain give similar results, whereas a remarkable difference can be noticed between the plane stress/ plane strain and the axisymmetric model. The shear stresses are non-linearly distributed along the interface. They reach their maximum at the edge of the HP and decrease to zero in the centre of the HP due to symmetry conditions.

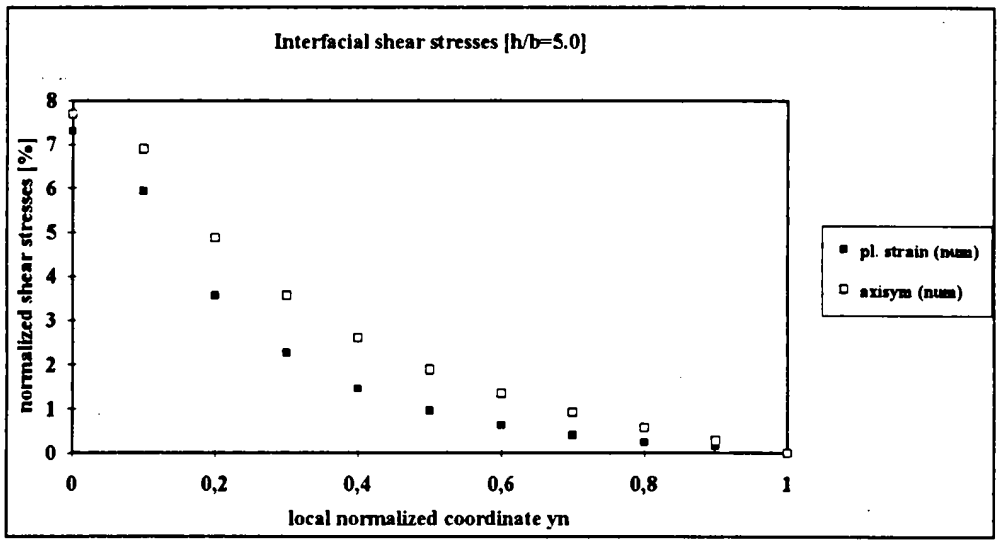

(a)

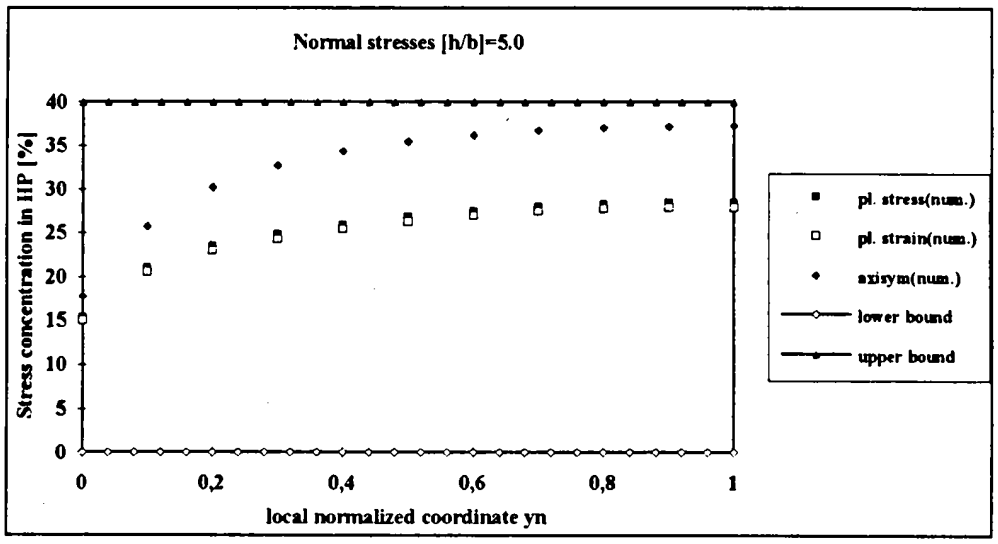

(b)

Fig. VI.B.1.3. Comparison between results of different models
a) Interfacial stresses b) normal stresses

Analytical model [GRO 95]

The development of an analytical model is helpful to evaluate the results of the numerical model. Furthermore, it explains the difference of the results between a 2D- and a 3D model.
We consider a stripe as thick as the HP. Modulus mismatch provokes shear stresses in the vicinity of the HP. Symmetry conditions allow to set τ=0 in the middle of the HP. The shear stresses increase along the interface and reach their maximum at the edge of the HP (Fig. VI.B.1.4a) The conditions of equilibrium are formulated for a cylindrical infinitesimal element of the HP. It is assumed that the normal stresses are constant over the section (Fig. VI.B.1.4b).

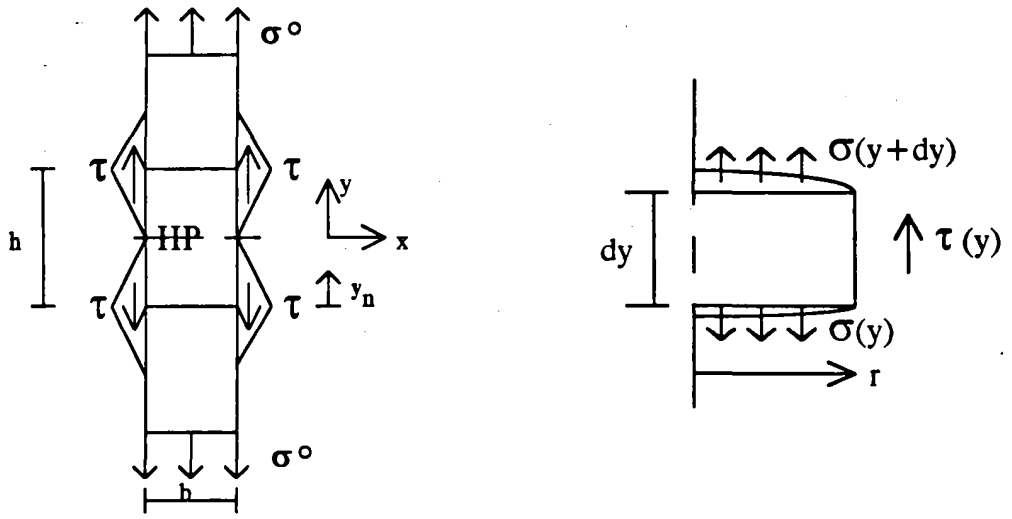

Fig. VI.B.1.4. Distribution of interfacial stresses (a) and conditions of equilibrium (b)

The conditions of equilibrium give

$$\tau(y)\cdot 2\pi r\cdot dy = -\{\sigma(y+dy)-\sigma(y)\}\cdot \pi r^2 \qquad \text{(VI.B.1.2)}$$

and in terms of the local normalized coordinate y_n

$$d\sigma = \frac{h}{r}\cdot \tau(y_n)\cdot dy_n \qquad \text{(VI.B.1.3)}$$

Integration of (VI.B.1.3) leads to

$$\sigma(y_n) = \frac{h}{r}\int_{y_n=0}^{y_n} \tau(y_n)\cdot dy_n + \sigma(y_n=0) \qquad \text{(VI.B.1.4)}$$

It was considered that the HP is cylindrical and totally embedded in the MM, which is equivalent with a 3D-model. In the 2D-model, the HP is rectangular with thickness t and has two free surfaces, so that the ratio of surface (A) to the section (B) will change.

$$\left(\frac{A}{B}\right)_{3D} = \left(\frac{2\pi r\cdot h}{\pi r^2}\right) = \frac{2h}{r}$$
$$\left(\frac{A}{B}\right)_{2D} = \left(\frac{2ht}{bt}\right) = \frac{2h}{b} \qquad \text{(VI.B.1.5)}$$

Consequently, eqn. (VI.B.1.5) is also valid for the 2D-model if we replace the radius r by the width b. The function $\tau(y_n)$ and the normal stress at the edge of the HP ($\sigma(y_n$=0)) are unknown

and depend on particle geometry, property mismatch between HP and MM and loading. To estimate this unknown function, we consider Fig. VI.B.1.5.

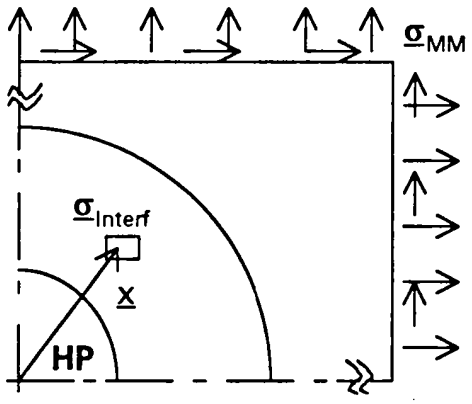

Fig. VI.B.1.5. Stress field in MM in the vicinity of a HP

The stress field of the MM is influenced by the presence of the particle. This influence becomes stronger in the vicinity of the HP. In case of elasticity the stress distribution can be described by the following formulation:

$$\sigma_{Interf} = \mathbf{M}\,\sigma_{MM}\,\mathbf{M}^T \qquad \text{(VI.B.1.6)}$$

where **M** is a transformation matrix, which depends on particle shape, property mismatch and coordinate **x**. It is a measure for the deformation constraint, which the HP exerts on the MM. In the considered case of uniaxial tension, characterized by

$$\sigma_{MM} = \begin{pmatrix} 0 & 0 \\ 0 & \sigma^\circ \end{pmatrix} \qquad \text{(VI.B.1.7)}$$

one gets for the symmetric tensor σ_{Interf}

$$\sigma_{Interf} = \begin{pmatrix} M_{12}^2 & M_{12}M_{22} \\ M_{12}M_{22} & M_{22}^2 \end{pmatrix} \qquad \text{(VI.B.1.8)}$$

The stress components σ_{yy}, σ_{xy} of this tensor are inserted into eqn. (VI.b.1.4). The resulting equation is changed into a format, which allows for comparison with the numerical formulation

$$\left(\frac{\sigma_n(y_n)-\sigma^\circ}{\sigma^\circ}\cdot 100\right) = \left(\frac{h}{r}\int_{y_n=0}^{y_n} M_{12}M_{22}\,dy_n + M_{22}(y_n=0)^2 - 1\right)\cdot 100 \qquad \text{(VI.B.1.9)}$$

The unknown values M_{12}, M_{22} are determined to approximate the numerical solution of the interfacial stress distribution (Fig.VI.B.1.6a). By this approximation, eqn. (VI.B.1.9) is determined. The resulting plots exhibit a good agreement between the numerical and the analytical solution for the 2D-as well as for the 3D-model (Fig.VI.B.1.6b).

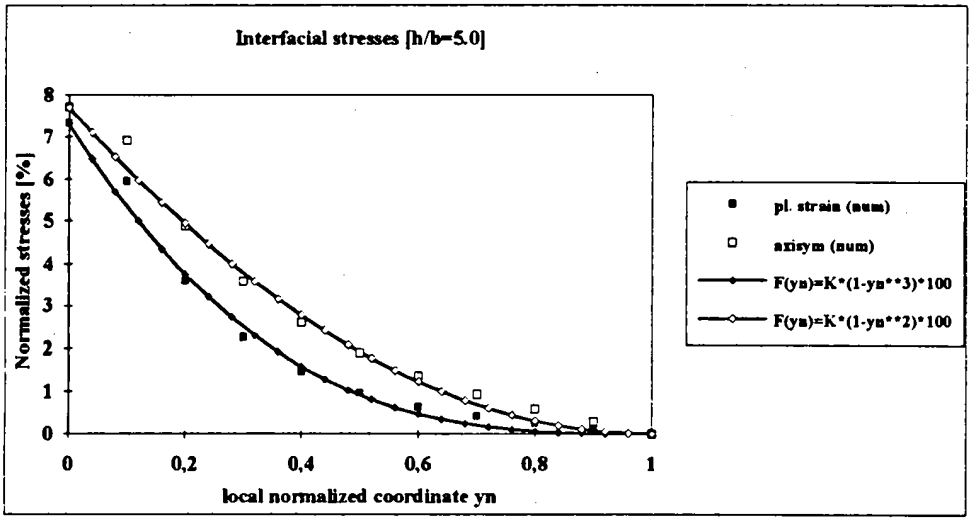

(a)

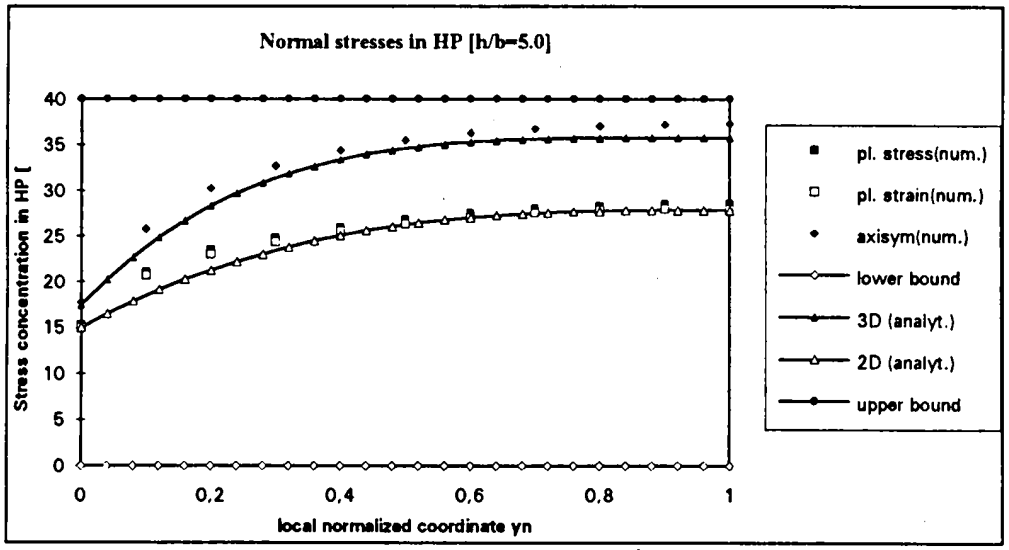

(b)

Fig. VI.B.1.6. Approximation of the distribution of the interfacial stresses (a) and Comparison between the numerical and the analytical solution (b)

VI.B.1.2-CRACK INITIATION AT A SPHERICAL HP WITH A STRONG OR WEAK INTERFACE

As discussed in the beginning decohesion mostly develops at spherical HP. In order to investigate this phenomenon a single spherical HP embedded in an infinite matrix was studied. Fig. VI.B.1.7 illustrates the model.

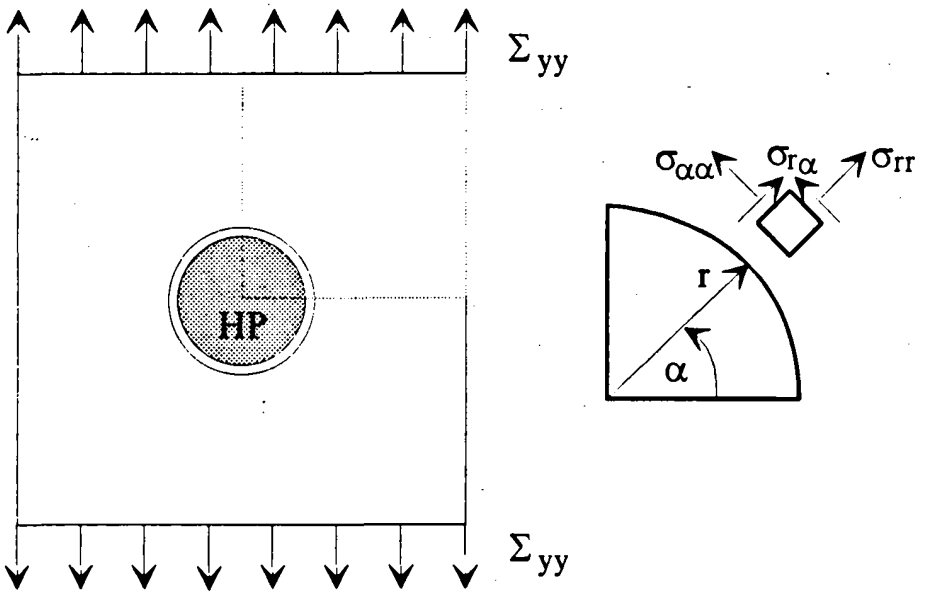

Fig. VI.B.1.7. Schematic of the numerical model and definition of the polar stress components

The failure mode of the interface is dependent on the polar stress components at the interface (Fig. VI.B.1.7). Therefore these values have been calculated and plotted over the angle α after each load increment (Fig. VI.B.1.7). This analysis aims to investigate the role of a *strong* or *weak interface* on the local mechanical behaviour. Different cases have been addressed:

strong interface	*weak interface*
• perfect bondings • brittle HP (σ_{Ic}=1400 MPa)	• Mode I under tension (σ_{Ic}=1400 Mpa) • Mode II under compression (σ_{IIc}=700 MPa) • Cavity as an extreme case of a weak interface

The elastic-plastic material parameters were taken for heat treatment "600" (see Annex A1, A3). Calculations have been carried out under plane strain conditions.
Special attention is devoted to the distribution of the circumferential, radial, shear and hydrostatic stresses over the half interface length. These quantities have been chosen, since the radial and shear stresses directly control initiation of interfacial debonding under pure mode I and mode II, respectively, whereas the hydrostatic and circumferential stresses are believed to play an important role for damage initiation in the matrix.
All values have been normalized by the applied macroscopic stress Σ_{yy}, therefore this ratio provides a direct measure for the stress concentration.

Strong Interface

The first case considers a perfect bonding between HP and MM. The HP is modelled elastic, the MM and the interface layer elastic-plastic with equal properties ("600" see Annex A1, A3). The polar stress components together with the hydrostatic stresses at two different load steps showing purely elastic and elastic-plastic behaviour have been plotted in Fig. VI.B.1.8 and VI.B.1.9, respectively. The values have been directly extracted from the calculations for $0<\alpha<90°$ and extended up to 180° respecting symmetry of the radial and circumferential stresses and antisymmetry of the shear stresses.

In the elastic regime (Fig. VI.B.1.8a) the whole interface is subjected to tensile loading. The maximum value of the circumferential stresses is at 0° that of the radial stresses at 90° where the factor of the stress concentration becomes 1,056. The absolute maximum of the shear stresses is found at 45°. Whereas all polar stress components strongly vary with angle α, only slight variations are found for the hydrostatic stresses. The extreme value is at 90°.

By these results, it seems likely that debonding will be initiated at $\alpha=90°$ under pure mode I and at $\alpha=45°$ under pure mode II.

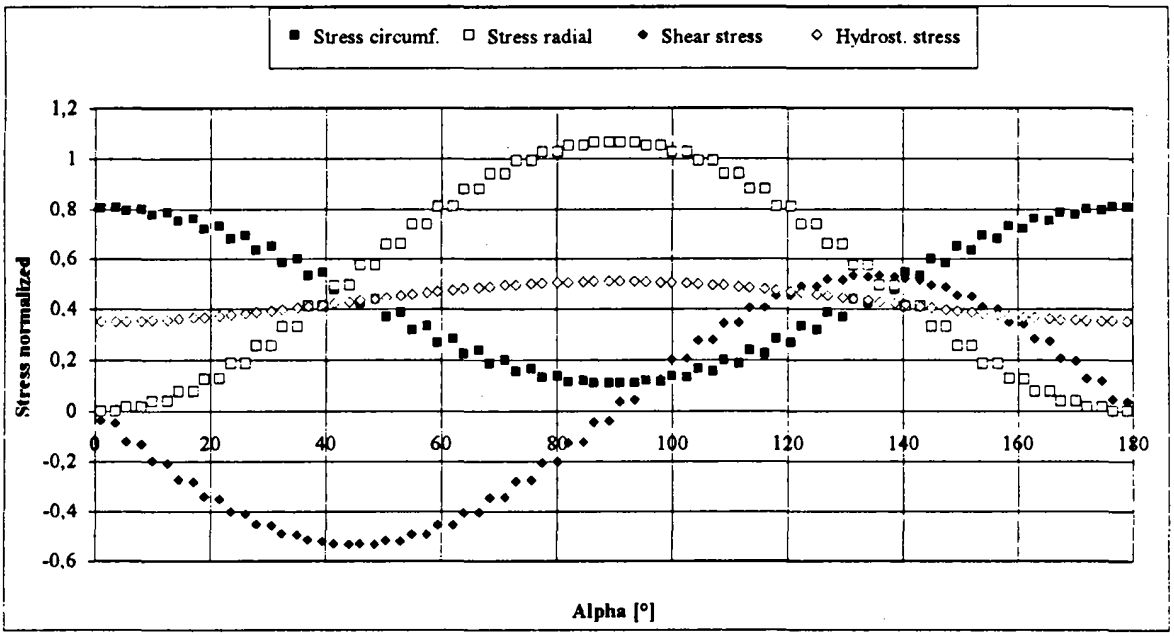

Fig. VI.B.1.8. Stress distribution along the interface- Elastic response

When the matrix and the interface undergo plastic deformation, the interface response is slightly different (Fig. VI.B.1.9). The distribution of the radial and shear stresses have not been qualitatively changed, however, the extreme values are slightly more pronounced. The maximum value of the radial stresses at $\alpha=90°$ has been increased from 1.056 to 1.069, whereas the minimum value at $\alpha=0°$ is shifted in the compressive range (-0.04) as a consequence of the plastic flow of the matrix in load direction. The absolute maximum of the shear stresses has been slightly raised ($0.53\rightarrow0.54$).

The curves of the circumferential and hydrostatic stresses, however, exhibit more deviations in the plastic range. Beside the maximum value at $\alpha=0°$ (slightly dropped $0.807\rightarrow0.742$), a second maximum value of the circumferential stresses arises at $\alpha=58°$ ($0.3\rightarrow0.53$). The maximum of the hydrostatic stresses has been moved from $\alpha=90°$ to $\alpha=67.5°$ with an increase from 0.51 to 0.63.

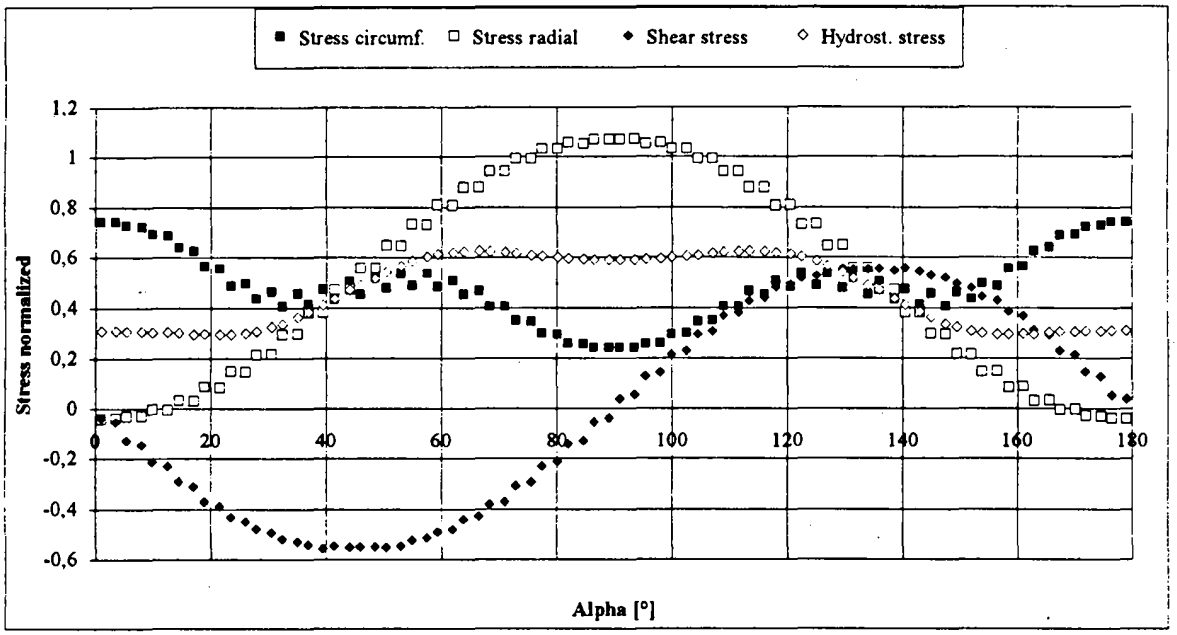

Fig. VI.B.1.9. Stress distribution along the interface-Elastic-plastic response Σ_{yy}/σ_{Y0} = 1,667

For a strong interface bonding, particle cracking might occur due to excessive loading. The figure below shows the stress distribution just after particle fracture at the load level of Σ_{yy}=1300 MPa (fracture strength of the HP: σ_{Ic}=1400 MPa).

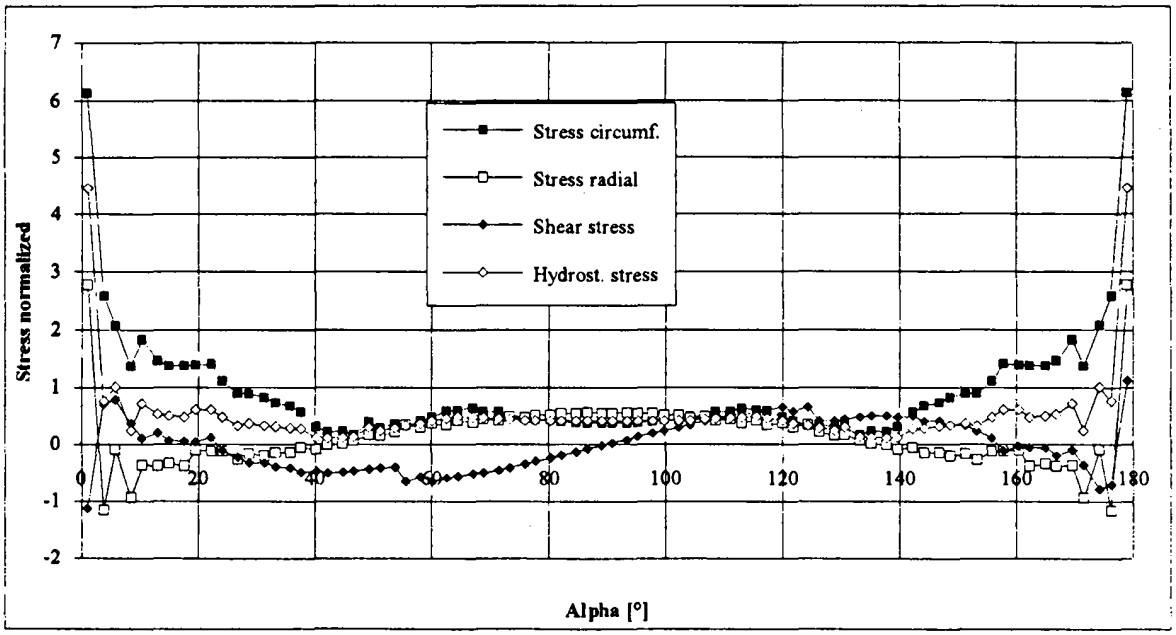

Fig. VI.B.1.10. Stress distribution along the interface after particle cracking Σ_{yy}/σ_{Y0} = 1,444

The load carrying capacity of the particle after sudden fracture is dramatically dropped. Only the half of the macroscopic stress is transmitted over the vertical pole of the interface (Normalized radial stress: 0.5 at α=90°). All values reach their maximum values at the crack tip for α=0°. A competition may exist whether the microcrack grows along the interface or

propagates into the matrix: The high shear (concentration factor 1.12) and radial stresses (concentration factor 2.77) may trigger initiation of debonding. On the other hand damage initiation in the matrix may be promoted by high circumferential (concentration factor 6.13) and hydrostatic (concentration factor 4.46) stresses.
The deformed plot (scaling factor 4%) of the system below shows the equivalent plastic strain field in the system. The maximum relative opening of the microcrack with respect to the HP diameter was found to be δ/d_{HP}=8,00%. In front of the crack tip plastic strains are accumulated with a maximum of 5.82%. It can be seen that the plastic zone is mainly spread out under an angle of $40°<\alpha<65°$ as typical for plane strain conditions (see Fig. I.3.5).

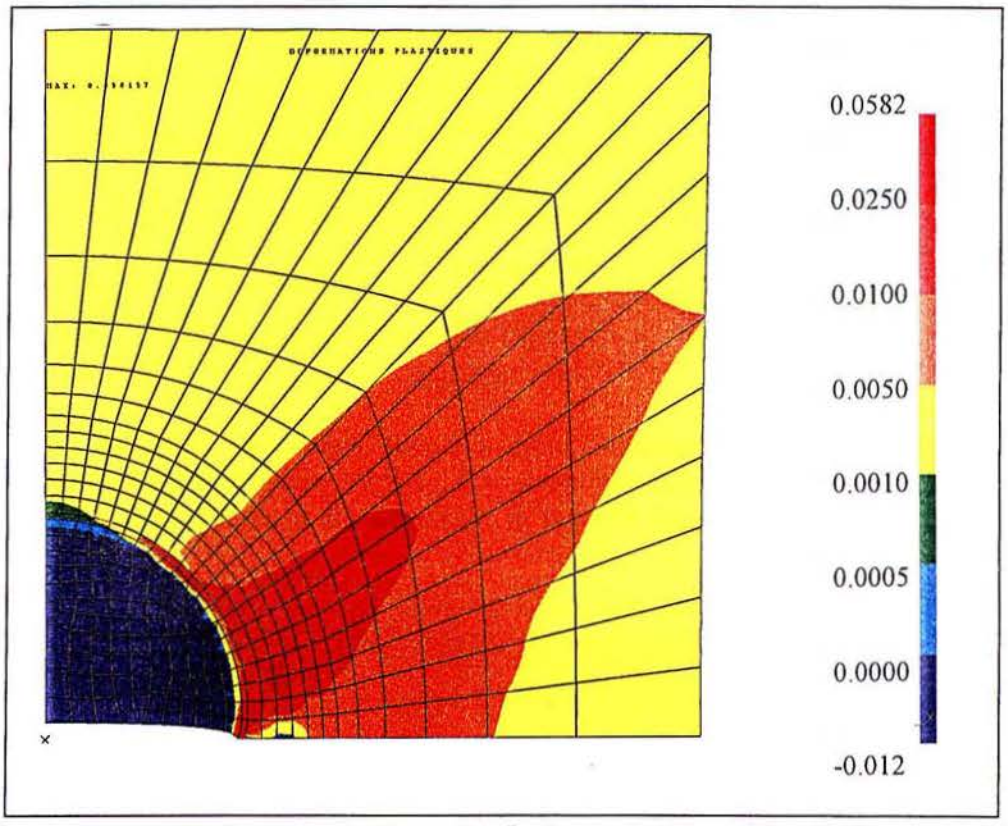

Fig. VI.B.1.11. Equivalent plastic strain ε_v^p after particle cracking Σ_{yy}/σ_{Y0} = 1,444

Weak interface subjected to tension

If the interface bonding is less strong, interfacial failure might occur prior to particle cleavage. The failure criterion of interfacial debonding under pure mode I (σ_{Ic}=1400 MPa) was fulfilled at the macroscopic load of 1320 MPa in one element at α=90. The figure below shows the stress distribution after the fourth subsequent load step (see chapter V.4.2) when the element stiffness and stress components were reduced to zero.
The stresses previously inherent in the failed element have been redistributed over the neighbouring elements. Consequently, the radial stresses are drastically raised in front of the crack tip driving the crack forward.

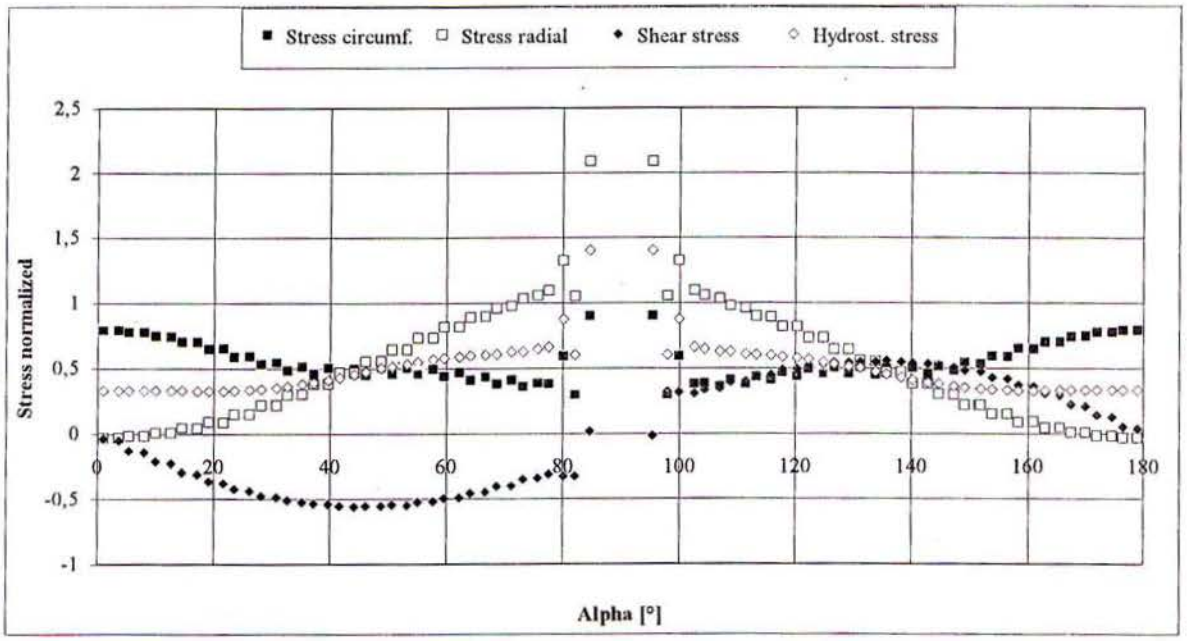

Fig. VI.B.1.12. Stress distribution along the interface after initiation of debonding- Σ_{yy}/σ_{Y0}=1,467

Subsequently, elements have been failed without increasing the external load only by redistribution of stresses. Figures VI.B.1.13a-d show the evolution of the plastic strain field with progressive degradation of the interface. In the last figure the interface crack has been stopped.

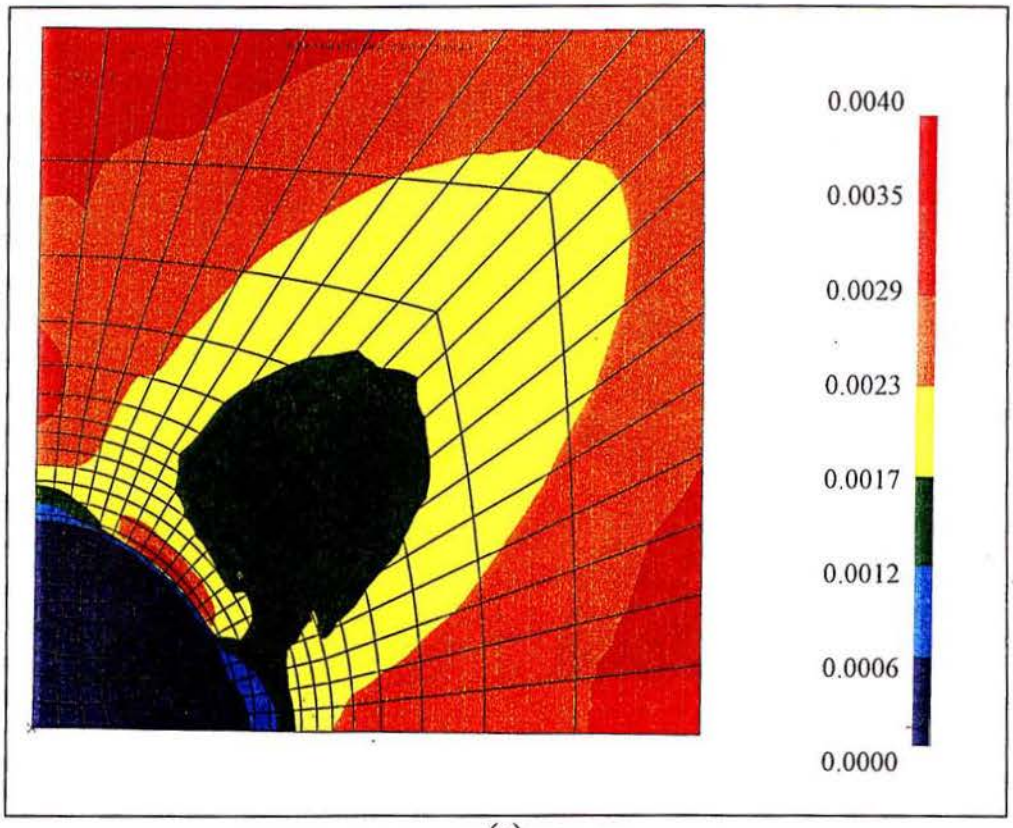

(a)

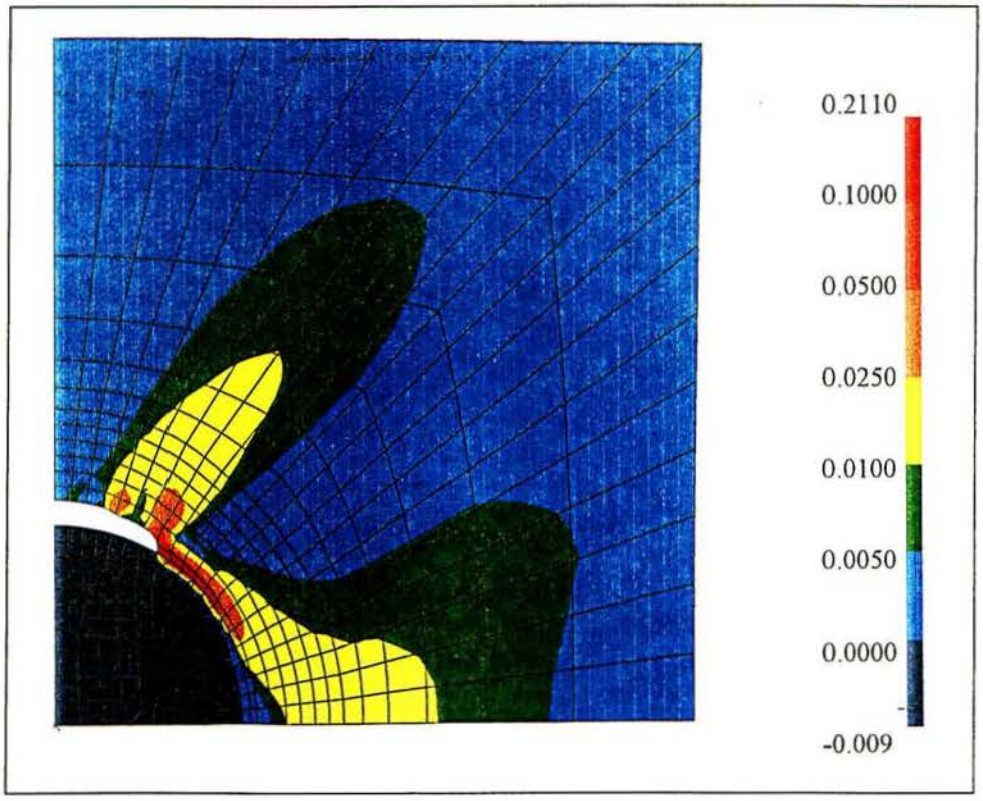
0.2110
0.1000
0.0500
0.0250
0.0100
0.0050
0.0000
-0.009

(b)

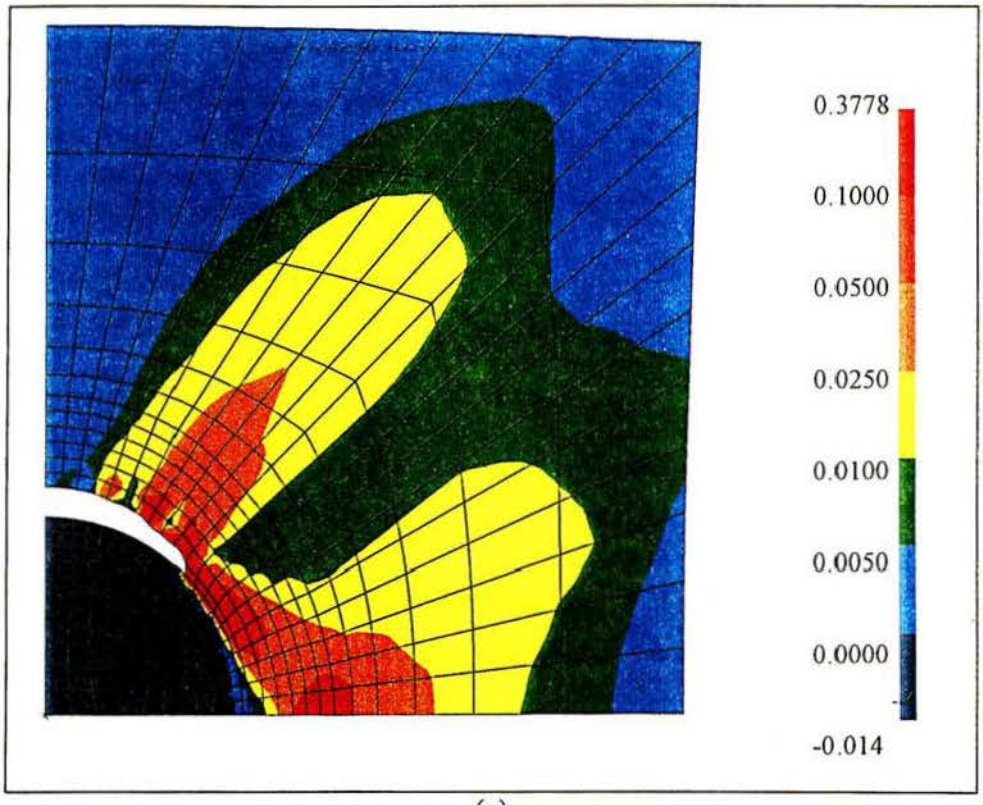
0.3778
0.1000
0.0500
0.0250
0.0100
0.0050
0.0000
-0.014

(c)

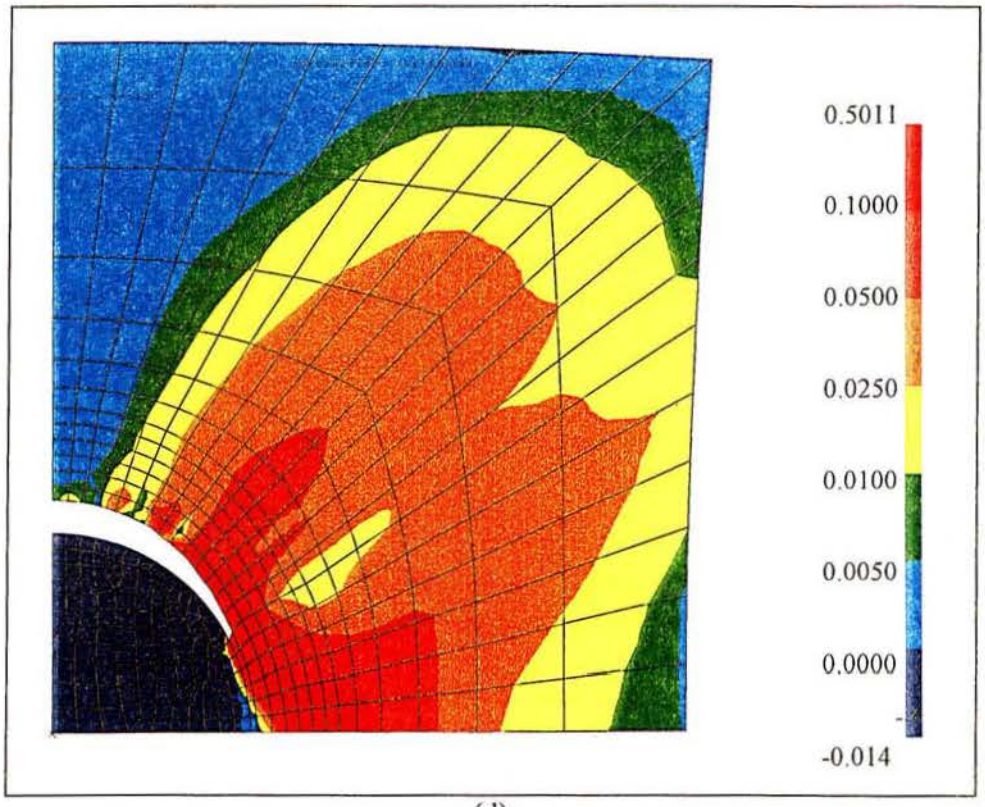

(d)

Fig. VI.B.1.13. Variation of the equivalent plastic strains ε_v^p with progressive deterioration of the interface, $\Sigma_{yy}/\sigma_{Y0} = 1{,}467$

The figures clearly exhibit the increase of the microcrack opening δ with progressive deterioration of the interface. The degradation of the interface might be quantified by the interface crack length γ. Both quantities are illustrated in Fig. VI.B.1.14.

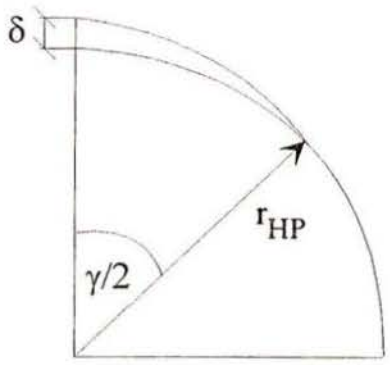

Fig. VI.B.1.14. Schematic of crack opening δ and interface crack length γ

The following values have been found for different lengths of the interface crack:

	Fig b; γ=63°	Fig c; γ=90°	Fig d; γ=126°
δ/d_{HP} [%]	5,67	6,66	8,00

The crack tip openings after debonding with an interface crack length of 126° and after particle cracking are identical (8%), however, plastic strains are much more elevated after debonding

differing of about one magnitude (50,11% after debonding, 5,82% after particle cracking). The following aspects are expected to play an important role in this context:

- The shape of the crack (straight or bended crack)
- The macroscopic stress at damage initiation (Σ_{yy}/σ_{Y0}=1,444, Σ_{yy}/σ_{Y0}=1,467)
- The simulation technique (introduction of additional nodes, elimination of elements)

The straight crack after particle cracking might promote brittle crack propagation into the matrix. This may be supported by the high stress concentration factors in front of the crack tip. In contrast the energy released by debonding is rather transformed into plastic deformation and favours hence ductile crack growth in the matrix.

Finally, the particle has been replaced by a void as an approximation of an extreme weak interface. Figure VI.B.1.15 shows the interface stress distribution at the load step Σ_{yy}/σ_{Y0} = 1,467.

Due to the existence of a free surface, the shear and radial stresses are almost equal to zero. The hydrostatic and circumferential stresses may be compressive or tensile depending on the angular position:

$0<\alpha<45$: stresses slightly decrease (maximum value at 0°, stress concentration factor for the hydrostatic stresses: 1, for the circumferential stresses: 2)

$45<\alpha<67,5$: stresses are drastically dropped and become compressive

$67,5<\alpha<87$: stresses are nearly constant and compressive (stress concentration factor for the hydrostatic stresses: -0.66, for the circumferential stresses: -1.31)

$87<\alpha<90$: the stresses are suddenly dropped to zero

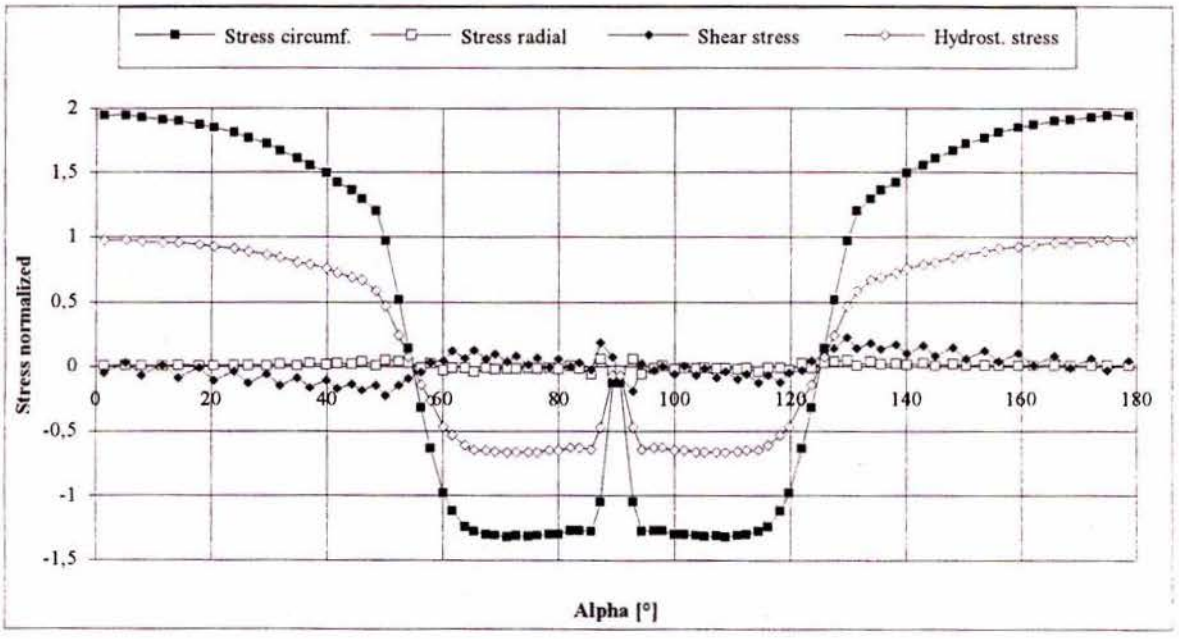

Fig. VI.B.1.15. Stress distribution along the boundary of a void: Σ_{yy}/σ_{Y0} = 1,4667

The evolution of the plastic strain field in the interface and in the matrix is documented in figures VI.B.1.16. It can be seen that plastic deformation in the matrix starts at a loading below the yield strength. With increasing loading the initially spherical void becomes an ellipsoid.

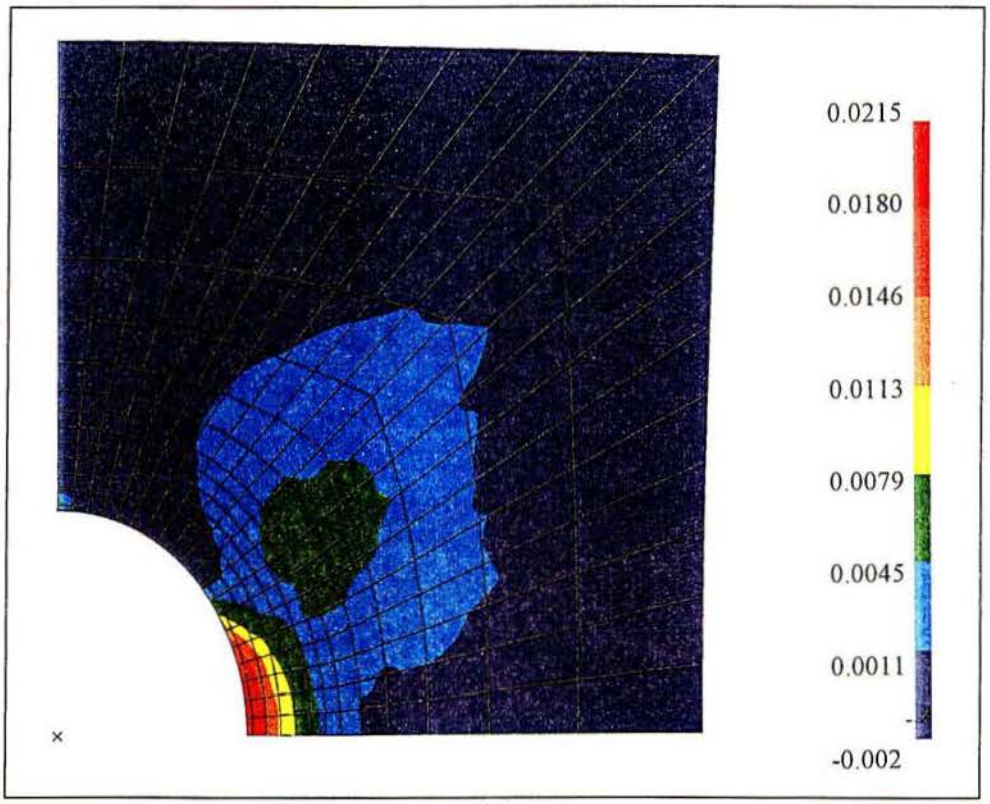

(a)

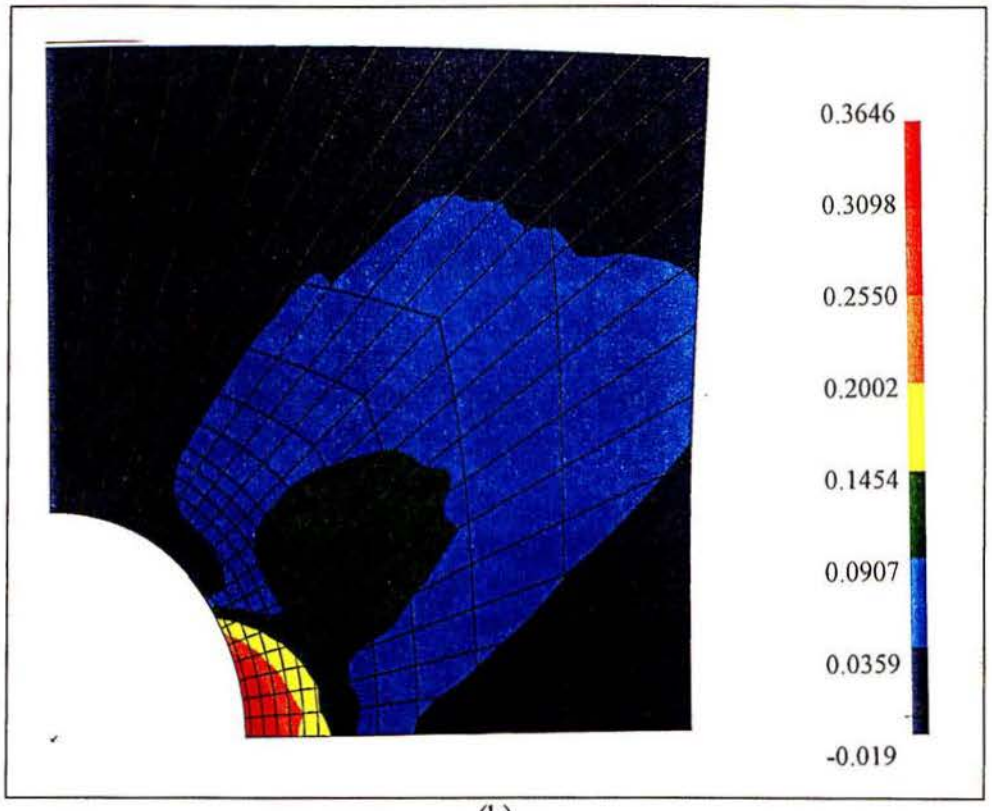

(b)

Fig. VI.B.1.16. Equivalent plastic strains ε_v^p at loading: $\Sigma_{yy}/\sigma_{Y0} = 0{,}889$ (a); $\Sigma_{yy}/\sigma_{Y0} = 1{,}467$ (b);

Weak interface subjected to compression

Most simulations of damage initiation in composites reported in the literature are conducted under tensile loading. Damage simulation under compression is known to be a complicated task. Indeed, non-trivial contact and friction conditions additionally enter the numerical problem. This study here intends to make a first step in the analysis of crack initiation under compression. Crack initiation is simulated by interfacial failure under pure mode II (shear failure σ_{IIc}=700 MPa) allowing a frictionless sliding motion of the interface (see chapter V.4.2).

As expected after studying the distribution of the shear stresses along the interface, interfacial debonding is initiated at α=45°. The figure below shows the plastic strain field after failure of three interface elements.

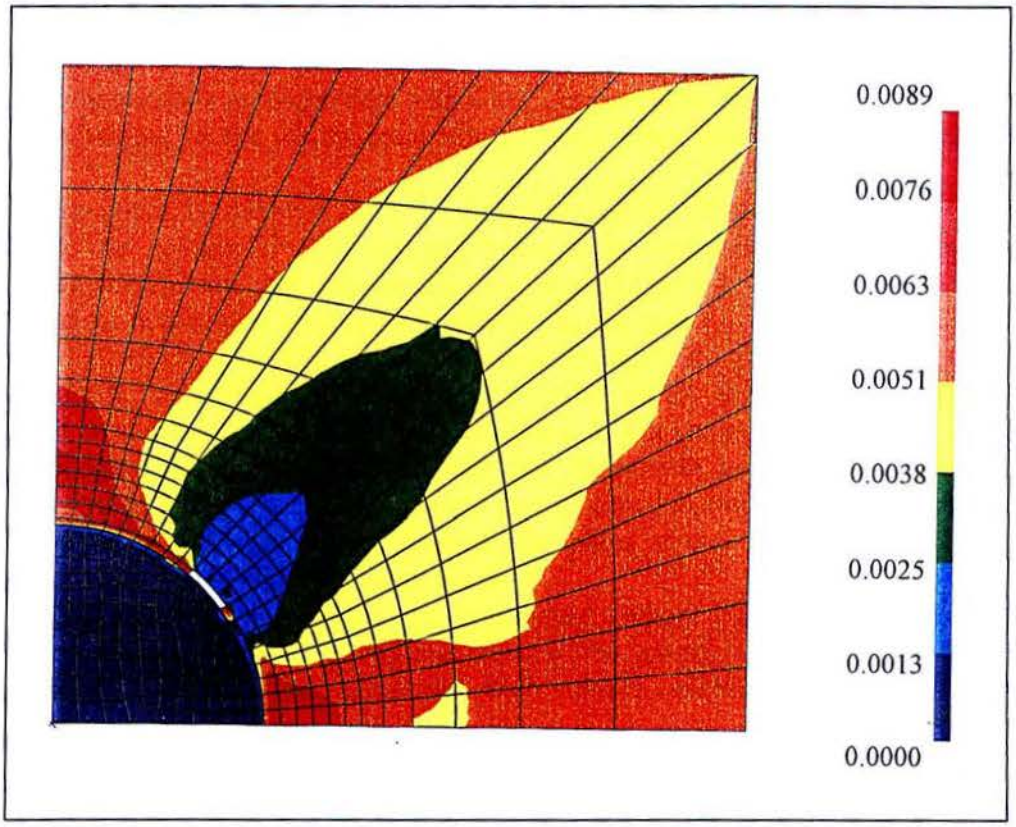

Fig. VI.B.1.17. Equivalent plastic strains ε_v^p after initiation of debonding under pure mode II at loading: Σ_{yy}/σ_{Y0} = 1,622

Before the onset of damage, plastic yielding at the interface evolved at α=45°. After initiation of debonding (at loading Σ_{yy}/σ_{Y0} = 1,467), plastic deformation mainly spreads out along the straight prolongation of the interface crack due to stress redistribution. The latter was the driving force to advance the interface crack under tensile loading. In a compressive regime this is, however, not sufficient, so that the interface crack does not proceed instantaneously.

Unfortunately, the simulation failed to further predict the evolution of the interface crack due to a numerical collapse: The next failed element was not located adjacent to the microcrack, the retained element between them became the source of that collapse.

VI.B.2-Modelling of different microscale arrangements- (Interaction between HP-HP)

VI.B.2.1-Model description

In the previous chapter it could be seen that the interaction between the MM and the HP gives rise to a highly inhomogeneous stress distribution despite of the imposed uniform remote stress. The stress disturbance in the matrix around the stiffer HP and the stress concentration within the HP could be associated to the mutual constraint of the deformation between HP and MM. An important impact on this parameter was found to be the particle shape. The extent of the region where the stress field is disturbed by the presence of the HP depends strongly on its shape. If more than one HP is inherent in the model one can already expect that the individual fields around the HP might cross and hence interaction between the HP becomes another important feature controlling the microscale stress and strain pattern. The main objective of these studies is on one hand to investigate this interaction behaviour and on the other hand to model specific microscale arrangements which are characteristic for the here investigated class of materials belonging to the matrix-inclusion topology. Four different arrangement types are treated:

The first arrangement considers a rather regular distribution of the HP. A perfect regularity would allow to use a single HP-MM unit cell model in the way described in chapter I.3. In this case hexagonal or quadratic unit cell models may be used (see fig. I.3.1). In the past they have been employed to investigate arrangement effects on the micro- and macroscale response of MMCs [e.g. BÖH 93A,B, COR 95]. However, a realistic microstructure does not exhibit such a perfect periodicity. In addition, they seem not to be useful for damage simulation, since microcracking would occur throughout the structure at the same time [GRO 95, MIC 93]. In order to investigate the evolution of damage due to particle cracking, a unit cell with 16 randomly distributed HP is used in the present study (called in the following Dispersion). The shape of the HP are assumed to be cylinders (for plane strain) or circular discs (for plane stress). In each case, all HP have the same shape.

Beside the dispersion, arrangements are considered, where HP have been concentrated together within one region with high volume content (the colony, see chapter II.2.1), the other region with no HP-presence. The region with high volume content, the colonies, are localized within

1-cylinders (or circular discs) these in turn are distributed perfectly within a hexagonal arrangement (see also fig. I.3.1) (called in the following Cluster).

2-the region around the above described cylinders (called in the following Net)

3-bands (called in the following Band)

The figure below illustrates schematically the unit cells of the different arrangements

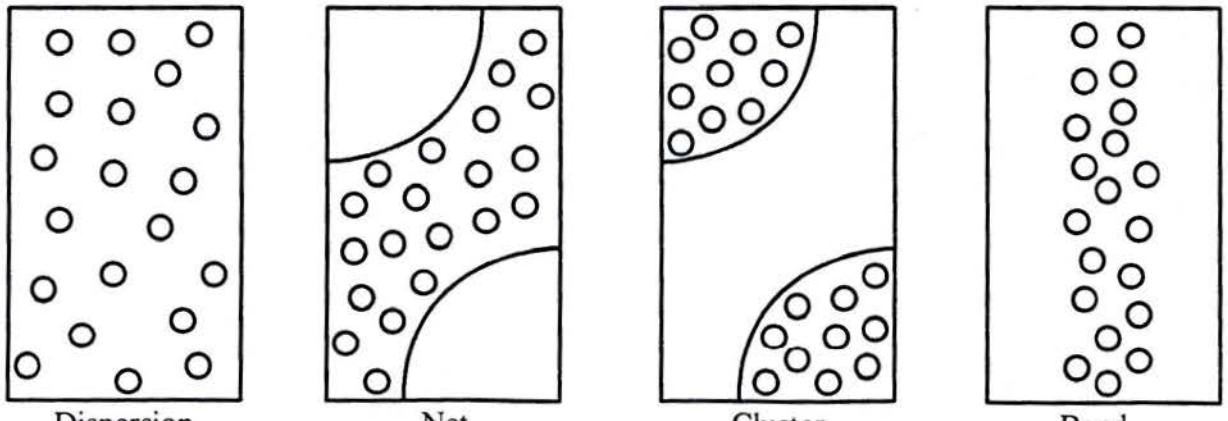

Fig. VI.B.2.1. Different classes of matrix-inclusion topologies inherent in the unit cells

The number of HP (N_{HP}=16) and the respective volume fraction (ξ_{HP}=15%) are equal in all unit cells. The considered arrangements are representative to a certain extent for the microstructural arrangement of the investigated materials. The band structure shall describe the microstructure after warm forging, the net-like structure that in the as-cast condition. The dispersion is achieved after a severe warm forging process but is also typical for materials manufactured by powder metallurgy (PM) and hot-isostatic pressing (HIP). These materials were investigated in a just offgoing project [BER 96]. In the same project the cluster arrangement has received much attention and the manufacture of such a material was realized using advanced manufacturing techniques [BER 96]. The volume content in the cells (ξ_{HP}=15%) is close to that in the considered material (ξ_{HP}=16%). The shape of the HP in the model (cylinders, or circular discs) and in the material (mostly aligned HP with aspect ratio different from unity) do not coincide. However, cylindrical (resp. discs) HP have been intentionally chosen since the main interest here should be centred on effects due to the arrangement of the HP rather than that of their shape.
The boundary conditions are taken such that symmetry is prescribed over all edges of the cell. The load is applied incrementally and displacement controlled. Load direction is the vertical axis. The macroscopic load is strain driven and computed through the imposed displacement values (eqn. V.5.2a). The material parameters are taken from the heat treatment condition 600 (see Appendix A.3). Damage evolution in this material is simulated by activating the local damage criterion of particle fracture and by quasi-static proportional loading applying successively small load steps. In the experiments particle cracking was observed to be the dominant damage mechanism, therefore, the effects of debonding and matrix damage are excluded in this analysis for the first. The fracture strength of the carbides is assumed to be 1800 MPa.

VI.B.2.2-Microscopic Response

Progressive carbide fracture

The following figures aim to illustrate how damage is initiated and evolves by progressive carbide fracture in the different microstructures (exemplary for the banded (Fig. VI.B.2.2; (a,b) load parallel to the bands, (c,d) load perpendicular to the bands), cluster (Fig. VI.B.2.3 a,b) and net-like structure (Fig.VI.B,2,3c,d)). The results show the maximum principal stress distribution. All values are given in MPa.

Stage up to initial damage: Before the onset of damage, stress concentrations arise mainly within the particle. This may be attributed, following the analytical model of the forgoing chapter, to the occurrence of interfacial shear stresses which give an important contribution to the transmission of the load over the particle. The development of interfacial stresses itself is dependent on how the deformation of the matrix is constrained by the stiffer particles. This is strongly influenced when HP are interacting with each other. HP-Interaction shall be understood as an intersection of local disturbed stress fields around individual HP. This interaction behaviour might have a shielding or an amplification character depending on the orientation of adjacent particles to the principal load direction. The stress concentration within the particle is increasing when the trajectory of adjacent HP is in line with the principal load path and decreasing when it is perpendicular to that. This effect becomes visible when studying the situation in the banded structure. If the load is applied parallel to the band (Fig. VI.B.2.2a) the stress values within the HP and in the matrix are different of order 1.160. When the load is applied perpendicular to it (Fig. VI.B.2.2.c) the ratio of the stresses in both regions is about 1.057. Increasing the HP-content in these bands would decrease the HP-spacing. As a consequence these results tend to approach the lower and upper bounds in elasticity (for plastic strains being negligible) according the models of Reuss (σ_{HP}/σ_{MM}=1.333) and Voigt (σ_{HP}/σ_{MM}=1.0) (previous chapter, see also chapter I.2).

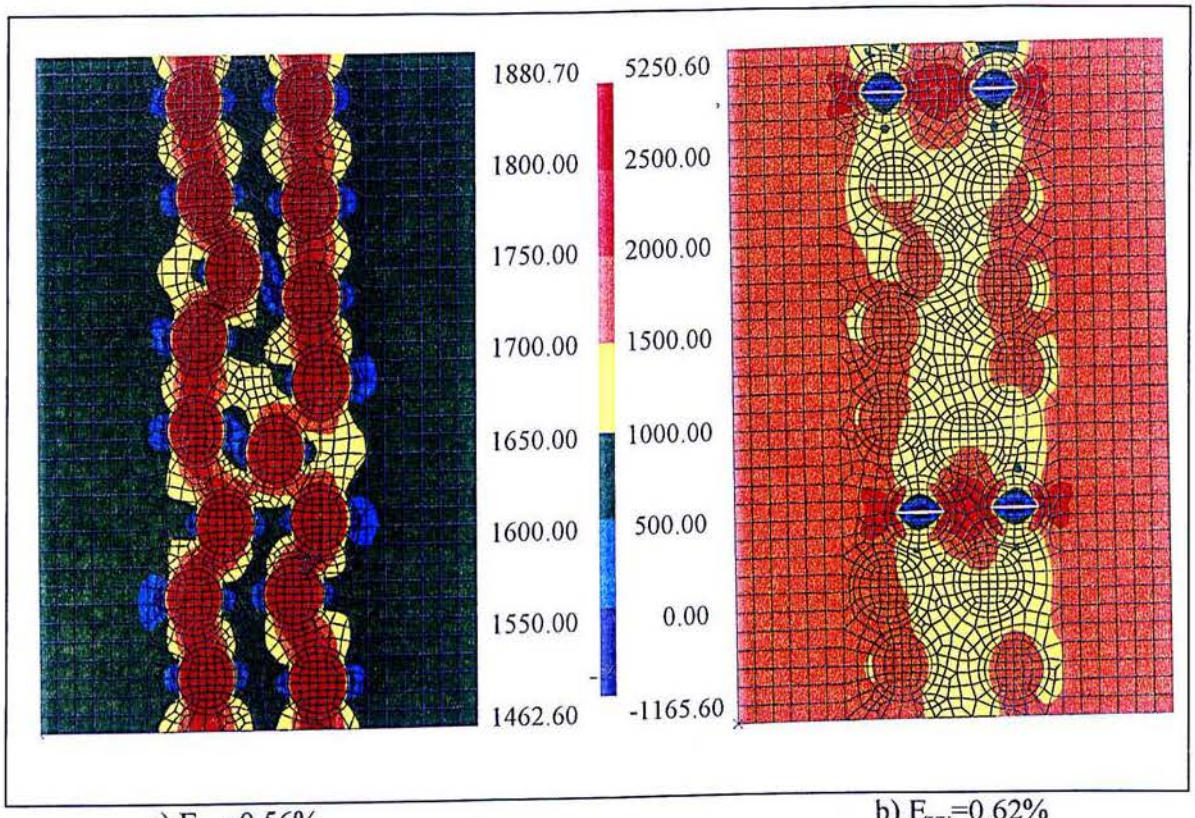

a) E_{yy}=0.56%

b) E_{yy}=0.62%

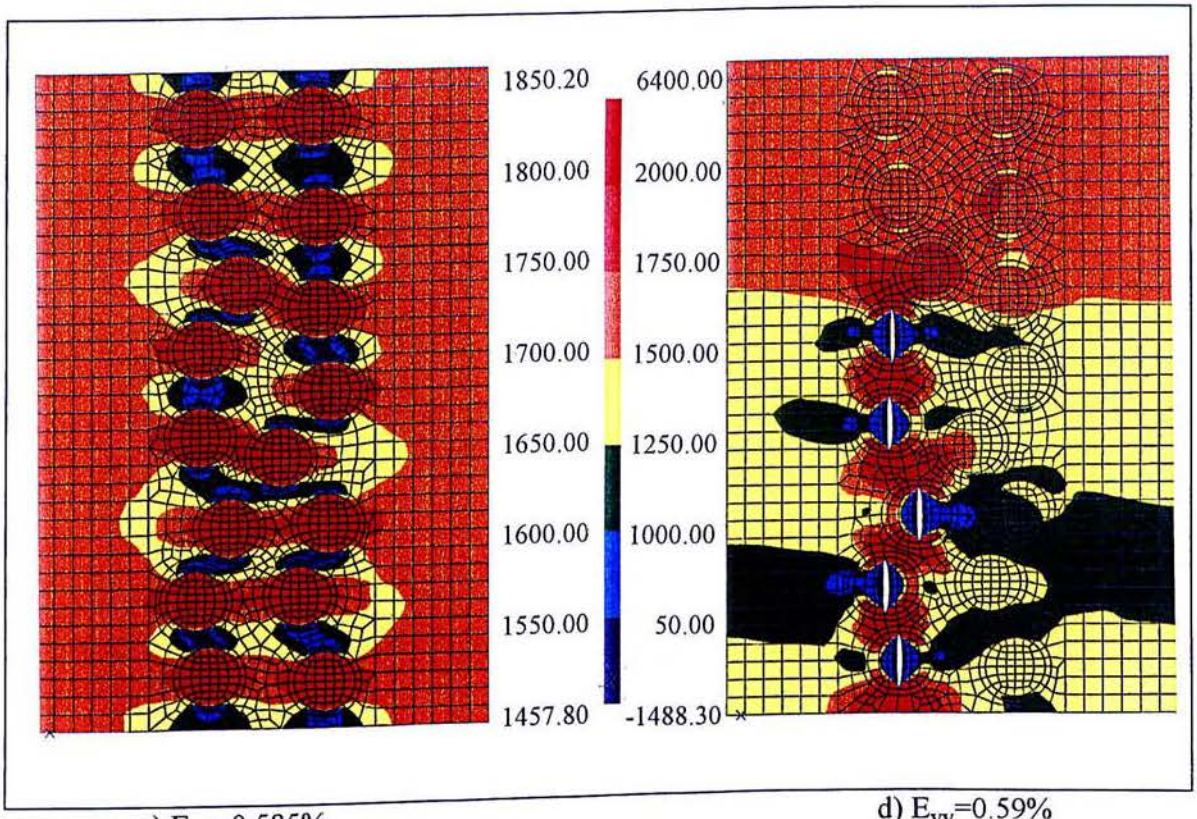

c) E_{yy}=0.585%

d) E_{yy}=0.59%

Fig. VI.B.2.2. Maximum principal stresses σ_I [MPa] in the banded arrangement (a-b) load in vertical axis; (c-d) load in horizontal axis

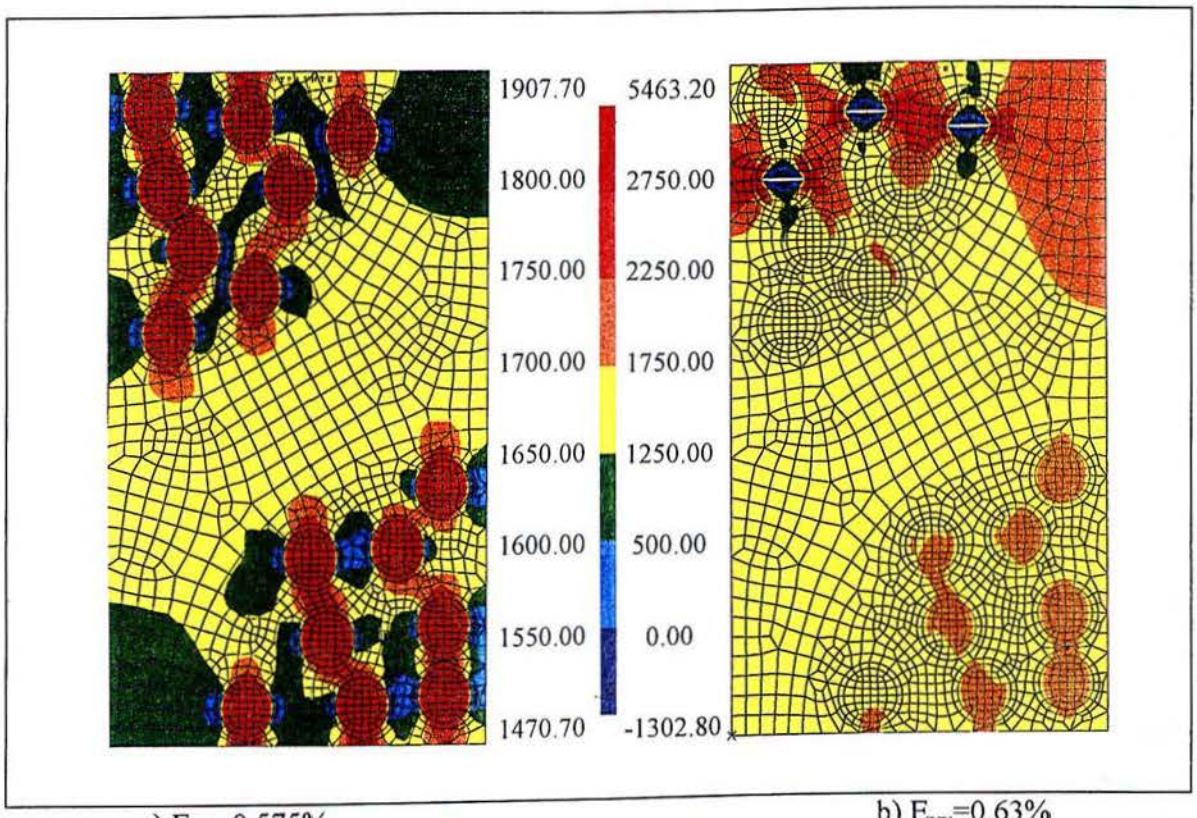

a) E_{yy}=0.575%

b) E_{yy}=0.63%

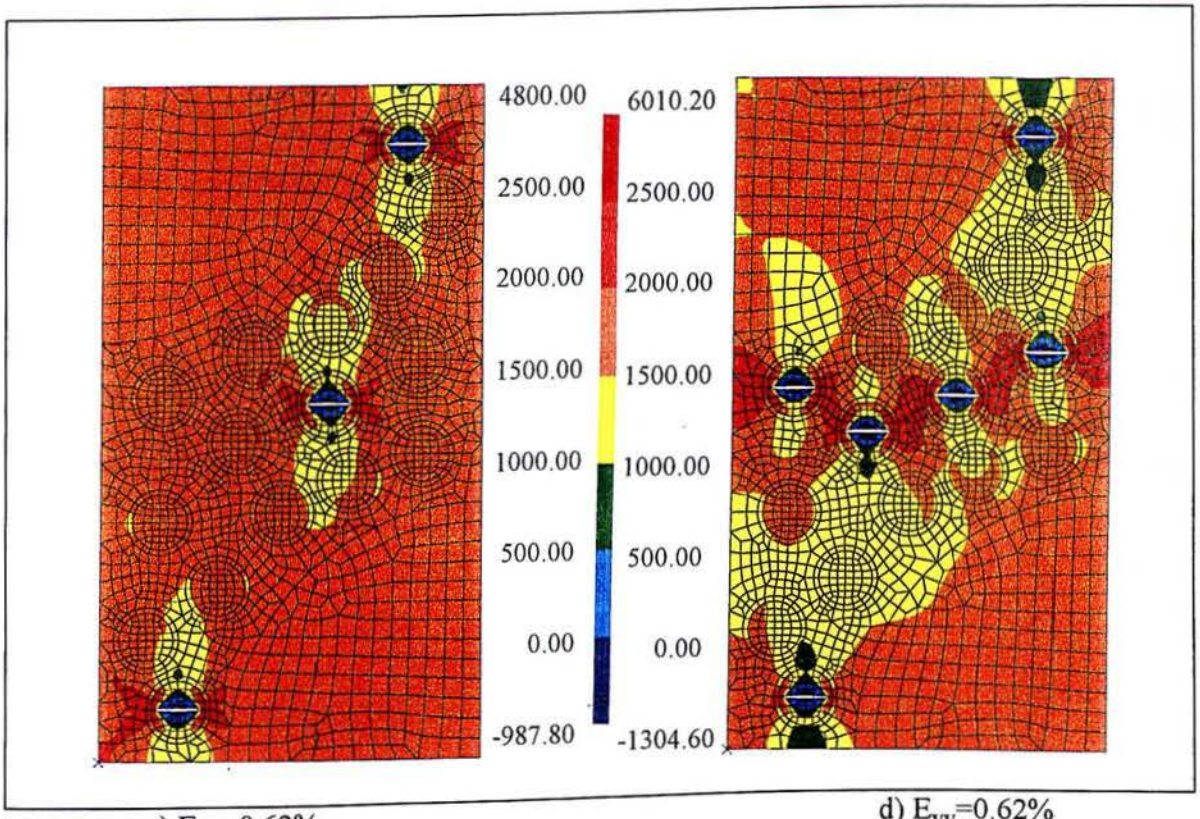

c) E_{yy}=0.62%

d) E_{yy}=0.62%

Fig. VI.B.2.3. Maximum principal stresses σ_I [MPa] in the (a-b) cluster arrangement; (c-d) net-like arrangement

This idea, that HP belonging to one row act as a single aligned HP, is furthermore supported when studying initial damage in the cluster (Fig. VI.B.2.3a,b) and particularly in the net-like structure (Fig. VI.B.2.3c,d).
In the latter arrangement damage is initiated in those particles located at the mid-length of one row in load direction (Fig. VI.B.2.3.c, Fig. VI.B.2.4)

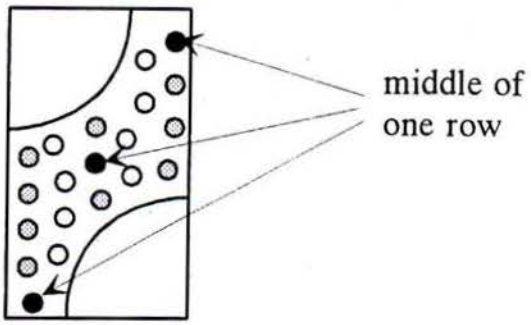

Fig. VI.B.2.4. Damage initiation in the net-like structure

Subsequent occurrence of damage: Subsequent failure of HP due to fracture is strongly related to their orientation to previously developed microcracks. Mostly, stress redistribution due to cracking of a HP leads to simultaneous microcracking of adjacent HP (in direction of the microcrack) without increasing the external load. In particular in the band direction, first HP-fracture leads to a chain reaction where subsequently the neighbouring particle is cracked.
Since all microcracks lie within a trajectory perpendicular to the load direction, final material failure is expected by fracture of the matrix ligaments under mode I. The failure in the matrix ligaments is believed to be dependent on the orientation and spacing of neighbouring microcracks and the ductility of the matrix. Accordingly the cluster arrangement seems to be most favourable since the large "matrix net" may act as an important obstacle for microcracks of neighbouring clusters to link together.

Competition between particle cracking and interfacial failure
The competition between both damage mechanisms is investigated exemplary for the dispersion (Fig. VI.B.2.5). In addition to particle cracking the failure criterion of interfacial failure under pure mode I was activated and assumed to be equal to the fracture strength of the particle (σ_{Ic}=1700 MPa). In the undamaged state, "streets" of highly loading following the particles in load direction can be made out (Fig. VI.B.2.5a).
The first microcrack develops at the interface (Fig. VI.B.2.5b) extending rather quickly up to a stabilization point where the upper half of the particle is totally debonded and the lower half is shielded by the deflection of the load. As a result, the load is carried by the neighbouring metal matrix which leads to stress concentration in nearby particles. Here, the orientation between neighbouring particles strongly influences the sites of maximum stress values and determines therefore the mode of failure (on the left side particle cracking, on the right side interfacial failure Fig. VI.B.2.5b).

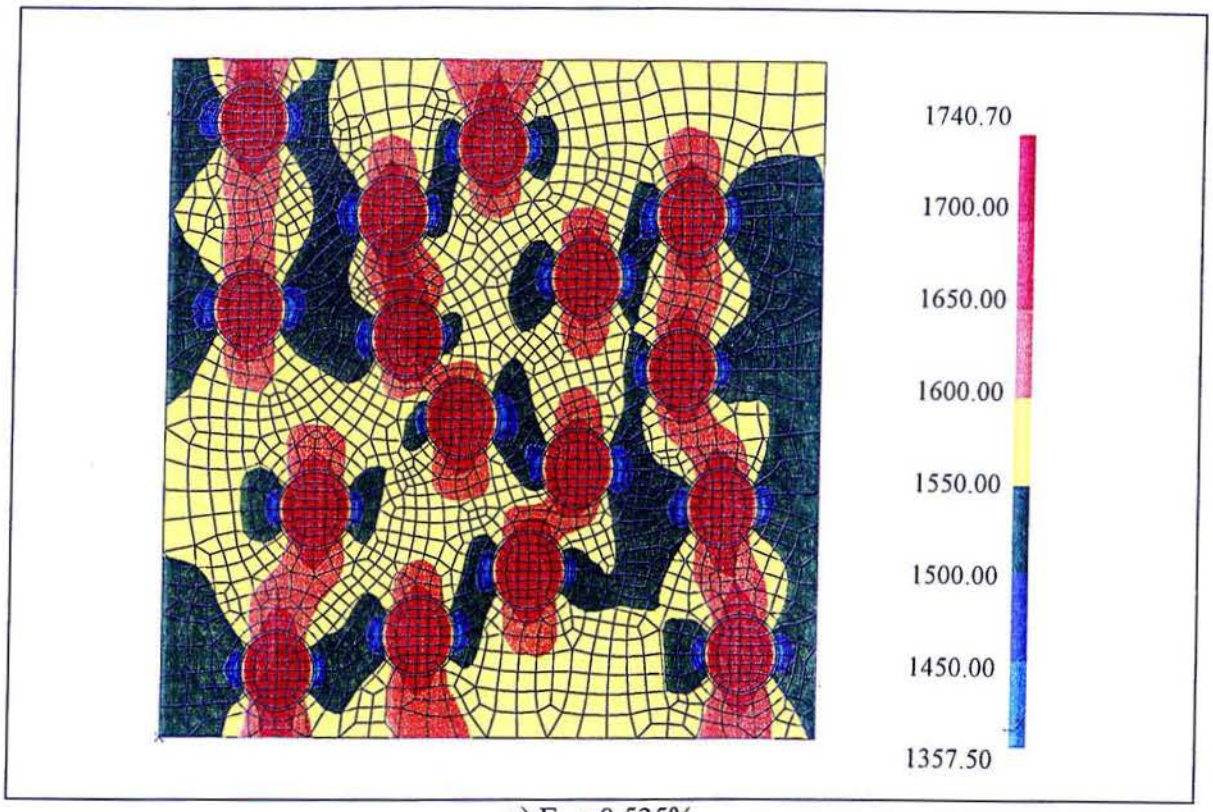

a) E_{yy}=0.535%

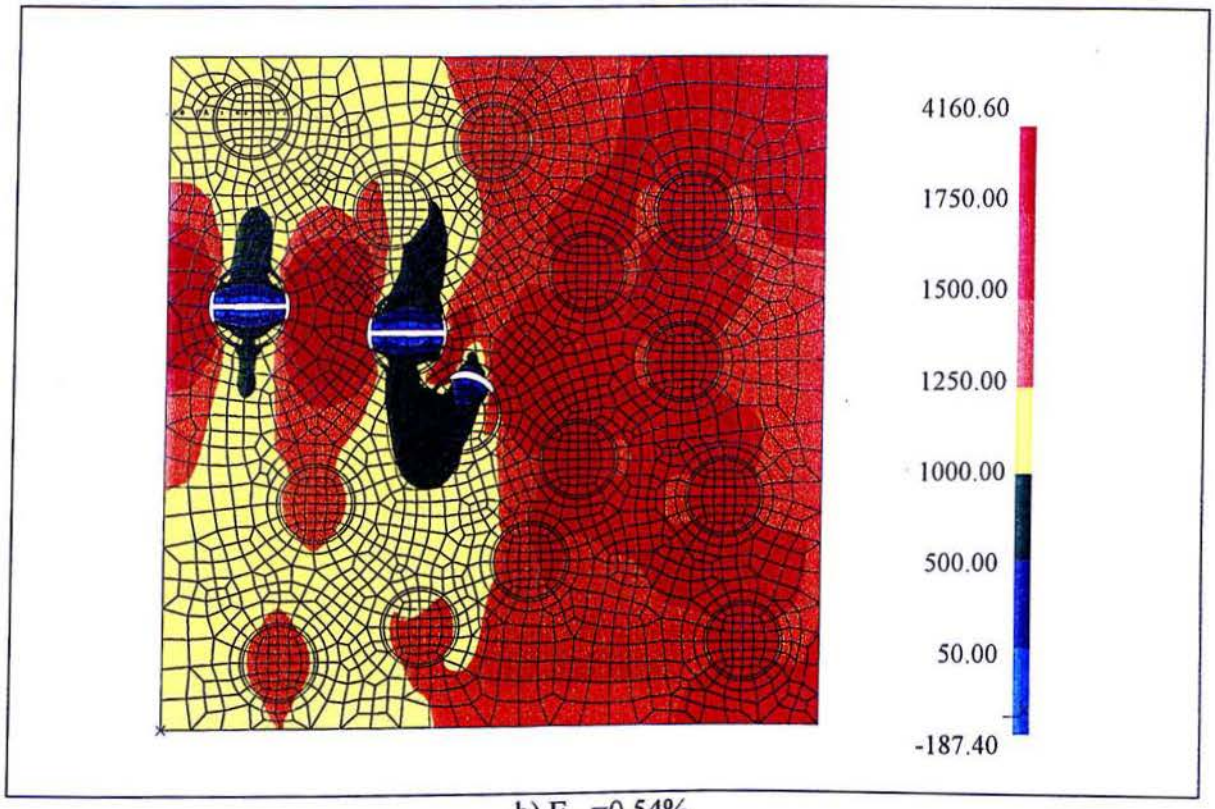

b) E_{yy}=0.54%

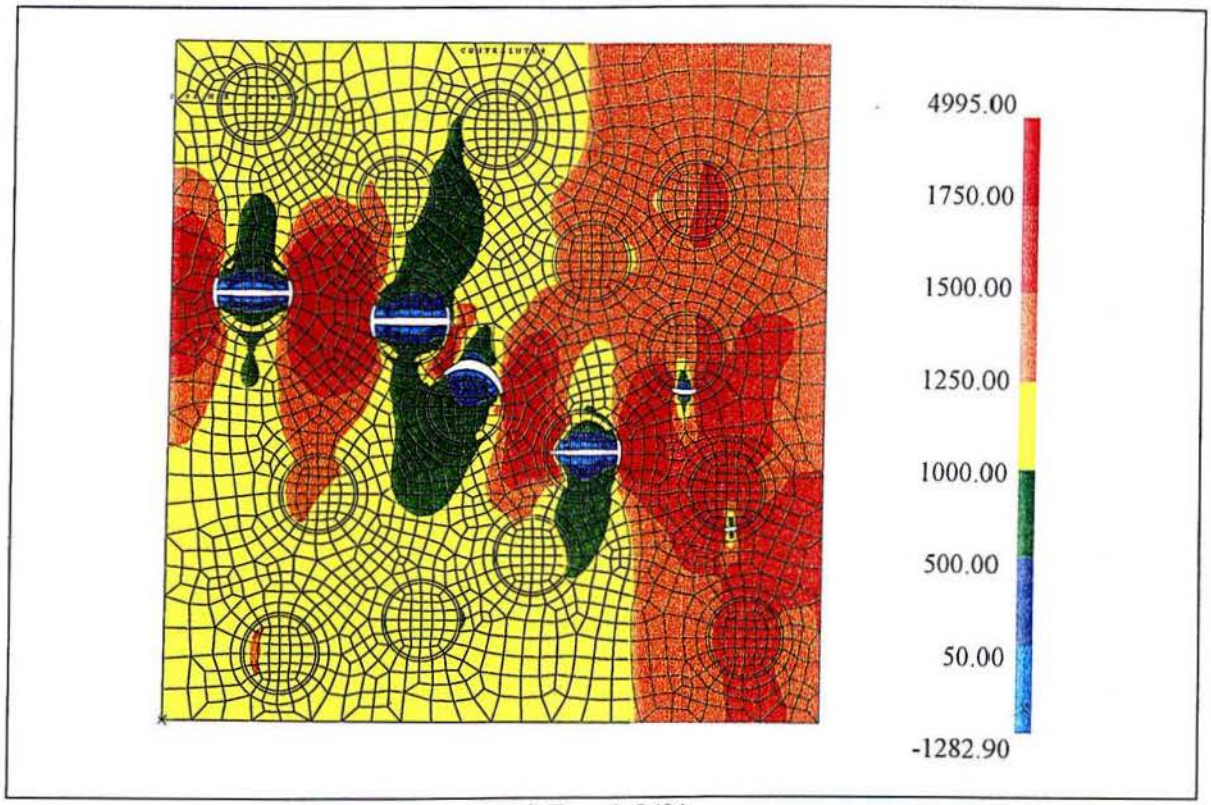

c) E_{yy}=0.54%

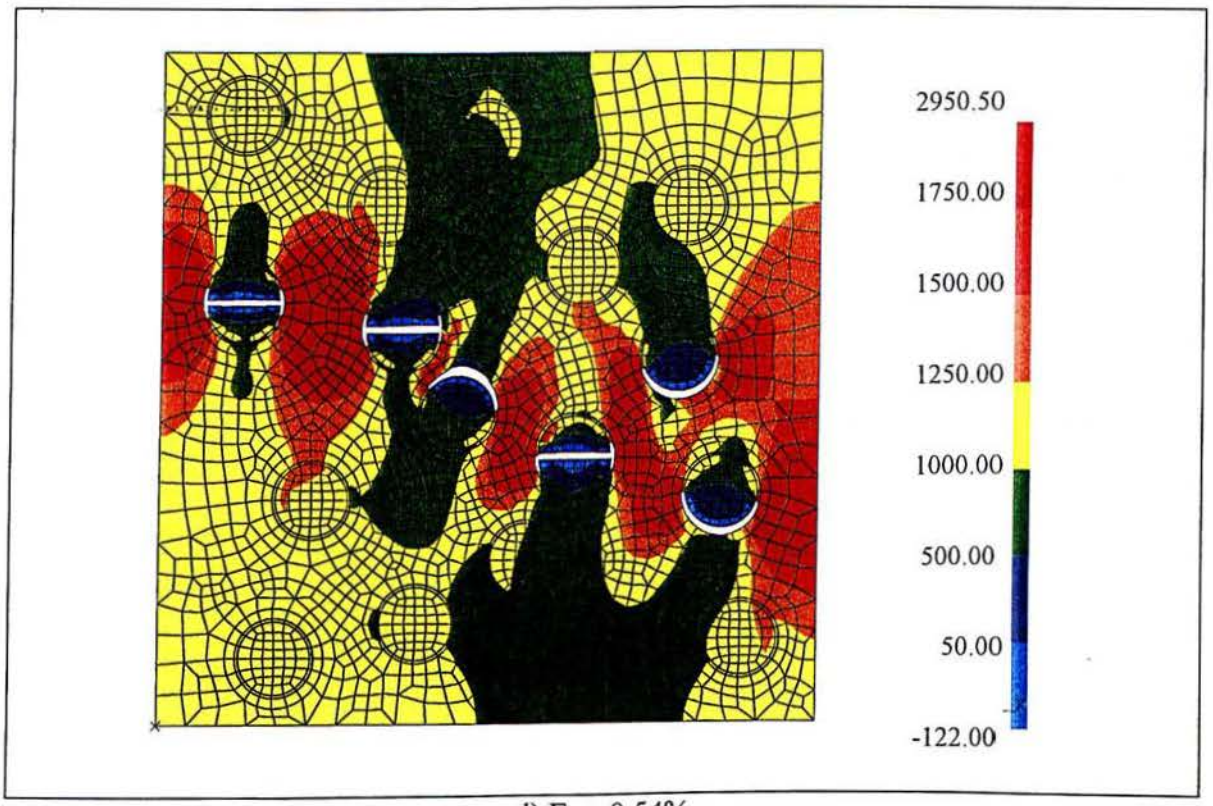

d) E_{yy}=0.54%

Fig. VI.B.2.5. Maximum principal stresses σ_I [MPa] in the dispersion

The sudden fracture of a HP changes completely the interfacial stresses (Fig. VI.B.2.6):
Before the fracture event the radial stresses are maximum (tensile) for α=90° and decrease with decreasing α; for α=0° they are almost zero or slightly compressive (see chapter VI.B.1).
Instantaneously after the failure event considerable radial stresses arise at the front of the crack tip (Fig.VI.B.2.6) which may trigger interfacial debonding. This effect could be reproduced in the simulations (Fig. VI.B.2.5b-d) and was equally observed in experiments (Fig. II.3.4).

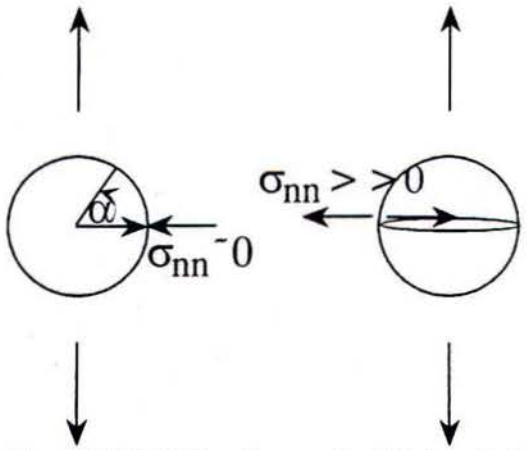

Fig. VI.B.2.6 Development of high radial stresses in front of the microcrack

Generally the release of energy by microcracking is absorbed by the MM and results in plastic deformation. The failed particles can no more transmit the load and are stress-free. Stress maxima are concentrated at the crack tips. With further evolution of damage (Fig. VI.B.2.5d) the matrix ligaments between the microcracks are extremely loaded. Above and under this "damage band" the stress pattern becomes rather homogeneous. The mutual deformation constraint becomes less important, stress concentrations will move out the particles (Fig. VI.B.2.5c,d).
In order to predict the crack path in the matrix three different damage indicators were used and plotted in the following. The first one is based on equivalent plastic strain ε_v^p (Fig. VI.B.2.7a,b). The regions in dark blue localize initial plastic deformation before the onset of damage. However, plastic strains are more elevated in front of the crack tips (up to 16%). The crossing of these local plastic fields leads to plastic bands connecting the individual microcracks.
Figures VI.B.2.8a and b show the distribution of the damage indicator after Fischmeister et al. (eqn. IV.1.6) and after Rice & Tracey (eqn. IV.1.5d for ε_0=0.04), respectively. The value for the failure strain ε_0 is in agreement with the mean value of the uniaxial failure strain of the matrix material in the heat treatment condition "600" of orientation L (A=6,35%) and T (A=2,28%) (see Tab.II.3.2).
The damage indicator of Fischmeister et al. has the dimension MPa that of Rice & Tracey is dimensionless. The damage indicator gets its significance when assuming a critical limit within the range of values where beyond this value matrix damage is considered. (Recall, that the critical value of the Rice & Tracey model is known and equal to one (see chapter IV.2).)
With respect to this definition the predicted crack path by Fischmeister et al. might not be physically reasonable, since one expects ultimate failure by linking together all microcracks. In contrast, the prediction by Rice & Tracey is in good agreement with the natural expectation. As a result of that model, it is believed that the triaxiality in a plastic field controls crack propagation in the matrix.

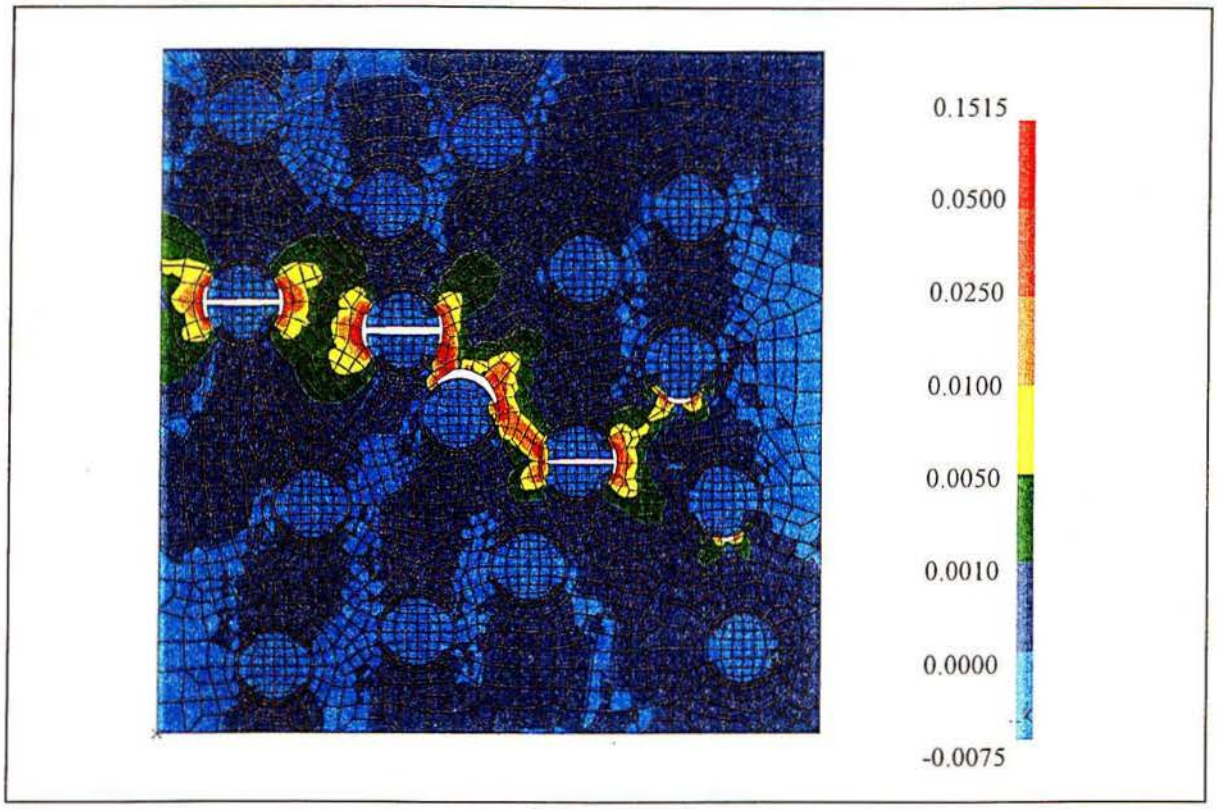

a) E_{yy}=0.54%

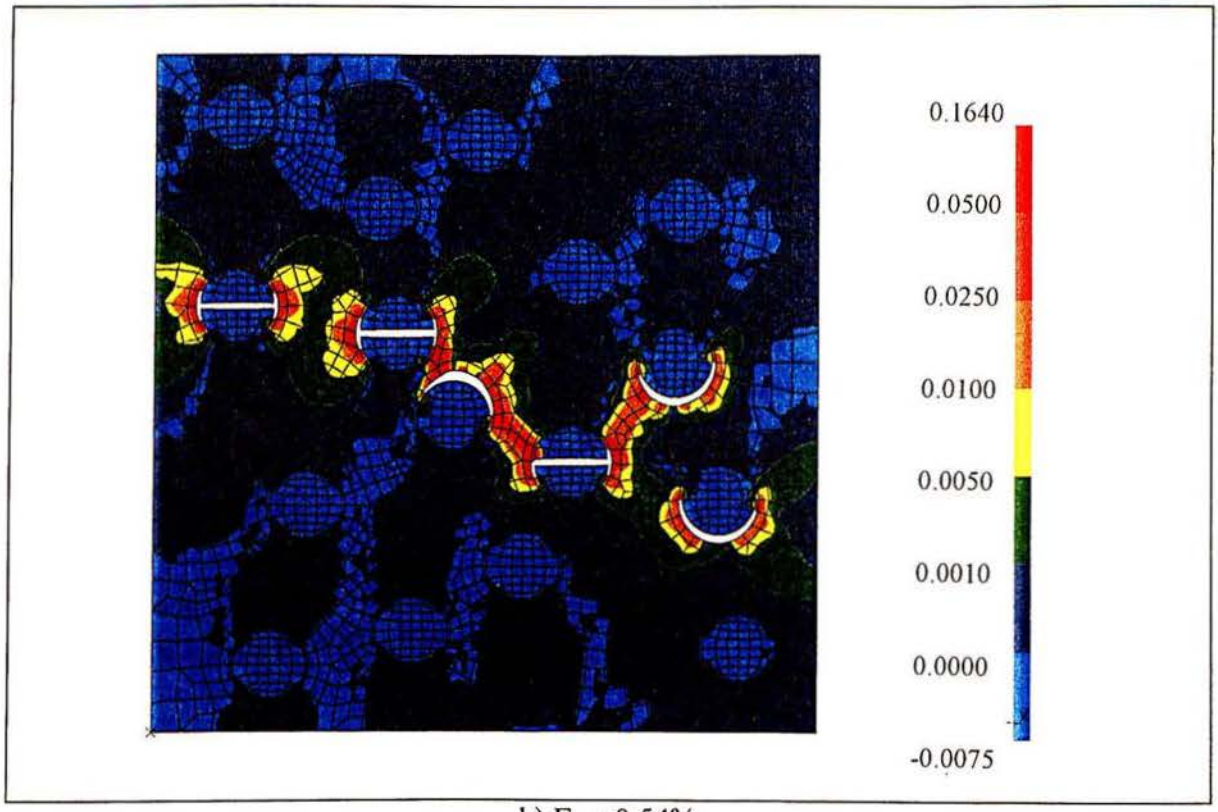

b) E_{yy}=0.54%

Fig. VI.B.2.7. Equivalent plastic strain ε_v^p [-] in the dispersion

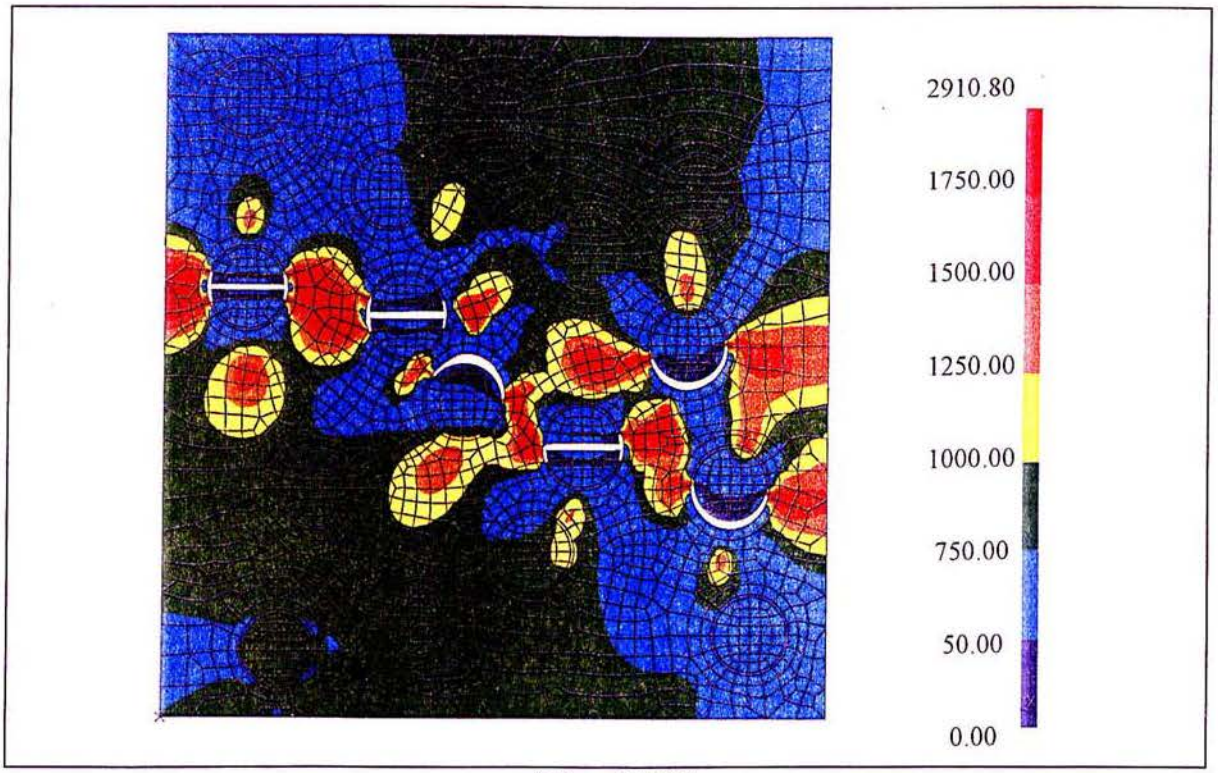

a) E_{yy}=0.54%

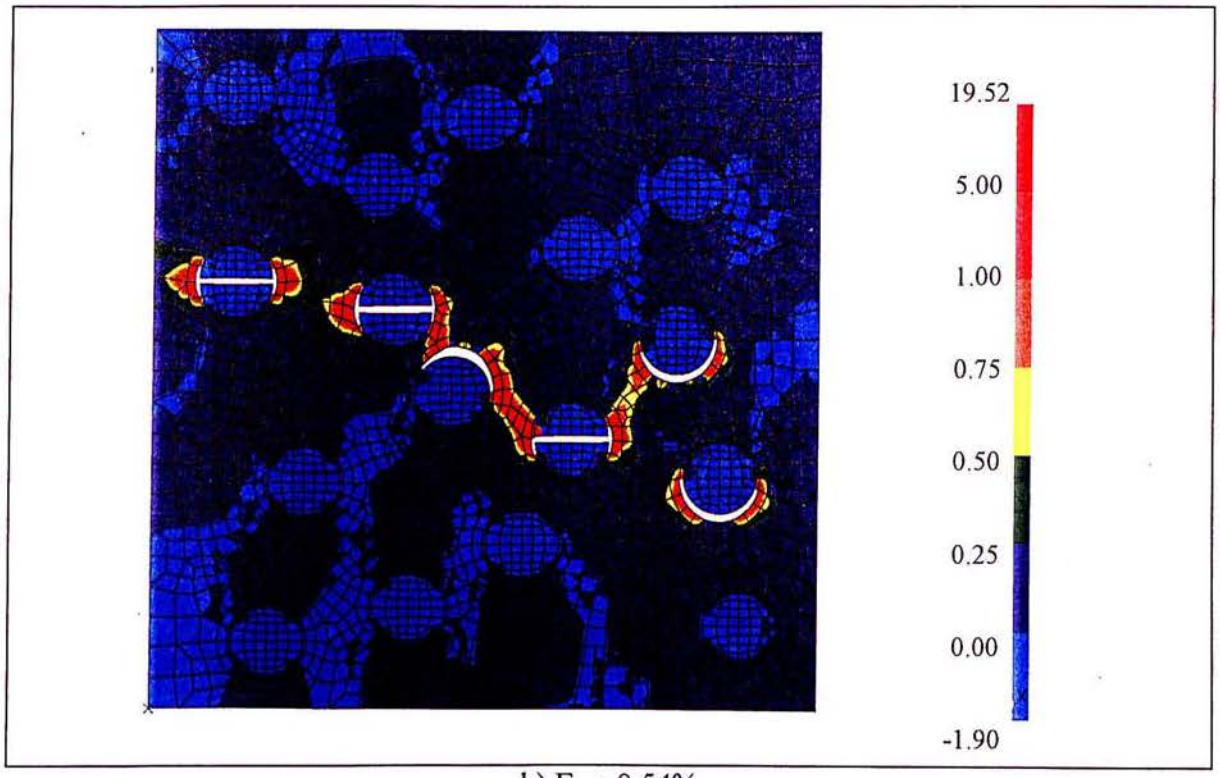

b) E_{yy}=0.54%

Fig. VI.B.2.8. Selected damage indicators

a) Fischmeister et al.: $D_i = \frac{\sigma_H^2}{\sigma_v}$ [MPa]; b) Rice&Tracey: $D_i = \int_0^{\varepsilon_y^p} \frac{\exp(1.5 \cdot \zeta)}{1.65 \cdot \varepsilon_0} d\varepsilon_v^p$ [-]

VI.B.2.3-Macroscopic response

The transition scheme from the micro- to the macroscale (eqn. V.5.1-V.5.3) allows to investigate the influence of microstructural parameters on the macroscopic response. Exemplary the influence of the arrangement on the elastic and on the damage response was studied. Table 5B.3 lists the predictions for the effective Young's modulus of the composite material together with the macroscopic strain at initial damage. The effective Young's modulus (predicted through the linear elastic constitutive relations for plane stress or plane strain) is slightly affected by the microscale arrangement (Tab. VI.B.2.1). All values are rather close, the most deviations are for the banded structure. Here a slight elastic anisotropy (E_l=219,10 GPa, E_q=218,49 GPa) is found. First occurrence of damage is strongly influenced by the orientation of neighbouring hard phases to the load direction. Small distances of neighbouring HP parallel to the load direction do favour initial damage, perpendicular to the load direction do not. Accordingly first initiation of damage is at different load levels in the different arrangements:

	Band (band parallel to load direction)	Net	Cluster	Dispersion	Band (band perpendicular to load direction)
effective Young's modulus [GPa]	219,10	218,56	218,61	218,92	218,49
initiation of damage at macroscopic strain E_{yy} [%]	0,56	0,57	0,58	0,58	0,59

Tab. VI.B.2.1. Arrangement effects on the macroscopic response

In addition the influence of the HP-content and the triaxiality on the damage evolution in a dispersion was investigated. For this purpose unit cells with up to 70 randomly distributed HP were used in this study. A rather coarse mesh was accepted being aware that the obtained microscale pattern of stresses and strains are not precise.

Damage evolution on the material is simulated by activating the damage criterion of particle fracture and by quasi-static proportional loading (Fig. VI.B.2.9) applying successively small load steps. If particle fracture occurs in one HP, a load-free increment is applied next, to better account for the stress redistribution effect. For simplicity the shape of HP was assumed quadratic.

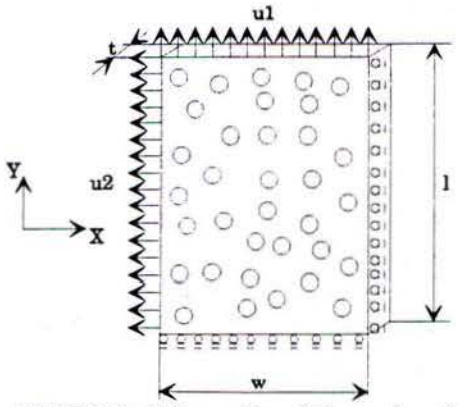

Figure VI.B.2.9. Schematic of the unit cells used in the simulations

The evolution of the damage parameter component D_y is evaluated as function of the prescribed macroscopic strain E_{yy}. In the present case, the resulting curve is approximately linear, so that the evolution function can be determined by either two or three parameters. The latter offers the possibility to define a critical state where global failure of the structure takes place. Therefore E_D, E_R, D_C represent strain at initial damage, strain at rupture and critical damage value, respectively, in accordance with the definition by Lemaitre (see chapter IV.3). Exemplary, the influence of HP volume fraction ξ_{HP} ("unidirectional" tension, u_2=0) on these

damage parameters is studied (Fig. VI.B.2.10). It can be seen that a high volume fraction favours initiation of damage due to particle cracking (e.g. E_D = 0.495% for ξ_{HP}=0.55, E_D=0.550% for ξ_{HP}=0.1778).

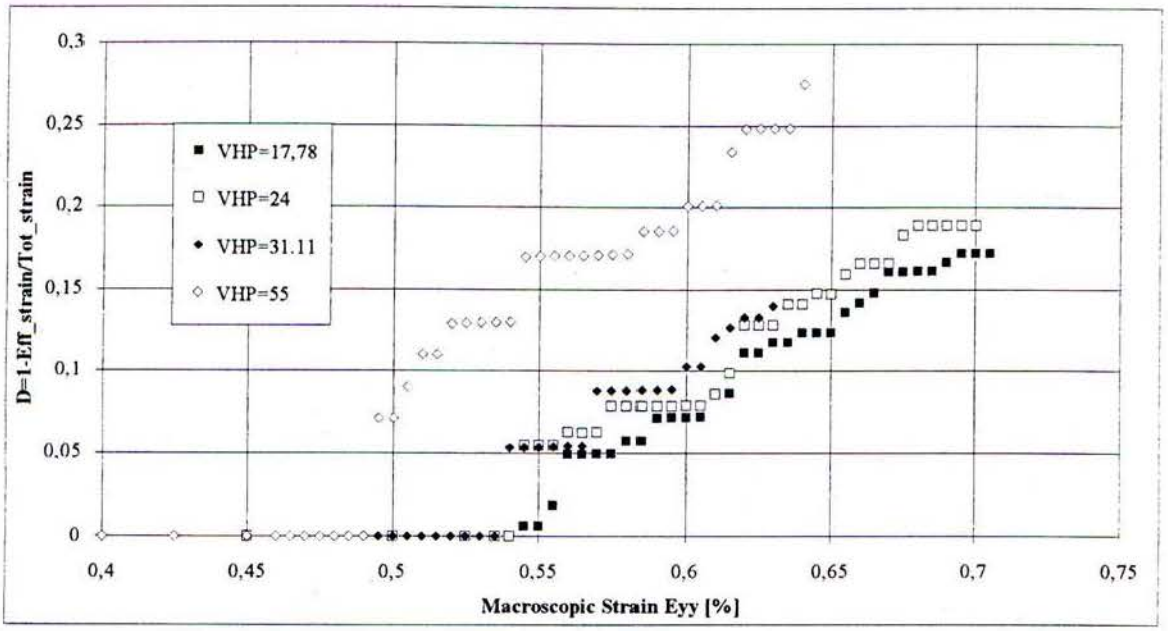

Figure. VI.B.2.10. Influence of HP-volume fraction on damage evolution

The influence of the multiaxiality of loading on occurrence and evolution of damage is reported in Fig. VI.B.2.11. The chosen ratio $u_2/u_1=E_{xx}/E_{yy}$ ranges between -1.0 to 1.0 with u_1 as fixed tensile displacement. The particles are only allowed to break in the horizontal direction. The multiaxiality of loading in terms of the ratio E_{xx}/E_{yy} has a direct impact on the triaxial state in the material. Applying the numerical integration scheme presented in chapter V.5.2 (eqn. V.5.1), the effective (mean) triaxial stress state in the composite has been calculated after each load increment. The respective values have been found to slightly vary during loading. Exemplary the values of the first (elastic behaviour) and the last increment are listed in table VI.B.2.2 together with the mean value of the equivalent plastic strain of the last increment.

	$\zeta_{firstinc}$	$\zeta_{lastinc}$	$\bar{\varepsilon}_v^p$ [%]	$0,5*(\zeta_{firstinc}+\zeta_{lastinc})$
a) E_{xx}/E_{yy}=-1.0	0,0018	-0,0068	1,543	0,0025
b) E_{xx}/E_{yy}=-0.5	0,358	0,499	0,317	0,4285
c) E_{xx}/E_{yy}=0.0	1,068	1,258	0,0679	1,163
d) E_{xx}/E_{yy}=0.1	1,118	1,372	0,0437	1,245
e) E_{xx}/E_{yy}=0.25	1,346	1,585	0,025	1,4655
f) E_{xx}/E_{yy}=0.5	1,618	1,382	0,019	1,5
g) E_{xx}/E_{yy}=1.0	2,159	1,731	0,0105	1,945

Tab. VI.B.2.2. Variation of stress triaxiality during loading

When the material is mainly strained along the y-direction, the progressive failure of carbides gives rise to an increase in triaxiality (see lines b-e). However, when the structure is initially

subjected to a rather hydrostatic stress state, then the restriction to unidirectional damage causes a decrease in triaxiality during deformation (line a, f, g).

A decreasing triaxial stress state favours plastic deformation in the material (see last column of table VI.B.2.2) whereas an increasing triaxial stress state gives rise to a brittle material response promoting particle fracture (e.g. E_D=0.39% for E_{xx}/E_{yy}=1, E_D=0.775% for E_{xx}/E_{yy}=-0.5).

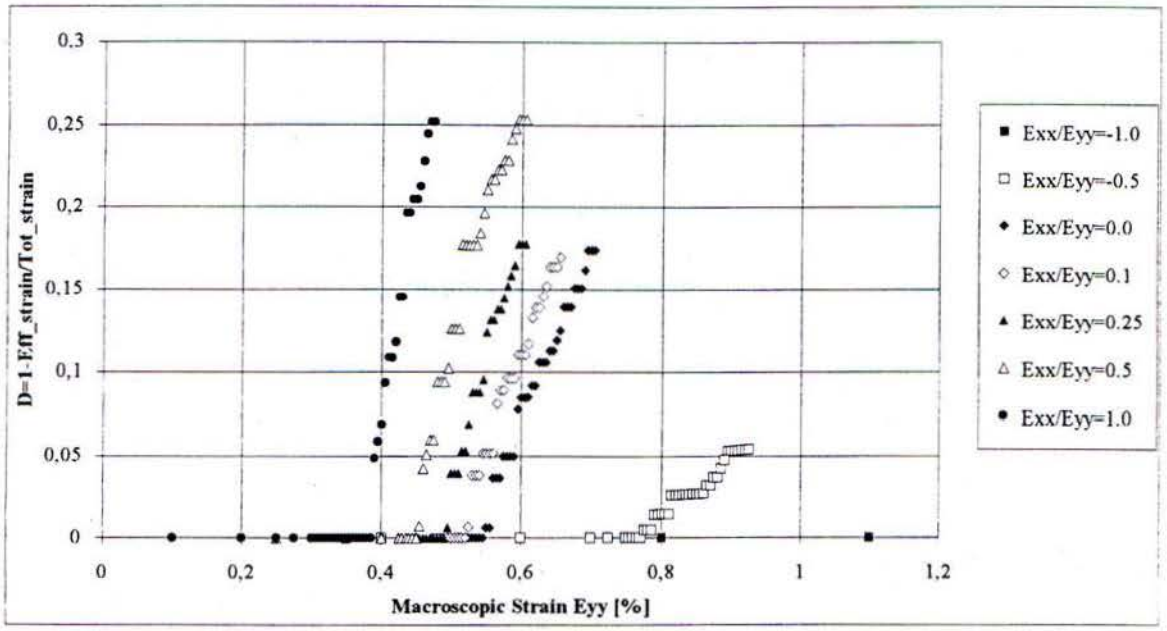

Fig. VI.B.2.11. Influence of multiaxiality on damage evolution (Prediction by simulation)

It seems interesting to compare these results with the model of Lemaitre. In order to apply this model three parameters have to be known (E_D, E_R, D_c see chapter IV.3) which are identified by uniaxial tensile tests. The followed strategy here is to determine these parameters from the results (figure VI.B.2.11) of the performed simulations on the microscale.
However, the simulation of an uniaxial tensile test within the unit cell technique requires a constraint condition which guarantees that the chosen "free" boundary will be kept straight during loading (by coupling of nodes). This constraint condition is up to now not implemented into Crackan, therefore an equivalent "uniaxial case" has to be found. A possible criterion might be that the triaxiality of the "equivalent" case is equal to that of the uniaxial case (ζ=0,3333). The closest value is found for the ratio E_{xx}/E_{yy}=-0,5 ($\zeta_{firstinc}$=0.358). The model of Lemaitre by eqn. IV.3.16 is calibrated by the ratio $D_c / (E_R - E_D)$ and by the strain at initial damage E_D. Both values can be extracted from figure VI.B.2.11:
$D_c / (E_R - E_D)$=30,8891 (being the gradient of the function); E_D = 0,0075.

With these parameters eqn. IV.3.16 has been evaluated for the same stress triaxialities present in the simulated examples (see Table VI.B.2.2) and plotted over the macroscopic strain (Here, macroscopic strains and equivalent plastic strains have been confined) (Fig. VI.B.2.12).

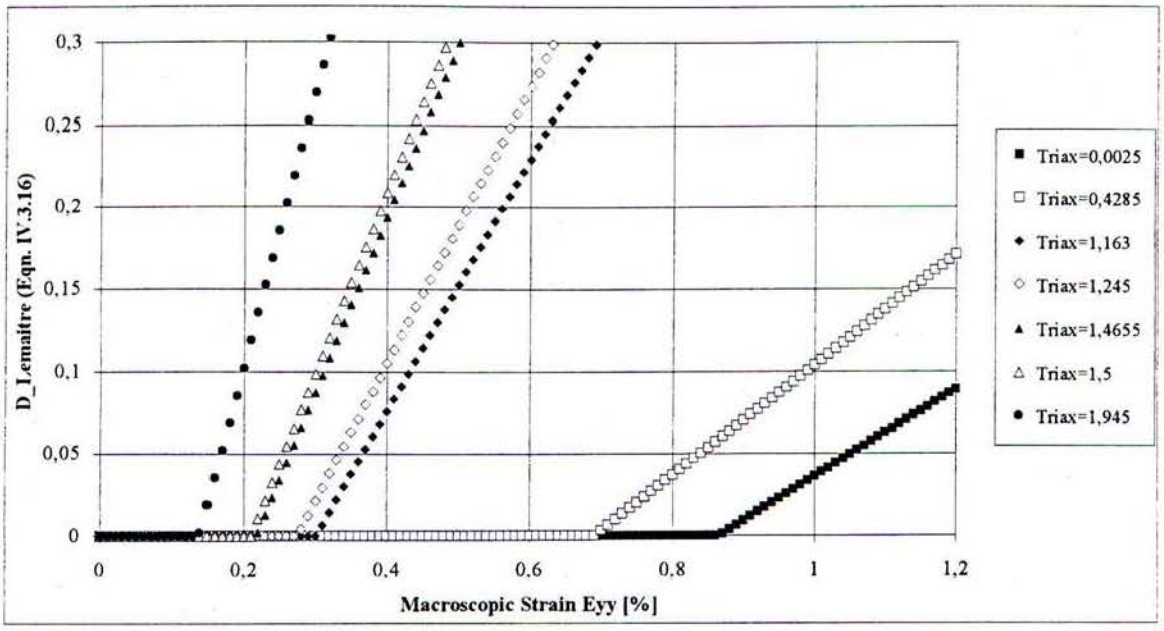

Fig. VI.B.2.12. Influence of stress triaxiality on damage evolution (Prediction by Lemaitre)

Despite the fact that the two approaches are based on somewhat different hypotheses (see chapter IV.3, V.5.2 and explanations above), both predictions agree surprisingly well. The curves of both figures show qualitatively the same features, the gradients of the different curves are almost equal in both figures. The strain at initial damage E_D predicted by the model of Lemaitre is slightly shifted to lower values. This might be explained by the fact that the curves are actually plotted over the equivalent plastic strains. If the equivalent elastic strains should be added, the curves would be moved to higher strains.

VI.C-FEM-Simulations-Inhomogeneous loading (non-uniform)

VI.C.1-Combined macro-microscopic simulation of a TPB-specimen

In the former parts it was assumed that the structure is subjected to a uniform loading. This has allowed to study the overall tensile behaviour. In most structural applications, however, is the loading not uniform and local regions may exist where the material undergoes severe straining. It is likely that first local material failure due to excessive loading is restricted to this region. This however, will not trigger the ultimate failure, since the size of the damage zone is normally small compared to the dimensions of the structure. Instead, these microcracks will grow and merge to form a macroscopic crack. The further mechanical behaviour is then governed by the interaction of the macroscopic crack with the HP ahead the crack tip (see also Fig. II.3.5, II.3.6), rather than by interaction between HP. This interaction is strongly amplified when the HP are failed by cleavage or debonding. This part is intended to study this interaction behaviour and to simulate progressive damage in front of a macroscopic crack.
For this purpose a microscopic surface section ahead of a main crack from a three-point bending sample (SAE-D3 in the annealed state, a/w=0.625, Fig. II.3.1) which is shown in Figure II.3.5 was modelled and embedded in the composite. To estimate realistic boundary conditions, the full sample was simulated by a macroscopic model using the homogeneous orthotropic properties of the composite. The obtained displacement data ahead of the crack tip were interpolated to adequately prescribe the boundary conditions for the microscopic model (see chapter V.5.1). The figure below shows the transition from the macro- to the microscopic model. Only the small interior region (region "B", Figure below) takes into account the inhomogeneous nature of the microstructure (by the two microconstituents HP + MM), the surroundings (region "A") is taken homogeneous with the properties of the composite.

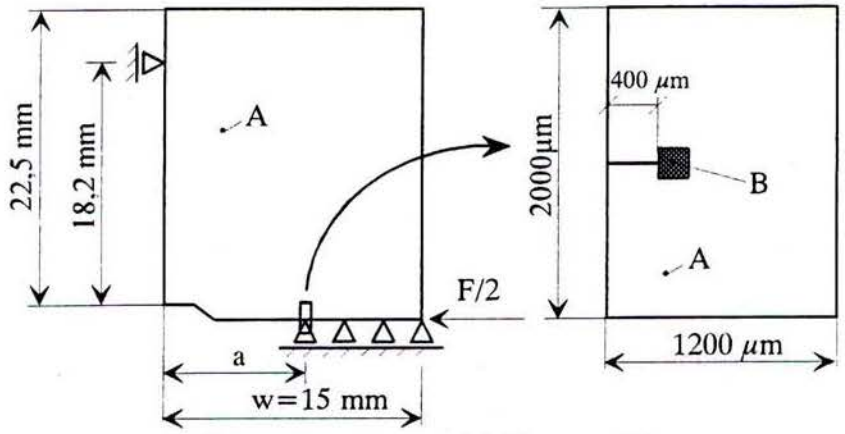

A: Homogeneous material (Composite)
B: Two-phase material (MM + HP) Size 50 x 50 μm

Fig. VI.C.1.1. Geometry of the macro- and microscopical model of a TPB-specimen

Broeckmann [BRO 94] has already simulated the evolution of damage by this coupling model but his calculations were restricted to the small deformation theory (chosen material properties were taken from state "380" instead of "Ann"). Hence, the blunting effect of the crack tip in the annealed state could not be covered. The extension of the FE-code to elastic finite plasticity (see chapter V.3.3) allows to simulate the deformation behaviour of the ductile matrix during progressive damage.

The MM and the HP in the interior region are modelled isotropic (elastic constants from Appendix A.1, the elasto-plastic properties of the MM from Appendix A.3 for "Ann"). The surroundings is assumed to be orthotropic with the elasto-plastic properties of the composite material (elastic constants from Appendix A.1, elasto-plastic properties from Appendix A.3 for "Ann"). Damage evolution is simulated by progressive carbide fracture. The effects of interfacial failure and matrix damage are not considered here. All hard phases have been allowed to fracture by attributing them a possible crack path. Due to the irregular mesh, different orientations of the crack paths had to be accepted. The carbide fracture strength is taken as σ_{Ic}=900 MPa. After occurrence of particle fracture, load-free increments are automatically applied to better account for the corresponding stress redistribution effects.
The occurrence of a damage zone in front of the macroscopic crack has been monitored by the macroscopic load. Fig. VI.C.1.2 shows exemplary the distribution of the effective plastic strain for two different load steps. HP are given in black in the figures. At the crack tip, high plastic strains up to 16% occur and lead to a blunting of the crack. In addition carbide cracking causes local plastic zones in front of the microcrack tips. The linking of these plastic zones with the large plastic zone at the macroscopic crack evidences the micro-macrocrack interaction. Studying the order of failed carbides with regard to the load level, it seems likely that beside the location of HP with regard to the macroscopic crack tip, the orientation of the crack path within the HP influence the failure moment (Recall, that the failure criterion is related to the normal direction of the crack path (see V.4.1)). Due to the unfavourable orientation of its crack path, the big carbide is cracked rather lately, in contrast with the experimental observation (see Fig. II.3.5).
Additional limits of these simulations (for the annealed state) become visible when regarding the high distortion of the elements which might cost the loss of an accurate deformation analysis. Indeed, the distribution of the field quantities at higher load levels (not illustrated here) seems to be not plausible from mechanical point of view. The use of automatic adaptive remeshing schemes in the future is desirable, not only to improve the accuracy of results but also to make possible the prediction of the further crack path in the matrix through an element elimination technique.

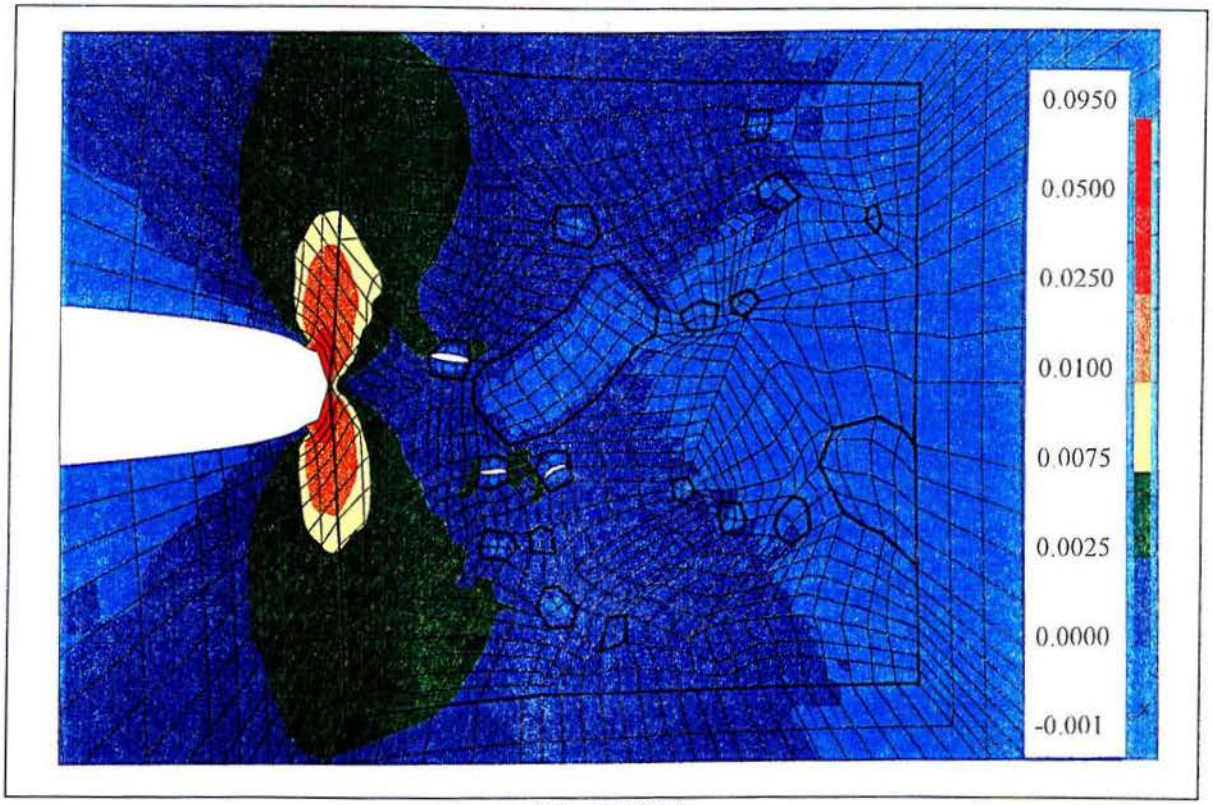

a) F=1000 N

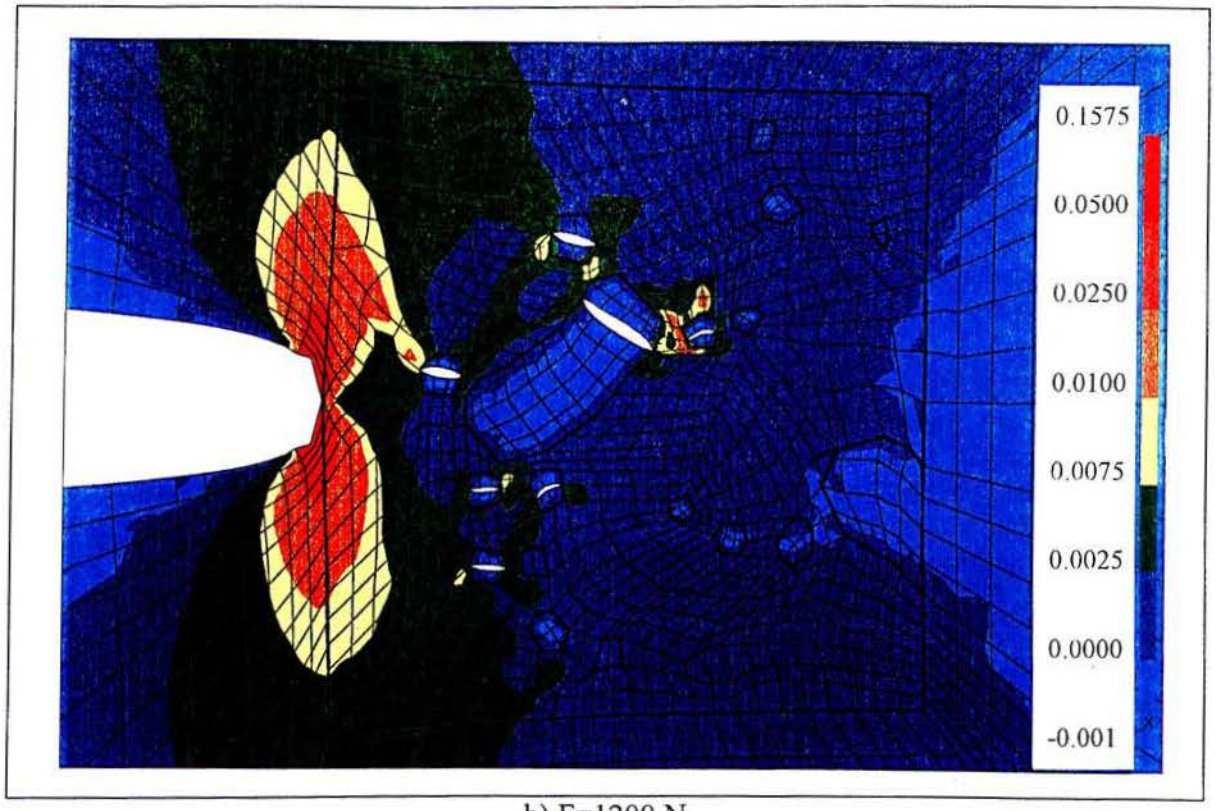

b) F=1200 N

Fig. VI.C.1.2. Development of the damage zone ahead the crack tip of a TPB-specimen in the annealed state ("Ann"), Distribution of the equivalent plastic strains ε_v^p [-]

GENERAL CONCLUSION

This work presents a FE-based micromechanical model which aims to investigate the deformation and damage behaviour of general particle reinforced MMCs. The chosen constitutive relations for the individual constituents within this model are motivated by experimental findings on a two-phase tool steel as a representative of the broad class of particle reinforced MMCs. Important physical effects as e.g. local failure of HP are taken into account by the model and enable to study the interaction between the components more realistically. The simulations prove that the model can be used as a tool to qualify and quantify the influence of microstructural parameters on the microscale deformation and damage response. In addition, transition schemes between the micro- and macroscopic model have been developed to predict the overall macroscopic mechanical behaviour in terms of effective properties of the composite. This is realized by the implementation of a post-processing routine into the FE-Code Crackan as well as by the numerical formulation of a semi-analytical mean field approach. The coupling between the micro- and macroscale is essential to establish the correlation between numerical predictions and experimental findings.

The reliability of the numerical predictions is related to the simplified assumptions within both, the geometrical and the material model. These hypotheses together with desirable further improvements in the future are discussed in the following.

The geometrical model is strongly limited by the analysis of real microstructures by 2D-plane strain or plane stress models. Although these models contribute to an important understanding of the influence on microstructural characteristics on the micro- and macroscopic response, they are not capable to provide an accurate analysis on an absolute scale. It seems reasonable in the future to study simple MM-HP systems with full 3D-models .

In order to improve the deformation analysis of the ductile matrix, the stress-strain analysis was extended to large deformation analysis. The restriction of the theory to small elastic strains within the theory is justified in view of the considered materials ($\varepsilon^e < 1\%$). Beside theoretical aspects, numerical characteristics like stability and rate of convergence, accuracy and path-dependency of results are important indicators for the model performance.
For a long time the FE-Code Crackan has used traditional methods like the Newton-Raphson scheme (with tangent stiffness) to satisfy global equilibrium and the explicit one-step-forward integration method to integrate the constitutive equations. These methods are not appropriate for an accurate deformation analysis at elevated plastic strains (convergence problems). In the future it seems to be important to incorporate advanced numerical schemes aiming to improve stability and accuracy. First attempts are made in this work by the implementation of alternative integration schemes (see chapter V, Appendix B.1).

The damage analysis addresses the prediction of failure events at the HP like particle cracking and interfacial debonding as well as ductile damage in the matrix. Major items of this analysis are the *failure criteria*, the *simulation technique* and the *calibration of the model*.
The chosen failure criteria:
A critical normal stress (fracture strength) is used as failure criterion for particle cracking. It seems to be likely that the fracture strength is not constant but dependent of additional parameters:

- Dependence on the particle size (supported by experimental findings): Larger particles may contain more defects and are more susceptible to fracture. A statistical criterion (e.g. by the Weibull-formulation eqn. IV.1.2) might be reasonable.
- Dependence on the stress triaxiality (supported by a recent study based on a correlation of experimental observations with FE-simulations [AKB 95]: This study is still going on and could not yet be exactly quantified.

Initiation of interfacial failure was simulated under pure mode I and pure mode II. However, often the interface is subjected to a multi-stress state. The inclusion of a failure criterion under mixed mode in the model is desirable in the future. Interfacial debonding was considered as a quasi-uniform separation process. The question of the propagation of an existing interface crack has not yet been addressed. Needleman's cohesive model could be applied in the future in order to bridge this gap (see chapter IV.1.1.2).

The damage criterion based on the model of Rice & Tracey seems to be appropriate in order to predict the crack path in a ductile matrix. Other authors [e.g. SCH 95] have equally reported on good agreement between the predictions of this model and experimental findings. As alternative a macroscopic continuum damage mechanics (CDM) formulation seems to be attractive. The implementation of the Gurson-model (see chapter IV.1.2) into Crackan has recently been realized [ABO 95].

The chosen simulation technique:
The automatic simulation of particle cracking by introducing additional nodes has been proven useful. The advantages are
- A small computational effort since possible crack paths were predefined.
- The CPU-time is retained since the introduction of additional nodes does not influence the solution scheme. Nodal numbering is not relevant for the used frontal method (see chapter V.2.4).
- The simulation of a microcrack is realized within only one additional load increment.
- The method has been proved to be rather stable, rarely convergence problems appeared.

However, a major drawback would arise if this method will be applied to a compressive stress state. In this case, the method would be confronted with contact problems (interpenetrating of adjacent elements).

The automatic simulation of interfacial failure and ductile damage growth in the matrix is proposed by modifying the elastic (isotropic or orthotropic) properties and the respective stress components. This method allows for the simulation of microcrack initiation by shear failure under a compressive stress state (see chapter V.4.2 V.4.3). However, this advantage is coupled with some inconveniences:
- Four subsequent relaxation substeps (without increasing the external load, see chapter V.4.2, V.4.3) are necessary to achieve satisfactory numerical stability of the method.
- Stress redistribution is certainly overestimated since stresses move out from the whole element.
- The method is highly mesh-dependent particularly in connection with quadratic quadrilateral elements. The elimination of such an element provides sharp edges which in turn strongly influences the local field quantities and hence the further crack path.

Further improvements are desirable in the future, in particular:
- The development of contact elements to handle the problem when existing cracks may close (for example under cyclic loading).

- The implementation of automatic remeshing algorithms [e.g. TAC 94] to adapt continuously the mesh size to local stress concentrations and to prevent excessive distortion of elements.

Calibration of the model:
The quantification of the local failure criteria is a rather complicated task since the microcomponents do not exist in the bulk state. Former works [BRO 94, AKB 95] have combined experiments with FE-simulations in order to estimate the fracture strength of M_7C_3-carbides. The correlation was established over the macroscopic load at which the carbides are broken. The numerically predicted carbide stress at this macroscopic load is assumed to be the fracture strength. However, the transition from the macro-to the microscale is accompanied by some hypotheses so that the results are not directly transferable. A direct correlation of the microfield quantities on the microscale might be preferred. This requires advanced experimental techniques, e.g. to measure the local strain field.
The quantification of the interface strength under different failure modes might be even more complicated since it is more difficult to detect interface cracks than carbide cracks in the unloaded state. Since interfacial failure was rarely found in SAE-D3, experimental investigations of interfacial debonding might be conducted on special developed model materials.
The subsequent processes of void formation, growth and coalescence have been addressed by a damage criterion based on Rice & Tracey's void growth model. This criterion contains as adjustable parameter the failure strain ε_0. In the calculations ε_0 was taken as the ultimate strain at failure of uniaxial tension tests. A more precise identification of ε_0 is described in [FIS 96] and may be applied to the considered material in the future.

Other related physical or chemical processes
Since the load history of the manufacturing process has not been taken into consideration, the initial state of the material was assumed to be stress-free. However, certain physical and chemical processes alter the mechanical characteristics of the material during the production process and may cause an initial anisotropy. This may be attributed to inhomogeneous irreversible processes (like plastic deformation or damage) which are mainly caused by the development of the microstructure (e.g. phase (martensitic) transformation or diffusion) or/and thermal dilatation and transition (e.g. different coefficients of thermal expansion). The extension of the FE-Code to account for these effects are actually going on within our research group.

The transition from the microscopic to the macroscopic model
A numerical and a semi-analytical based transition scheme have been developed in order to predict the overall properties of the composite. The semi-analytical approach is based on the Mori-Tanaka model in conjunction with Eshelby's equivalent solution method. When applied to simple load cases (proportional monotonic loading) this model is attractive since it gives a full 3D-analysis by only low computation times. However, the simplified description of the geometrical and mechanical characteristics may affect the accuracy of the obtained results. By the implementation of the model into Tractan, the overall effective deformation characteristics could be successfully determined. Damage related phenomena are not considered by the programme.

A more detailed geometrical and mechanical description of the microstructure is provided by the FE-model. The transition from the micro- to the macroscale is achieved via the unit-cell technique. The overall behaviour of the material is predicted by the homogenized response of the unit cell. For this the microfield quantities are numerically integrated over the cell domain.

The corresponding mean values and the imposed field quantities at the boundary are identical in the elastic-plastic setting but differ after initial damage. This motivated to define a macroscopic damage parameter characterizing the effective damage state in the composite. An accurate analysis of this transition scheme is mainly influenced by the following aspects

- the degree of randomness in the cell (e.g. number of particles in the cell)
- the mesh density in the cell compared to the size of the microcomponents
- cell boundary effects (e.g. symmetric "ghost" reflections of the components see Fig. I.3.4)
- the approximation of a three dimensional microstructure by states of plane strain or stress

In general it is not possible to respect simultaneously all items mentioned above. In particular one is limited by the computational effort (e.g. number of elements in the cell) and it depends on the specific application whether one item becomes more important. For instance a higher degree of randomness is desired for simulations of progressive damage; a higher mesh density is required for a precise stress-strain analysis.

The overall elastic plastic characteristics are determined by uniaxial loading of the unit cell. For this case the uniaxial macroscopic predicted field quantities are identical with the equivalent quantities of the 3D analysis. The simulation of the uniaxial case by the unit cell technique requires special attention for the boundary conditions: One outer edge has to be constrained to remain straight keeping nodes on the same straight line while allowing free relative movement along the line. The implementation of this constrained condition into Crackan is planned in the future. This implementation would also allow to link the local approach to damage with the CDM-model proposed by Lemaitre (see chapter IV.3):

The adjustable parameters associated to the uniaxial case within the model of Lemaitre could be identified by micromechanical simulations of damage (see chapter VI.B.2). Therefore a direct relationship between material characteristics (e.g. fracture strength of the HP) and effective damage parameters used in CDM-models could be assessed. This coupling might be useful for materials with non-homogeneous distribution of particles. For instance the cluster (or double dispersion) arrangement could be simulated within two steps: The first step would only focus on the clustered region. The respective unit cell contains a dispersion with a HP volume content identical with that within the clustered region. Competing local failure criteria are activated. With help of the uniaxial cell simulation the adjustable parameters E_D, E_R and D_C are approximated. The second step simulates a dispersion of clusters. The clusters are modelled as one single phase using the constitutive CDM-model of Lemaitre where occurrence and evolution of damage are smeared over the entire phase. The computational effort within the individual steps would be much less than in a single step simulation.

REFERENCES

[ABO 96] ABOUTAYEB, S.M. AND WEICHERT D., "Influence of porosity on fracture of hard two-phase materials", to be published, 1996

[AKB 95] AKBARI-POUR, M., "Bruch von eutektischen Karbiden im Stahl X210Cr12-Experiment und Simulation", Diploma Thesis, Ruhr-Universität Bochum, 1995

[ALL 94] ALLAIS, L., BORNERT, M., BRETHAU, T. AND CALDEMAISON, D., "Experimental characterization of the local strain field in a heterogeneous elastoplastic material", Acta metall. mater. 42, 3865-3880, 1994

[ANK 82] ANKEM, S. AND MARGOLIN, H., Metall. Trans. 13A, 595, 1982

[ARA 85] ARAVAS, N. AND MC MEEKING R.M., "Microvoid growth and failure in the ligament between a hole and a blunt crack tip", Int. J. of fracture, 29, 21-38, 1985

[ASH 64] ASHBY, M.F., "The hardening of metals by non-deforming particles", Z. Metallkunde, 55, 5-17, 1964

[ASH 70] ASHBY, M.F., Phil. Mag. 21, 399-, 1970

[AST 76] ASTM, Standard test method E 399-74 for plane-strain fracture toughness of metallic materials, 1976 annual book of ASTM standards, Philadelphia, 1976

[BAG 93] BAGHDADI, A.H., "Modélisation en grandes déformations des solides et des sols-application aux fondations", Thèse de Doctorat, Div. Modèles Numériques en Mécanique, Université de Technologie de Compiègne, 1993

[BAO 91] BAO, G., HUTCHINSON, J.W., MCMEEKING, R.M., "Particle reinforcement of ductile matrices against plastic flow and creep", Acta metall. mater., 39, 1871-1882, 1991

[BAO 92] BAO, G., "Damage due to fracture of brittle reinforcements in a ductile matrix", Acta metall. mater., 40, 2547-2555, 1992

[BAT 75] BATHE, K.-J., RAMM, E., WILSON, E.L., "Finite element formulations for large deformation dynamic analysis, Int. J. for Num. Meth: Eng., 9, 353-386, 1975

[BAT 86] BATHE, K.-J., "Die Methode der Finiten Elemente", Springer Verlag, Berlin, 1986

[BEN 87] BENVENISTE Y., "A new approach to the application of Mori-Tanaka's theory in composite materials", Mechanics of materials, 6, 147-157, 1987

[BER 74] BERNS, H., "Restaustenit in ledeburitischen Chromstählen und seine Umwandlung durch Kaltumformen, Tiefkühlen und Anlassen, HTM, 29, 4, 236-247, 1974

[BER 76] BERNS, H., KETTEL, J., "Ermittlung der Zusammensetzung von Grundmasse und Carbiden durch Rückstandsisolierung bei ledeburitischen Chromstählen", Arch. Eisenhüttenwesen, 47, 6, 391-393, 1976

[BER 93] BERNS, H., "Stahlkunde für Ingenieure", Springerverlag, Berlin Heidelberg, 1993

[BER 96] BERNS, H., MELANDER, A., WEICHERT, D., BROECKMANN, C., ASNAFI, N AND GROSS-WEEGE, A., "A new material for cold forging tools", to be published, 1996

[BÖH 93A] BÖHM H.J., RAMMERSTORFER, F.G. AND WEISSENBEK, E., "Some simple models for micromechanical investigations of fiber arrangement effects in MMCs", Comput. Mater. Sc. 1, 177-194, 1993

[BÖH 93B] BÖHM H.J. AND RAMMERSTORFER, F.G., "Micromechanical models for investigating fibre arrangements in metal matrix composites", Mecamat 93, Int. seminar on micromechanics of materials, Moret-sur-Loing, France, 6-8 July, 383-394, 1993

[BÖH 94] BÖHM H.J., RAMMERSTORFER, F.G., FISCHER, F.D., AND SIEGMUND T., "Microscale arrangement effects on the thermomechanical behaviour of advanced two-phase materials", Transactions of the ASME, 116, 268-273, 1994

[BOR 93] BORNERT, M., HERVÉ, E., STOLZ C. AND ZAOUI A., "Modelling the strain heterogeneities in a two phase elastoplastic material", Mecamat 93, International seminar on micromechanics of materials, 26-37, 7-8 July 1993

[BOU 94] BOURGEOIS, N., "Caractérisation et modélisation micromécanique du comportement et de l'endommagement d'un composite à matrice métallique:Al/SiCp, Doctoral thesis, Ecole Centrale Paris, 1994

[BRA 86] BRAUDEL, H.J., ABOUAF, M. AND CHENOT, J.L., "An implicit incrementally objective formulation for the solution of elastoplastic problems at finite strain by the F.E.M.", Comp. and struct., 24, 825-843, 1986

[BRA 94] BRAESS, D., Private communication, Ruhr-University Bochum, 1994

[BRO 71] BROWN, L.M. AND STOBBS, W.M., Phil. Mag., 23, 1201, 1971

[BRO 91] BROCKENBROUGH, J.R., SURESH, S. AND WIENECKE, H.A., "Deformation of metal-matrix composites with continuous fibers: geometrical effects of fiber distribution and shape", Acta metall. mater., 39, 735-752, 1991

[BRO 94] BROECKMANN, C., "Bruch karbidreicher Stähle - Experiment und FEM-Simulation unter Berücksichtigung des Gefüges", Dissertation Ruhr-Universität Bochum, s.a. Fortschr.-Ber. VDI, Reihe 18, Nr. 169, Düsseldorf, 1994

[BUD 65] BUDIANSKY, B., "On the elastic moduli of some heterogeneous materials", J. Mech. Phys. Solids, 13, 223-234, 1965

[BUN 58] BUNGARDT, K., KUNZE, E. AND HORN, E., "Untersuchungen über den Aufbau des Systems Eisen-Chrom-Kohlenstoff, Arch. Eisenhüttenwesen, 29, 193-203, 1958

[CAE 90] CAEDS, "Finite Element Modeling", User's Guide Handbuch, SDRC, 1990

[CHA 88] CHABOCHE, J. L., "Continuum damage mechanics-Part I-II", Journal of applied mechanics, 55, 59-72, 1988

[CHE 92] CHENG, Y. M., TSUI, Y., "Limitations to the large strain theory", Int. J. Num. Meth. Eng., 33, 101-114, 1992

[CHR 79] CHRISTENSEN, R.M. AND LO, K.H., "Solutions for effective shear properties in three phase sphere and cylinder models", J. Mech. Phys. Solids, 27, 315-330, 1979

[CHR 88] CHRISTMAN, T., AND SURESH, S., "Microstructural development in an aluminium alloy-SiC whisker composite", Acta metall. mater., 36, 1691-1704, 1988

[CHR 89] CHRISTMAN, T., NEEDLEMAN, A. AND SURESH, S., "An experimental and numerical study of deformation in metal-ceramic composites", Acta metall. mater., 37, 3029-3050, 1989

[CLI 68] MC CLINTOCK, F., "A criterion for ductile failure by the growth of holes", ASME J. of Applied Mechanics, 363-371, 1968

[COR 95] CORNEC A. AND LIN GUOYU, "Elastisch-plastisches Spannungs-Dehnungs-verhalten von zweiphasig hexagonal angeordneter Mikrostruktur", Technical Note GKSS/WMA/95/3, 1995

[DAB 94] DABOUNOU, J., "Resolution des problèmes de grandes transformations par la méthode des éléments finis", Thèse doctorat d'Université de Technologie de Compiègne, 1994

[DAF 83] DAFALIAS, Y.F., "A missing link in the macroscopic constitutive formulation of large plastic deformation", Plasticity today, Modelling and applications, 1983

[DIE 79] DIENES, J.K., "On the analysis of rotation and stress rate in deforming bodies", Acta Mech., 32, 217-232, 1979

[DIE 93] DIETRICH CH., POECH, M.H., FISCHMEISTER H.F. AND SCHMAUDER, S., "Stress and strain partitioning in a Ag-Ni fibre composite under transverse loading", Comput. Mater. Sc. 1, 195-202, 1993

[ESH 57] ESHELBY, J.D., "The determination of the elastic field of an ellipsoidal inclusion, and related problems", Proc. R. Soc. London, A241, 376-396, 1957

[EXN 86] EXNER, H.E., HOUGARDY H.P., "Einführung in die quantitative Gefüge-analyse", DGM INformationsgesellschaft, Oberursel, 1986

[EXN 93] EXNER, H.E. ET AL., "Quantitative Beschreibung der Gefügegeometrie- Eine praktische Anleitung zu manuellen Verfahren- Teil I-VII", Prakt. Metallographie, 30, 216-, 1993

[FIS 73] FISCHMEISTER, H.F., HJÄLMERED, J.O., KARLSSON, B, LINDÉN, G., SUNDSTRÖM, B., "Plastic deformation of two-phase materials with coarse microstructure", Proc. 3rd Int. Conf. on Strength of Metals and Alloys, pp. 621-625, Inst. of Metals London, 1973

[FIS 77] FISCHMEISTER, H.F. AND KARLSSON, B, G., "Plastizitätseigenschaften grob-zweiphasiger Werkstoffe", Z. Metallkunde, 68, 311-327, 1977

[FIS 88] FISCHMEISTER, H.F., SCHMAUDER S. AND SIGL, L.S., "Finite Element Modelling of crack propagation in WC-Co hard metals", Mater. Sci. Eng., A105/106, 305-311, 1988

[FIS 89] FISCHMEISTER, H.F., EXNER, H.E., POECH, M.HJ., KOHLHOFF, S., GUMBSCH, P., SCHMAUDER S., SIGL, L.S. AND SPIEGLER, R., "Modelling fracture processes in metals and composite materials", Z. Metallkunde, 80, 839-846, 1989

[FIS 92] FISCHER F.D., "Transformation induced plasticity in triaxially loaded steel specimens subjected to a martensitic transformation", Eur. J. Mech., A/Solids, 11, 233-244, 1992

[FIS 96] FISCHER F.D., KOLEDNIK, O., SHAN, G. AND RAMMERSTORFER, F.G., "A note on calibration of ductile failure damage indicators", Int. J. of Fracture, in print, 1996

[FIT 95] FITOUSSI, J., BOURGEOIS, N, GUO, G. AND BAPTISTE, D., "Prediction of the anisotropic damaged behaviour of composite materials: introduction of multi-local failure criteria in a micro-macro relationship", accepted to be published in Comp. mater. sci., 1995

[FOX 68] FOX, N., "On the continuum theories of dislocations and plasticity", Quart. J. Mech. Appl. Math., vol. 21, 1968, pp.67-75

[GIN 94] GIN, A. AND BAKALEMIAN, P.Y., "Création d'interfaces entre le mailleur Caeds et le processeur Crackan", Projet 2ème année, EUDIL, Lille, 1994

[GOO 79] GOODS, S.H. AND BROWN, L.M., "The nucleation of cavities by plastic deformation", Act. Metall. mater. 27, pp.1-15, 1979

[GRE 65] GREEN, A.E., NAGHDI, P.M., "A general theory of an elastic plastic continuum" Arch. Rat. Mech. Appl. math., Vol. 21, 1968, pp.251-281

[GRO 92] GROSS-WEEGE, A., "Numerical investigations of cleavage and decohesion in heterogeneous materials", Diplomarbeit, Lille, Bochum, 1992

[GRO 95] GROSS-WEEGE, A., WEICHERT, D., AND BROECKMANN, C., "Finite Element Simulation of crack initiation in hard two-phase materials", accepted to be published in Comput. Mater. Sci., 1995

[GUN 91] GUNAWARDENA, S.R., JANSSON, S. AND LECKIE, F.A., "Transverse ductility of metal matrix composites", in "Failure mechanisms in high temperature composite materials", pp. 23-30, AD-Vol.22/AMD-Vol.122, ASME, NY, 1991

[GUR 58] GURLAND, J., Transactions AIME 212, 452-455, 1958

[GUR 63] GURLAND, J. AND PLATEAU, J., Trans. ASM 56, pp. 442, 1963

[GUR 77] GURSON, A.L., "Continuum theory of ductile rupture by void nucleation and growth: Part I-Yield criteria and flow rules for porous ducctile media", J. Engng Mater. Tech., 99, 2-15, 1977

[HAD 95] HADDI, A. AND WEICHERT D., "On the computation of the J-Integral for three-dimensional geometries in inhomogeneous materials", accepted to be published in Comput. Mater. Sci., 1995

[HAE 90] HÄNSCH, W., "Gefüge und Bruchzähigkeit ledeburitischer Chromstähle-Messung und Finite-Elemente-Nachbildung", Dissertation Ruhr-Universität Bochum, s.a. Fortschr.-Ber. VDI, Reihe 18, Nr. 81, Düsseldorf, 1990

[HAH 73] HAHN, G.T. AND ROSENFIELD, A.R., "Relations between microstructure and the fracture toughness of metals" , Dritte internationale Tagung über den Bruch, München, I.Pl III-211, 1973

[HAS 63] HASHIN, Z. AND SHTRIKMAN, S., "A variational approach to the theory of the elastic behaviour of multiphase materials", J. Mech. Phys. Solids, 11, 127-140, 1963

[HAS 83] HASHIN, Z., "Analysis of composite materials: a survey", J. Appl. Mech., 50, 481-505, 1983

[HER 54] HERSHEY, A.V., "The elasticity of an isotropic aggregate of anisotropic cubic crystals", J. Appl. Mechanics, 21, 236, 1954

[HIB 70] HIBBIT, H.D., MARCAL, P.V. AND RICE, J.R., "A finite element formulation for problems of large strain and large displacement", Int. J. Solids Structures, 6, 1069-1086, 1970

[HIB 79] HIBBIT, H.D., "Some follower forces and load stiffness", Int. J. Num. Meth. Eng., 14, 937-941, 1979

[HIB 90] HIBBIT, KARLSSON, SORENSON, Inc., ABAQUS, User's Manual, Version 4.8, Providence, 1990

[HIL 59] HILL, R., "Some basic principles in the mechanics of solids without a natural time", J. Mech. Phys. Solids, 7, 209, 1959

[HIL 63] HILL, R., "Elastic properties of reinforced solids: some theoretical principles", J. Mech. Phys. Solids, 11, 357-372, 1963

[HIL 65] HILL, R., "A self-consistent mechanics of composite materials", J. Mech. Phys. Solids, 13, 213-222, 1965

[HIL 68] HILL, R., "On constitutive inequalities for simple materials I-II", J. Mech. Phys. Solids, 16, 229, 1968

[HIN 74] HINTON, E. AND CAMPBELL, J.S., "Local and global smoothing of discontinuous finite element function using a least squares method", Int. J. Num. Meth. Eng., 8, 461-480, 1974

[HOG 84] HOGER, A., CARLSON, D.E., "Determination of the stretch and rotation in the polar decomposition of the deformation gradient", Quart. App. Math., 10, 1984

[HUG 80] HUGHES, T.J.R., WINGET, J., "Finite rotation effects in numerical integration of rate constitutive equations arising in large deformation analysis", Int. J. Num. Meth. Eng., 15, 1862-1867, 1980

[HUT 87] HUTCHINSON, J.W., "Crack tip shielding by micro-cracking in brittle solids", Acta metall. mater., 35, 1605-1619, 1987

[KAC 58] KACHANOV, L.M., "Time of the rupture process under creep conditions," Izv. Akad. Nauk, S.S.R., Otd, Tech. Nauk, N°8, 26-31, 1958

[KAS 77] KASTEELE VAN DE, J.C., BROEK, D., "The failure of large second phase particles in a cracking aluminium alloy", EFM, 9, 625-635, 1977

[KEY 82] KEY, S.W. AND KRIEG, R.D., "On the numerical implementation of inelastic time dependent and independent, finite strain constitutive equations in structural mechanics", Int. J. Num. Meth. Eng., 33, 439-452, 1982

[KNO 90] KNOTT, J.W. AND KING, J.E., "Fatigue in metallic alloys containing non-metallic particles", Proc. of Fatigue 90, 1990

[KON 93] KONG, X., SCHLÜTER, N. AND ARNDT, J., "Effects of the constraint parameter triaxial stress on the failure behaviour of steels", Steel research, 64, 401-406, 1993

[KRI 76] KRIEG, R.D. AND KEY, S.W., "Implementation of a time dependent plasticity theory into structural computer programs", in Constitutive equations in visco-plasticity: Comput. and eng. aspects, (J.A. Stricklin and K.J. Saczalski, Eds.), AMD-20, ASME, New York, pp. 125-137, 1976

[KRÖ 58] KRÖNER, E., "Berechnung der elastischen Konstanten des Vielkristalls aus den Konstanten des Einkristalls", Z. Phys., 151, 504-, 1958

[KRÖ 61] KRÖNER, E., "Zur plastischen Verformung des Vielkristalls", Acta Metall. 9, 155-161, 1961

[LEE 67] LEE, E.H., LIU, D.T., "Finite strain elastic-plastic theory with application to plane-wave analysis", J. Appl. Phys. 38, 19-27, 1967

[LEE 69] LEE, E.H.,"Elasto-plastic deformation at finite strains", J. Appl. Mech. 36, 1-6, 1969

[LEE 83] LEE, E.H., MALLETT, R.L., WERTHERMER, T.B., "Stress analysis for anisotropic hardening in finite-deformation plasticity", Elastic-plastic deformation at finite strains", J. Appl. mech. ASME, 50, 554-560, 1983

[LEM 85A] LEMAITRE, J., "A continuous damage mechanics model for ductile fracture", J. Eng. Mat. Tech., 107, 83-89, 1985

[LEM 85B] LEMAITRE, J. AND CHABOCHE, J.L., "Mécanique des matériaux solides", Dunod, Paris, 1985

[LIP 93] LIPETZKI, P., SCHMAUDER, S. AND FISCHMEISTER, H.F., "Geometrical factors related to composite microcracking", Comput. mater. sci., 1, 325-332, 1993

[LLO 91A] LLORCA, J., NEEDLEMAN, A. AND SURESH, S., "An analysis of the effects of matrix void growth on deformation and ductility in metal-ceramic composites", Acta metall. mater., 39, 2317-2335, 1991

[LLO 91B] LLOYD, D.J., "Aspects of fracture in particulate reinforced metal matrix composites", Acta metall. mater., 39, 59-71, 1991

[LLO 93] LLORCA, J., MARTIN, A., RUIZ, J. AND ELICES, M., "Particulate fracture during deformation of a spray formed metal-matrix composite", Metallurgical Transactions A, 24A, 1575-1588, 1993

[LLO 95] LLORCA, J., "An analysis of the influence of reinforcement fracture on the strength of discontinuously-reinforced metal matrix composites", Acta metall. mater., 43, pp. 181-192, 1995

[LÜS 95] LÜSEBRINK, O., "Rißausbreitung in einem grob-zweiphasigen Gußgefüge-Experiment und FEM-Simulation", Diploma-Thesis, Ruhr-Universität Bochum, 1995

[MAN 72] MANDEL, J., "Plasticité classique et viscoplasticité", Cours au C.I.S.M., Udine, 1972

[MCH 93] MC HUGH, P.E., ASARO, R.J. AND SHIH, C.F., "Computational modeling of metal matrix composite materials" Part I-IV, Acta metall. mater., 41, 1461-1510, 1993

[MCH 94] MC HUGH, P.E. AND CONNOLLY, P., "Modelling the thermomechnical behaviour of an Al alloy-SiCp composite-Effects of particle shape and microscale fracture", Comput. mater. sci., 3, 199-206, 1994

[MEE 75] MCMEEKING, R.M., AND RICE, J.R., "Finite-element formulations for problems of large elastic-plastic deformation", Int. J. Solids Structures, 11, 601-616, 1975

[MEE 90] MCMEEKING, R.M., AND HOM, C.L., "Finite-element analysis of void growth in elastic-plastic materials" Int. J. of Fracture, 42, 1-19, 1990

[MEG 93] MEGUID, S.A., "Mechanics and mechanisms of toughnening of advanced ceramics", in: Advances in materials and processing technologies, 1119-1129, 1993

[MIC 93] MICHEL, J.C., "A numerical study of the effects of particle cracking and particle debonding on matrix void growth in Al-SiC composites", Mecamat 93, Int. seminar on micromechanics of materials, Moret-sur-Loing, France, 6-8 July, 395-405, 1993

[MOC 91] MOCHIDA, T., TAYA, M. AND OBATA, M., "Effect of damaged particles on the stiffness of a particle/metal matrix composite", JSME International Journal, 34, 187-193, 1991

[MOL 86] MOLENKAMP, F., "Limits to the Jaumann stress rate", Int. J. Num. Anal. Methods geomech., 10, 151-176, 1969

[MOR 70] MORI T. AND TANAKA K., Acta metall. mater., 18, 931, 1970

[MOR 73] MORI T. AND TANAKA K., "Average stress in matrix and average elastic energy of materials with misfitting inclusions", Acta metall. mater., 21, 571-574, 1973

[MUM 93] MUMMERY, P.M., DERBY, B. AND SCRUBY, C.B., "Acoustic emission from particulate-reinforced metal matrix composites", Acta metall. mater., 41, 1431-1445, 1993

[MUR 87] MURA, T., "Micromechanics of defects in solids", Second revised edition, Martinus Nijhoff Publishers, 67-84, 1987

[NAR 92] NARASIMHAN, R., ROSAKIS, A.J. AND MORAN, B., "A three-dimensional numerical investigation of fracture initiation by ductile failure mechanisms in a 4340 steel", Int. J. of Fracture, 56, 1-24, 1992

[NAG 81] NAGTEGAAL, J.C. AND VELDPAUS, F.E., "Some computational aspects of elasto- plastic large strain analysis", Int. J. Num. Meth. Eng., 17, 15-????, 1981

[NEE 84] NEEDLEMAN, A., TVERGAARD, V., "Analysis of the cup-cone fracture in a round tensile bar" Acta Metall. mater. 32, pp. 157-169, 1984

[NEE 87] NEEDLEMAN, A., "A continuum model for void nucleation by inclusion debonding, J. of applied mechanics, 54, 525-531, 1987

[NEE 90] NEEDLEMAN, A., "An analysis of decohesion along an imperfect interface", Int. J. of Fracture, 42, 21-40, 1990

[NEE 91] NEEDLEMAN, A., TVERGAARD, V., "A numerical study of void distributrion effects on dynamic, ductile crack growth, EFM, 38, 157-173, 1991

[NEE 92] NEEDLEMAN, A., "Micromechanical modelling of interfacial decohesion", Ultramicroscopy 40, pp. 203-214, 1992

[NEM 93] NEMAT-NASSER, S. AND HORI, M., "Micromechanics: Overall properties of heterogeneous materials", North-Holland series in Applied Mathematics and Mechanics, 37, 1993

[OLA 93] OLAF, J.M. AND POMPE, W., "Finite element analysis of indentation experiments in surfaces and surface coated materials", Comput. mater. sc. 1, 276-282, 1993

[ORT 85] ORTIZ, M. AND POPOV, E.P., "Accuracy and stability of integration algorithms for elastoplastic constitutive relations", Int. J. Num. Meth. Eng., 21, pp. 1561-1576, 1985

[OWE 77] OWEN, D.R.J., AND HINTON, E., "Finite element programming", Academic press, London, 1977

[OWE 80] OWEN, D.R.J., AND HINTON, E., "Finite elements in plasticity, Theory and practice", Pineridge Press Limited, Swansea, U.K., 1980

[OWE 83] OWEN, D.R.J., AND FAWKES, A.J.F., "Engineering fracture mechanics: numerical methods and applications", Pineridge Press Limited, Swansea, U.K., 1983

[PLA 95] PLAQUIN J. AND KASMI J.P., "Mise en oeuvre numérique du modèle de Mori-Tanaka et application à l'essai de traction monotone", Projet de fin d'études, EUDIL, Lille, 1995

[POE 92A] POECH M.-H. AND FISCHMEISTER, H.-F., "Mechanische Eigenschaften von Martensit-Austenit-Modellegierungen, Teil I-Verformungsverhalten und Bruchfestigkeit", Z. Metallkunde, 83, 176-182, 1992

[POE 92B] POECH M.-H. AND FISCHMEISTER, H.-F., "Mechanische Eigenschaften von Martensit-Austenit-Modellegierungen, Teil II-Gefügeanordnung und Bruchzähigkeit", Z. Metallkunde, 83, 379-385, 1992

[POE 92C] POECH M.-H. AND FISCHMEISTER, H.-F., "Deformation of two-phase materials: a model based on strain compatibility", Acta metal. mater. 40, 487-494, 1992

[POE 93] POECH M.-H., FISCHMEISTER, H.-F., KAUTE, D. AND SPIEGLER, R., "FE-modelling of the deformation behaviour of WC-Co alloys", Comput. mater. sc., 1, 213-224, 1993

[POE 94] POECH M.-H. AND RUHR, D., "Die quantitative Charakterisierung der Gefüge-anordnung", Prakt. Metallogr. 31, 70-77, 1994

[PYZ 94] PYZALLA-SCHIECK, A., "Thermische Mikroeigenspannungen in Stück-verbunden", Dissertation Ruhr-UNiversität Bochum, s.a. Fortschr.-Ber. VDI, Reihe 5, Grund-und Werkstoffe, Nr. 420

[REU 29] REUSS, A., "Berechnunge der Fließgrenze von Mischkristallen aufgrund der Plastizitätsbedingung für Einkristalle", ZAMM, 9, 49-58, 1929

[RIC 69] RICE, J.R. AND TRACEY D.M., "On the ductile enlargement of voids in triaxial stress fields", J. Mech. Phys. Solids, 17, 201-217, 1969

[RIC 73] RICE, J.R. AND TRACEY D.M., "Computational fracture mechanics" in Proc. Symp. on Numerical and Computer Methods in Structural Mechanics, Urbana, Illinois, 1971 (Ed. J.S. Fenves), Academic Press, New York, p. 585, 1973

[ROS 82] ROSMANITH, H.P.: "Grundlagen der Ingenieur-Bruchmechanik", in Grundlagen der Bruchmechanik, Hrsg.: Rossmanith, H.P., Springer Verlag, Wien New York, 1982

[RÜH 87] RÜHLE, M., EVANS, A.G., MC MEEKING, R.M., CHARALAMBIDES, P.G., AND HUTCHINSON, J.W., "Microcrack toughnening in alumina/zirconia", Acta metall., 35, 2701-2710, 1987

[SAU 93] SAUTTER, M., DIETRICH, CH., POECH, M.H., SCHMAUDER, S. AND FISCHMEISTER, H.F., "Finite element modelling of a transverse-loaded fibre composite", Comput. mater. sc., 1, 225-233, 1993

[SCH 91] SCHULZ, M., "Orthotropy in elasticity and in plasticity and J-Integral evaluation, Studienarbeit, Lille, Bochum, 1991

[SCH 96] SCHMAUDER, S., WULF, J., STEINKOPFF, TH. AND FISCHMEISTER, H.F., "Micromechanics of plasticity and damage in an Al/SiC metal matrix composite", to be published, 1996

[SID 82] SIDOROFF, F. "Cours sur les grandes deformations", Rapport GRECO-France, N°51, 1982

[SIE 93] SIEGMUND T., WERNER, E., AND FISCHER, F.D., "Structure-property relations in duplex materials", Comput. mater. sc. 1, 234-240, 1993

[SIG 88] SIGL, L.S. AND FISCHMEISTER, H.F., "On the fracture toughness of cemented carbides", Acta Metall. 36, 887-897, 1988

[SIM 85] SIMO, J.C., AND TAYLOR, R.L., "Consistent tangent operators for rate independent elasto-plasticity", Comp. Meth. Appl. Mech. Eng., 48, 101-118, 1985

[SIM 86] SIMO, J.C., AND TAYLOR, R.L., "A return mapping algorithm for plane stress elastoplasticity", Int. J. Num. Meth. Eng., 22,649-670, 1986

[SLO 87] SLOAN, S.W. "Substepping schemes for the numerical integration of elasto-plastic stress-strain relations", Int. J. Num. Meth. Eng., 24, 893-911, 1987

[SÖR 94] SÖRENSEN, N.J., SURESH, S., TVERGAARD, V. AND NEEDLEMAN, A., "Effects of reinforcement orientation on the tensile response of metal matrix composites", Internal Report RIS•, Materials Department Ris• National Laboratory Denmark, 1994

[STU 93] STUMPF, H., "Theoretical and computational aspects in the Shakedown analysis of finite elastoplasticity", Int. J. of plasticity, vol.9, pp.583-602, 1993

[STU 94] STUMPF, H., "Kinematics and constitutive model in finite elastoplasticity", Seminar, LML, 2 June 1994, Lille

[SUQ 93] SUQUET, P.M., "Bounds and estimates for the overall properties of nonlinear composites", Mecamat 93, Int. seminar on micromechanics of materials, Moret-sur-Loing, France, 6-8 July, 361-382, 1993

[TAC 94] TACK, L.H., SCHNEIDERS, R., DEBYE, J., KOPP, R. AND OBERSCHELP, W., "Two- and three-dimesional remeshing, mesh refinement and application to simulation of micromechanical processes", Comput. material science, 3, 241-247, 1994

[TAM 73] TAMURA, I., TOMOTA, Y. AND OZAWA, H., Proc. 3rd int. conf. on the strength of metals and alloys, Cambridge, 1, 611, 1973

[TAN 70] TANAKA, K., MORI, T. AND NAKAMURA, T., Philos. Mag. 21, pp. 267, 1970

[TAN 88] TANDON, G.P. AND WENG, G.J., "A theory of particulate-reinforced plasticity", J. of Applied Mechanics", 55, 126-135, 1988

[TEI 88] TEIRLINCK, D., ZOK, F., EMBURY, J.D., AND ASHBY, M.F., "Fracture mechanism maps in stress space", Acta Met., 36, 1213-1228, 1988

[TRU 77] TRUESDELL, C., "A first Course in Rational Continuum Mechanics", Vol 1, Academic Press, New York, (1977)

[TVE 82] TVERGAARD, V., Journal of the Mechanics and Physics of Solids 30, 399-425, 1982

[TVE 90A] TVERGAARD, V., "Effect of fibre debonding in a whisker-reinforced metal", Mater. sci. eng., A125, 203-213, 1990

[TVE 90B] TVERGAARD, V., "Analysis of tensile properties for a whisker-reinforced metal-matrix composite", Acta metall. mater. 38, 185-194, 1990

[TVE 93] TVERGAARD, V., "Effect of volume fraction on fibre cracking and debonding in a whisker reinforced metal", Mecamat 93, Int. seminar on micromechanics of materials, Moret-sur-Loing, France, 6-8 July, 177-187, 1993

[UGG 82] UGGOWITZER, P. AND STÜWE H.P., "Plastizität von ferritisch-martensitischen Zweiphasenstählen", Z. Metallkunde, 73, 277-285, 1982

[VOI 10] VOIGT, W., "Lehrbuch der Kristallphysik", Teubner, Berlin, 1910

[WAL 69] WALPOLE, L.J., "On the overall moduli of composite materials", J. Mech. Solids, 17, 235-251, 1969

[WEB 90] WEBER, G.G., LUSH, A.M., ZAVALIANGOS, A., AND ANAND, L., "An objetive time integration procedure for isotropic rate-independent and rate-dependent elastic-plastic constitutive equations", Int. J. of Plasticity, 6, 701-744, 1990

[WEI 93A] WEICHERT, D. AND SCHULZ, M., "J-integral concept for multi-phase materials", Comput. Mat. Sci., 1, 241-248, 1993

[WEI 93B] WEIHE, S.AND KRÖPLIN B.H., Mecamat 93, Int. seminar on micromechanics of materials, Moret-sur-Loing, France, 6-8 July, 1993

[WEN 84] WENG, G.J., "Some elastic properties of reinforced solids, wih special reference to isotropic ones containing spherical inclusions", Int. J. Eng. Science, 22, 845-856, 1984

[WER 90] WERNER, E. AND PRANTL, W., "Slip transfer across grain and phase boundaries", Acta metall. mater., 38, 533-537, 1990

[WIL 64] WILKINS, M.L., "Calculation of elastic-plastic flow", in Methods of Computational Physics 3 (B. Alder et al., Eds.), Academic Press, New York, 1964

[WIT 89] WITHERS, P.J., STOBBS, W.M. AND PEDERSEN, O.B., "The application of the Eshelby method of internal stress determination to short fibre MMCs", Acta Metallurgica, 37, 3061-3084, 1989

[WUL 93] WULF, J., SCHMAUDER, S. AND FISCHMEISTER, H.F., "Finite element modelling of crack propagation in ductile fracture", Comput. mater. sci.,1, 297-301, 1993

[WUL 94] WULF, J., SCHMAUDER, S. AND FISCHMEISTER, H.F., "Simulation of experimental force-displacement curves by a finite element elimination technique", Comput. mater. Sci. 3, 300-306, 1994

[ZIE 79] ZIENKIEWICZ, O.C., "The finite element method", New-York, McGraw-Hill, 1979

[ZHA 89] ZHANG, K.S., HUA, L.S., ZHENG, C.Q. AND RADON, J.C., "A computer Simulation of ductile fracture inititation in TPB Specimen-An application of VGC-Criterion, EFM, 33, 671-677, 1989

[ZHU 92] ZHU, Y., "Contribution to the local approach of fracture in solid dynamics", Thèse de Doctorat, MSM., Université de Liège, 1992

[ZUM 80] ZUM GAHR, K.H., "Fracture analysis of white cast iron", Z. Metallkunde, 71, 103-109, 1980

APPENDIX

Appendix A-Material parameters used in simulations
A.1-Elastic constants used in simulations for the composite and their components
A.2-Stress-strain curves used in simulations for the composite
A.3-Stress-strain curves used in simulations for the metal matrix (MM)

Appendix B-On the numerical implementation of the elasto-plastic constitutive model
B.1-Local integration algorithms
- B.1.1-Explicit forward Euler integration algorithms
  - B.1.1.1-General matrix formulation
  - B.1.1.2-Classical forward Euler first order integration algorithm
  - B.1.1.3-Modified forward Euler second order integration algorithm
- B1.2-Implicit backward Euler integration algorithm (radial return algorithm)

B.2-Evaluation of the elasto-plastic matrix (tangent operator) C^{ep}
- B.2.1-Continuum tangent operator
- B.2.2-Consistent tangent operator (consistent with radial return algorithm)

B.3-Polar decomposition scheme

Appendix C-The Mori-Tanaka approach
C.1-Elasticity (Formulation by Benveniste)
C.2-Extension to plasticity (Secant approach)

A-MATERIAL PARAMETERS USED IN SIMULATIONS

A.1-Elastic constants used in simulations for the composite and their components

material	E in [GPa]	ν
SAE-D3 (l)	220	0,3
SAE-D3 (q)	215	0,3
MM	210	0,3
HP (M_7C_3)	280	0,3

A.2-Stress-strain curves used in simulations for the composite

Material	heat treatment		longitu-dinal			transverse	
		σ [MPa]	ε [%]	E* or E_T [MPa]	σ [MPa]	ε [%]	E* or E_T [GPa]
	"Ann"	311	0,14	222142*	343	0,16	214375*
		420	0,58	24773	443	0,63	21276
		559	1,53	14631	580	1,73	12455
		630	2,50	7319	624	2,57	5238
		742	4,33	6120	651	3,50	2903
		825	6,00	4970	684	6,00	1320
SAE-D3	"600"	1073	0,49	218980*	1071	0,50	214200*
		1256	0,81	57187	1243	0,65	114667
		1360	1,14	31515	1306	0,85	31500
		1443	1,50	23055	1423	1,61	15395
		1526	2,43	8925	1526	3,53	5365
		1601	6,00	2100	1602	6,00	3077
	"380"	1460	0,66	221212*	1380	0,64	215625*
		1730	0,91	108000	1525	0,78	103571
		1840	1,08	64706	1722	1,02	82083
		1938	1,30	44545	1935	1,38	59167
		2014	1,59	26207	2023	1,57	46316
		3165	6,00	26100	3400	6,00	31083

A.3-Stress-strain curves used in simulations for the matrix

Material	heat treatment			
		σ [MPa]	ε [%]	E* or E_T [MPa]
Model matrix	"Ann"	310$	0,15	206667*
		380$	0,58	16280
		520$	1,53	14737
		560$	2,50	4124
		670$	5,00	4400
		870$	11,0	3333
		1068#	20,0	2200
		1627#	50,0	1863
		2308#	100,0	1362
		3340#	200,0	1032
	"600"	900$	0,43	209302*
		1080$	0,60	105882
		1200$	0,90	40000
		1400$	1,50	33333
		1480$	3,26	4545
		1780#	10,00	4451
		2071#	20,00	2910
		2599#	50,00	1760
		3146#	100,00	1094
		3866#	200,00	720
	"380"	1550$	0,74	209460*
		1620$	0,79	140000
		1730$	0,91	91667
		1890$	1,32	39024
		2180$	2,53	23967
		2515#	10,0	4485
		2843#	20,0	3280
		3433#	50,0	1967
		4043#	100,0	1220
		4844#	200,0	801

* Young's modulus determined by the slope of the experimental curve
$ taken from [BRO 94]
# determined by the model of Ludwik (see Tab. VI.A.2.1)

B ON THE NUMERICAL IMPLEMENTATION OF THE ELASTO-PLASTIC CONSTITUTIVE MODEL

B.1-Local integration algorithm schemes

B.1.1-Explicit forward Euler integration algorithms

B.1.1.1- General Matrix formulation

The following matrix formulation is adopted so that it holds for a large class of constitutive models. The yield criterion may be written as

$$F(\sigma,\kappa) = f(\sigma) - k(\kappa) = 0 \tag{B.1.1}$$

By differentiating, we obtain the consistency condition

$$dF = \frac{\partial F}{\partial \sigma} d\sigma + \frac{\partial F}{\partial \kappa} d\kappa = 0 \tag{B.1.2}$$

or

$$\mathbf{a}^T d\sigma - A d\lambda = 0 \tag{B.1.3a}$$

with the definitions (the vector **a** being termed flow vector)

$$\mathbf{a}^T = \frac{\partial F}{\partial \sigma} = \left(\frac{\partial F}{\partial \sigma_{xx}} \quad \frac{\partial F}{\partial \sigma_{yy}} \quad \frac{\partial F}{\partial \sigma_{zz}} \quad \frac{\partial F}{\partial \sigma_{yz}} \quad \frac{\partial F}{\partial \sigma_{zx}} \quad \frac{\partial F}{\partial \sigma_{xy}} \right) \tag{B.1.3b}$$

and

$$A = -\frac{1}{d\lambda} \frac{\partial F}{\partial \kappa} d\kappa \tag{B.1.3c}$$

With the assumption of the additive decomposition of the total strain rates, one obtains

$$d\varepsilon = \mathbf{C}^{e^{-1}} d\sigma + d\lambda \frac{\partial F}{\partial \sigma} \tag{B.1.4}$$

Premultiplying both sides of (B.1.4) by $\mathbf{d}_D^T = \mathbf{a}^T \mathbf{C}^e$ and eliminating $\mathbf{a}^T d\sigma$ by use of (B.1.3a), the plastic multiplier is obtained

$$d\lambda = \frac{1}{A + \mathbf{a}^T \mathbf{C}^e \mathbf{a}} \mathbf{a}^T \mathbf{C}^e d\varepsilon \tag{B.1.5}$$

It remains to compute the hardening parameter κ and the scalar A. The work hardening hypothesis relates the plastic strain rate to the rate of the hardening parameter by

$$d\kappa = \sigma^T d\varepsilon^p \tag{B.1.6}$$

and with the normality condition

$$d\kappa = \sigma^T d\varepsilon^p = \sigma^T d\varepsilon^p = \sigma^T d\lambda\, \mathbf{a} = d\lambda\, \mathbf{a}^T \sigma \tag{B.1.7}$$

The equivalent plastic strain rate is obtained using above equation in terms of the effective values:

$$\boldsymbol{\sigma}^T d\boldsymbol{\varepsilon}^p = \sigma_v d\varepsilon_v^p = d\lambda\, \mathbf{a}^T \boldsymbol{\sigma} \quad \Rightarrow d\varepsilon_v^p = \frac{d\lambda\, \mathbf{a}^T \boldsymbol{\sigma}}{\sigma_v} \tag{B.1.8}$$

Comparison with the uniaxial case, where the stresses and plastic strain rates coincide with the effective stresses and equivalent plastic strain rate, respectively, results in

$$d\lambda = d\varepsilon_v^p \tag{B.1.9}$$

$$A = H' \tag{B.1.10a}$$

$$H' = \frac{d\sigma_v}{d\varepsilon_v^p} = \frac{d\sigma_Y}{d\varepsilon_\varpi^p} = \frac{E_T}{1 - \frac{E_T}{E}} \tag{B.1.10b}$$

E_T is the elasto-plastic tangent modulus. Thus A is obtained to be the local slope of the uniaxial stress/plastic strain curve and hence can be determined experimentally.

B.1.1.2-Classical forward Euler first order integration algorithm

a: Determination of initial yielding via the factor α:

$$F\left(\boldsymbol{\sigma}_n + d\boldsymbol{\sigma}_{n+1}^e, \kappa\right) = 0 \tag{B.1.11}$$

with

$$d\boldsymbol{\sigma}_{n+1}^e = \alpha \cdot d\boldsymbol{\sigma}_{n+1}^{trial} \tag{B.1.12a}$$

and

$$\alpha = (1 - R) = \frac{\sigma_{v_{n+1}}^{trial} - \sigma_Y}{\sigma_{v_{n+1}}^{trial} - \sigma_{v_n}}, \quad 0 \le \alpha \le 1 \tag{B.1.12b}$$

If the Gauss point has yielded previously, R becomes obviously 1 and α takes the value 0.

b: Radial corrector:

The predicted trial stress state has to be "returned" to the yield surface (radial to the yield surface at time t_n ! (see Fig. V.3.2).

$$\boldsymbol{\sigma}_{n+1} = \boldsymbol{\sigma}_n + (1 - R) \cdot d\boldsymbol{\sigma}_{n+1}^{trial} + R \cdot d\boldsymbol{\sigma}_{n+1}^{trial} - d\lambda \cdot d\mathbf{d}_D \tag{B.1.13}$$

However, since this explicit method is not adequate for larger time steps, the stability is improved by subdividing this time step into m substeps, each of them with the same size Δt (Subincremental-technique):

$$\boldsymbol{\sigma}_{n+1} = \boldsymbol{\sigma}_n + (1 - R) \cdot d\boldsymbol{\sigma}_{n+1}^{trial} + \Delta t \cdot \left(R \cdot d\boldsymbol{\sigma}_{n+1}^{trial} - d\lambda \cdot d\mathbf{d}_D\right) \tag{B.1.14}$$

The plastic multiplier is obtained from (B.1.5) and the equivalent plastic strain is updated by (B.1.8).

$$\varepsilon^{p}_{v_{n+1}} = \varepsilon^{p}_{v_n} + \frac{d\lambda\, \mathbf{a}^T \boldsymbol{\sigma}}{\sigma_v} \tag{B.1.15}$$

The size of the substep Δt is determined empirically by

$$\Delta t = \frac{1}{m} \quad \text{with } m = \text{Integer}\left(\frac{\sigma^{trial}_{v_{n+1}} - \sigma_{Y_n}}{\sigma_{Y_0}} \right) \cdot 8 + 1 \tag{B.1.16}$$

Since the updated stresses (B.1.13) may not satisfy the yield criterion they are corrected to be scaled onto it

$$\boldsymbol{\sigma}_{n+1} = R_{Corr} \cdot \boldsymbol{\sigma}_{n+1} \tag{B.1.17a}$$

with

$$R_{Corr} = \frac{\sigma_{Y_{n+1}}}{\sigma_{v_{n+1}}} \tag{B.1.17b}$$

B.1.1.3-Modified forward Euler second order integration algorithm with error control [SLO87]

a: Determination of initial yielding via the factor α:

$$F\left(\boldsymbol{\sigma}_n + \alpha \cdot d\boldsymbol{\sigma}^{trial}_{n+1}, \kappa\right) = 0 \tag{B.1.18}$$

Since the above equation defines a single non-linear equation of the form $F(\alpha)=0$, a more accurate estimate for α than that in (B.1.12b) may be obtained by a local Newton-Raphson scheme:

$$d\boldsymbol{\sigma}^{e}_{n+1_k} = \alpha_k \cdot d\boldsymbol{\sigma}^{trial}_{n+1} \tag{B.1.19a}$$

$$\alpha_{k+1} = \alpha_k + \Delta\alpha_{k+1} \tag{B.1.19b}$$

$$\Delta\alpha_{k+1} = -\frac{F\left(\boldsymbol{\sigma}_n + d\boldsymbol{\sigma}^{e}_{n+1_k}, \kappa\right)}{\frac{\partial F}{\partial \alpha}} = -\frac{F\left(\boldsymbol{\sigma}_n + d\boldsymbol{\sigma}^{e}_{n+1_k}, \kappa\right)}{\mathbf{a}_k^T \frac{\partial \boldsymbol{\sigma}}{\partial \alpha}} = -\frac{F\left(\boldsymbol{\sigma}_n + d\boldsymbol{\sigma}^{e}_{n+1_k}, \kappa\right)}{\mathbf{a}_k^T d\boldsymbol{\sigma}^{trial}_{n+1}} \tag{B.1.19c}$$

The iteration may be started for an initial guess for α by (B.1.12b) and terminated when the relative error in the norm of the stresses, defined by $\|\boldsymbol{\sigma}_{k+1} - \boldsymbol{\sigma}_k\| / \|\boldsymbol{\sigma}_k\|$, is less than some specified tolerance.

b: Radial corrector:

The same steps as in the classical Euler scheme have to be followed, however, within each substep the integration is performed twofold. The following steps give a summary of the algorithm:

1. Set t=0 and $\Delta t=1$
2. While t< 1, do steps 3 to 7
3. Compute $\Delta\sigma_i$ and $\Delta\varepsilon^p_{v_i}$ for i=1,2, according to

$$\Delta\sigma_i = \Delta t\cdot\left(R\cdot d\sigma^{trial}_{n+1} - d\lambda_i\cdot dd_{D_i}\right) \tag{B.1.20a}$$

$$d\varepsilon_{vp_i} = \frac{d\lambda\,\mathbf{a}^T\boldsymbol{\sigma}}{\sigma_v}\Big|_i \tag{B.1.20b}$$

and

$$\begin{aligned}\boldsymbol{\sigma}_1 &= \boldsymbol{\sigma}, & \varepsilon^p_{v_1} &= \varepsilon^p_v\\ \boldsymbol{\sigma}_2 &= \boldsymbol{\sigma}+\Delta\sigma_1, & \varepsilon^p_{v_2} &= \varepsilon^p_v+\Delta\varepsilon^p_{v1}\end{aligned} \tag{B.1.20c}$$

4. Compute an estimate of the local truncation error for the substep Δt according to

$$\mathbf{E} = \frac{1}{2}\left(-\Delta\sigma_1+\Delta\sigma_2\right) \tag{B.1.21a}$$

and the new stresses by

$$\hat{\boldsymbol{\sigma}} = \boldsymbol{\sigma}+\frac{1}{2}\left(\Delta\sigma_1+\Delta\sigma_2\right) \tag{B.1.21b}$$

5. compute the relative error for the substep Δt from

$$R_{er} = \max\left\{EPS, \frac{\|\mathbf{E}\|}{\|\hat{\boldsymbol{\sigma}}\|}\right\} \tag{B.1.22}$$

where EPS indicate the smallest error that may be calculated (normally $10^{-14}<EPS<10^{-16}$)

6. if R >Tol (normally $10^{-2}<Tol<10^{-5}$), then go to step 7. Else, this substep is accepted so update Δt, the stresses and the equivalent plastic strains according to

$$t = t+\Delta t \tag{B.1.23a}$$

$$\boldsymbol{\sigma} = \hat{\boldsymbol{\sigma}} \tag{B.1.23b}$$

$$\varepsilon^p_v = \varepsilon^p_v+\frac{1}{2}\left(\Delta\varepsilon^p_{v_1}+\Delta\varepsilon^p_{v_2}\right) \tag{B.1.23c}$$

Then extrapolate to obtain the size of the next substep by [SLO 87]

$$q = \min\left\{0.8\sqrt{\frac{Tol}{R_{er}}}, 2\right\} \tag{B.1.23d}$$

$$\Delta t = q\cdot\Delta t \tag{B.1.23e}$$

check that the integration does not proceed beyond t=1 by

$$\Delta t = \min\left\{\Delta t, 1-t\right\} \tag{B.1.23f}$$

return to step 2

7. This substep has failed, so extrapolate to obtain a smaller dimensionless time step by [SLO 87]

$$q = \max\left\{0.8\sqrt{\frac{Tol}{R_{er}}}, 0.1\right\} \tag{B.1.24a}$$

$$\Delta t = q \cdot \Delta t \tag{B.1.24b}$$

return to step 2.

8. exit with stresses at time t_{n+1} given by $\sigma_{n+1}=\sigma$.

This algorithm has been implemented into the FE-Code Crackan with the aim to control the error during the integration process.

B.1.2-Implicit backward Euler integration algorithm (radial return algorithm)

The radial return algorithm [SIM 85, 86] is formulated as follows (radial to the yield surface at time t_{n+1} ! (see Fig. V.3.2))

$$\varepsilon^p_{n+1} = \varepsilon^p_n + \dot{\lambda}\,\sigma^D_{n+1} \tag{B.1.25a}$$

$$\varepsilon^p_{v_{n+1}} = \varepsilon^p_{v_n} + \dot{\lambda}\sqrt{\frac{2}{3}\sigma^{D\,T}_{n+1}\,\mathbf{P}\,\sigma^D_{n+1}} \tag{B.1.25b}$$

$$\sigma^D_{n+1} = G\left(\varepsilon^D_{n+1} - \varepsilon^p_{n+1}\right) \tag{B.1.26a}$$

$$\mathbf{P} = \begin{pmatrix} 1 & 0 & 0 \\ 0 & 1 & 0 \\ 0 & 0 & 2 \end{pmatrix} \tag{B.1.26b}$$

$\dot{\lambda}$ is obtained by satisfaction of the yield criterion at the end of the step

$$F\left(\sigma_{n+1}, \varepsilon^p_{v_{n+1}}\right) = \frac{1}{2}\sigma^{D\,T}_{n+1}\,\mathbf{P}\,\sigma^D_{n+1} - \frac{1}{3}\kappa^2\left(\varepsilon^p_{v_{n+1}}\right) = 0 \tag{B.1.27a}$$

with

$$\kappa\left(\varepsilon^p_{v_{n+1}}\right) = \sigma_{Y0} + H\,\varepsilon^p_{v_{n+1}} \tag{B.1.27b}$$

being the current yield surface. If we substitute (B.1.25) and (B.1.26) in (B.1.27), one obtains after some manipulations the non-linear equation only dependent of $\dot{\lambda}$

$$\rho\left(\dot{\lambda}\right) = \frac{1}{2}\frac{\sigma^{D\,T}_{n+1}\,\mathbf{P}\,\sigma^D_{n+1}}{\left(1+G\dot{\lambda}\right)} - \frac{1}{3}\kappa^2\left(\varepsilon^p_{v_{n+1}}\right) = 0 \tag{B.1.28a}$$

$$\varepsilon^{p}_{v_{n+1}} = \varepsilon^{p}_{v_n} + \frac{\dot{\lambda}}{1+G\dot{\lambda}}\sqrt{\frac{2}{3}\boldsymbol{\sigma}^{trD\,T}_{n+1}\,\mathbf{P}\,\boldsymbol{\sigma}^{trD}_{n+1}} \qquad \text{(B.1.28b)}$$

where $\boldsymbol{\sigma}^{trD}_{n+1}$ is the elastic predictor at t_{n+1}

$$\boldsymbol{\sigma}^{trD}_{n+1} = \boldsymbol{\sigma}^{trD}_{n} + G\,\mathbf{D}^{D}_{n+1} \qquad \text{(B.1.28c)}$$

The plastic multiplier is determined from equation (B.1.28a) applying a local Newton-Raphson scheme. The remaining unknowns are obtained from the plastic multiplier.

B.2-Evaluation of the elasto-plastic matrix (tangent operator) C^{ep}

B.2.1-Continuum tangent operator

The continuum tangent operator is simply obtained when the expression for the plastic multiplier (B.1.5) is used in (B.1.4). It leads to

$$d\boldsymbol{\sigma} = \mathbf{C}^{ep}\,d\boldsymbol{\varepsilon} \qquad \text{(B.2.1a)}$$

$$\mathbf{C}^{ep} = \mathbf{C}^{e} - \frac{\mathbf{d}_D\mathbf{d}_D^{T}}{A + \mathbf{d}_D^{T}\mathbf{a}} \qquad \text{(B.2.1b)}$$

B.2.2-Consistent tangent operator (consistent with radial return algorithm)

The consistent tangent operator is computed directly from the integration algorithm by

$$d\boldsymbol{\sigma}_{n+1} = \mathbf{C}^{ep}\,d\boldsymbol{\varepsilon}_{n+1} \quad \text{with } \mathbf{C}^{ep} = \frac{\partial\boldsymbol{\sigma}_{n+1}}{\partial\boldsymbol{\varepsilon}_{n+1}} \qquad \text{(B.2.2)}$$

After eqns. (B.1.25a) and (B.1.26a) one obtains

$$d\boldsymbol{\sigma}^{D}_{n+1} = G\left(d\boldsymbol{\varepsilon}^{D}_{n+1} - \lambda d\boldsymbol{\sigma}^{D}_{n+1} - d\lambda\boldsymbol{\sigma}^{D}_{n+1}\right) \qquad \text{(B.2.3a)}$$

and therefore

$$d\boldsymbol{\sigma}^{D}_{n+1} = \frac{G}{1+G\lambda}\left(d\boldsymbol{\varepsilon}^{D}_{n+1} - d\lambda\boldsymbol{\sigma}^{D}_{n+1}\right) \qquad \text{(B.2.3b)}$$

The satisfaction of the yield criterion gives

$$\boldsymbol{\sigma}^{D\,T}_{n+1}\,\mathbf{P}\,d\boldsymbol{\sigma}^{D}_{n+1} - \frac{2}{3}\kappa\left(\varepsilon^{p}_{v_{n+1}}\right)\kappa'\left(\varepsilon^{p}_{v_{n+1}}\right)d\varepsilon^{p}_{v_{n+1}} = 0 \qquad \text{(B.2.4a)}$$

$$d\varepsilon^{p}_{v_{n+1}} = \sqrt{\frac{2}{3}}\left(d\lambda\,\phi + \lambda\frac{\boldsymbol{\sigma}^{D\,T}_{n+1}\,\mathbf{P}\,d\boldsymbol{\sigma}^{D}_{n+1}}{\phi}\right) \qquad \text{(B.2.4b)}$$

$$\phi = \sqrt{{\sigma^D_{n+1}}^T \mathbf{P}\, d\sigma^D_{n+1}} \tag{B.2.4c}$$

Satisfying the yield criterion at the end of the time step

$$\sqrt{\frac{2}{3}}\kappa = \phi \tag{B.2.5}$$

and after some developments, one obtains

$$d\lambda = \frac{1-\frac{2}{3}\kappa'\lambda}{\frac{2}{3}\kappa'\phi^2}{\sigma^D_{n+1}}^T \mathbf{P}\, d\sigma^D_{n+1} \tag{B.2.6}$$

The relation leads to

$${\sigma^D_{n+1}}^T \mathbf{P}\, d\sigma^D_{n+1} = \frac{G}{1+G\lambda}\left({\sigma^D_{n+1}}^T \mathbf{P}\, d\varepsilon^D_{n+1} - d\lambda\phi^2\right) \tag{B.2.7}$$

The last two relations serve to evaluate the plastic multiplier by

$$d\lambda = \frac{1-\frac{2}{3}\kappa'\lambda}{\left(1+\frac{2}{3}\frac{\kappa'}{G}\right)\phi^2}{\sigma^D_{n+1}}^T \mathbf{P}\, d\varepsilon^D_{n+1} \tag{B.2.8}$$

and using eqn. (B.2.3a) gives finally

$$d\sigma^D_{n+1} = \frac{G}{1+G\lambda}\left(d\varepsilon^D_{n+1} - \frac{1-\frac{2}{3}\kappa'\lambda}{\left(1+\frac{2}{3}\frac{\kappa'}{G}\right)\phi^2}\sigma^D_{n+1}{\sigma^D_{n+1}}^T \mathbf{P}\, d\varepsilon^D_{n+1}\right) \tag{B.2.9}$$

From this equation, the tangent operator consistent with the radial return algorithm is derived satisfying eqn (B.2.2). Therefore it holds

$$\mathbf{C}^{ep} = \mathbf{A} - \frac{1}{3}(\mathbf{A} - K\,\mathbf{I})\,\mathbf{U} \tag{B.2.10}$$

with

$$K = \frac{E}{(1-2\nu)} \tag{B.2.11a}$$

$$\mathbf{U} = \begin{bmatrix} 1 & 1 & 0 \\ 1 & 1 & 0 \\ 0 & 0 & 0 \end{bmatrix} \tag{B.2.11b}$$

$$\mathbf{A} = \frac{G}{1+G\lambda}\left(\mathbf{I} - \frac{1-\frac{2}{3}\kappa'\lambda}{\left(1+\frac{2}{3}\frac{\kappa'}{G}\right)\phi^2}\sigma^D_{n+1}\sigma^{D\ T}_{n+1}\mathbf{P}\right) \qquad \text{(B.2.11c)}$$

B.3-Polar decomposition scheme

Several algorithms are proposed in the literature to realize the polar decomposition of **F**. As described in Chapter III one method to obtain **R** is to solve the eigenvalue problem. Hoger and Carlson [HOG 84] proposed a method which is based on the Cayley-Hamilton theorem and which avoids the calculation of the eigenvalues. We use the method proposed by Dabounou [DAB 94], which is restricted to 2D but in that case simple and effective.
The matrix **R** is then described by

$$\mathbf{R} = \begin{pmatrix} \cos\theta & \sin\theta \\ -\sin\theta & \cos\theta \end{pmatrix}, \quad \mathbf{U} = \begin{pmatrix} U_{11} & U_{12} \\ U_{12} & U_{22} \end{pmatrix} \qquad (3.29)$$

Introducing I_f, C_f and I_u by

$$\begin{aligned} &I_F = F_{11} + F_{22}, \quad C_F = F_{12} - F_{21}, \\ &I_U = \sqrt{I_F^{\,2} + C_F^{\,2}} \end{aligned} \qquad (3.30)$$

we obtain for cosθ, sinθ

$$\cos\theta = \frac{I_F}{I_U}, \quad \sin\theta = \frac{C_F}{I_U} \qquad (3.31)$$

Finally we determine **U** by

$$\mathbf{U} = \mathbf{R}^T\mathbf{F} \qquad (3.32)$$

C THE MORI-TANAKA APPROACH

C.1-Elasticity (Formulation by Benveniste)

Benveniste [BEN 87] established the relationship between the Mori-Tanaka Model and Eshelby's equivalent dilute solution. Eshelby introduced the strain localisation tensor $\mathbf{A}_r$ by

$$\boldsymbol{\varepsilon}_r^{Esh} = \mathbf{A}_r^{Esh}\mathbf{E} \tag{C.1.1a}$$

with

$$\mathbf{A}_r^{Esh} = \left[\mathbf{I}+\mathbf{S}_r\mathbf{C}_0^{-1}(\mathbf{C}_r-\mathbf{C}_0)\right]^{-1} \tag{C.1.1b}$$

Since this solution does not imply interaction effects between HP, the Mori-Tanaka model suggested

$$\boldsymbol{\varepsilon}_r^{Esh} = \mathbf{T}_r^{MT}\boldsymbol{\varepsilon}_0 \tag{C.1.2}$$

Indeed, since the remote macroscopic strain field $\mathbf{E}$ is replaced by the mean strain experienced by the matrix, the mutual deformation constraint of the HP is described to some extent. The tensor $\mathbf{T}_r$ is taken to coincide with the strain localisation tensor of Eshelby. This expression is equivalent to that used in (I.2.42b).

The following steps have to be performed in order to obtain the effective elastic moduli for the composite. These steps have been implemented into the Fortran-Code "Tractan". A more detailed description of the programme can be found in [PLA 95]. Readers which are more interested in the theoretical background may be referred to [e.g. BEN 87, BOU 94].

1. Enter the volume fraction and the isotropic elastic characteristics of the matrix E_0, ν_0 and of the individual phases E_r, ν_r, respectively

2. Fix the shape of the individual phases (ellipsoid, sphere, cylinder, penny-shape etc.)

3. Enter the boundary conditions (here the macroscopic stress $\boldsymbol{\Sigma}$)

4. Compute the elastic and the compliance matrix of the metal matrix $\mathbf{C}_0$, $\mathbf{M}_0$ and of the individual phases $\mathbf{C}_r$, $\mathbf{M}_r$

5. Compute the Eshelby tensor $\mathbf{S}_r$ of the individual phases respecting the chosen shape for them (step 2)

6. Compute the tensors $\mathbf{T}_r$ and $\mathbf{W}_r$

$$\mathbf{T}_r^{Esh} = \left[\mathbf{I}+\mathbf{S}_r\mathbf{C}_0^{-1}(\mathbf{C}_r-\mathbf{C}_0)\right]^{-1} \tag{C.1.3a}$$

$$\mathbf{W}_r^{Esh} = \left[\mathbf{I}-\mathbf{C}_0(\mathbf{S}_r-\mathbf{I})(\mathbf{M}_r-\mathbf{M}_0)\right]^{-1} \tag{C.1.3b}$$

7. Compute the effective elastic matrix $\mathbf{C}$

$$\mathbf{C}^{MT} = \left(\sum_{r=0}^{r=N}\xi_r\mathbf{C}_r\mathbf{T}_r^{MT}\right)\left(\sum_{r=0}^{r=N}\xi_r\mathbf{T}_r^{MT}\right)^{-1} \tag{C.1.4}$$

with $\mathbf{T}_0=\mathbf{I}$

8. Compute the effective strain

$$\mathbf{E}^{MT} = \mathbf{C}^{MT^{-1}}\boldsymbol{\Sigma} \tag{C.1.5}$$

9. Compute the mean strain within the phases

$$\boldsymbol{\varepsilon}_0 = \left(\sum_{r=0}^{r=N}\xi_r \mathbf{T}_r^{MT}\right)^{-1}\mathbf{E} \tag{C.1.6a}$$

$$\boldsymbol{\varepsilon}_r = \mathbf{T}_r^{MT}\left(\sum_{r=0}^{r=N}\xi_r \mathbf{T}_r^{MT}\right)^{-1}\mathbf{E} \tag{C.1.6b}$$

10. Compute the mean stress within the phases

$$\boldsymbol{\sigma}_0 = \mathbf{C}_0^{MT}\boldsymbol{\varepsilon}_0 \tag{C.1.7a}$$

$$\boldsymbol{\sigma}_r = \mathbf{C}_r^{MT}\boldsymbol{\varepsilon}_r \tag{C.1.7b}$$

Remark
The different tensors of Eshelby for different reinforcement shapes may be found in [MUR 87, BOU 94]. The conventions used for the tensor operations throughout the programme and the notation for the isotropic and orthotropic elastic and compliance matrix, respectively may be found in [BOU 94, PLA 95].

C.2-Extension to Plasticity-Secant approach

The secant approach [see e.g. TAN 88, BOU 94] is an effective method to account for matrix plasticity by simply extending the relations in elasticity. In all equations the tensor of the elastic moduli of the matrix is replaced by that of the *secant* moduli. These moduli are computed for an isotropic matrix as follows:

Secant Young's modulus of the matrix (eqn. I.2.48) (Equivalence of uniaxial and triaxial stress state)

$$E_0^{sec} = \frac{\sigma_v}{\varepsilon_v^e + \varepsilon_v^p} = \frac{1}{\dfrac{1}{E_0} + \dfrac{\varepsilon_v^p}{\sigma_{Y0} + h_0\left(\varepsilon_v^p\right)^n}} \tag{C.2.1}$$

Secant Poisson ratio of the matrix

$$\nu_0^{sec} = \frac{1}{2} - \left(\frac{1}{2} - \nu_0\right)\frac{E_0^{sec}}{E_0} \tag{C.2.2a}$$

The latter relation was obtained by the following hypotheses:
1-The matrix is assumed to be plastically incompressible therefore the bulk modulus K_0 and the secant bulk modulus K_0^{sec} of the matrix are identical:

$$K_0^{sec} = K_0 \tag{C.2.2b}$$

2-The relations between the secant moduli are the same as for the elastic moduli:

$$K_0^{sec} = \frac{E_0^{sec}}{3\left(1-2\nu_0^{sec}\right)}, \qquad G_0^{sec} = \frac{E_0^{sec}}{2\left(1+\nu_0^{sec}\right)} \tag{C.2.2c}$$

If the matrix is subjected to a monotonic proportional loading, the state of plasticity in the matrix is determined when E_0^{sec}, E_0 and ν_0 are known

The following relations provide the basis for this elastic-plastic analysis. This set of equations has to be solved in an iterative manner [PLA 95] (for an imposed macroscopic stress Σ):

• Relation of the stress concentration in the matrix

$$\boldsymbol{\sigma}_0 = \mathbf{B}_0^{Sec}\,\boldsymbol{\Sigma} \quad \text{with} \quad \mathbf{B}_0^{Sec} = \mathbf{L}_0^{Sec}\left(\xi_0\,\mathbf{L}_0^{Sec} + \sum_{r=1}^{N}\xi_r\,\mathbf{L}_r\,\mathbf{T}_r^{Sec}\right)^{-1} \tag{C.2.3a}$$

and

$$\mathbf{T}_r^{Sec} = \left[\mathbf{I} + \mathbf{S}_r\left(\mathbf{L}_0^{Sec}\right)^{-1}\left(\mathbf{L}_r - \mathbf{L}_0^{Sec}\right)\right]^{-1} \tag{C.2.3b}$$

• Expression of the secant compliance matrix of the composite

$$\mathbf{M}^{Sec} = \left(\xi_0\,\mathbf{I} + \sum_{r=1}^{N}\xi_r\,\mathbf{T}_r^{Sec}\right)\left(\xi_0\,\mathbf{L}_0^{Sec} + \sum_{r=1}^{N}\xi_r\,\mathbf{L}_r\,\mathbf{T}_r^{Sec}\right)^{-1} \tag{C.2.4}$$

• constitutive relation of the matrix (written schematically, see relations in elasto-plasticity chapter III, V, Annex B)

$$\boldsymbol{\sigma}_0 = f\left(\mathbf{L}_0^{Sec}\right) \tag{C.2.5}$$

• Decomposition of the total deformation of the composite into an elastic and a plastic part

$$\mathbf{E} = \mathbf{E}^e + \mathbf{E}^p = \mathbf{M}\,\boldsymbol{\Sigma} + \mathbf{E}^p \tag{C.2.6a}$$

with

$$\mathbf{E}^p = \left(\mathbf{M}^{Sec} - \mathbf{M}\right)\boldsymbol{\Sigma} \tag{C.2.6b}$$

The compliance and the constitutive tensor of the composite are retained, e.g.

$$\mathbf{M} = \left(\sum_{r=0}^{N}\xi_r\,\mathbf{T}_r\right)\left(\sum_{r=0}^{N}\xi_r\,\mathbf{L}_r\,\mathbf{T}_r\right)^{-1} \text{ with } \mathbf{T}_r = \left[\mathbf{I} + \mathbf{S}_r(\mathbf{L}_0)^{-1}(\mathbf{L}_r - \mathbf{L}_0)\right]^{-1} \tag{C.2.7}$$

RÉSUMÉ

Durant les dernières années, l'intérêt des industriels pour les matériaux avancés possédant des caractéristiques mieux adaptées à leur utilisation a intensifié considérablement la recherche en micromécanique. L'objectif est d'acquérir une meilleure compréhension de la liaison entre la microstructure et les caractéristiques mécaniques macroscopiques. Les paramètres d'influence de cette relation sont d'une part la topologie de la microstructure et d'autre part le comportement de chaque composant individuel (déformation plastique, endommagement, etc.).

Le développement d'un modèle numérique, basé sur les observations expérimentales d'un acier d'outil bi-phasique, a permis d'étudier le comportement et l'endommagement de composites renforcés à matrice métallique. Différents critères d'endommagement locaux combinés à des méthodes de simulations avancées ont été proposés. Ceci afin de simuler la défaillance locale des phases dures (HP) par fissuration ou décohésion et afin de prévoir l'initiation de l'endommagement ductile de la matrice métallique (MM). Pour une analyse précise du comportement de la matrice à hautes déformations plastiques, la théorie géométriquement linéaire élasto-plastique a été étendue aux grandes déformations.

Les simulations à l'échelle microscopique montrent une forte influence des paramètres géométriques tels que la quantité, la forme et la distribution des phases dures sur le champs local de contraintes et de déformations. L'apparition initiale d'endommagement est contrôlée par la forme, la distance et l'orientation des phases dures voisines par rapport à la direction principale de charge. La perte soudaine de capacité de charge par microfissuration affecte la redistribution des contraintes et favorise la défaillance des phases dures voisines. Dans le cas où celles-ci ne sont pas distribuées régulièrement sur la microstructure mais concentrées en dehors des colonies, le degré de la continuité de ces colonies devient un paramètre important. La largeur des "bandes de la matrice" dans le cas d'arrangements groupés ("clusters") agit comme un obstacle à l'unification des microfissures des"clusters" adjacents.

Par ailleurs, différentes méthodes de transition entre l'échelle micro et macroscopique ont été développées. Des méthodes d'homogénéisation sont appliquées afin de prévoir le comportement global a partir des propriétés équivalentes du composite. Une nouvelle approche est proposée qui consiste à dériver un paramètre d'endommagement équivalent par des simulations incrémentales de microfissuration progressive. Cette méthode permet de mettre en valeur l'influence des caractéristiques microstructurales sur la réponse globale d'endommagement. Finalement, une section microscopique à la pointe d'une fissure de fatigue d'une éprouvette sollicitée en flexion trois points est modélisée. Les conditions aux limites réelles sont reproduites en combinant le modèle macro et microscopique. La rupture progressive des phases dures est visualisée au fur et à mesure du chargement macroscopique.

Mots-clés
matériau bi-phasique, composite à matrice métallique, méthode des éléments finis, homogénéisation, plasticité, endommagement, rupture des particules, décohésion matrice/renfort, grandes déformations